TOPOLOGICAL STUDIES OF CIRCULAR AND ELLIPTIC JETS IN A CROSS FLOW

NEW TZE HOW, DANIEL

NATIONAL UNIVERSITY OF SINGAPORE

2004

TOPOLOGICAL STUDIES OF CIRCULAR AND ELLIPTIC JETS IN A CROSS FLOW

NEW TZE HOW, DANIEL
(B. Eng. (Hons), NUS)

A THESIS SUBMITTED

FOR THE DEGREE OF DOCTOR OF PHILOSOPHY

DEPARTMENT OF MECHANICAL ENGINEERING

NATIONAL UNIVERSITY OF SINGAPORE

2004

Acknowledgements

The author would like to take this opportunity to extend his gratitude to those whose valuable contributions have made this project a possibility. They are:

My supervisors, Associate. Prof. Lim Tee Tai and Associate. Prof. Luo Siao Chung for their guidance, support and encouragement throughout this research project.

Professor Julio Soria for his advice and guidance in conducting PIV measurements.

Fluid Mechanics laboratory Officers, Mr Yap Chin Seng, Mr Tan Kim Wah, Mr James Ng Chun Phew, Mr Yap Khai Seng and the staff of the Engineering Workshop for their advice and for constructing various pieces of experimental equipment.

Dr Lua Kim Boon and fellow student Mr Teo Chiang Juay for their technical assistance and many late-night discussions that somehow kept going back to Fluid Mechanics.

Past and present undergraduate students that I have tutored for keeping me motivated and sane all this while.

National University of Singapore for providing Research Scholarship to carry out this project.

Summary

The present project was divided into two parts. The first part examined the effects of jet exit velocity profiles on the flow structure development of a circular jet in cross flow (henceforth referred to as CJICF), and the second part looked at the effects of jet exit geometry on the characteristics of non-circular jet in a cross flow. In all cases, the cross flow was maintained in a laminar condition and qualitative flow visualization and quantitative particle image velocimetry investigations were carried out on the flow field. For the first task, three sets of top-hat and parabolic velocity profile circular jets of varying diameters (Re=625 to 1645, depending on exact jet geometry and MR=2.31 to 5.77) were subjected in a cross flow environment, and the results show that the thicker shear layer associated with the parabolic velocity profiles (henceforth referred to as parabolic jet) is inherently more stable than the thin shear layer in the top-hat profiles (henceforth referred to as top-hat jet). As a result, the production of leading-edge vortices in the parabolic jet was delayed much further downstream, and these vortices were formed less coherently than their top-hat counterparts. Unexpectedly, the results also show that production of the leading edge vortices was not coupled with the production of lee side vortices. This finding suggested that the current practice of using vortex rings to model the large-scale jet structures might not give a true representation of the actual flow situation, since the vortex ring model implies that the generation of a leading edge vortex must be accompanied by a corresponding lee side vortex. This anomaly prompted us to probe deeper into the matter. And the results showed that, unlike the free jet, the presence of a counter rotating vortex pair (henceforth referred to as CVP) in CJICF inhibited the formation of the vortex rings. Instead two independent rows of interconnecting vortex loops were formed at the leading edge and lee side of the jet column. As these vortices convected downstream, the "side arms" of these vortices

eventually merged with the CVP. In the light of this finding, a new vortex skeleton model for CJICF is proposed.

As for the second task, although non-circular jet encompassed a wide range of geometry, such as rectangle, square and ellipse, our attention is focused primarily on the last geometry. The ellipse was chosen because it was a logical extension of the circular jet, since the orifice perimeter varies smoothly without any sharp corners. In fact, a circle could be viewed as a special case of an ellipse with an aspect ratio of one. In the present investigation, two aspect ratios of the ellipse (i.e. 2 and 3) were considered, and they were aligned with their major axes either normal or parallel to the cross flow (AR=0.3, 0.5, 2 and 3 for VR=1 to 5, Re_h=890 to 4440 for AR=0.3 and 3 elliptic jet, and 1020 to 5090 for AR=0.5 and 2 elliptic jet). In both cases, the exit areas of the ellipses were the same. Qualitative investigations using flow visualization show that, regardless of the aspect ratios and orientation of the jet, the far-field large-scale jet structures were similar for both geometry, and akin to that of a circular geometry. This suggests that the far-field jet structures depend only on the gross geometry of the nozzle, and are independent of its shape. However, in the near-field, the situations are quite different. Here, the flow structures depended not only on aspect ratios, but also on the orientation of the jet with respect to the cross flow. With the major-axis of the ellipse aligned with the cross flow, the jet shear layer was found to develop two sets of CVP, namely primary CVP and a much weaker secondary CVP. As they traveled downstream, the secondary CVP was eventually overwhelmed by the primary CVP, and once merged, the overall jet structures were similar to that of a CJICF. Also, the leading edge vortices were more intense than their counterpart in the case of the major-axis aligned with the cross flow, and this invariably led to stronger vortex interaction and subsequent pairing as they convected downstream. To better understand this pairing process, quantitative measurements using

particle image velocimetry (PIV) were carried out and the results are reported in the thesis. With the major-axis normal to the cross flow, no such vortex pairing was observed. Furthermore, the jet shear layer in this configuration was found to develop additional pairs of folds at the leading edge of the jet column, and depending on the manner in which they were produced, could lead to what Haven and Kurosaka (1997) referred to "kidney" and "anti-kidney" vortices. Although our results generally agree with the finding of Haven and Kurosaka (1997), they differed in the interpretation of how the two above mentioned vortices are produced. In addition, our investigation revealed certain flow features, which have not been reported previously. Based on our findings, the vortex skeleton models for the elliptic jets are proposed, which agree with the experimental observation. In the far-field, the models are no different from that of a circular jet, however in the near field, they are distinct variations in their flow features because of the additional folds in shear layer of the elliptic jet. The details are reported in the thesis.

List of Figures

List of Tables

List of Symbols

AR	Aspect ratio, streamwise axis to cross stream axis ratio
CJICF	Circular jet in cross flow
CVP	Counter-rotating vortex pair
EJICF	Elliptic jet in cross flow
JICF	Jet in cross flow
MR	Jet to cross flow momentum ratio, $\dfrac{\int \rho_{\text{jet}} V_{\text{jet}}^2 dA}{\rho_{\text{crossflow}} V_{\text{crossflow}}^2 A_{\text{jet}}}$
VR	Jet to cross flow velocity ratio, $\dfrac{V_{\text{jet}}}{V_{\text{crossflow}}}$
A_{jet}	Cross-sectional area of jet
D	Circular jet diameter
D_h	Jet hydraulic diameter
D_{major}	Major-axis diameter of elliptic jet
D_{minor}	Minor-axis diameter of elliptic jet
r	Velocity ratio (Smith and Mungal, 1998)
Re	Jet Reynolds number, $\dfrac{V_{\text{jet}}D}{\nu_{\text{jet}}}$
s	Distance from the jet exit along the mean jet trajectory
u	Mean velocity component along the cross flow direction
v	Mean velocity component normal to the cross flow direction
$\langle V \rangle$	Mean velocity magnitude, $\sqrt{u^2 + v^2}$

$V_{crossflow}$	Mean cross flow velocity
V_{jet}	Mean jet velocity
x	Distance downstream from jet exit centre
y	Distance normal to cross flow from jet exit centre
z	Distance vertically away from jet exit
$\rho_{crossflow}$	Density of cross flow fluid
ρ_{jet}	Density of jet fluid
ν_{jet}	Kinematic viscosity of jet fluid

Chapter 1

Introduction

1.1   Background

A jet in cross flow (JICF) is a flow scenario whereby a jet exhausts into a uniform free stream or cross flow at a certain angle. Of the many possible configurations, the one with the jet exhausting normally into the cross flow generates the most interest as it represents the bulk of the flow situations encountered in real-life engineering applications. Therefore, the JICF phenomenon has seen important developments and applications in numerous areas such as film cooling for turbines and combustors, fuel injection for burners, thrust reversers for propulsive systems as well as in the research of S/VTOL aircrafts, to name a few. More recently, interest in the extent of air and water pollution in terms of smoke and effluent discharge into the natural environment via the same phenomenon promotes further research in this area. Figure 1.1 shows several images depicting some of the above applications.

Despite more than six decades of research in this area, complete understanding of the JICF phenomenon still eludes the research community. Numerous studies, both experimentally and numerically, have been previously carried out by Keffer and Baines (1963), Pratte and Baines (1967), Durando (1971), McMahon et al. (1971), Kamotani and Greber (1972), Fearn and Weston (1974), Chassaing et al. (1974), Bergeles et al. (1976), Moussa et al. (1977), Patankar et al. (1977), Crabb et al. (1981), Andreopoulos (1982), Rajarantnam (1983), Andreopoulos and Rodi (1984), Broadwell and Briedenthal (1984), Nunn (1985), Karagozian (1986), Sykes et al. (1986), Wu et al. (1988), Needham et al. (1988 & 1990), Coelho and Hunt (1989), Krothapali et al. (1990), Claus and Vanka (1992),

1

(a)

(b)

(c)

Figure 1.1   Some applications of jet in a cross flow: (a) S/VTOL aircraft propulsion used by BAE SYSTEMS and Boeing in the Harrier aircraft, (b) volcanic dispersion, and (c) pollution caused by smoke stack emission.
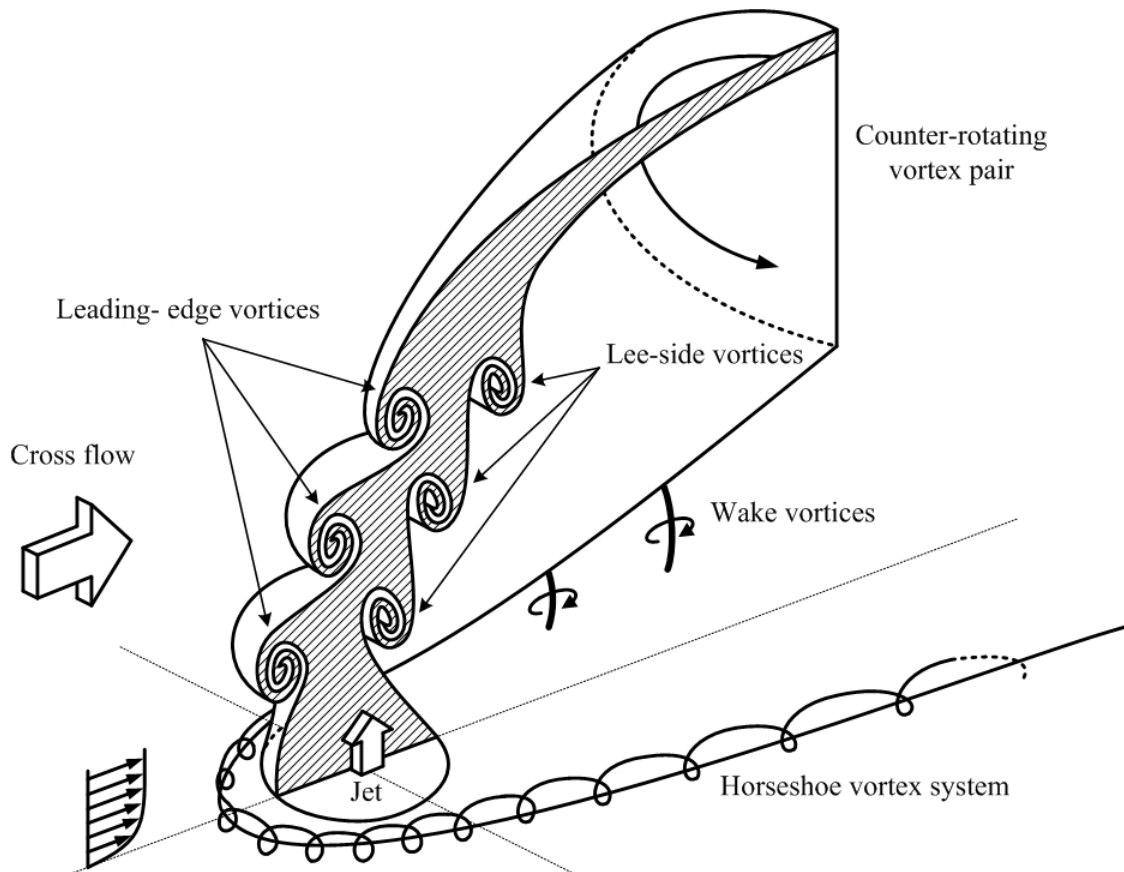
Figure 1.2   Schematics of vortex structures of a circular jet in cross flow. The shaded region indicates the cross-section obtained along the symmetrical plane.

Fric and Roshko (1994), Kelso and Smits (1995), Chang and Vakili (1995), Kelso et al. (1996), Rudman (1996), Eiff and Keffer (1997), Haven and Kurosaka (1997), Brizzi et al. (1998), Smith and Mungal (1998), Blanchard et al. (1999), Yuan et al. (1999), Lee et al. (1999), Hale et al. (2000), Kim et al. (2000), Lim et al. (2000), Hasselbrink and Mungal (2001a, 2001b), Rivero et al. (2001), Cortelezzi and Karagozian (2001) and Gollahalli and Pardiwalla (2002). One of the main reasons why analysis of this particular flowfield is so daunting lies in the highly complex three-dimensional flow structures, which are made up of four dominant vortical structures. They are namely, the horseshoe vortex system, the counter-rotating vortex pair (CVP), the leading-edge (or shear layer) vortices with lee-side vortices and the wake vortices (see Figure 1.2). These four vortical structures interact with one another, resulting in a highly three-dimensional flow, which more often than not, made detailed observations difficult.
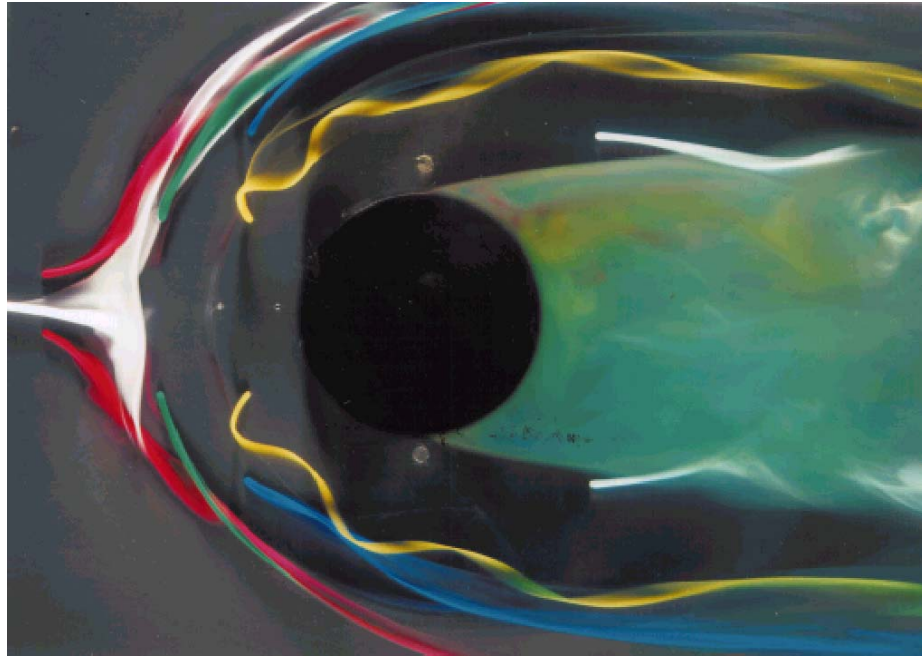
Figure 1.3   Horseshoe vortex systems in front of cylinder/surface junction. Different colour dye was used to illustrate different flow regimes of the vortex system at selected locations upstream of the circular cylinder (Reproduced with permission from Délery (2001), ONERA document by Henri Werlé).

1.1.1   Horseshoe Vortex System

The horseshoe vortex system is similar to that which occurs in flow past a bluff body/surface junction (see Figure 1.3), where the presence of an obstruction causes the vorticity in the approaching boundary layer to roll up into a system of horseshoe vortices. However, the case for a JICF differs from that of a bluff body in that the obstructing structure is a transverse jet, which interacts with the horseshoe vortex system, resulting in changes in the overall flow topology. Furthermore, the formation of the leading-edge vortices is highly-dependent on the instability of the jet shear layer and therefore, any external influence exerted by other flow structures, such as the horseshoe vortices, may lead to greater level of instability. Kelso and Smits (1995) and Kelso et al. (1996) further found that the horseshoe vortex system, which is actually comprised of two or more counter-clockwise and clockwise vortices (depending on the flow conditions), might be responsible for the observed near-wall secondary CVP and the wake vortices.
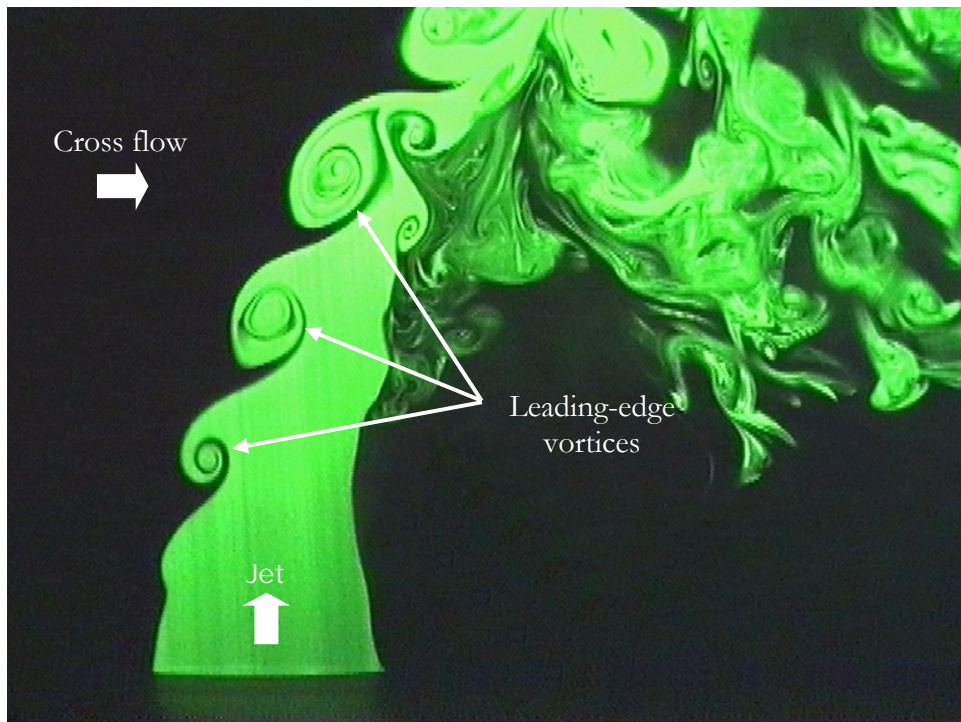
Figure 1.4   Leading-edge or shear layer vortices shedding regularly along the leading-edge region of the jet/cross flow interface (from present study).

1.1.2   Leading-Edge Vortices

One of the most prominent features of JICF is the coherent leading-edge vortices as illustrated in Figure 1.4. Also known as jet shear layer vortices, they usually appear as a train of "daisy-chained" interconnecting vortices along the leading-edge region of the jet shear layer/cross flow interface. It has been previously reported by Becker and Massaro (1968) and Gutmark and Ho (1983) that these vortices are essentially the same as the vortex rings in free jets, largely accepted to be due to the Kelvin-Helmholtz instability of the annular jet shear layer. Because of this, many of the current models of JICF were based on the vortex rings. For example, Kelso et al. (1996) made use of vortex rings to explain their experimental observations in a circular JICF, and likewise, Skyes et al. (1986) and Chang and Vakili (1995) have used vortex rings as the fundamental building block to model their JICF simulations. In fact, the prevalence of this widely-accepted notion could be seen in the experimental works by Chang and Vakili (1995) and Lim et al. (1998)
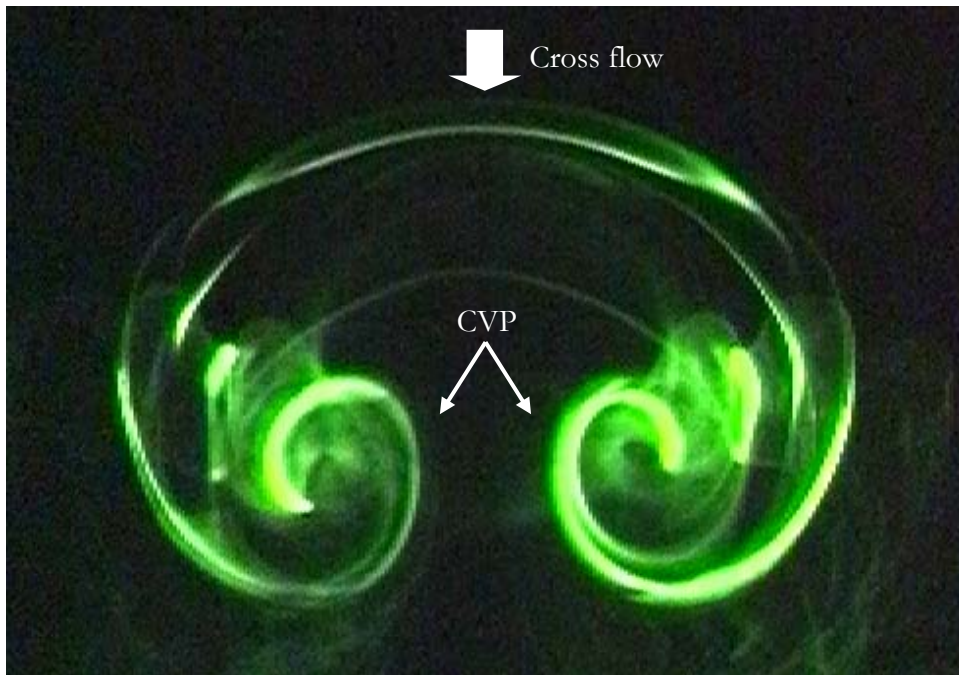
Figure 1.5   A typical counter-rotating vortex pair (CVP) arising from a circular JICF (from present study).

who went on to fire circular vortex rings into a cross flow to determine their behaviour so as to correlate with actual JICF behaviour.

1.1.3   Counter-Rotating Vortex Pair (CVP)

The CVP, on the other hand, is a result of the realignment of the jet shear layer by the cross flow and is shown in Figure 1.5. Kamotani and Greber (1972), Fearn and Weston (1974) and Moussa et al. (1977) have studied the CVP in detail and concluded that it remains the dominant mechanism behind mass entrainment for large distances downstream. While it is a widely-held belief that the CVP is formed by the jet shear layer emerging from the jet orifice, the evolution process in terms of initiation and development remained unresolved. Kelso et al. (1996) and Yuan et al. (1999) carried out experimental and computational studies, respectively to resolve the issue and both studies showed a close link between the realignment of the jet shear layer and the development of the CVP. Interestingly, the two studies also revealed the tendency for the CVP to suffer

vortex breakdowns, which suggests a possible long-term stability problem with the CVP. This fact was accentuated by the observation of Smith and Mungal (1998) when they reported that " … *creating a transverse jet flow field that is symmetric about $z = 0$ is not regularly accomplished in laboratory studies, thus determination of the ultimate symmetry or asymmetry of the transverse jet is an open question.*" However, the key features of CVP development remain more or less undisputed. Because the interface between the cross flow and the transverse jet is compliant, the former is able to tug-in at both sides of the jet as it closes in at the lee-side of the jet. This stretching pinches two "tails" off the sides of the jet and the closing-in of the cross flow causes the "tails" to loop back towards the lee-side of the jet. The resulting CVP gains strength as the jet penetrates further into the cross flow, accounting for much of the entrainment process of the JICF phenomenon in the far-field. The presence of the weaker near-wall secondary CVP is generally perceived to be a result of velocity induction that the primary CVP has on the separated boundary layer downstream of the jet column. Available information suggesting this includes the corresponding increase in the strength of the secondary CVP when the primary CVP strength is increased with increasing velocity ratios. In addition, experimental observations by Kelso et al. (1996) have linked it to the horseshoe vortex system. However, this particular vortex system attracts very little attention primarily because it does not affect the main flow significantly.

1.1.4 Wake Vortices

Lastly, the wake vortices are formed when the boundary layer is separated behind the jet with its vorticity transported almost vertically towards the entraining CVP. Cross-sections of these vortices are observed to resemble von Karman vortices typical of the flow past bluff bodies, exhibiting different shedding patterns at different flow conditions. Fric and Roshko (1994) were amongst the first to carry out a comprehensive experimental
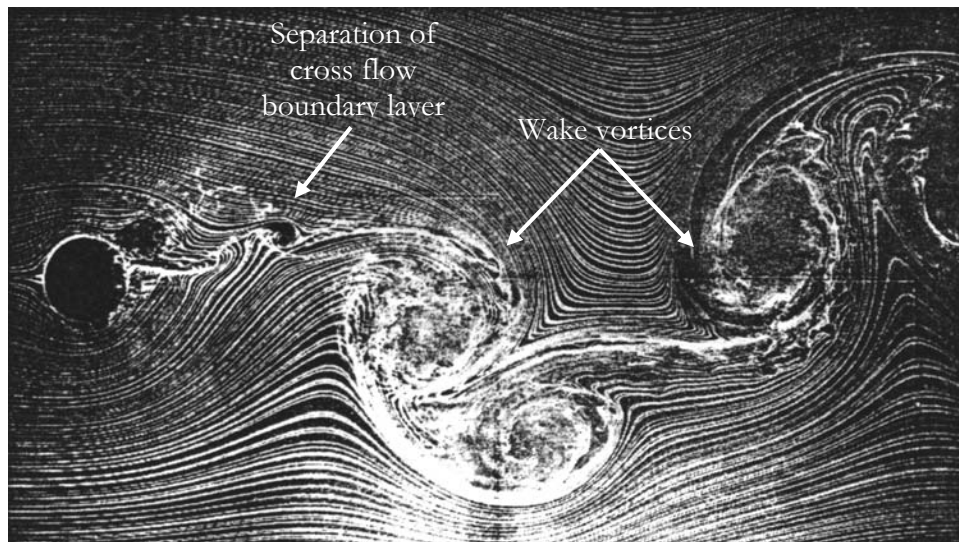
Figure 1.6   Visualization of wake vortices behind a circular JICF with smoke wire close to the test section floor by Fric and Roshko (1994). Separation of cross flow boundary layer was shown very clearly in the lee-side vicinity directly behind the jet orifice (Reproduced with permission from Fric and Roshko (1994)).

study and arrived at the above conclusion (see Figure 1.6). They reported the appearance of the wake vortices when the velocity ratios (ratio of mean jet-velocity to mean cross flow velocity) used were relatively high, typically around four or higher. Follow-up flow visualization studies by Kelso et al. (1993) and Kelso et al. (1996) further indicated that filaments of the wake vortices could be traced back to one of the vortices within the horseshoe vortex system upstream of the jet column. Therefore, the wake vortices could be considered as part of the horseshoe vortex system, and like the near-wall secondary CVP, are seen as a resolved problem.

1.2   Literature Survey

Early studies on JICF focused on obtaining the deflected jet trajectories and a general scaling law for prediction. Many studies were carried out for circular JICF using the hot-wire technique, pressure as well as tracer concentration measurements. These studies included those performed by Ruggeri et al. (1950), Ivanov (1952), Bryant and Cowdry (1955), Jordinson (1956), Shandorov (1957), Gordier (1959), Keffer and Baines

(1963), Patrick (1967), Kamotani and Greber (1972) and many others. The angle of injection was usually taken as the direction normal to the cross flow, though oblique angles were also used. Realization of a general scaling law for a JICF phenomenon is however, still the ultimate aim, and has been attempted by Keffer and Baines (1963), Pratt and Baines (1967), Broadwell and Breidenthal (1984) and more recently, Smith and Mungal (1997). Accumulated results suggest that the jet generally scales with three length scales in the near and far-field, namely d, rd and r^2d, where d is the diameter of the jet and r is the velocity ratio.

Other areas of JICF examined by early research workers include the use of mean and fluctuating velocity components of the resultant flow to evaluate the three-dimensional mean flow and turbulence field properties. Andreopoulos and Rodi (1982) made use of a three-sensor hot-wire to obtain the three mean-velocity components and discovered that for jets with velocity ratios at 1 and 2, vertical mean velocity profiles taken at various downstream positions along the symmetrical plane demonstrated a wall-jet characteristic near the wall below the CVP. This jet-like characteristic gradually weakened and eventually disappeared further downstream, with the near-wall flow returning to the typical boundary layer characteristics thereafter. The phenomenon became more apparent as the velocity ratios were increased and it was postulated that the pair of near-wall secondary CVP mentioned earlier might have been responsible for it. It is highly plausible that this near-wall secondary CVP was induced by the main CVP since higher velocity ratios led to a stronger main CVP and in turn was able to induce a stronger near-wall response. Unfortunately their measurement resolution was not high enough to fully determine the characteristics of the near-wall vortex. Further hot-wire studies by Andropoulos (1985) for lower velocity ratio cases revealed that vortical structure evolution was significantly different from that of higher velocity ratio cases due to the

small penetration of the jet. The cross flow was observed to behave like a "cover" over the jet, playing the dominating role in the resultant vortical structures. No signs of near-wall vortex flow were found in this particular study, possibly because the resultant wake-like flow of the deflected jet was mostly embedded within the boundary layer.

Studies were also carried out to ascertain the effect of the jet exit geometry on the resultant jet penetration into the cross flow by Ruggeri et al. (1950), Weston and Thames (1979), Haven and Kurosaka (1997) and Gollahalli and Pardiwalla (2002). Early experiments carried out by Weston and Thames (1979) on rectangular jets revealed that the low aspect ratio configuration jets (major-axis parallel to cross flow) penetrated the cross flow more than the high aspect ratio jets (minor-axis parallel to cross flow) did, with trajectories of the circular jets lying in between. Moreover, for the same experimental parameters, vorticity is higher for low aspect ratio jets than for high aspect ratio jets. Early studies on the effect of different jet geometries concentrated mainly on bulk transportation of the jet momentum into the cross flow in wind tunnels until recently, when Haven and Kurosaka (1997) investigated the flow fields at low velocity ratios in a water tunnel. They were concerned with the film cooling properties of the various jet geometries and examined the problem through the differences in the formation mechanism. Due to the nature of film cooling process, the deflected jets have to stay near to the surfaces to be cooled in order to be effective and therefore low velocity ratios were used. However, the distance from the surfaces to be cooled to the deflected jet depends heavily on the jet geometry, provided all other parameters remain the same. An ideal injection geometry would have to produce a wide lateral spreading of the cooling fluid while at the same time staying close to the surfaces to be cooled. Based on their end-view laser-induced fluorescence (LIF) visualization, Haven and Kurosaka (1997) found that the resultant characteristics of the various jet geometries could be broadly

classified into two categories: Class 1, which consisted of square, circular, low aspect ratio rectangular and elliptic jet geometries, produces "unsteady upper kidney shaped vortices"; and Class 2 which consisted of high aspect ratio rectangular and elliptic geometries, produces "unsteady upper anti-kidney shaped vortices". They concluded that the difference in the sense of rotation of these vortices was the result of the warping of the leading-edge vortex loops caused by the cross flow. The nature of their study meant that the velocity ratio used has to be kept low with the cross flow dominating the resultant flow. Based on the values of du/dy they obtained through particle image velocimetry (PIV), where u is the cross flow velocity and y is the lateral distance across the jet geometries, it was suggested that the cross flow penetrated deeply into the low aspect ratio jet columns and deformed the leading-edge vortex loops inwards and vice versa for high aspect ratio jet columns. Flow visualization results were then used to support their theory.

It is clear that while significant progress has been made over the past years, many questions regarding the JICF phenomenon remain unresolved. For example, some of the most fundamental questions are: How does the thickness of the jet shear layer affect the resultant flow structures of JICF? Also, could the resultant jet structures be adequately explained in terms of those associated with a free jet? Previous studies (see for example, Skyes et al. (1986), Kelso et al. (1996) and Haven and Kurosaka (1997)) have used vortex rings as basic building blocks to model JICF phenomenon. While these studies have managed to explain adequately certain large-scale flow structures (such as the leading edge and lee-side vortices near the jet exit) by bending and titling the vortex rings, complication sets in when one tries to explain the formation of the CVP using vortex rings. Therefore, the validity of employing vortex rings to model a JICF remains an open debate.

Another area of the JICF phenomenon which has received very little attention until recently is the effect of jet geometries on the flow structures in a cross flow environment. A majority of the early studies was concentrated on circular geometry. There were many advantages in using circular jets: Firstly, they possess uniform geometrical curvature which in turn led to uniform distribution of displacement/momentum thickness along the entire circumference. Secondly, the relatively simple geometry of circular jet makes it relatively easier to compute or analyze theoretically. In contrast, non-circular jets in cross flow are largely unexplored. Previous studies have concentrated mainly on their bulk transport properties, with the aim of evaluating the feasibility of utilising non-circular jet geometries as means of flow control as well as enhancing combustion. However, the evolution and the topological structures of non-circular jet are largely unknown.

1.3   Research Aims and Scope

The foregoing discussion leads to the following aims of this investigation:

1. To study the effect of jet shear layer thickness on the resultant flow structures. Parabolic and top-hat jets will be used for this purpose. The study includes flow visualization and quantitative measurements using PIV techniques.

2. To study the large-scale structures of a circular jet in cross flow and to examine the validity of using vortex rings as building blocks to model this flow.

3. To study elliptic jets of different orientations in a cross flow, and to identify the effects of jet geometry on the development of the large-scale jet structures.

4. To measure the velocity field of elliptic jets in a cross flow using PIV techniques, and to compare with the corresponding measurements in a circular JICF.

1.4   Organization of Thesis

The organization of the thesis is as follows: In Chapter 2, a detailed discussion of the experimental setups and techniques is presented.   In Chapter 3 and 4, flow visualization and PIV results of the parabolic and top-hat circular jets are presented, and differences in their flow characteristics are highlighted.   In Chapter 5, the flow model based on "vortex loops" instead of "vortex rings" is proposed. Experimental data will be used to support the proposed flow model.   This is followed by the study of the effect of jet geometry on the overall flow structures. Chapter 6 provides an overview of the flow visualization results on the EJICF, and based on these results obtained, detailed flow models are presented. To obtain a deeper understanding of the flow field, PIV measurements are presented in Chapter 7 to shed light on the vorticity evolution, especially with respect to the generation and interaction of the leading-edge vortices. Finally in Chapter 8, conclusions of the present study and potential future work are given.

Chapter 2

Experimental Setup and Techniques

2.1 Water Tunnel and Jet Supply Facility

The experiments were carried out in the re-circulating water tunnel in the Fluid Mechanics Laboratory of the National University of Singapore (see Figure 2.1). The test section measures 183cm in length and has a cross-section of 40cm (W) by 45cm (H) and constructed entirely out of Plexiglas, thus allowing easy high-quality flow visualization from almost any angle. A variable speed pump was used to drive the water through the water tunnel. Before the water entered the test section, it passed through a honeycomb grid and three layers of fine screens with decreasing grid sizes. This was to ensure that the turbulence level of the cross flow remained low throughout. Furthermore, the water-tunnel was washed regularly to ensure dirt did not build up during the course of the investigation.

A small quantity of water from the water tunnel was constantly channeled into an overhead water tank to provide the fluid for the jets. The jet fluid was in turn channeled to the jet injection tube via a rubber hose. For the parabolic jets, the jet fluid was made to travel over a large distance (≈10m) before entering a long straight injection tube of predetermined diameters (see Figure 2.2(a)). This was to ensure that the jet flows were fully-developed when they were exhausted into the cross flow. To obtain top-hat jets, suitable contraction sections were used prior to the jet fluid exhausting into the cross flow (see Figure 2.2(b)). For the elliptic jets, four aspect ratios (hereby defined as the ratio of cross-stream jet dimension to streamwise jet dimension) were considered, namely 0.3, 0.5, 2, and 3 and the injection tubes were shaped according to the jet exit geometry and
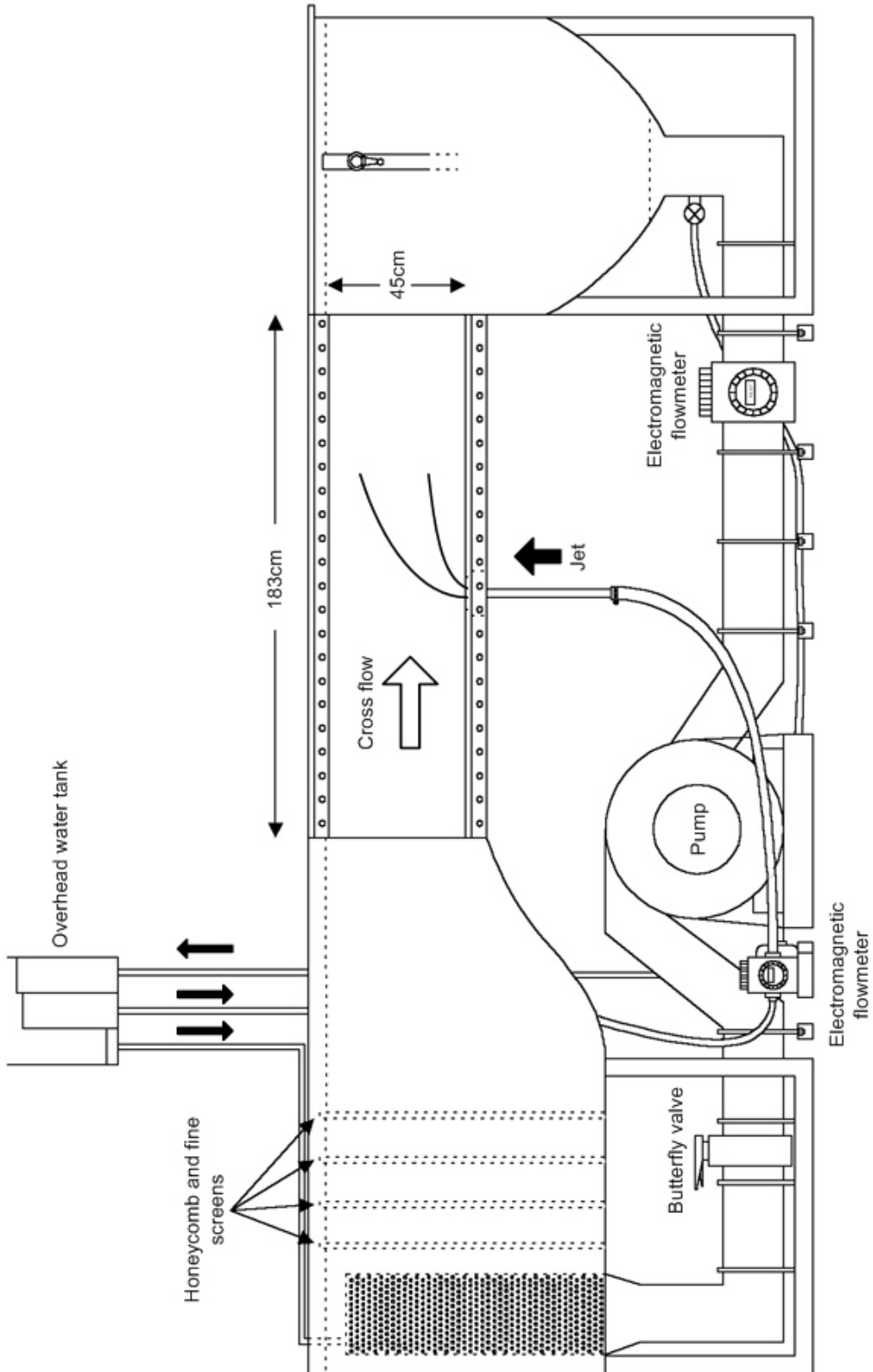
Figure 2.1. Schematics of the recirculating water tunnel used in the present experimental study.
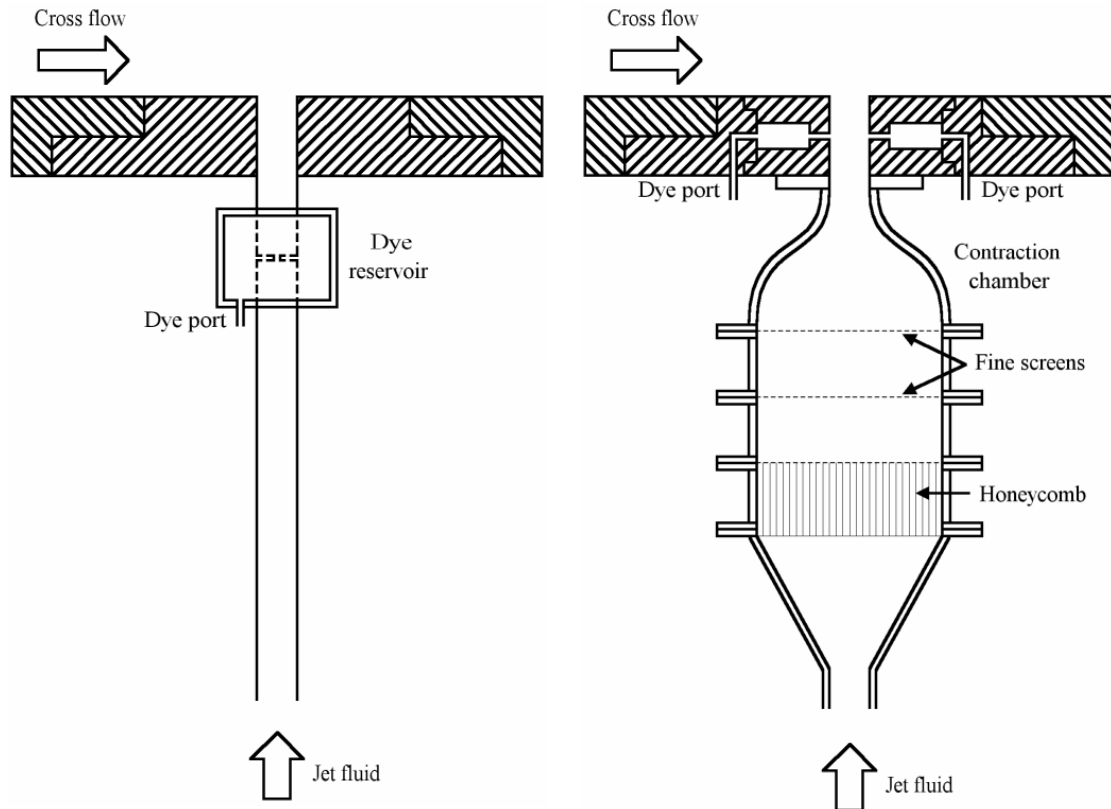
Figure 2.2.   (a) A typical long injection tube for producing parabolic jets and (b) a typical contraction chamber for producing top-hat jets.

measured 70cm in length. More information on the jet apparatus will be given in more details later. In all cases, the tubes were mounted flushed with the test section floor with the jets exiting normally into the cross flow. All flowrates, namely the cross flow and the jet, were measured using two separate electromagnetic flowmeters.

Due to the nature of the study, the elliptic injection tubes were fabricated to rotate freely about its centerline axis using a set of worm-gears as shown in Figure 2.3. The worm-gears enabled the elliptic tubes to be rotated to the required positions with a higher degree of precision than would be by hand. Honeycombs were also placed at the entrances of the injection tubes to straighten the flow. Depending on the jet geometry, up to twelve dye ports were incorporated into the injection tubes to allow direct-injection at various strategic locations.
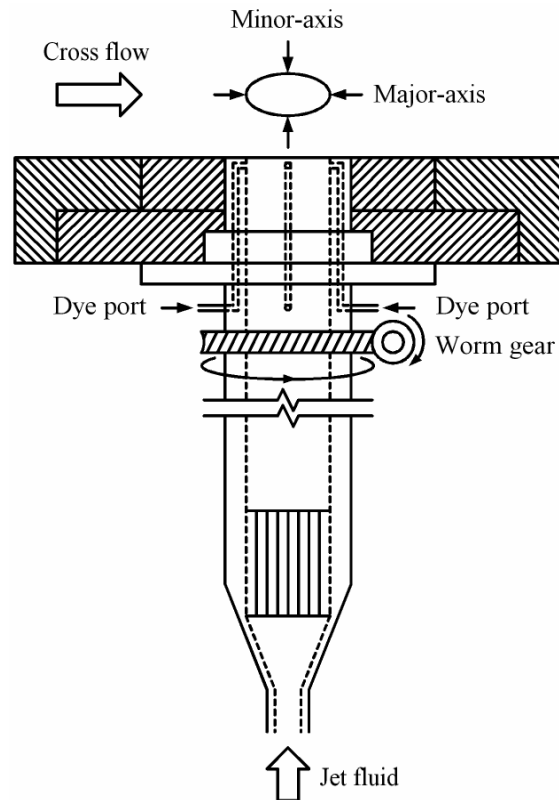
Figure 2.3.   A typical elliptic injection tube with a set of worm-gear for orientation control.

Both the jet Reynolds number and velocity ratio are used to parameterise the resultant jet behaviour with their definitions as given follows:

$$\text{Jet Reynolds number, } Re = \frac{V_{jet} D}{\nu_{jet}}$$

$$\text{Velocity Ratio, } VR = \frac{V_{jet}}{V_{crossflow}}$$

where D is the jet diameter, ν_{jet} is the kinematic viscosity, V_{jet} is the mean jet velocity and $V_{crossflow}$ is the mean cross flow velocity. It should be noted that the mean cross flow velocity was not that external to the cross flow boundary layer but evaluated with the boundary layer included. In the case of elliptic jets, D is defined as the hydraulic diameter, $D_h = {}^{4A}\!/_{P}$. The velocity ratio was derived from the ratio of the jet momentum to the cross flow momentum over equal areas (momentum ratio) by setting the density of

the jet and cross flow to be the same, and assuming a flat velocity profile for the jet. The momentum ratio is given as:

$$\text{Momentum Ratio, } MR = \frac{\int \rho_{\text{jet}} V_{\text{jet}}^2 dA}{\rho_{\text{crossflow}} V_{\text{crossflow}}^2 A_{\text{jet}}}$$

In all cases considered here, the cross flow boundary layer was ascertained to be laminar and followed Blasius profile very closely. At the location where the jets were located, the cross flow boundary layer thickness (δ) was approximately 25mm.

2.2   Circular Jet Configuration

For this part of the investigation, three circular jets with different diameters of 9.5mm, 13.5mm and 32.5mm were used, and two different exit velocity profiles, namely parabolic and top-hat, were considered. Relative to the cross flow boundary layer at the point of exhausting, the jet diameters measured 0.38δ, 0.54δ and 1.3δ respectively. As the studies carried out by Kelso (1991) pointed out, the boundary layer thickness will influence the formation of the horseshoe vortex system upstream of the jet and in turn affect subsequent generation and shedding of the leading-edge vortices, the cross flow conditions were maintained constant throughout the entire study. While the jet diameters used covered from 0.38δ to 1.3δ, it is believed that the local effects of jet shear layer differences will dominate over the relative size of the jet diameters to the cross flow boundary layer as will be shown later.

To obtain the desired parabolic velocity profiles, one end of the injection tube was mounted with its exit flushed with the floor of the test-section, and the other end was connected through a long straight hose to the overhead tank. On the other hand, top-hat

velocity profiles were obtained with the aid of the contraction section, very much like that in a wind tunnel. The contraction was designed based on the technique outlined by Mehta and Bradshaw (1979). To confirm that all jet exit velocity profiles achieved the desired outcome, hot-film anemometry was used to measure the mean velocities at discrete spatial locations of 0.5mm apart across the jet diameters for all prescribed jet Reynolds numbers without the presence of the cross flow. A Dantec hot-film probe connected to a Dantec constant temperature anemometer channeled the signals to a data acquisition board in a computer after appropriate signal filtering and conditioning has been carried out. Due to the difference in the velocity profiles, momentum ratios (MR) were used instead of the velocity ratios for comparison between the different profiled jets, and they ranged from MR=1.15 to 5.77 with the corresponding Reynolds numbers varying approximately from 625 to 1645, depending on the exact circular jet. The MR and Reynolds numbers were selected such that they facilitated the careful study of the flow structure evolution. While practical applications usually have high Reynolds number flow fields, it is believed that any insights inferred from low Reynolds number flow fields can be valuable as well.

2.3   Elliptic Jet Configuration

One of the key parameters to be investigated is the effect of the orientation of the elliptic jets with respect to the free stream direction, and for the ease of reference, the following convention is adopted: Unless otherwise stated, the aspect ratio (AR) of the elliptic jet is defined as the ratio of the cross-stream axis of the nozzle to the streamwise axis. For example, AR<1 implies that the major-axis of the ellipse is aligned with the cross flow, and likewise, AR>1 refers to the case where the major-axis is normal to the cross flow. Table 2.1 shows the various nozzle orientations used in the present study. For convenience, jets with AR<1 are labeled as low AR jets and those with AR>1 are
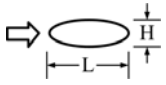
Configuration	Jet exit shape	Dimensions (mm)		Hydraulic diameter, D_h (mm)	Aspect Ratio (AR=H/L)
		H	L		
1		18.5	55.5	24.8	0.3
2		22.5	45.0	28.5	0.5
3		31.6	31.6	31.6	1
4		45.0	22.5	28.5	2
5		55.5	18.5	24.8	3

Table 2.1.   Jet exit geometries used in the present experiment. The arrows denote the cross flow direction. H is the cross-stream axis and L is the streamwise axis with the aspect ratio defined as H/L.

referred to high AR jets (see also Figure 2.4).

Due to the non-uniform curvature of the jet geometries, the velocity profiles and hence momentum and displacement thicknesses of the elliptic jets along major and minor-axes would be different. But since the present study was concerned primarily with the effects of the exit geometry on the flow structures, no deliberate alterations to the jet velocity profiles were carried out, unlike in some previous studies of free elliptic jets where sandpaper (Husain and Hussain, 1990) was used to "trip" the elliptic jet boundary layers to a turbulent one. In all the cases, bulk jet velocity was used to determine the velocity ratio (VR) which in the present study ranged from VR=1 to 5, based on similar formulation given earlier. The velocity ratios used were again determined by the need to assess the interaction between the jet and cross flow when the exhausting jet is able to have a significant impact on the cross flow, but not so high until the flow structure evolution is difficult to detect. Based on the predetermined cross flow velocity of 30mm/s, the corresponding jet Reynolds number, based on the hydraulic diameter and
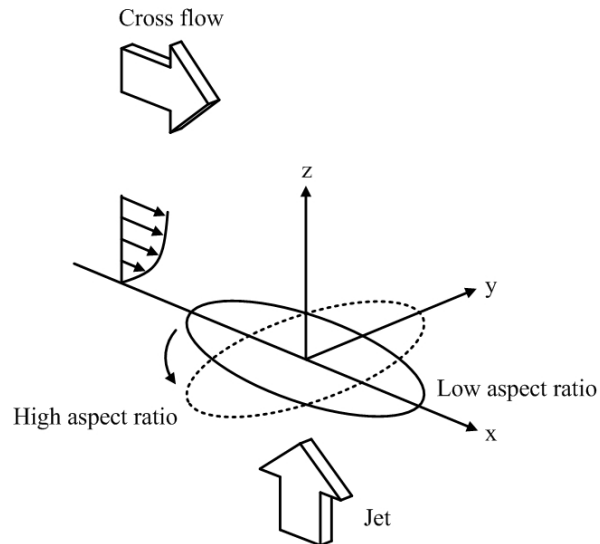
Figure 2.4. Low and high AR elliptic jet configuration.

mean velocity, varied from 900 to 5700, depending on the specific jet geometry.

2.4   Dye-Injection Apparatus Setup

Dye injection was facilitated by the numerous dye-injection ports and slits prefabricated into the jet apparatus (see Figures 2.2 and 2.3). Point-injection of dye was carried out when certain desired flow structures were to be visualized while slit-injection was normally used when the entire jet shear layer was to be mapped out. The blue and red dye used were derived from non-toxic food dye and premixed with alcohol to achieve the specific gravity of approximately one. Gravity-feed method augmented by small control valves allowed good control of the dye flow rate without disturbing the flow excessively. A CCD video camera was used to record the flow structures to a SVHS video recorder. The use of video recording enabled the analysis of the flow dynamics, as well as allowing still images to be captured via a frame grabber card in a PC.

2.5   Laser-Induced Fluorescence (LIF) Apparatus Setup

A Spectra-Physics 5W argon-ion laser coupled with beam-steering optics and a cylindrical prism provided the laser sheet to visualise the cross-sections of the deflected jets at any desired location. Fluorescein disodium was used as the fluorescent dye and was premixed with the jet fluid prior to entering the test section. Laser cross-sections were made for three different orientations (see Figure 2.5), with the laser sheet aligned (a) along the plane of symmetry of the deflected jets, (b) normal to cross flow direction at various downstream locations and (c) normal to the mean jet trajectories at various locations along the jet axis. For the second orientation, the cross sections were made at up to 4D downstream from the axis of symmetry of the injection tube. As for the last orientation, the mean jet trajectories were determined by averaging 200 images of the jet fluid boundaries obtained from the first orientation. This method of determining the mean jet trajectories was more suitable for flow visualization than the usual method of defining jet trajectories as the loci of maximum mean velocity or maximum mean concentration. Similarly, a CCD camera was used to record LIF images for subsequent analysis.

2.6   Particle Image Velocimetry (PIV) Apparatus Setup

For this study, quantitative data on the flowfield was obtained by carrying out particle image velocimetry (PIV) measurements using a Dantec PIV2100 processor system with a Continuum 200mJ Nd:YAG laser system capable of producing 2×200mJ laser pulses at 10Hz each. Both the water tunnel and the jet fluid were seeded with either 30 or 60 micron particles prior to the experiments and the particles were illuminated by a laser sheet aligned along the symmetrical plane of the deflected jet in the cross flow direction. Scattered light from the particles was captured by a Kodak ES 1.0 Megapixel

(a) Vertically along the symmetrical plane

(b) Laterally across the deflected jet at various points downstream

(c) Perpendicularly across the deflected jet at various points along the mean jet trajectories
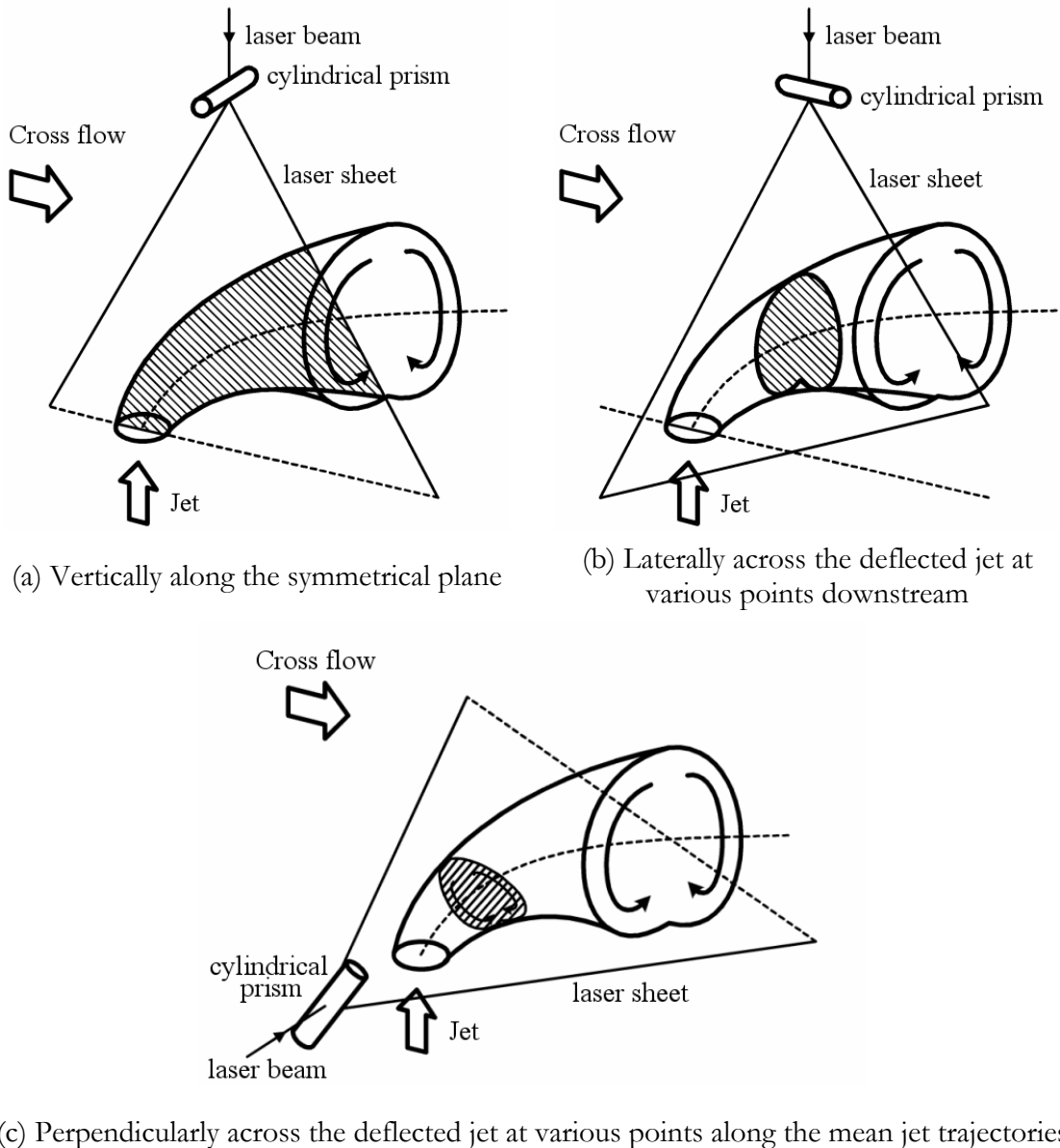
Figure 2.5.   Schematics of various laser cross-sections for laser-induced fluorescence imaging.

8-bit Digital CCD Camera with a CCD array size of 1016 pixel by 1008 pixel and the recorded particle image-pairs were transferred to a workstation for post-processing. A time separation of 10 msec was used for the image pairs to evaluate the velocity vectors with each image pair taken at 100 msec apart. This particular timing has been found to be satisfactory for the present flow conditions and was kept constant throughout the experiments. For post-processing, Dantec FlowManager software was used to derive the
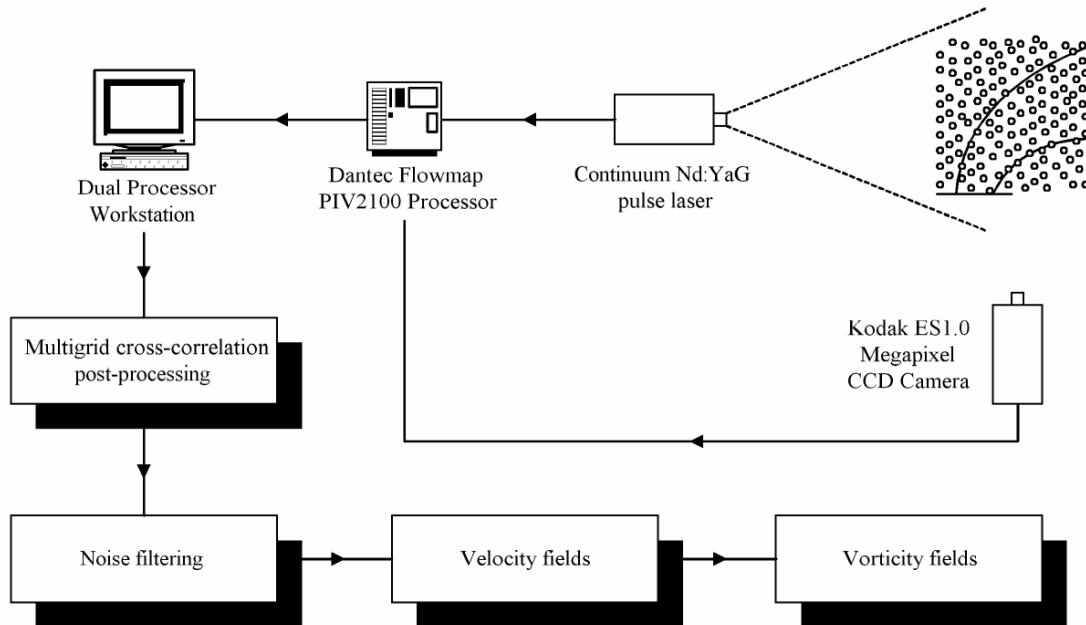
Figure 2.6. Procedure of particle image velocimetry experiments.

velocity and vorticity fields.   A two-pass multigrid cross-correlation using an initial interrogation window size of 128 pixel by 128 pixel with 25 percent vertical and horizontal overlapping area was employed to yield the raw velocity fields.   Final Interrogation window size is 32 pixel by 32 pixel. After the bad velocity vectors were removed by global and local rejection criteria, an averaging window of 3 pixel by 3 pixel was used to interpolate between them. To smooth the velocity fields, a moving-averaging smoothing filter of 5 pixel by 5 pixel was applied before finally determining the vorticity fields.   It was calculated that the CCD camera has an initial spatial resolution of 0.111mm/pixel, both horizontally and vertically, and covers an effective imaging area of approximately 112.18mm x 112.18 mm. The spatial resolution of the final derived velocity was estimated to be 1.809mm. A schematic of the PIV procedures is shown in Figure 2.6.

Chapter 3

Flow Visualization of Circular Jet in a Cross Flow: Effects of Jet Shear Layer Thickness

3.1 Introduction

To date, most of the experimental and numerical investigations on JICF are restricted to jets with the "top-hat" exit velocity profiles. This is partly because space constraint in most engineering applications required the use of short entrance lengths for the jets, and partly because the elimination of the jet boundary layers simplifies both theoretical and computational analyses. However, the author believes that velocity profiles at the jet exits also play an important role in the overall topology of JICF because past studies have shown that a thin shear layer is inherently unstable, and more likely to roll up than a thick shear layer. This may have profound influence on the mixing processes. However, the extent to which the velocity profiles affect the flow structures is not well understood despite earlier studies by Brundage et al. (1999), Hale et al. (1999) and Peterson and Plesniak (2002). The lack of understanding in this area motivated the author to carry out the present investigation. Here, the attention is focused on two exit velocity profiles, namely top-hat profile (i.e. thin shear layer) and parabolic profile (i.e. thick shear layer), and over a range of Reynolds number and momentum ratios.

3.2 Dye-Injection Visualization Studies

In these flow visualization studies, dye injection and laser-induced fluorescence (LIF) techniques were used. A wide range of Reynolds number (Re=635 to 1645, depending on exact jet geometry) and momentum ratios (MR) were considered, with MR=2.31 to 5.77. As mentioned previously, momentum ratio is defined as the ratio of

the jet momentum to that of the cross flow over the same jet exit area, and they were used instead of the velocity ratios because of the non-uniform exit velocity profiles for parabolic jets. Three different circular jets with diameters of 9.5mm, 13.5mm and 32.5mm were used in conjunction with two separate sets of flow conditioners to produce parabolic or top-hat velocity profiles for each diameter. Prior to flow visualization, hot-film anemometry was used to ascertain the desired velocity profiles in the absence of the cross flow and Figure 3.1 shows the results obtained. It should be noted that the velocity profiles were also taken at MR=1.15, however the results are not shown here because the top-hat profiles for this condition could not be achieved under the present set-up. Besides, at this MR, the flow structures were found to be more wake-like. As for the other MR, the results obtained are reasonably close to the intended profiles.

With reference to Figure 3.1 (a), (c) and (e), the velocity profiles of the three circular jets, while resembling parabolic velocity profiles, do not follow the theoretical parabolic velocity profiles very closely. This is especially so when the diameter of the circular jet is larger. One reason could be that the distance of the free surface of the water tunnel from the jet exit influences the jet exhaust condition slightly, especially when the circular jet diameter gets larger. Nevertheless, the slight deviation from the ideal parabolic velocity profile does not pose any problem since the focus of the present study is to look at the effect of the shear layer thickness on the flow topology. For example, the flow visualization images for the 9.5mm diameter parabolic jet, which incidentally possesses a velocity profile closest to that of a parabolic, do not seem to differ from those obtained for the 32.5mm diameter parabolic jet. On the other hand, their flow visualization images deviate significantly from their top-hat counter-parts. In all cases, both direct-injection of food dye and LIF technique were used to visualize the flow. The

(a) 9.5mm diameter parabolic jet

(b) 9.5mm diameter top-hat jet
(Re=660 to 1645)

(c) 13.5mm diameter parabolic jet

(d) 13.5mm diameter top-hat jet
(Re=625 to 1560)

(e) 32.5mm diameter parabolic jet

(f) 32.5mm diameter top-hat jet
(Re=750 to 1500)
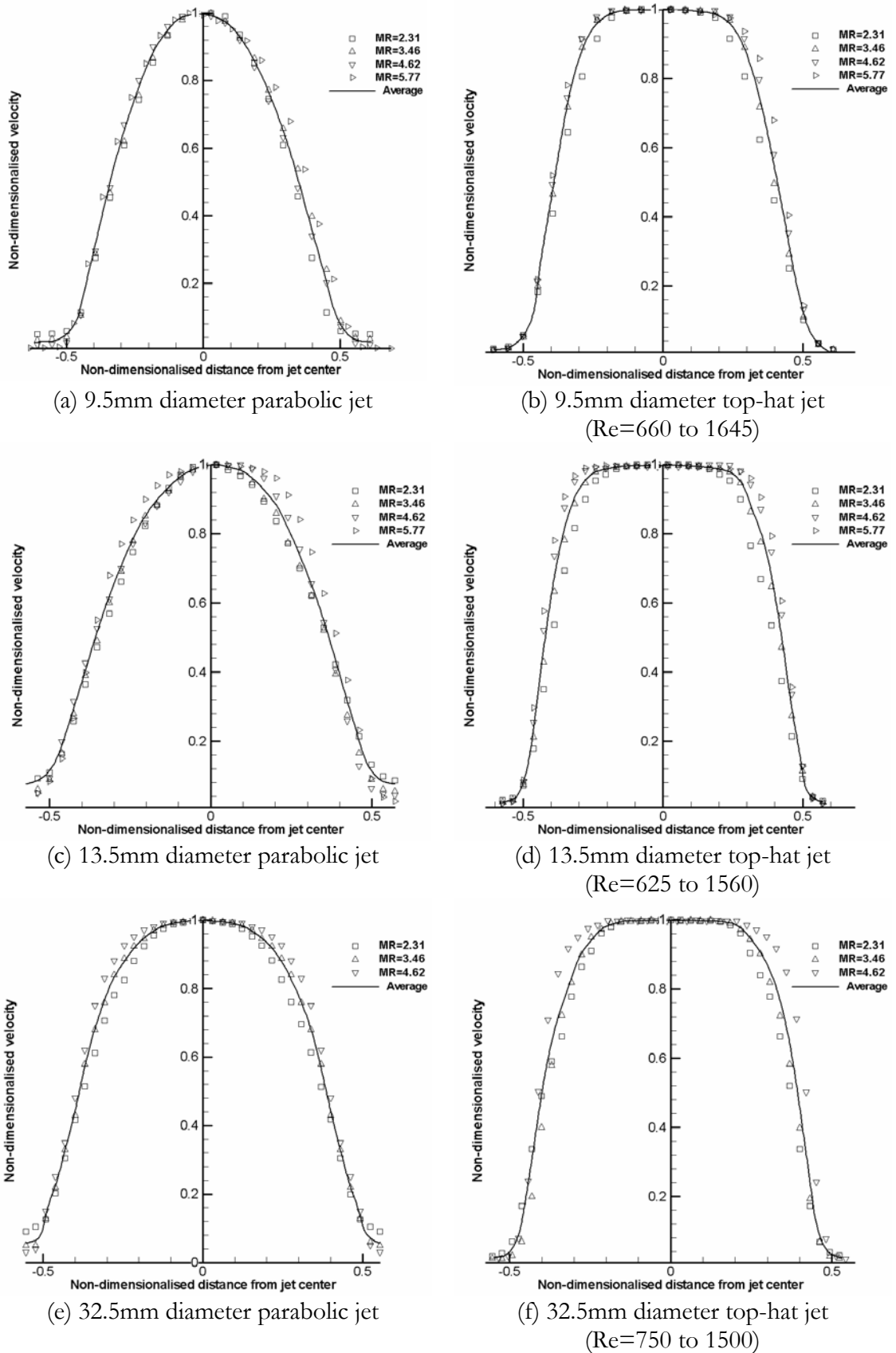
Figure 3.1.   A velocity profile comparison between the parabolic and top-hat jets used in
the study. Reynolds numbers are given with respect to the momentum ratio
indicated.

latter was accomplished by illuminating the jet that had been premixed with fluorescein

dye with a thin laser sheet produced by beam-steering optics and a cylindrical prism.

Figures 3.2 to 3.7 show the side-views of the flow structures obtained by

imposing parabolic and top-hat profiles at the jet exits using direct-injection of food dye.

Close examination of the pictures reveals that the shear layer from the top-hat profile

rolled up more readily, and the vortices extended for a greater streamwise distance than

those from the parabolic profile. In addition, the initiation of the leading edge vortices

for the top-hat profile appeared to form closer to the jet exit as MR increases. This can

be clearly seen in Figure 3.8, where the distance of initiation measured along the mean jet

axes is plotted against MR for the three jet nozzles. It can be seen from the figures that

the leading-edge vortices from the top-hat JICF, on an average, were initiated two to

three jet diameters earlier than for the parabolic jets at the corresponding MR.

As mentioned in Chapter 2, the three jet diameters covered from 0.38δ to 1.3δ

and while there were no deliberate attempts to collate the effects of the cross flow

boundary layer thickness to the jet diameter, the figures showed clearly the effects of

increased jet shear layer thicknesses with the cross flow boundary layer thickness kept

fixed throughout. In general however, it could still be detected from Figure 3.8 that when

the cross flow boundary layer thickness decreases relative to the jet diameter, formation

and subsequent shedding of the leading-edge vortices would commence earlier. This is

due to the higher shear levels developed along the jet/cross flow interface for relatively

thinner cross flow boundary layers than for thicker cross flow boundary layers. For the

former, the cross flow external of the boundary layer will affect the jet close to the jet exit

and thus creating higher shear levels conducive to vortex roll-ups. However for the latter

case, the cross flow external of the boundary layer will affect the jet significantly further

(i) MR=2.31

(i) MR=2.31, Re=660

(ii) MR=3.46

(ii) MR=3.46, Re=985

(iii) MR=4.62

(iii) MR=4.62, Re=1320

(iv) MR=5.77

(iv) MR=5.77, Re=1645

(a) Parabolic
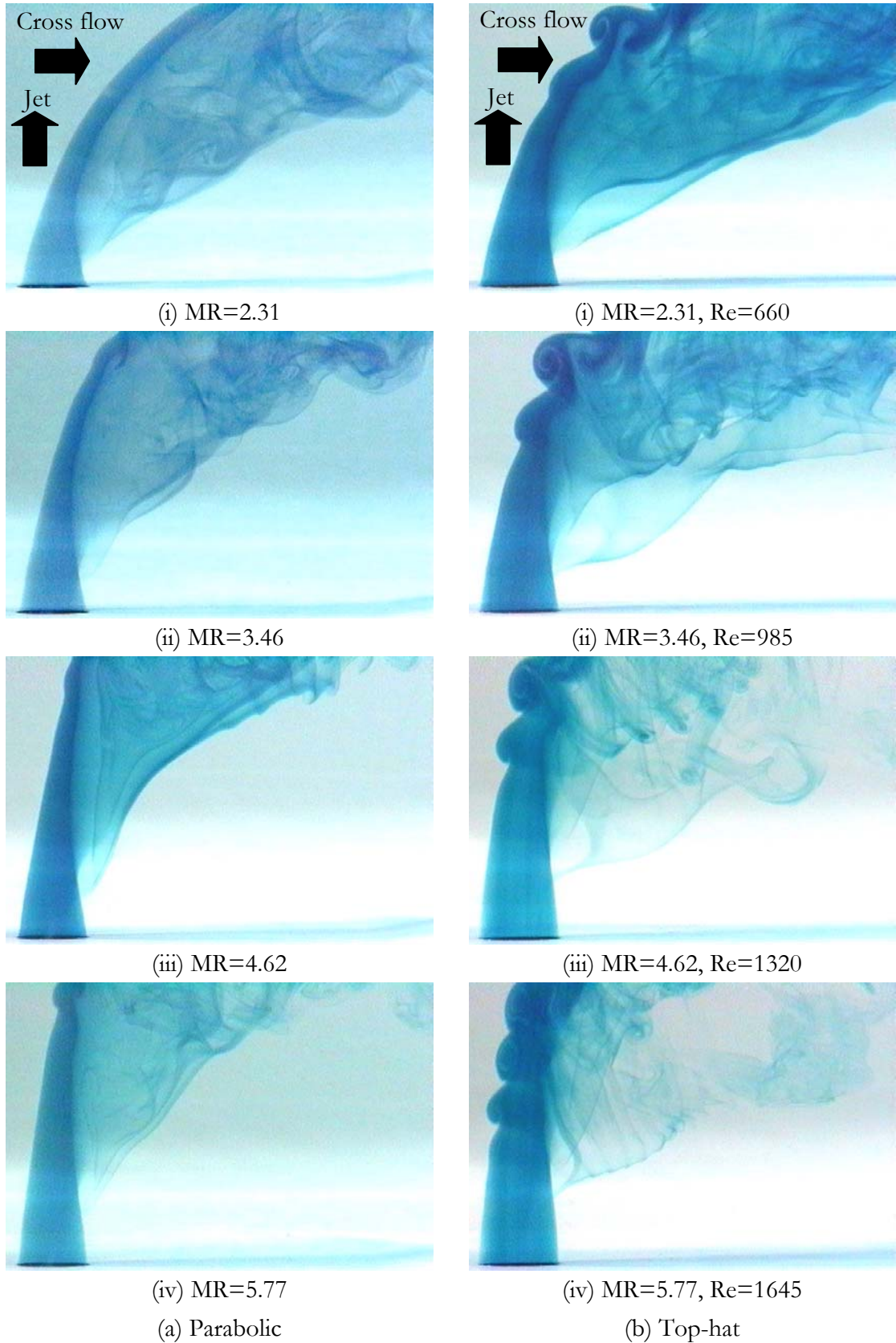
(b) Top-hat

Figure 3.2.   A near-field dye-injection comparison between a parabolic and top-hat 9.5mm (0.38δ) circular JICF.

(i) MR=2.31

(i) MR=2.31, Re=660

(ii) MR=3.46

(ii) MR=3.46, Re=985

(iii) MR=4.62

(iii) MR=4.62, Re=1320

(iv) MR=5.77

(iv) MR=5.77, Re=1645

(a) Parabolic
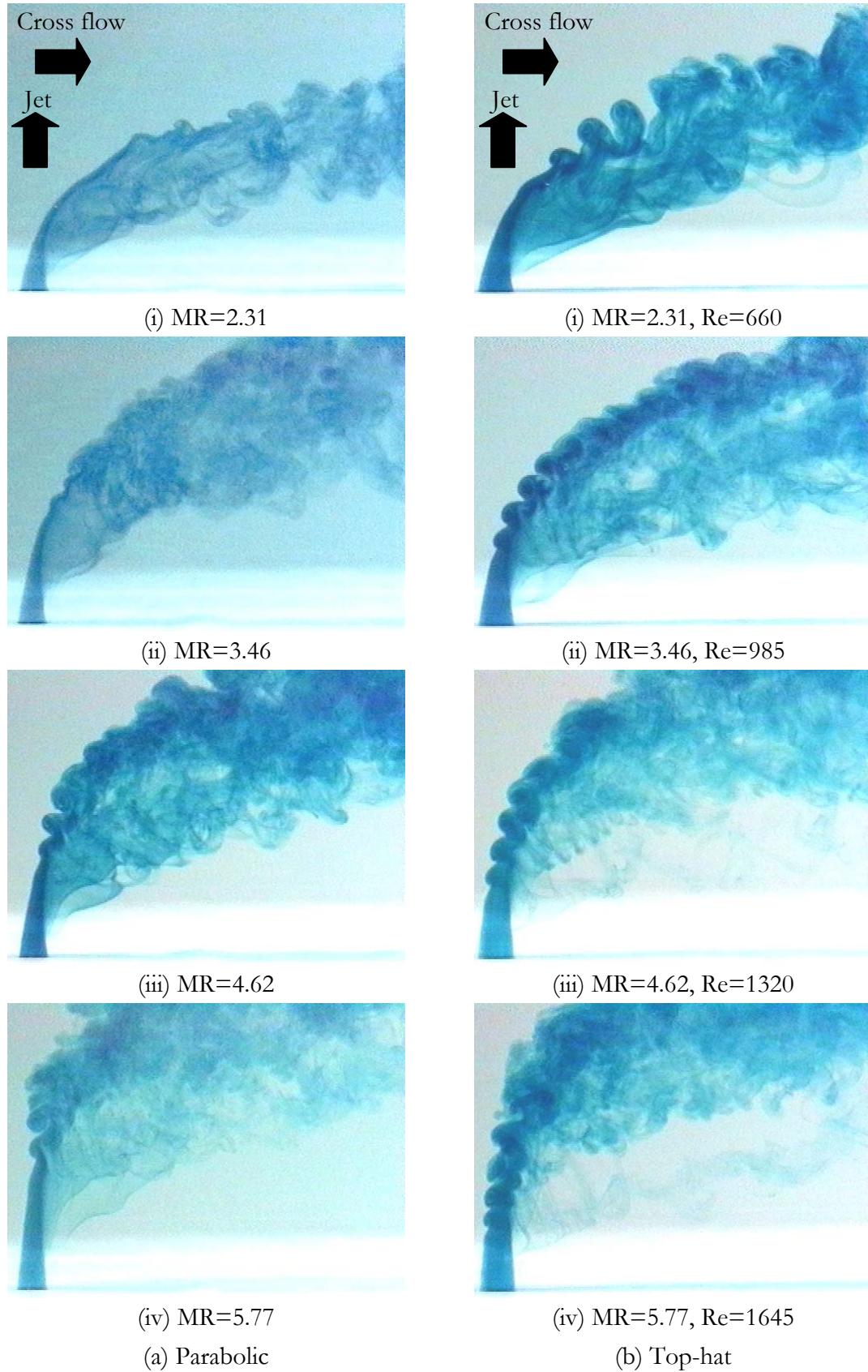
(b) Top-hat

Figure 3.3.   A far-field dye-injection comparison between a parabolic and top-hat 9.5mm
(0.38δ) circular JICF.

(i) MR=2.31   (i) MR=2.31, Re=625

(ii) MR=3.46   (ii) MR=3.46, Re=935

(iii) MR=4.62   (iii) MR=4.62, Re=1250

(iv) MR=5.77   (iv) MR=5.77, Re=1560

(a) Parabolic   (b) Top-hat
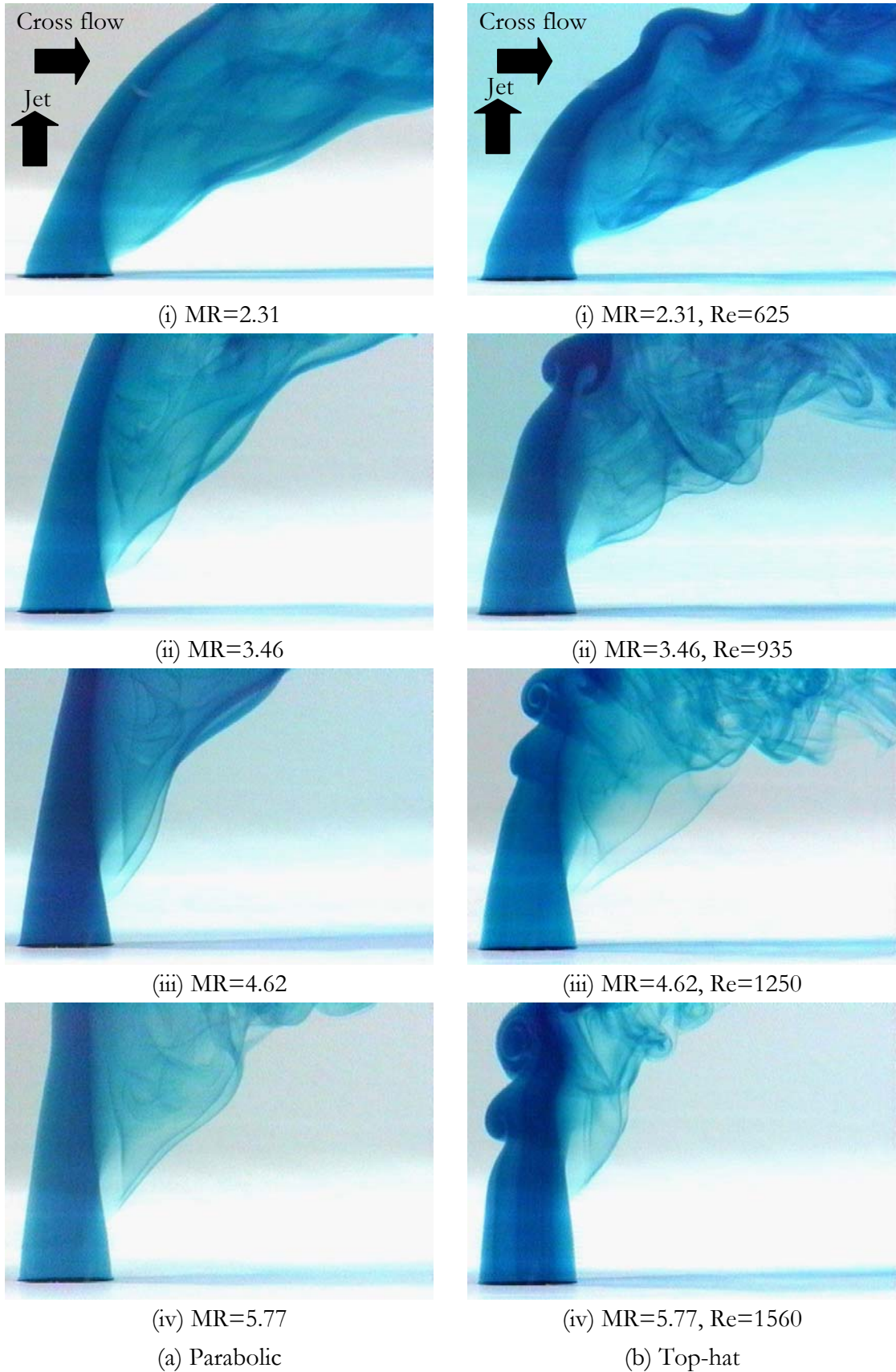
Figure 3.4.   A near-field dye-injection comparison between a parabolic and top-hat 13.5mm (0.54δ) circular JICF.

(i) MR=2.31 (i) MR=2.31, Re=625

(ii) MR=3.46 (ii) MR=3.46, Re=935

(iii) MR=4.62 (iii) MR=4.62, Re=1250

(iv) MR=5.77 (iv) MR=5.77, Re=1560

(a) Parabolic (b) Top-hat
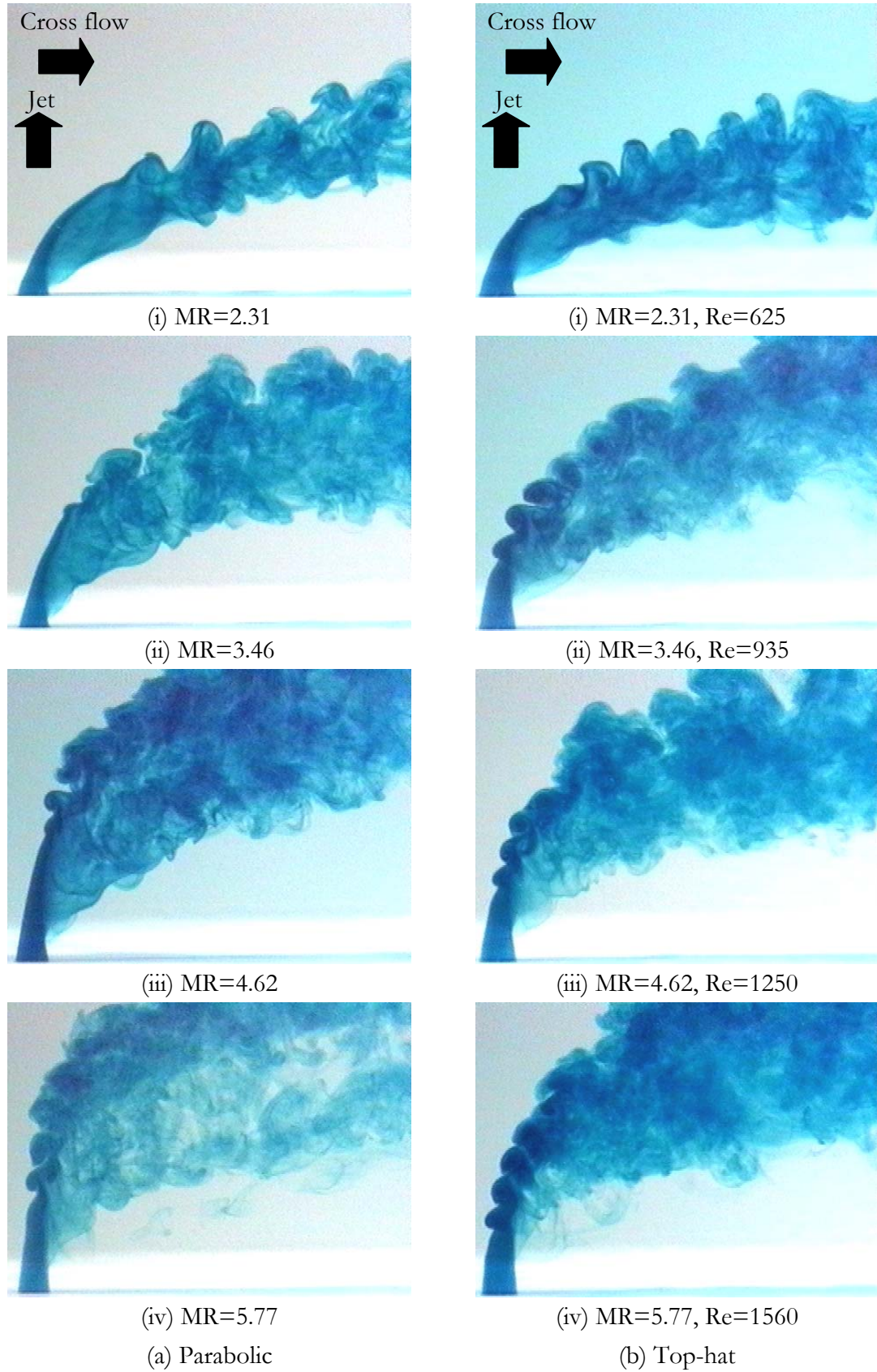
Figure 3.5.   A far-field dye-injection comparison between a parabolic and top-hat 13.5mm (0.54δ) circular JICF.

<div align="center">

(i) MR=2.31   (i) MR=2.31, Re=750

(ii) MR=3.46   (ii) MR=3.46, Re=1125

(iii) MR=4.62   (iii) MR=4.62, Re=1500

(a) Parabolic   (b) Top-hat

</div>
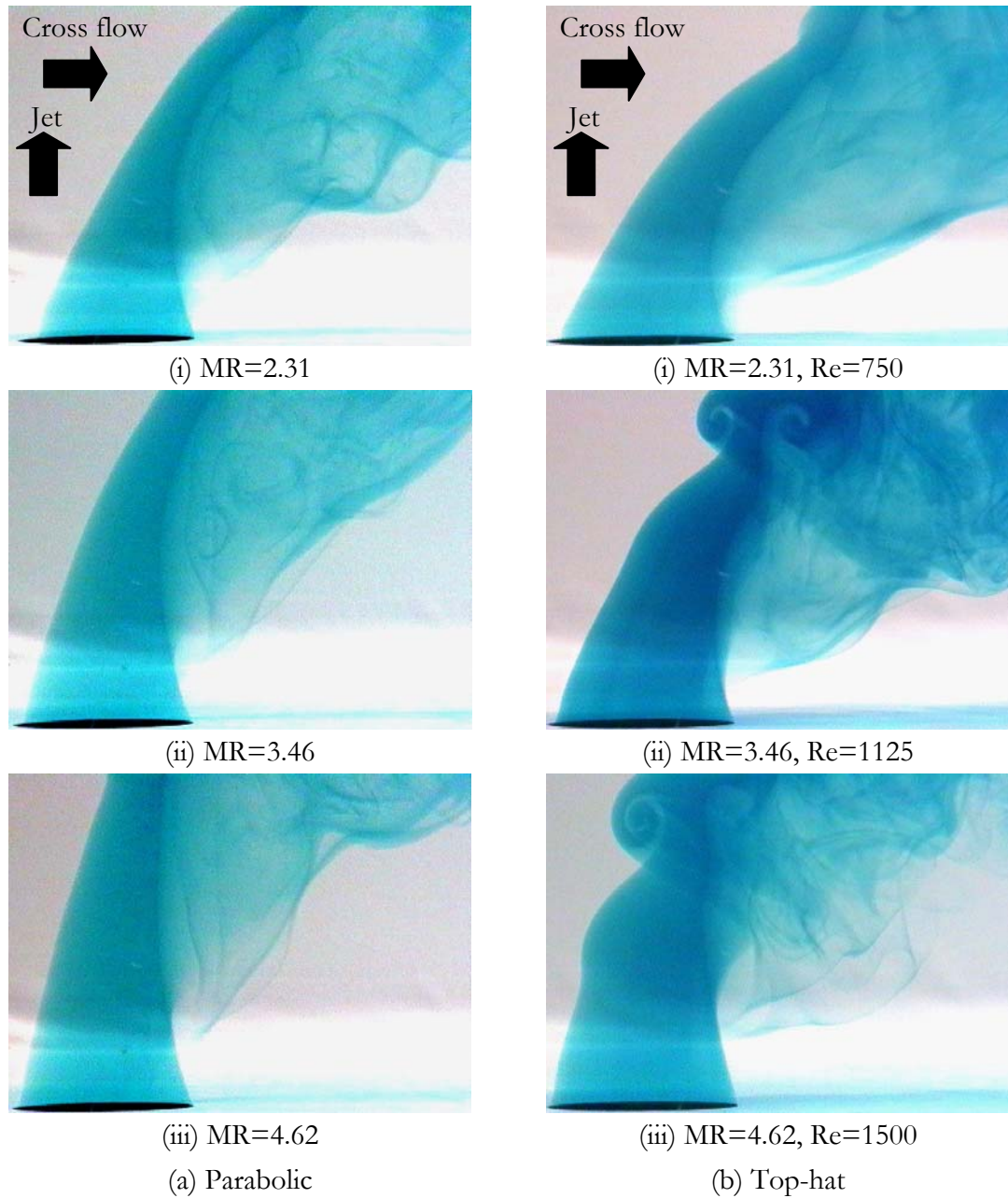
Figure 3.6.   A near-field dye-injection comparison between a parabolic and top-hat 32.5mm (1.3δ) circular JICF.

away from the jet exit where the shear levels between the cross flow and the jet will intuitively remain low.

(i) MR=2.31	(i) MR=2.31, Re=750
(ii) MR=3.46	(ii) MR=3.46, Re=1125
(iii) MR=4.62	(iii) MR=4.62, Re=1500
(a) Parabolic	(b) Top-hat
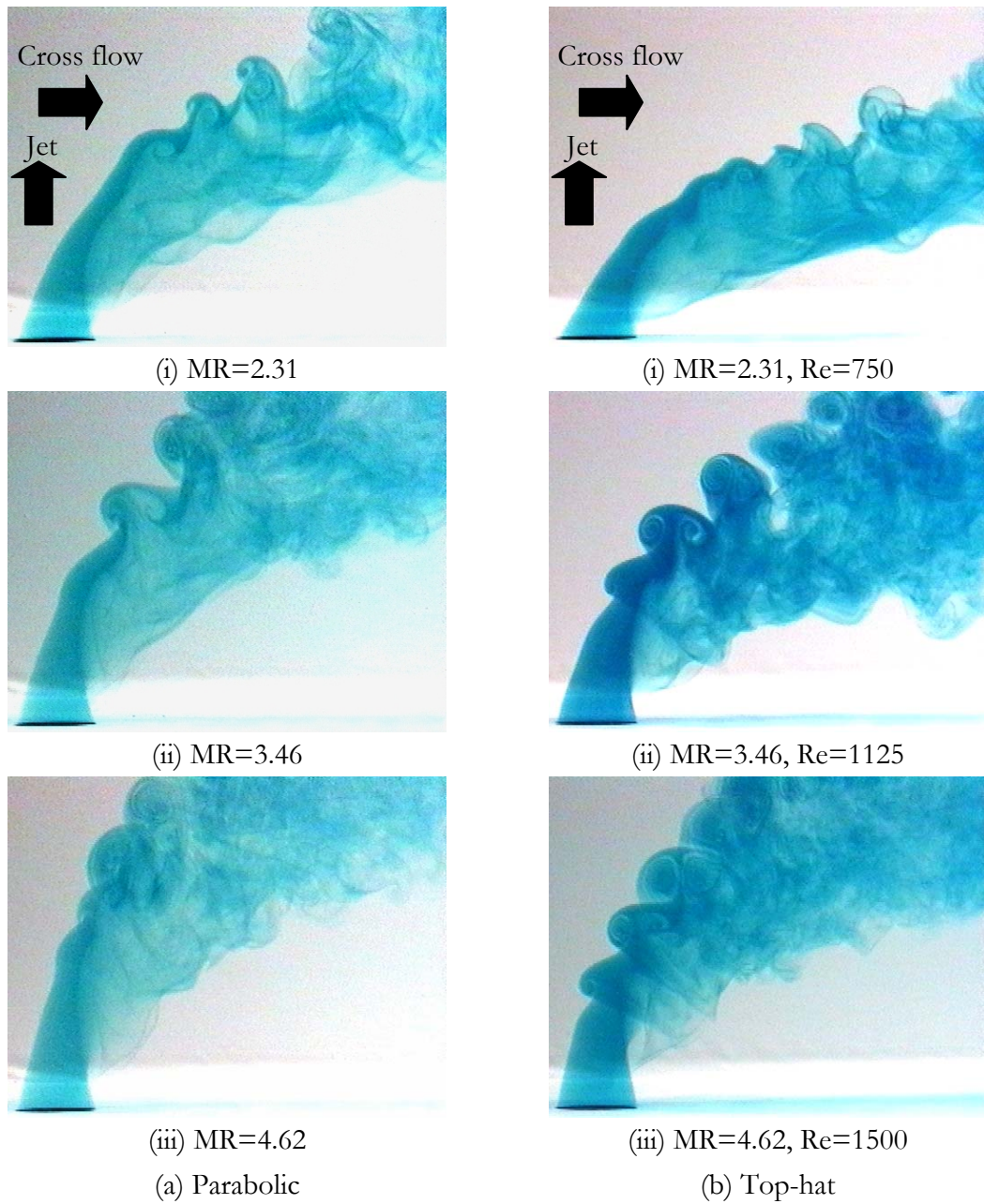
Figure 3.7.   A far-field dye-injection comparison between a parabolic and top-hat 32.5mm (1.3δ) circular JICF.

(a) 9.5mm diameter parabolic and top-hat jet

(b) 13.5mm diameter parabolic and top-hat jet

(c) 32.5mm diameter parabolic and top-hat jet
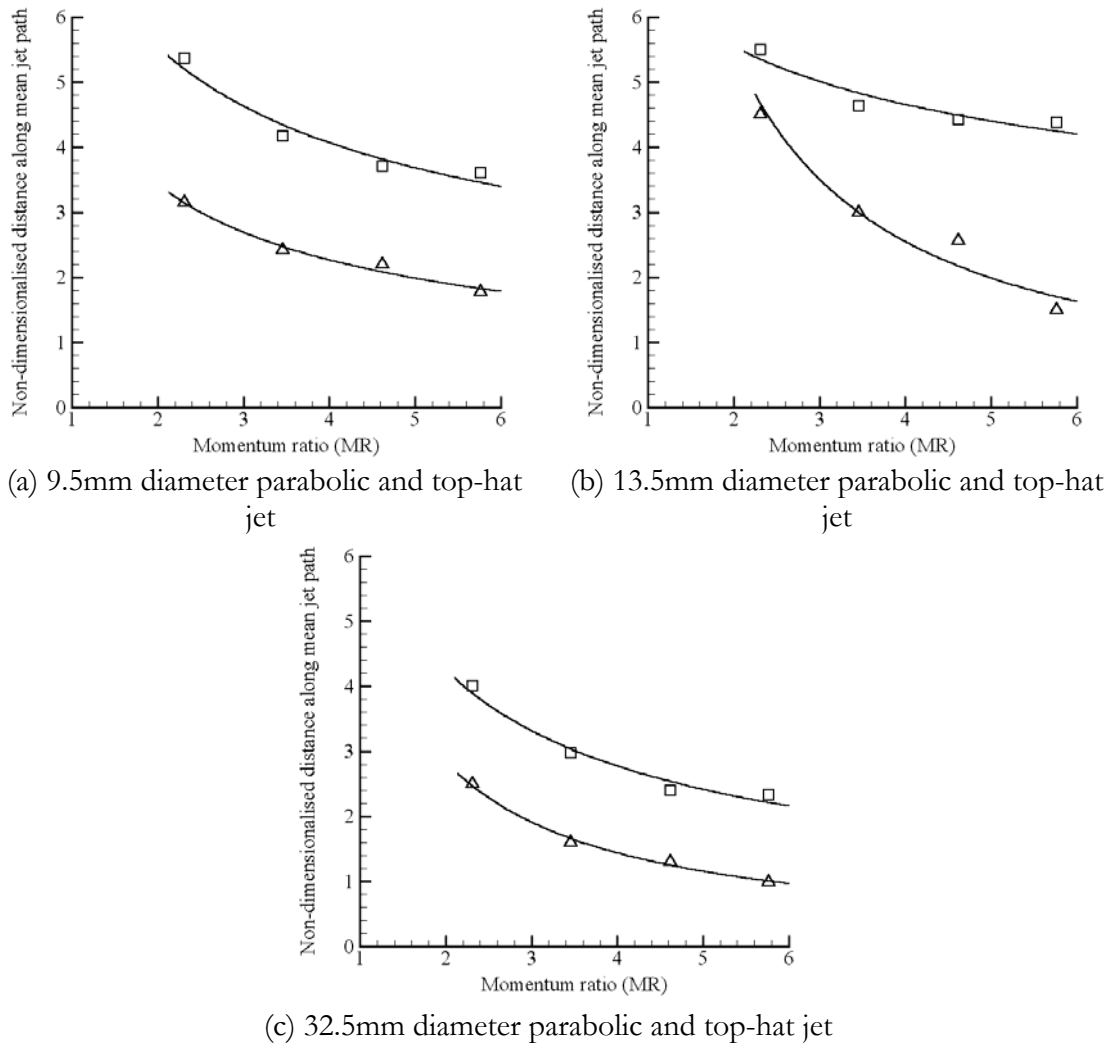
Figure 3.8. A comparison of non-dimensionalised distances measured along the mean jet axes where leading-edge vortices were first initiated between parabolic and top-hat jets of all three jet diameters. ($\triangle$: top-hat, $\square$: parabolic)

3.3 Laser-Induced Fluorescence (LIF) Imaging Along Jet Center-Line

To examine the "internal" structures of the leading edge vortices, LIF was carried out along the jet centrelines along the streamwise direction. Figures 3.9 to 3.14 show the laser cross-sections obtained. From the results, it is obvious that a thicker shear layer in parabolic jets is less susceptible to flow instability compared with the top-hat jets. Hence, by virtue of having thicker jet shear layers, parabolic jets could delay the initiation of leading-edge vortices. Also, the formation of these vortices for the parabolic jets was

(i) MR=2.31

(i) MR=2.31, Re=660

(ii) MR=3.46

(ii) MR=3.46, Re=985

(iii) MR=4.62

(iii) MR=4.62, Re=1320

(iv) MR=5.77

(iv) MR=5.77, Re=1645

(a) Parabolic
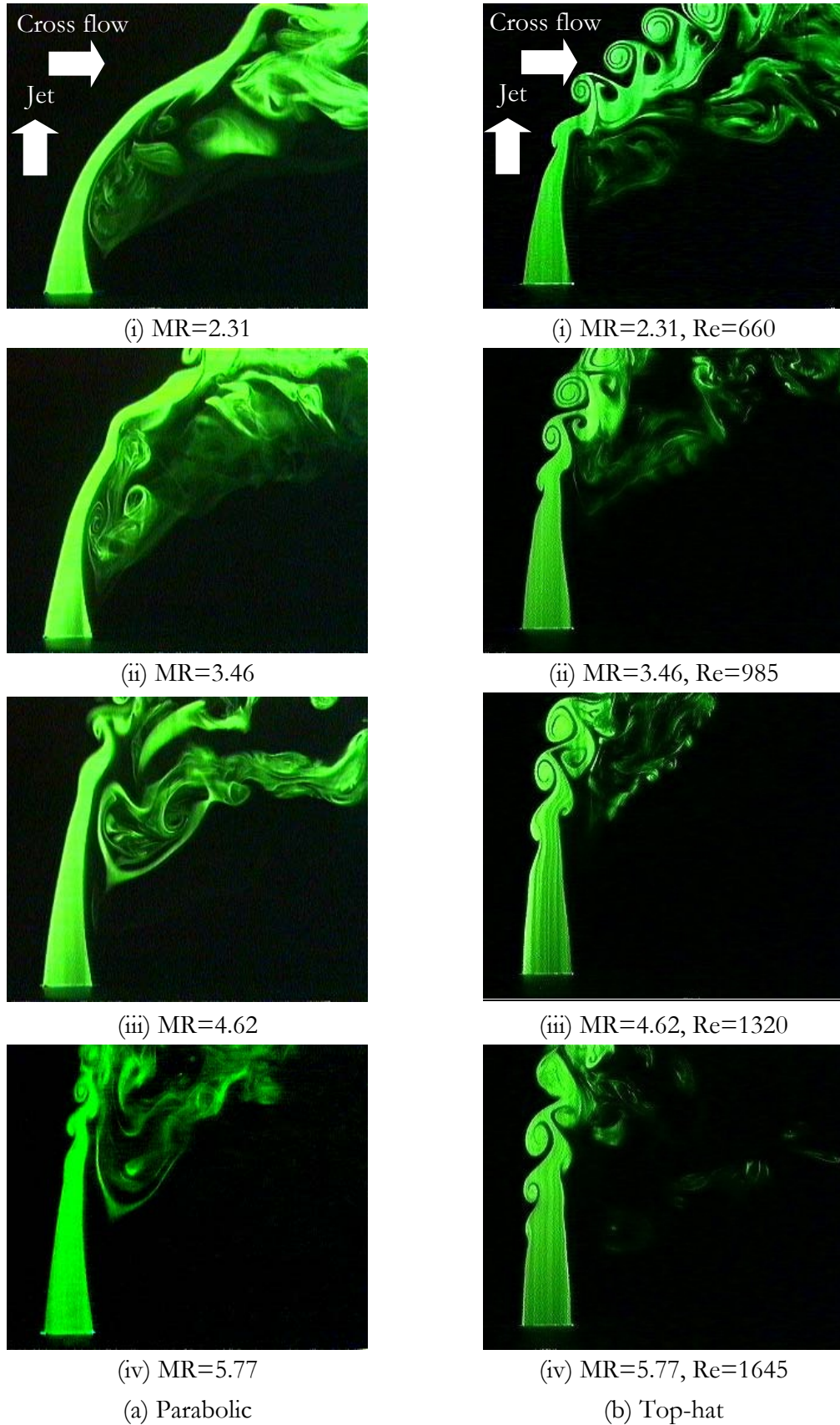
(b) Top-hat

Figure 3.9.   A near-field LIF comparison between a parabolic and top-hat 9.5mm diameter (0.38δ) circular JICF.

(i) MR=2.31   (i) MR=2.31, Re=660

(ii) MR=3.46   (ii) MR=3.46, Re=985

(iii) MR=4.62   (iii) MR=4.62, Re=1320

(iv) MR=5.77   (iv) MR=5.77, Re=1645

(a) Parabolic   (b) Top-hat
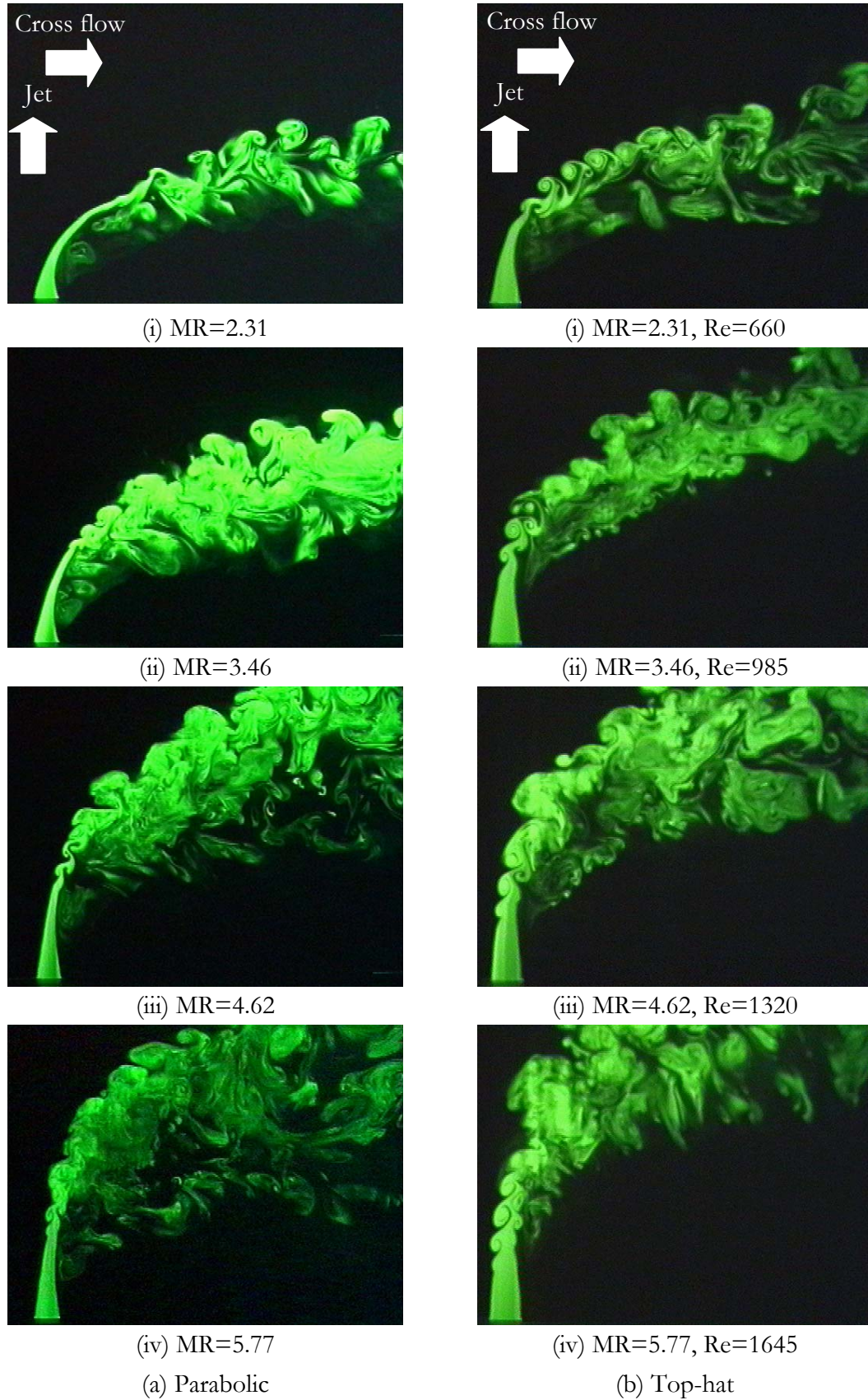
Figure 3.10.   A far-field LIF comparison between a parabolic and top-hat 9.5mm diameter (0.38δ) circular JICF.

(i) MR=2.31 (i) MR=2.31, Re=625

(ii) MR=3.46 (ii) MR=3.46, Re=935

(iii) MR=4.62 (iii) MR=4.62, Re=1250

(iv) MR=5.77 (iv) MR=5.77, Re=1560

(a) Parabolic (b) Top-hat
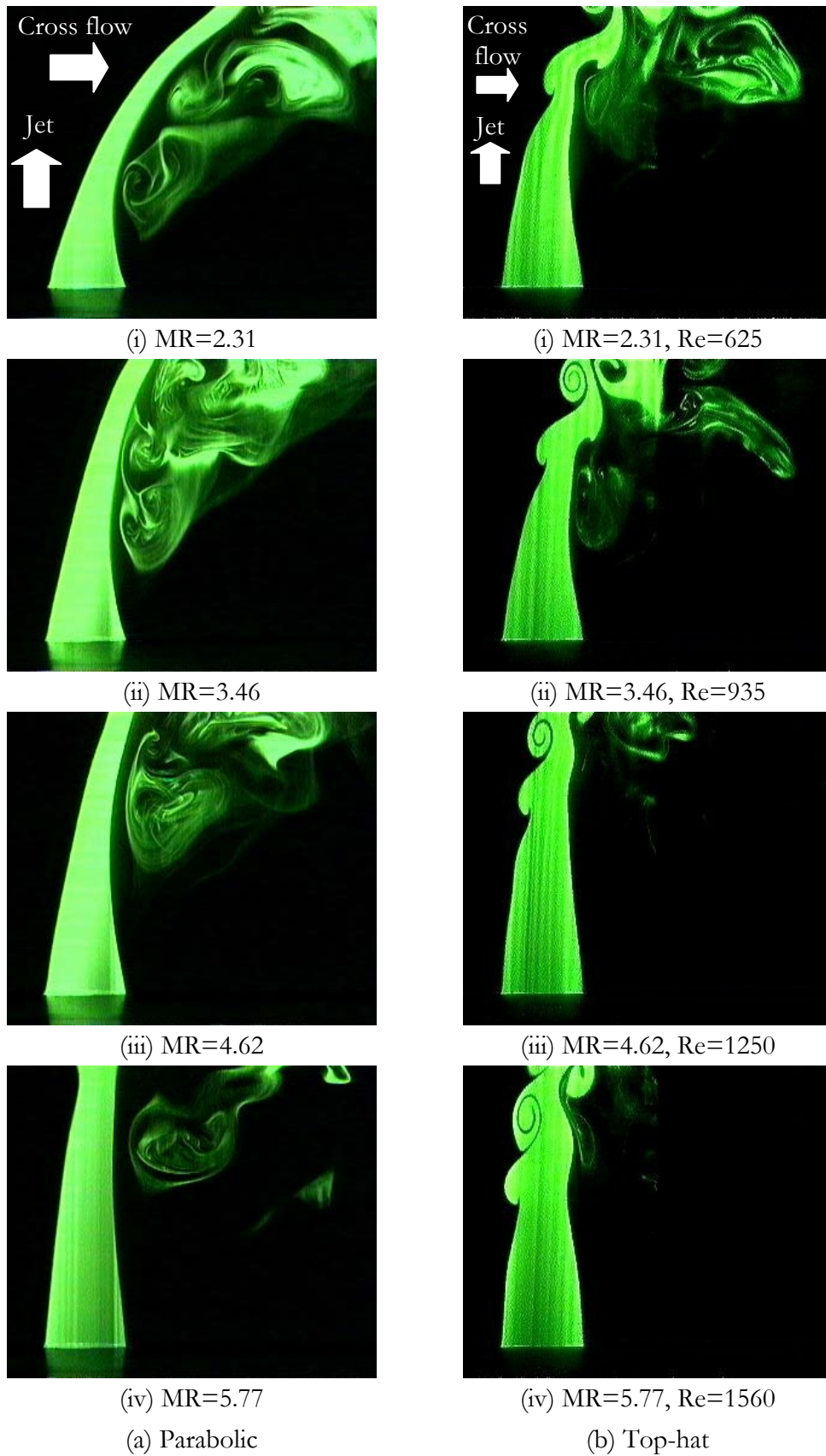
Figure 3.11. A near-field LIF comparison between a parabolic and top-hat 13.5mm diameter (0.54δ) circular JICF.

(i) MR=2.31　　　　　　　　　　(i) MR=2.31, Re=625

(ii) MR=3.46　　　　　　　　　　(ii) MR=3.46, Re=935

(iii) MR=4.62　　　　　　　　　　(iii) MR=4.62, Re=1250

(iv) MR=5.77　　　　　　　　　　(iv) MR=5.77, Re=1560

(a) Parabolic　　　　　　　　　　(b) Top-hat
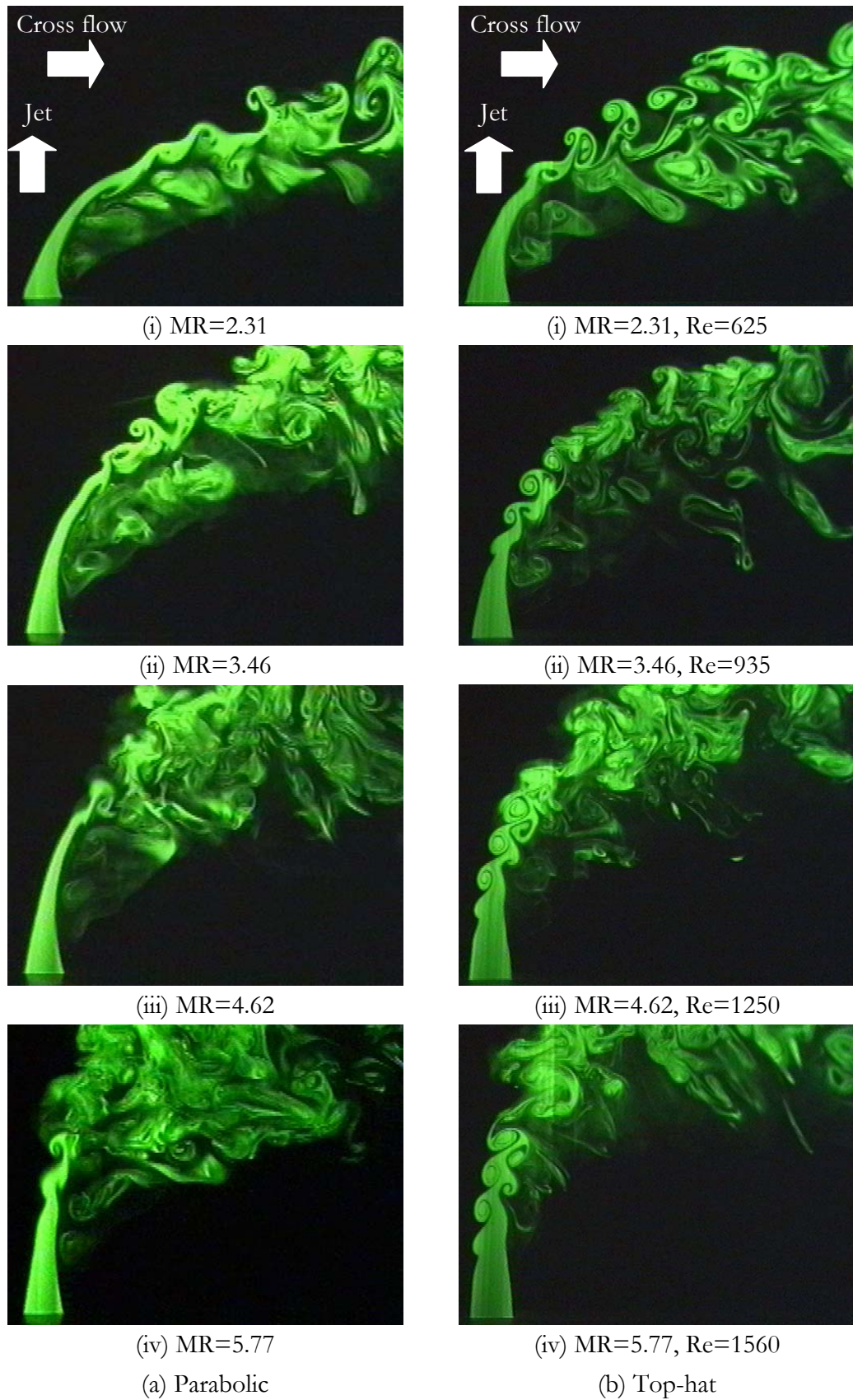
Figure 3.12.　　A far-field LIF comparison between a parabolic and top-hat 13.5mm diameter (0.54δ) circular JICF.

(i) MR=2.31   (i) MR=2.31, Re=750

(ii) MR=3.46   (ii) MR=3.46, Re=1125

(iii) MR=4.62   (iii) MR=4.62, Re=1500

(a) Parabolic   (b) Top-hat
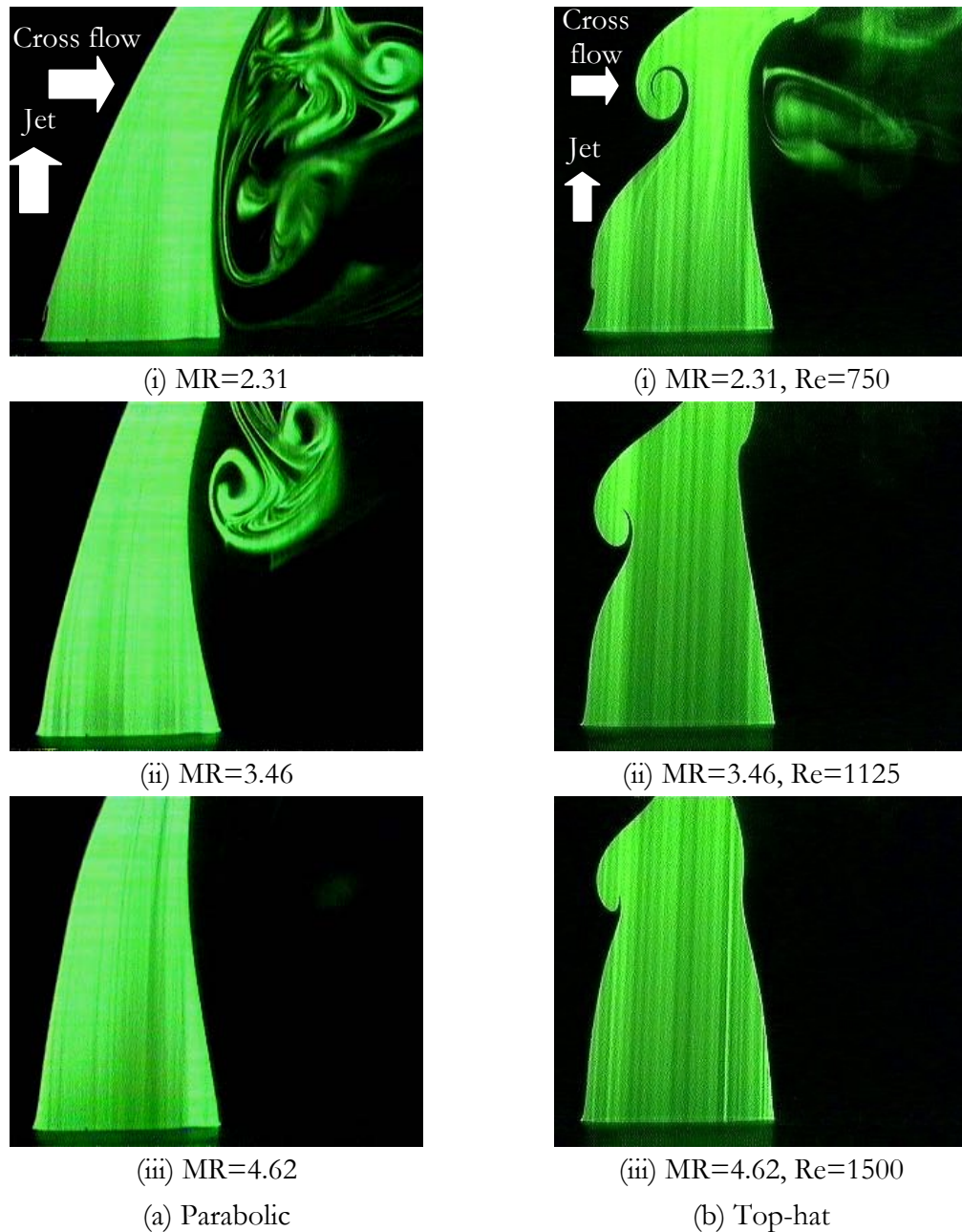
Figure 3.13.   A near-field LIF comparison between a parabolic and top-hat 32.5mm diameter (1.3δ) circular JICF.

profoundly influenced by the bending caused by the cross flow, as can be seen in the figures. Interestingly, up to MR=3.46, the leading-edge vortices appeared to form very close to the region of maximum jet-bending for parabolic JICF. It is likely the extra strain on the jet shear layer due to bending, coupled with the cross flow disturbance, caused the jet to roll up into vortices, thus leading to entrainment of cross flow fluid into the jet. As

(i) MR=2.31   (i) MR=2.31, Re=750

(ii) MR=3.46   (ii) MR=3.46, Re=1125

(iii) MR=4.62   (iii) MR=4.62, Re=1500

(a) Parabolic   (b) Top-hat
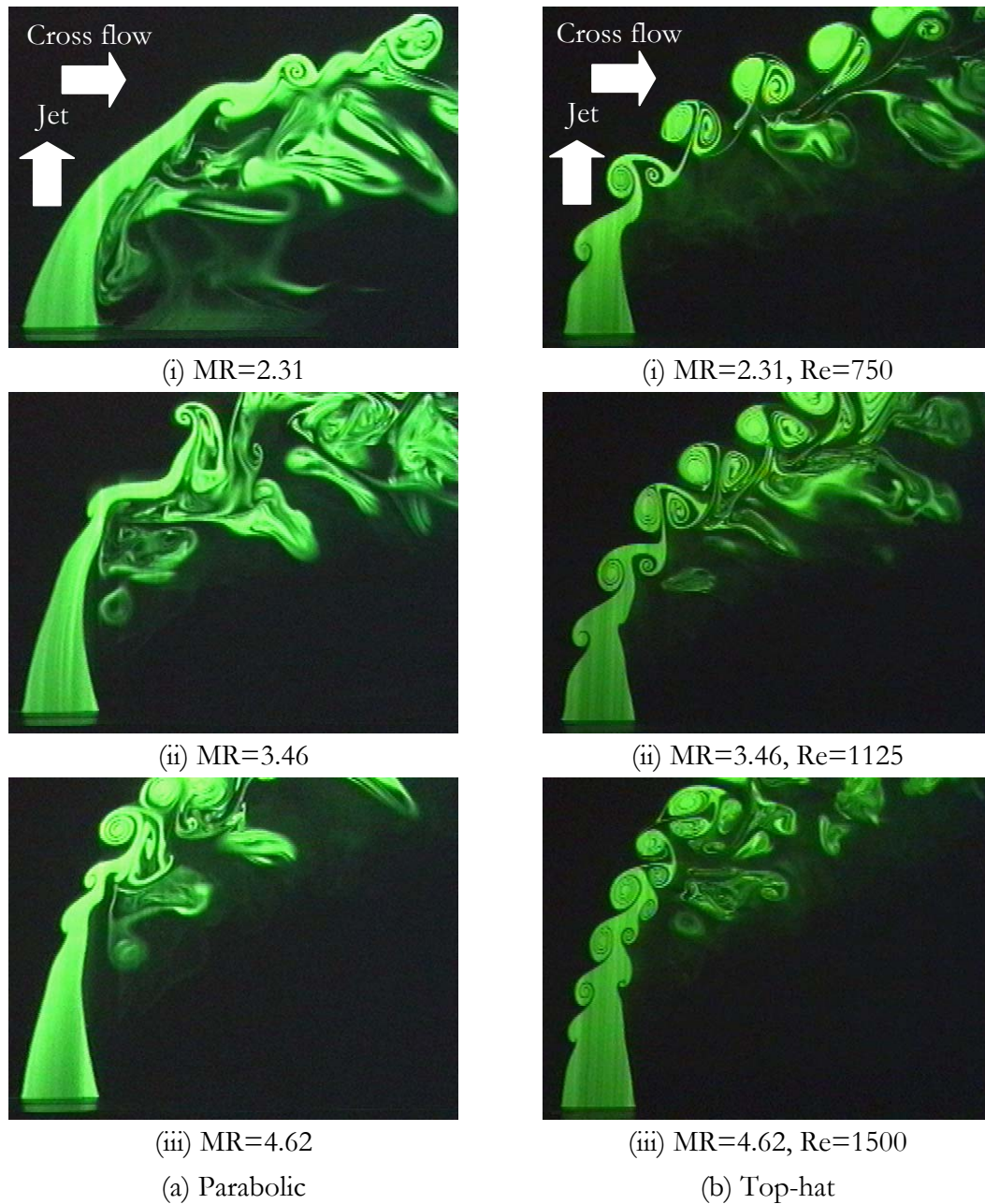
Figure 3.14.   A far-field LIF comparison between a parabolic and top-hat 32.5mm diameter (1.3δ) circular JICF.

for MR>3.46, leading-edge vortices seem to form before the region of maximum jet-bending, probably due to the stronger interaction between the jet and the cross flow which renders the jet shear layer more unstable.
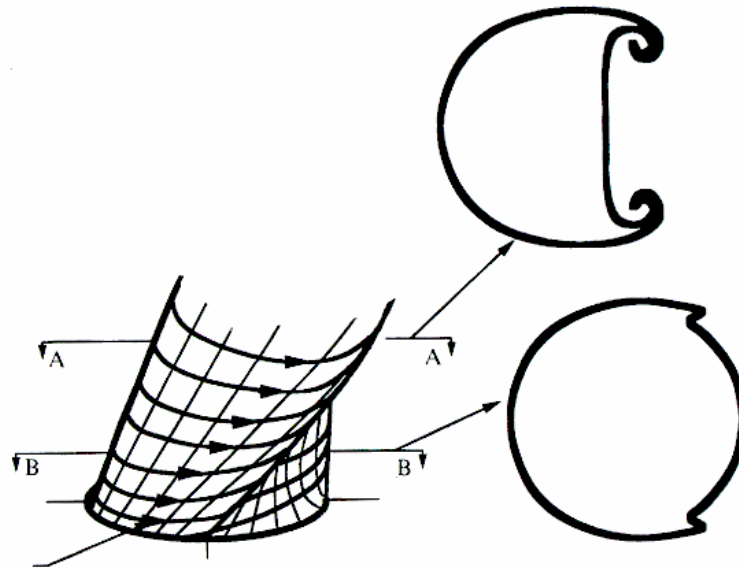
Figure 3.15.   Folding of jet shear layer at the lee-side region of the jet to form the CVP as suggested by Kelso et al. (1996).

Another distinct feature of the parabolic JICF was the randomness of the leading-edge vortices compared to those from the top-hat profile, which were more regular, at least initially. It was suspected that the randomness could be due to the uneven shear layer thickness caused by the complex interaction between the cross flow and the jet. With the top-hat profile, the shear layer thickness was more uniform on exiting the jet nozzle, whereas with the parabolic profile, the shear layer was thick to start with. But as the parabolic jet shear layer interacted with the cross flow, uneven stretching might have caused the shear layer to thin unevenly, thus leading to the observed behaviour. These findings suggest that the jet exit velocity profile is likely to have profound effects on the mixing processes in JICF.

It has been noted earlier (Michalke, 1984) that for free circular jets, the unstable frequencies which cause the vortex roll-ups are inversely proportional to the initial jet shear layer thickness. This will predict lower vortex roll-up frequencies for the free parabolic jets over top-hat jets. The results shown here qualitatively agree well with the prediction during the experiments, even though no measurements were actually taken.

The similarities between the earlier findings for free jets and jets in a cross flow environment here points to similar initial jet shear layer conditions and could attest to the effects of initial jet shear layer thickness on the final flowfields.

3.4   Laser-Induced Fluorescence (LIF) Imaging Across Mean Jet Path

In the search for possible enhancements to mixing and entrainment capabilities of the JICF phenomenon, the CVP has been studied extensively over the years. Past research has established that the CVP is produced at both sides of the jet as a result of the folding of the cylindrical jet shear layer (see Figure 3.15) and is the main driving mechanism behind the entrainment behaviour at the far-field. However, with different exit velocity profiles investigated here, an inevitable question arises as to whether the initiation and development of the CVP for parabolic JICF be any different from the top-hat jets? Since the evolution process of the CVP is dictated by the modification of the jet shear layer by the cross flow, one would expect that a difference in the shear layer thickness, as in the case for parabolic JICF, may lead to differences that could promote or impede the development of the CVP. With that in mind, a series of laser cross-sections were obtained for all three parabolic and top-hat JICF at regular intervals along the mean jet paths as described in the previous chapter.

Figures 3.16 to 3.27 show the laser cross-sections obtained for the 13.5mm and 32.5mm jet diameters using both parabolic and top-hat velocity profile jets with MR from 3.46 to 5.77, and with the distance s along the mean jet trajectory typically from 0.5D to about 3D. To save space, cross-sections for the 9.5mm jet were not included as they closely resembled those of 13.5mm jet. The MR range was chosen to reflect the typical intermediate JICF behaviour where the jet influence on the cross flow remained

43

(a) s=0.5D

(b) s=1.0D

(c) s=1.5D

(d) s=2.0D

(e) s=2.5D

(f) s=3.0D
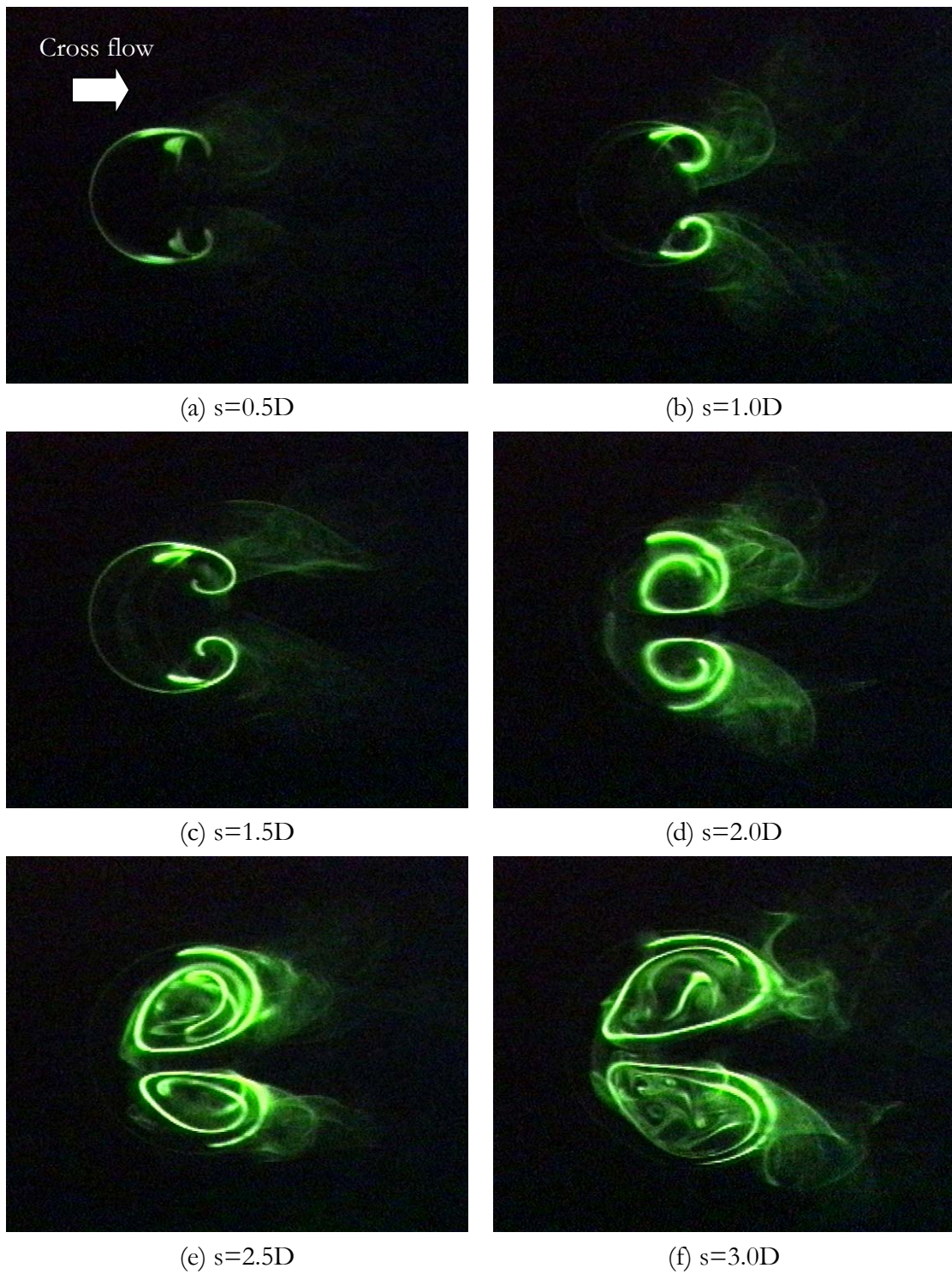
Figure 3.16.   Laser cross-section of the jet body at various mean jet path locations for MR=3.46 parabolic 13.5mm diameter (0.54δ) jet.

<table>
<tr><td>(a) s=0.5D</td><td>(b) s=1.0D</td></tr>
<tr><td>(c) s=1.5D</td><td>(d) s=2.0D</td></tr>
<tr><td>(e) s=2.5D</td><td>(f) s=3.0D</td></tr>
</table>
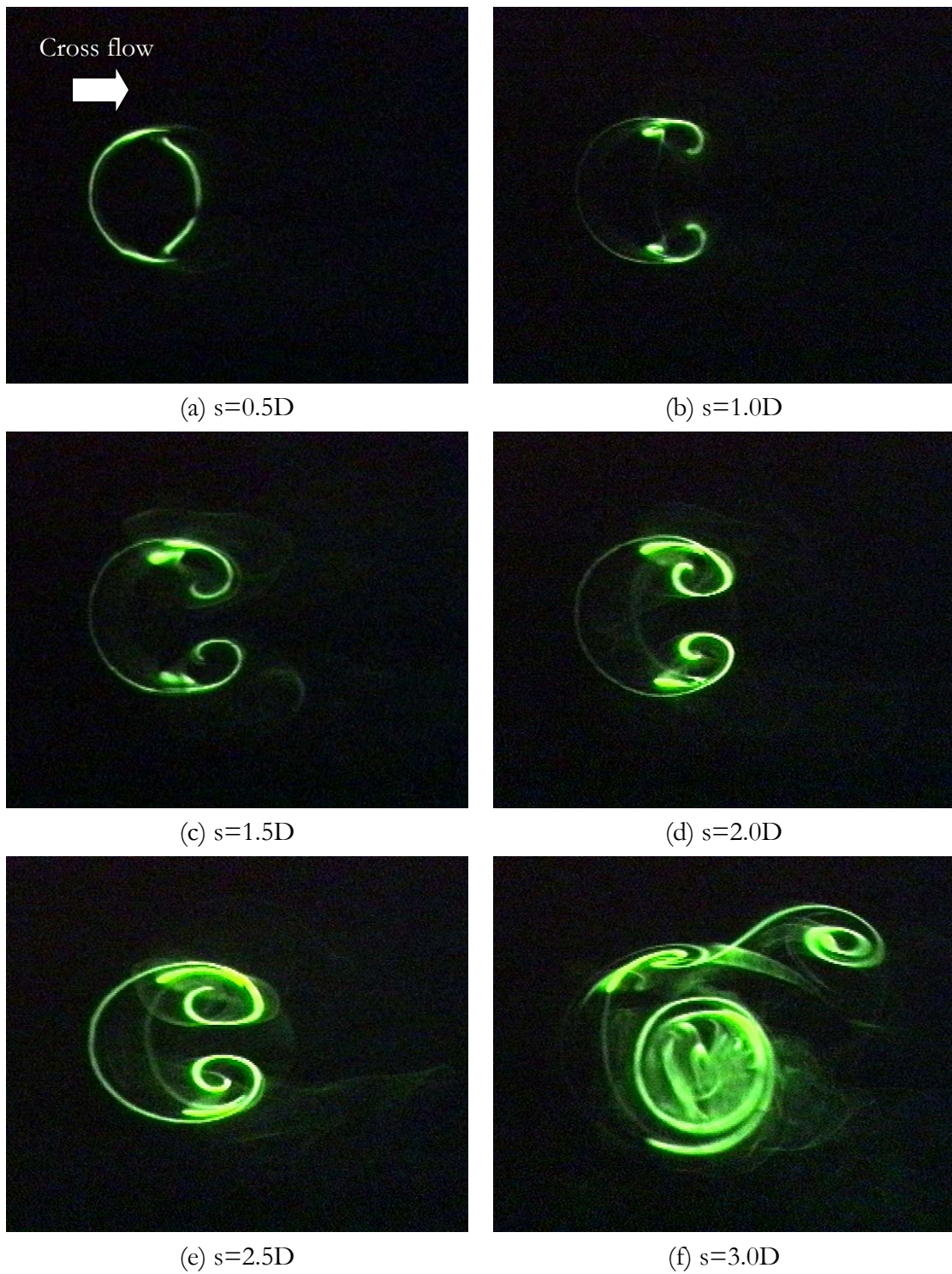
Figure 3.17.   Laser cross-section of the jet body at various mean jet path locations for MR=4.62 parabolic 13.5mm diameter (0.54δ) jet.

(a) s=0.5D

(b) s=1.0D

(c) s=1.5D

(d) s=2.0D

(e) s=2.5D

(f) s=3.0D
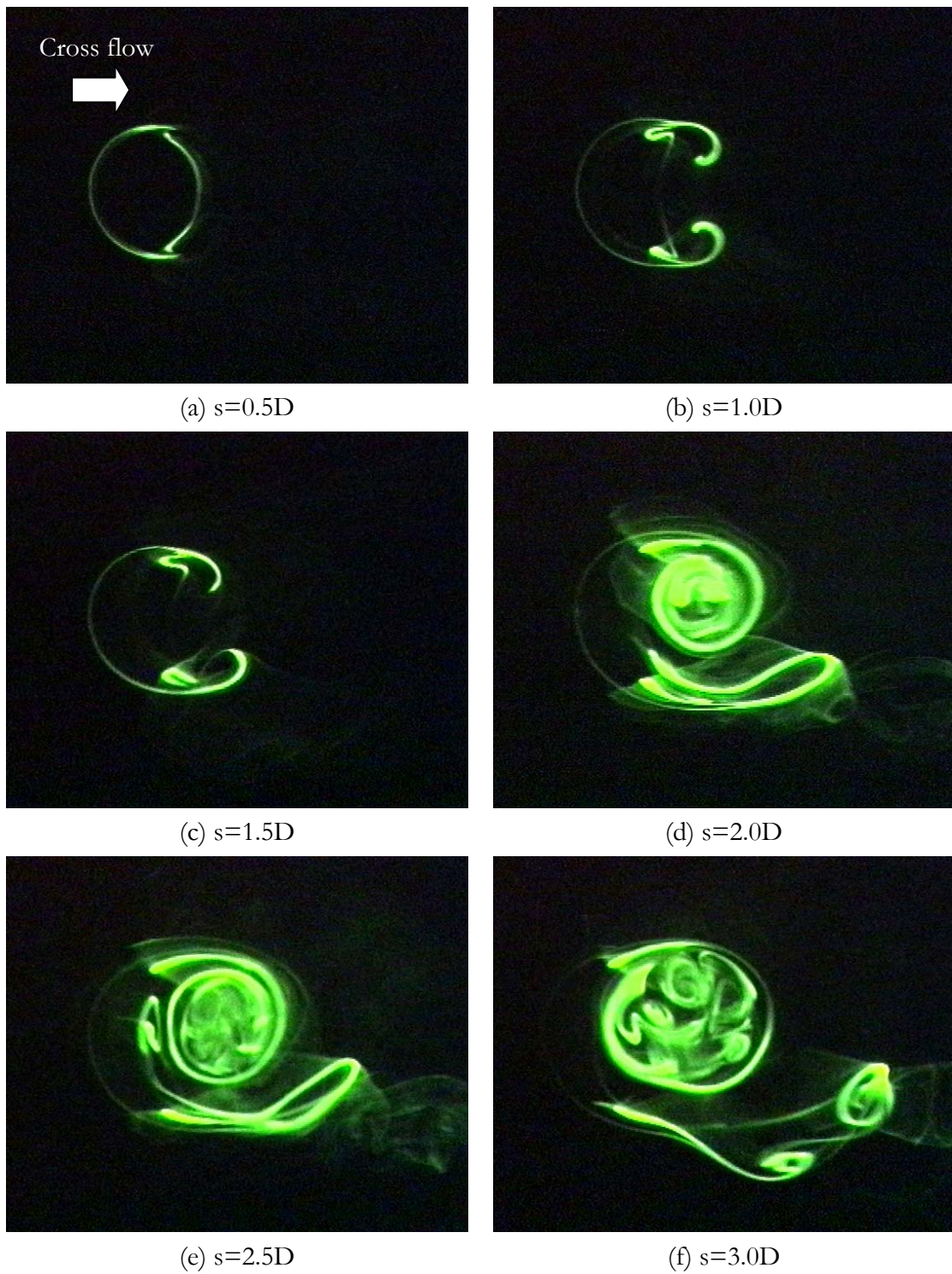
Figure 3.18.   Laser cross-section of the jet body at various mean jet path locations for MR=5.77 parabolic 13.5mm diameter (0.54δ) jet.

<div align="center">

(a) s=0.5D   (b) s=1.0D

(c) s=1.5D   (d) s=2.0D

</div>
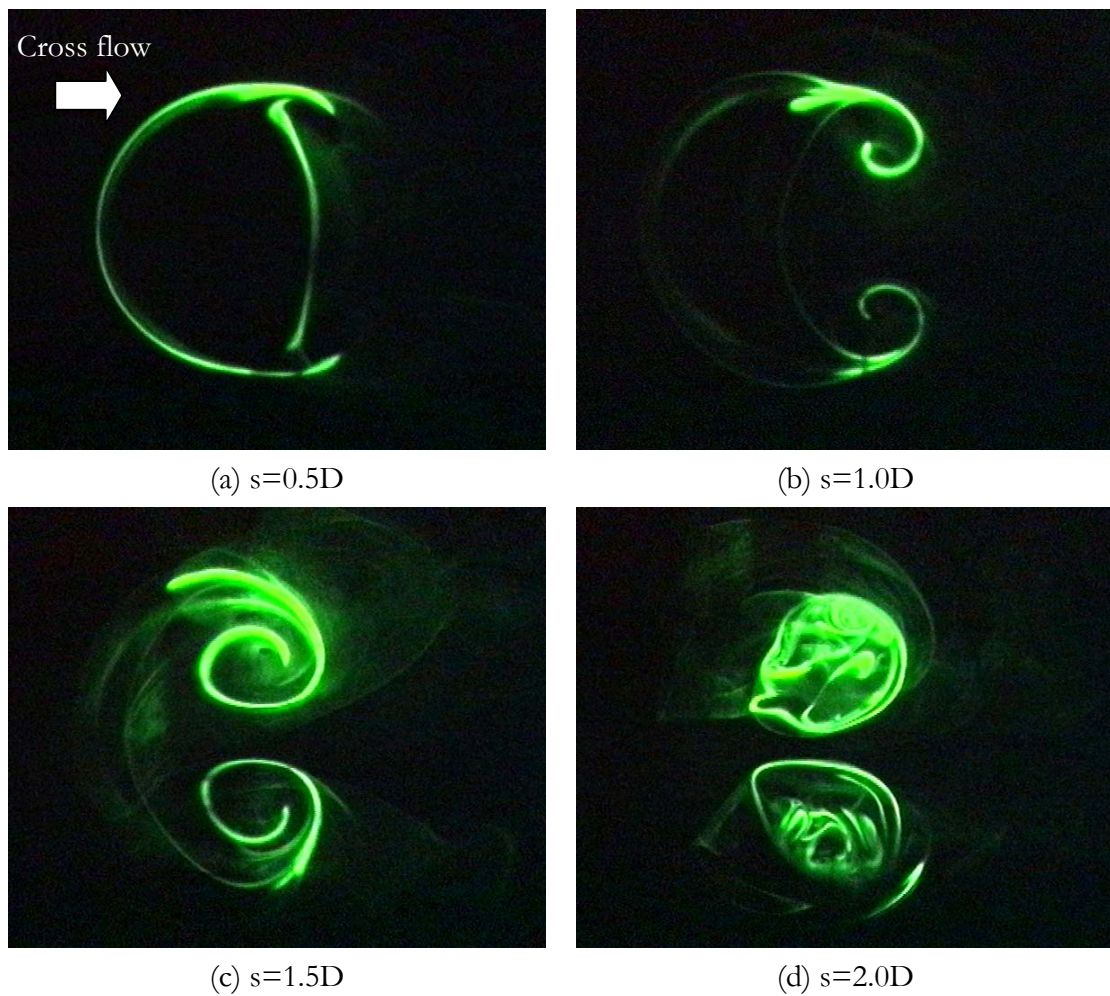
Figure 3.19.   Laser cross-section of the jet body at various mean jet path locations for MR=3.46 parabolic 32.5mm diameter (1.3δ) jet.

significant. Generally, the initiation of the CVP was found to be similar for both parabolic and top-hat jets and subsequent flow development also did not deviate too much from each other. One could clearly observe the folding of the jet shear layers at the lee-side region of the jets into CVPs, which gradually increased in size with downstream distance, presumably by the entrainment of the cross flow fluid and viscous diffusion. However, one could certainly discern a higher level of flow distortions in the case of parabolic jets over the top-hat jets, especially at high momentum ratios. For the parabolic jets, LIF images revealed cross sections that were not that symmetrical under certain flow circumstances. More often, they were heavily distorted at the upper limits of the distance

(a) s=0.5D

(b) s=1.0D

(c) s=1.5D

(d) s=2.0D

(e) s=2.5D
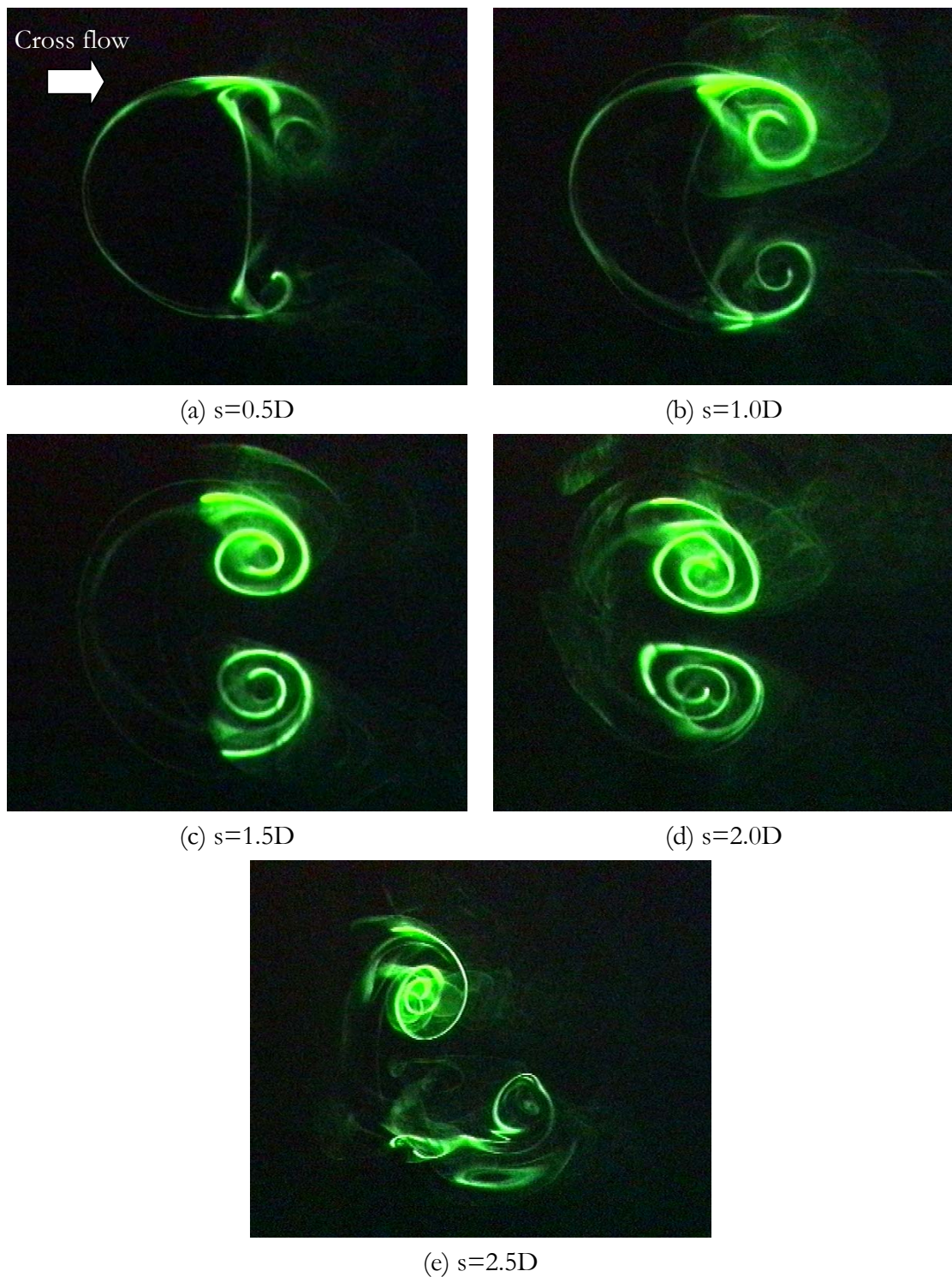
Figure 3.20.   Laser cross-section of the jet body at various mean jet path locations for MR=4.62 parabolic 32.5mm diameter (1.3δ) jet.

(a) s=0.5D

(b) s=1.0D

(c) s=1.5D

(d) s=2.0D

(e) s=2.5D

(f) s=2.5D
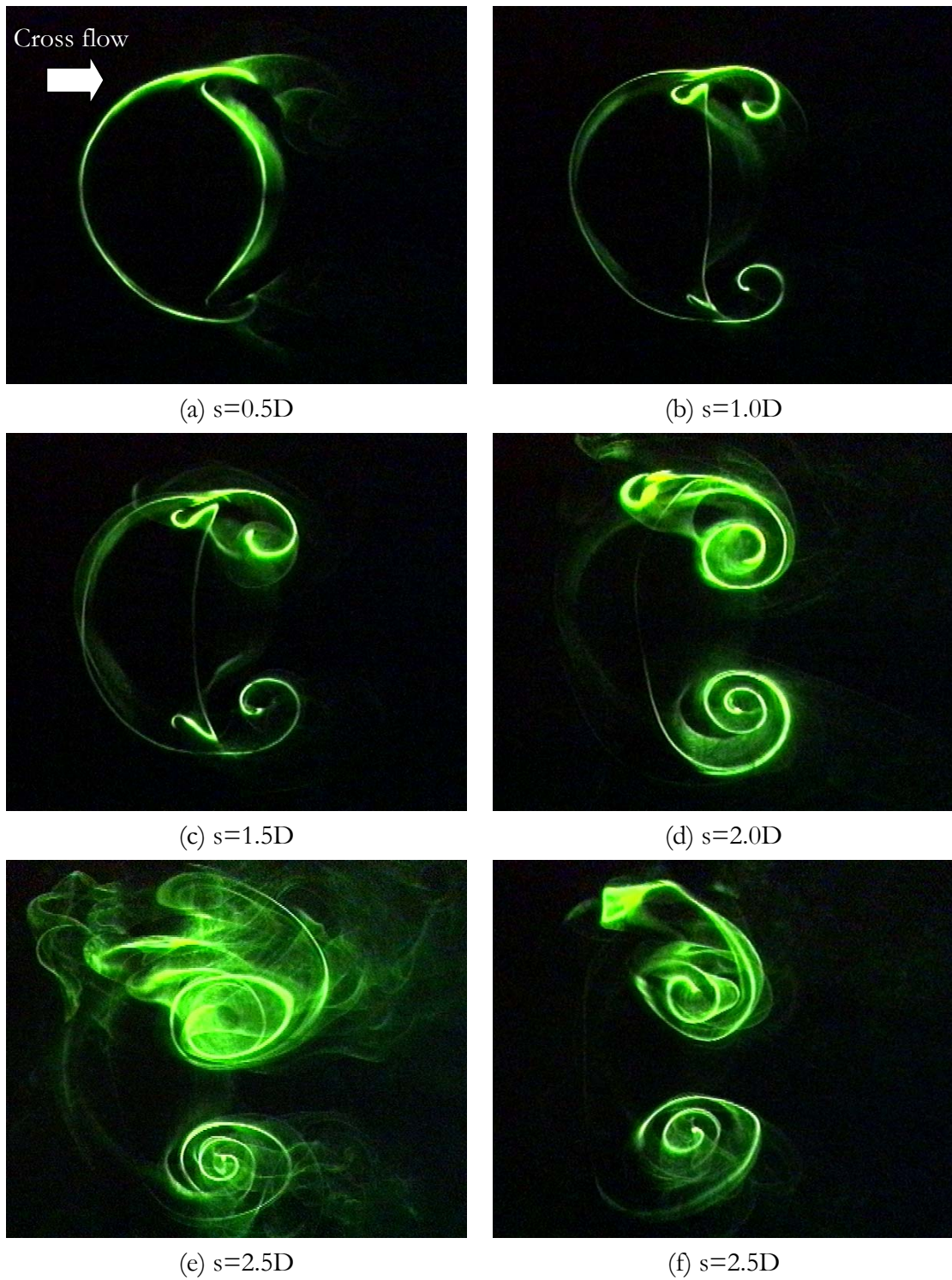
Figure 3.21.   Laser cross-section of the jet body at various mean jet path locations for MR=5.77 parabolic 32.5mm diameter (1.3δ) jet.

(a) s=0.5D

(b) s=1.0D

(c) s=1.5D

(d) s=2.0D

(e) s=2.5D

(f) s=3.0D
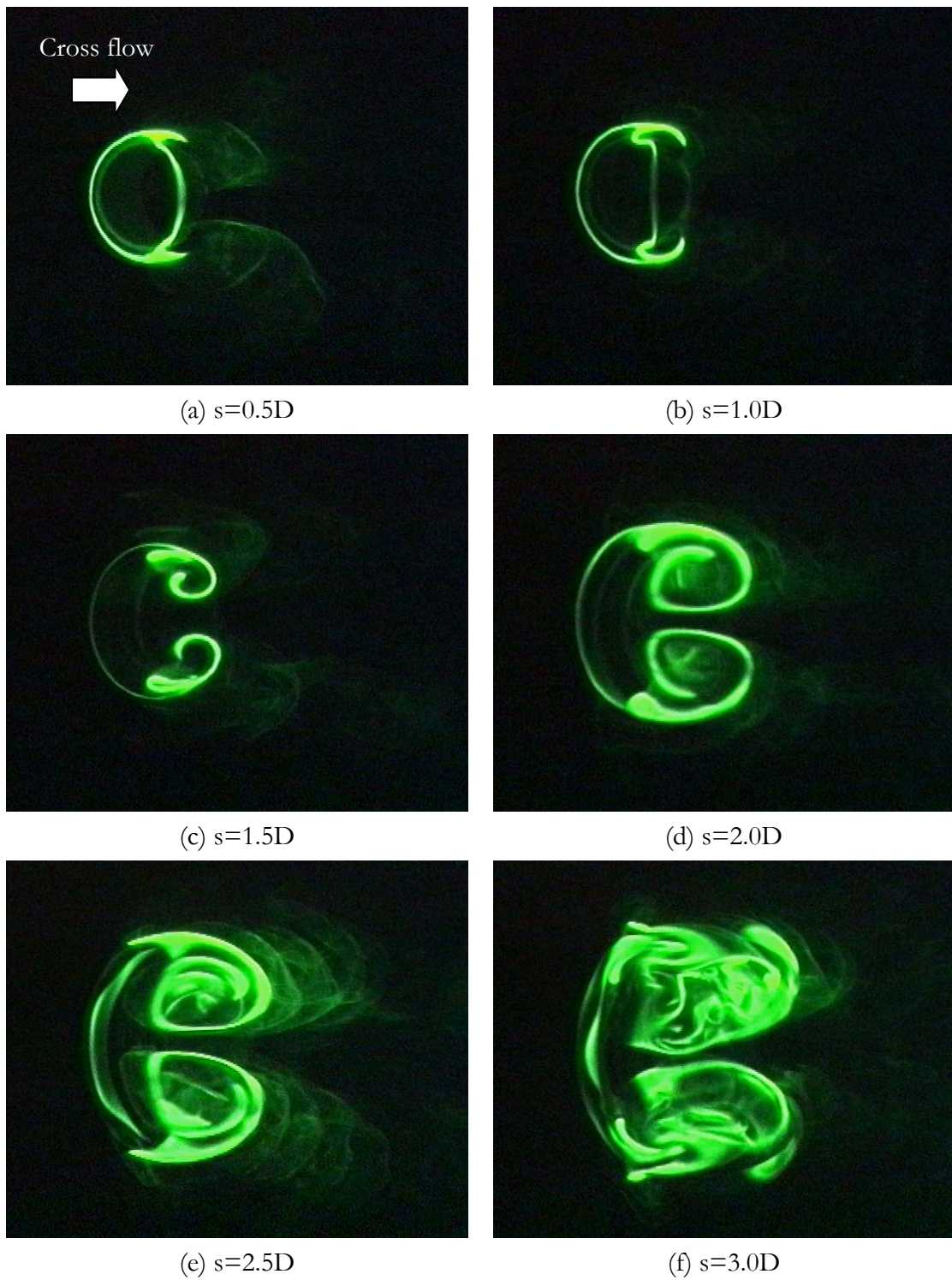
Figure 3.22.   Laser cross-section of the jet body at various mean jet path locations for MR=3.46 top-hat 13.5mm diameter (0.54δ) jet.

(a) s=0.5D   (b) s=1.0D

(c) s=1.5D   (d) s=2.0D

(e) s=2.5D   (f) s=3.0D
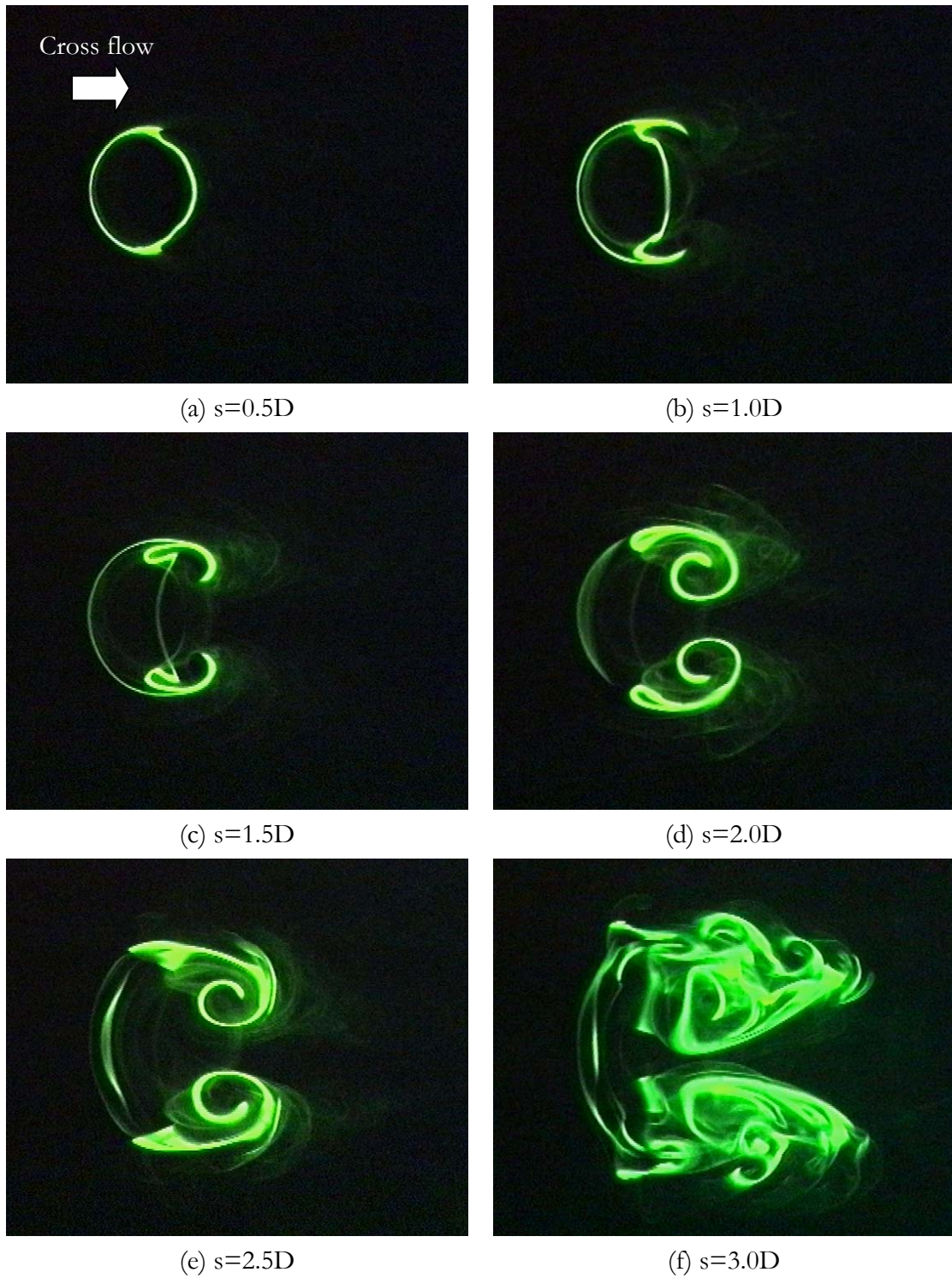
Figure 3.23.   Laser cross-section of the jet body at various mean jet path locations for MR=4.62 top-hat 13.5mm diameter (0.54δ) jet.

(a) s=0.5D   (b) s=1.0D

(c) s=1.5D   (d) s=2.0D

(e) s=2.5D   (f) s=3.0D
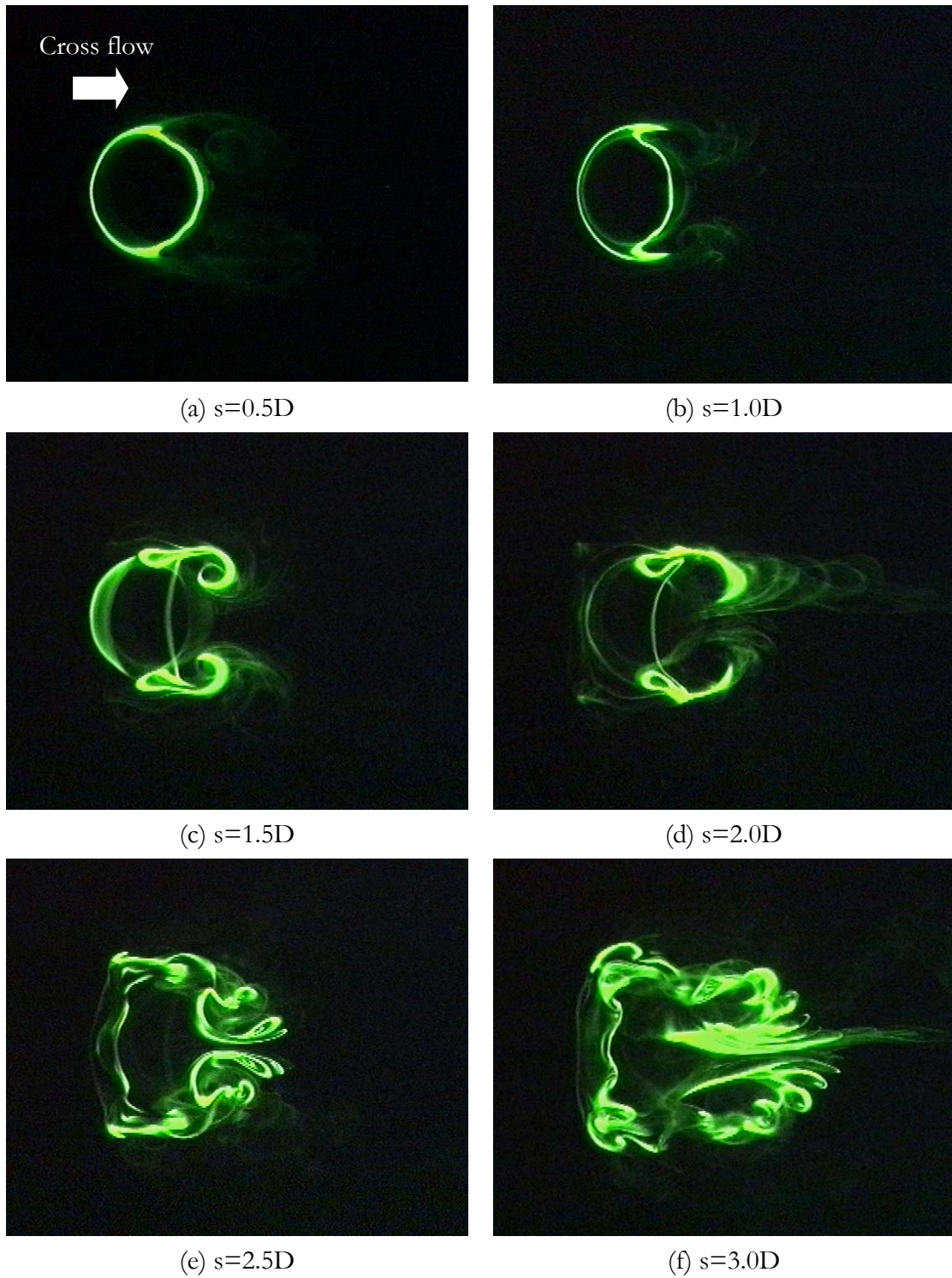
Figure 3.24.   Laser cross-section of the jet body at various mean jet path locations for MR=5.77 top-hat 13.5mm diameter (0.54δ) jet.

(a) s=0.5D   (b) s=1.0D

(c) s=1.5D   (d) s=2.0D

(e) s=2.5D
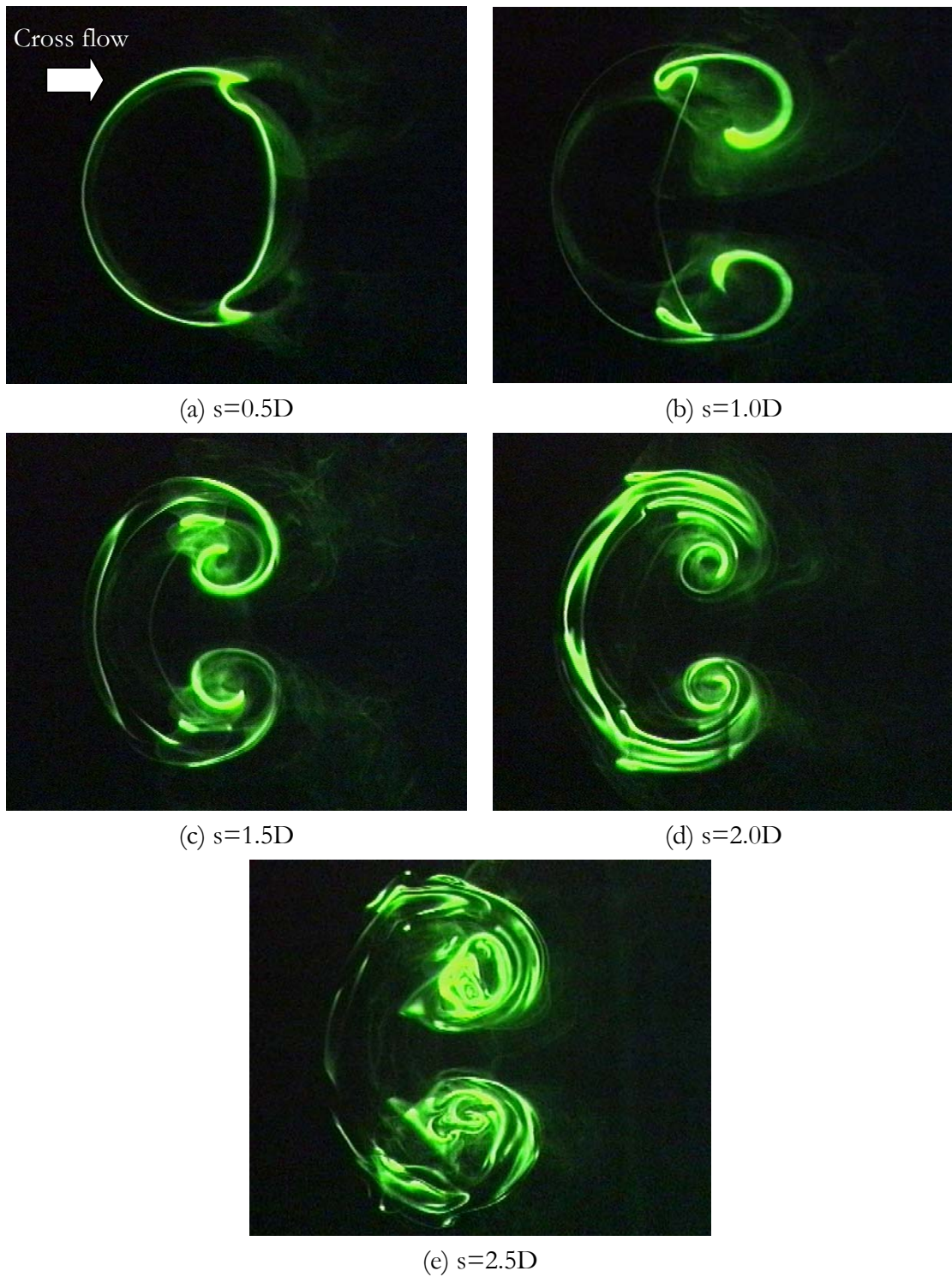
Figure 3.25.   Laser cross-section of the jet body at various mean jet path locations for MR=3.46 top-hat 32.5mm diameter (1.3δ) jet.

(a) s=0.5D

(b) s=1.0D

(c) s=1.5D

(d) s=2.0D

(e) s=2.5D
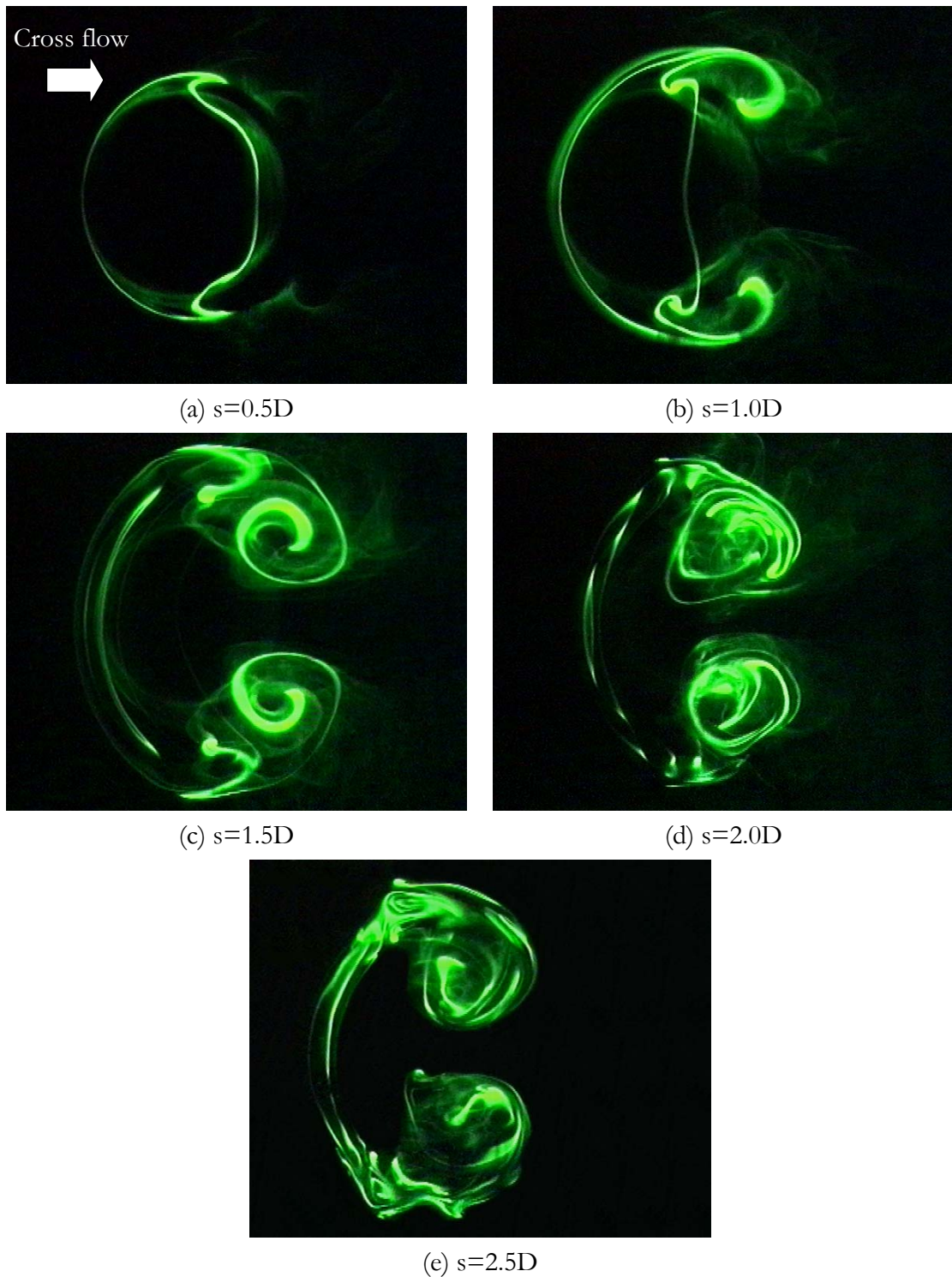
Figure 3.26.   Laser cross-section of the jet body at various mean jet path locations for MR=4.62 top-hat 32.5mm diameter (1.3δ) jet.

(a) s=0.5D

(b) s=1.0D

(c) s=1.5D

(d) s=2.0D

(e) s=2.5D
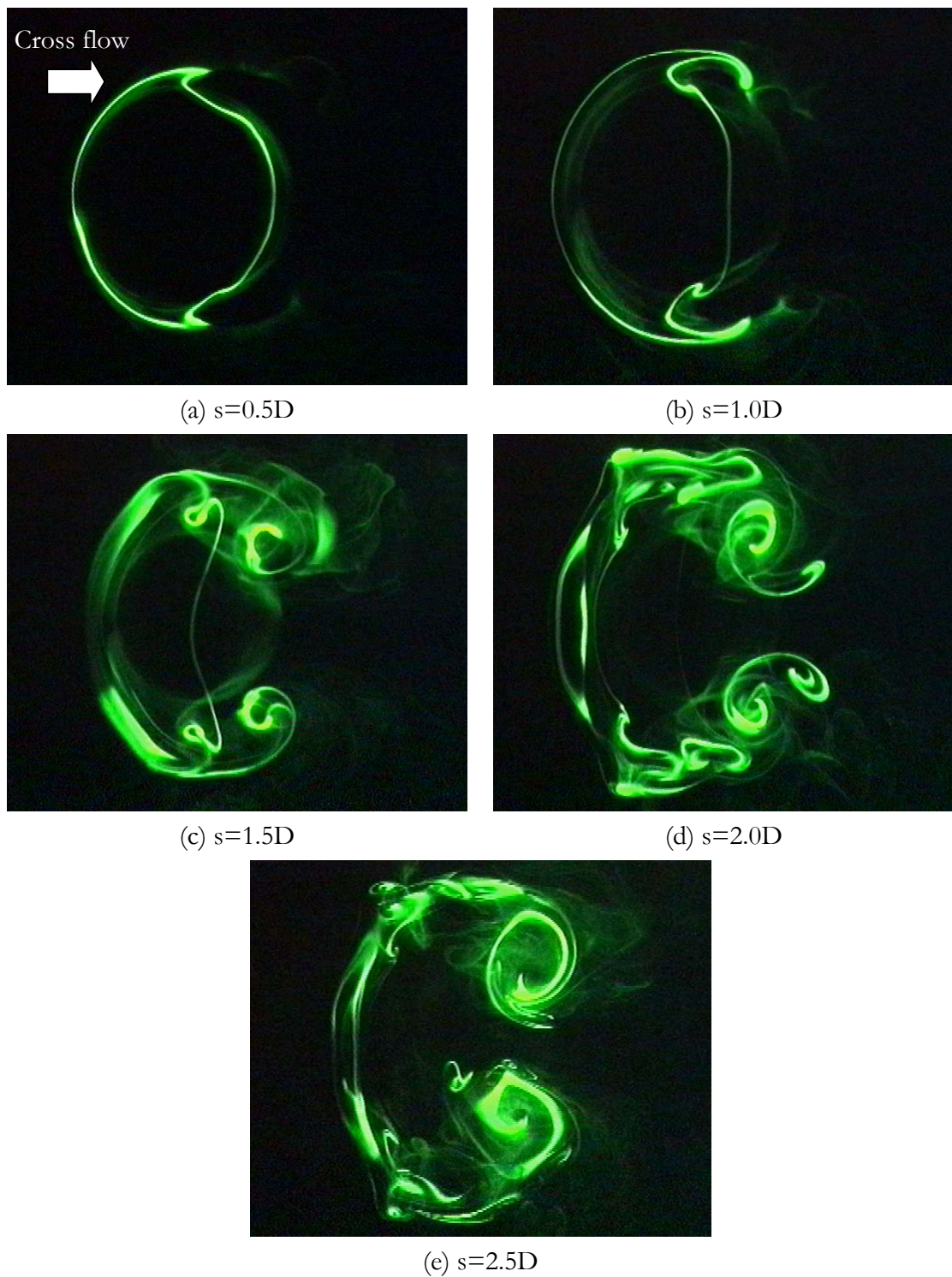
Figure 3.27.   Laser cross-section of the jet body at various mean jet path locations for MR=5.77 top-hat 32.5mm diameter (1.3δ) jet.

s, with the distortion seemingly random and usually accentuated by the onset of the wake vortices. The unsteadiness of the CVPs and their subsequent distortion could be attributed to the random asymmetrical thinning and vortex stretching of the shear layer discussed earlier. In particular, asymmetrical flow would lead to similar asymmetrical forces acting on the deflected jets, and this would in turn lead to distortions in the CVP. In the near-field, the cross-sections remained stable since the jet potential cores remained stable and also there is no jet shear layer disturbances caused by shedding of the leading-edge vortices. In contrast, the top-hat jet shear layer is uniformly thin to begin with, and this is likely to lead to a more symmetrical flow field than that of a parabolic jets.

Moreover, the appearance of wake vortices at high momentum ratios further contributed to the unsteadiness of the resultant flow. Wake vortices, as investigated by Fric and Roshko (1994), were a result of the boundary layer separating behind the jet and forming wake-like vortex structures which shows remarkable resemblance to the von Karman vortex street usually formed behind bluff bodies. Intriguingly, though the wake vortices originated from the cross flow boundary layer, the entire vortex filament remained almost visually vertical and connected to the CVP. Unfortunately, the mechanism of the connection between these wake vortices and the CVP remained unclear till today, although Kelso et al. (1993) made an attempt to account for it. But it was clear from the LIF figures that the wake vortices could greatly disrupt the symmetrical formation of the CVP. The vertically-orientated wake vortices ensured a regular fluctuating pressure distribution on the lee-side region of the deflected jets, much like the one existing at the lee-side region of a bluff body. Such a scenario would definitely have imposed additional flow disturbances to the development of the CVP.

Chapter 4

PIV Measurements of Circular Jet in a Cross Flow: Effects of Jet Shear Layer Thickness

4.1   Introduction

In the previous chapter, flow visualization results revealed a difference in the flow behaviour between parabolic and top-hat JICF, particularly with respect to the interaction between the jet shear layer and the cross flow. The former was postulated to be influenced by non-uniform stretching of the thicker parabolic jet shear layer, while the latter was a result of the inherently unstable thin shear layer associated with top-hat jet profile. To complement our visual results, particle image velocimetry measurements were carried out to obtain both velocity and vorticity fields of these two flow conditions.

4.2   Instantaneous Vorticity Fields

Figures 4.1 to 4.6 showed the contour plots for the vorticity fields obtained via PIV for all three jet diameters with top-hat and parabolic velocity profile JICF. The vorticity measured was the out-of-plane vorticity component and calculated using an analytic differentiation of the relationship

$$X = \frac{\partial v}{\partial x} - \frac{\partial u}{\partial y}$$

It was calculated that the CCD camera has an initial resolution of 0.11mm/pixel, both horizontally and vertically, and covered an effective imaging area of approximately 112.18mm by 112.18mm. The spatial resolution of the final derived velocity was estimated to be 1.81mm. In terms of the jet diameters studied, the resolution constitutes 0.19D, 0.13D and 0.06D of the 9.5mm, 13.5mm and 32.5mm circular jets respectively.

(a) MR=2.31   (b) MR=3.46

(c) MR=4.62   (d) MR=5.77
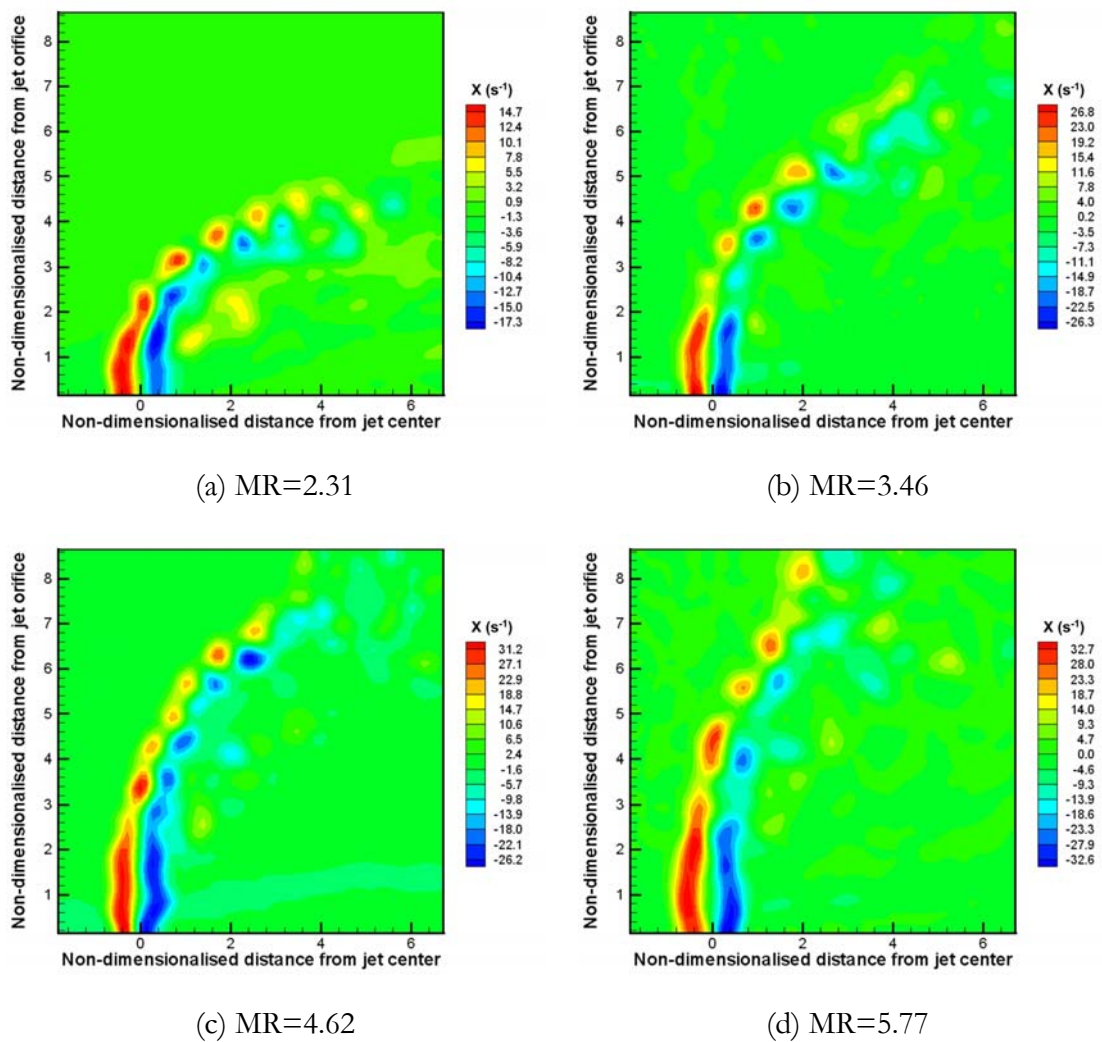
Figure 4.1.   Instantaneous vorticity plots along streamwise jet centre-line for 9.5mm top-hat JICF from MR=2.31 to 5.77.

Not surprisingly, these vorticity fields confirmed our observation in Chapter 3 that top-hat JICF readily produced leading-edge vortices in a seemingly coherent manner, while parabolic JICF did not seem to exhibit the same phenomenon. A closer examination of the vorticity fields also confirmed the expected thicker jet shear layer of the parabolic jet as is indicated by the larger red (positive vorticity levels, counter-clockwise orientation) and blue (negative vorticity levels, clockwise orientation) coloured-regions. There is also a smooth and gradual decrease in the vorticity levels in the downstream jet shear layer before forming individual vortices. In contrast, the shear layer

(a) MR=2.31

(b) MR=3.46

(c) MR=4.62

(d) MR=5.77
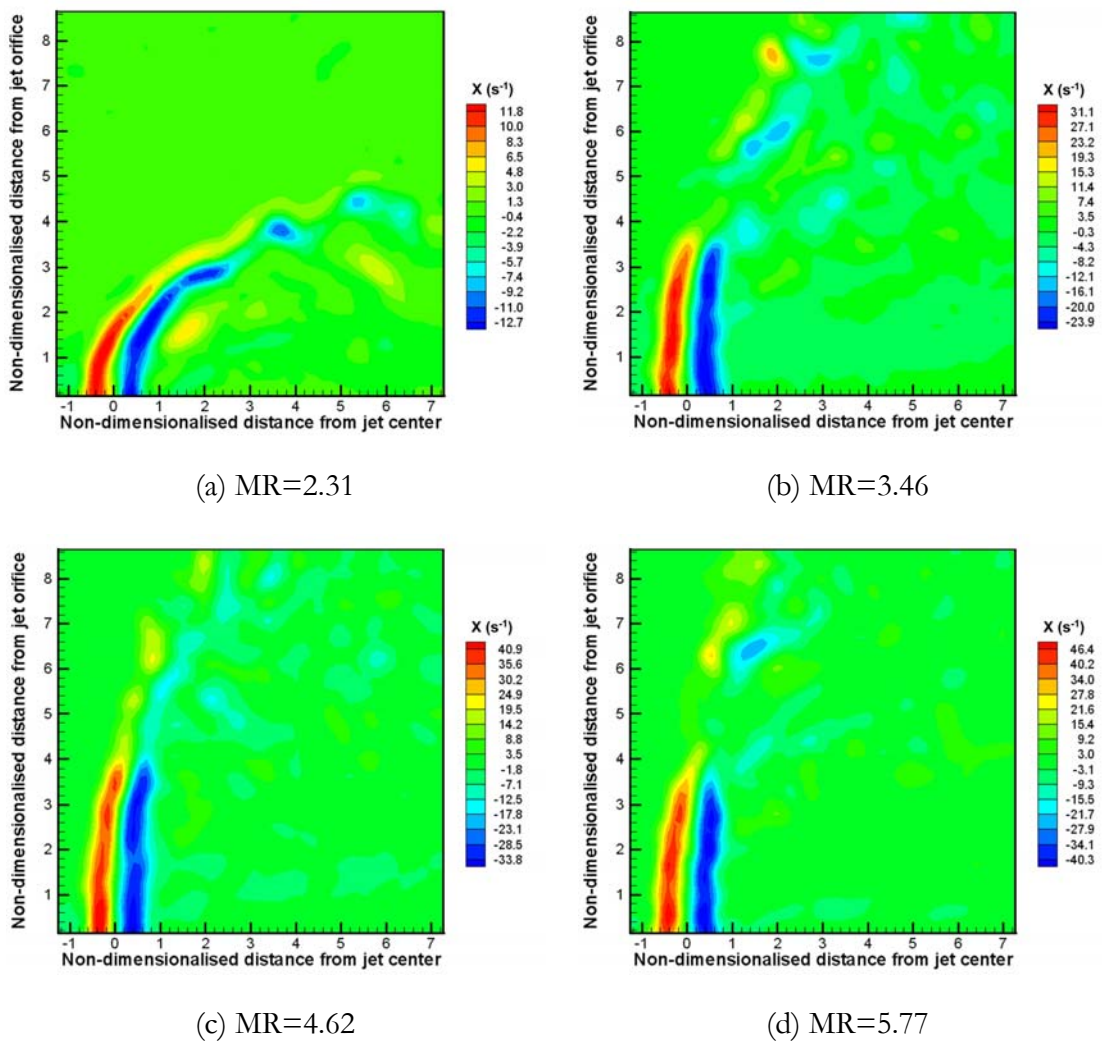
Figure 4.2.   Instantaneous vorticity plots along streamwise jet centre-line for 9.5mm parabolic JICF from MR=2.31 to 5.77.

of the top-hat JICF, upon leaving the jet exit, quickly rolls up into periodic leading-edge vortices, presumably via Kelvin- Helmholtz-like instability. The reduction in the jet shear layer vorticity values with downstream distance indicates the combined effects of viscous diffusion and vorticity **annihilation**. Take for example, leading-edge vortices resulting from the 13.5mm top-hat JICF initially started out with a peak vorticity value of about 13.86 s^{-1} (see Figure 4.3b), but as they convected downstream, they suffered a persistent drop in their vorticity strength (until approximately 7 s^{-1}) probably due to the dominance of the vortex diffusion and **annihilation** over the effect of vortex stretching. The same

(a) MR=2.31

(b) MR=3.46

(c) MR=4.62

(d) MR=5.77
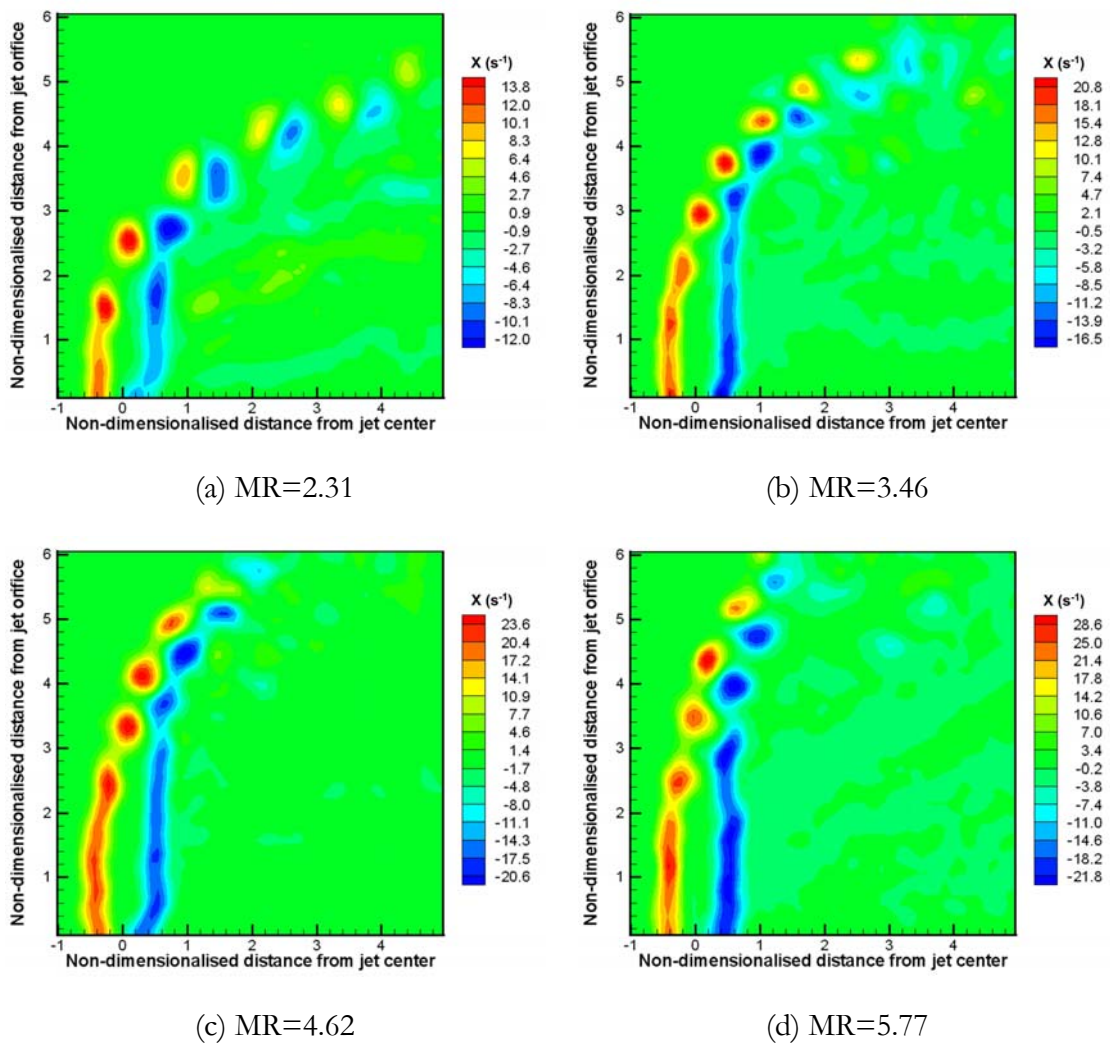
Figure 4.3.   Instantaneous vorticity plots along streamwise jet centre-line for 13.5mm top-hat JICF from MR=2.31 to 5.77.

situation is applicable for the parabolic JICF in the sense that while the stretching of the jet shear layer should logically cause the vorticity within the shear layer to increase, strong viscous diffusion and vorticity **annihilation** seem to dominate here. Unfortunately, PIV measurements cannot isolate the effects of vortex stretching from vortex diffusion. Note that when comparing the results of parabolic and top-hat jets presented here, one should be mindful that the color-coding used to indicate the level of vorticity is not the same for both cases. This is a direct consequence of the difference in the maximum values of vorticity. Another distinct feature of the parabolic jet in cross flow is the shedding of the

(a) MR=2.31   (b) MR=3.46

(c) MR=4.62   (d) MR=5.77
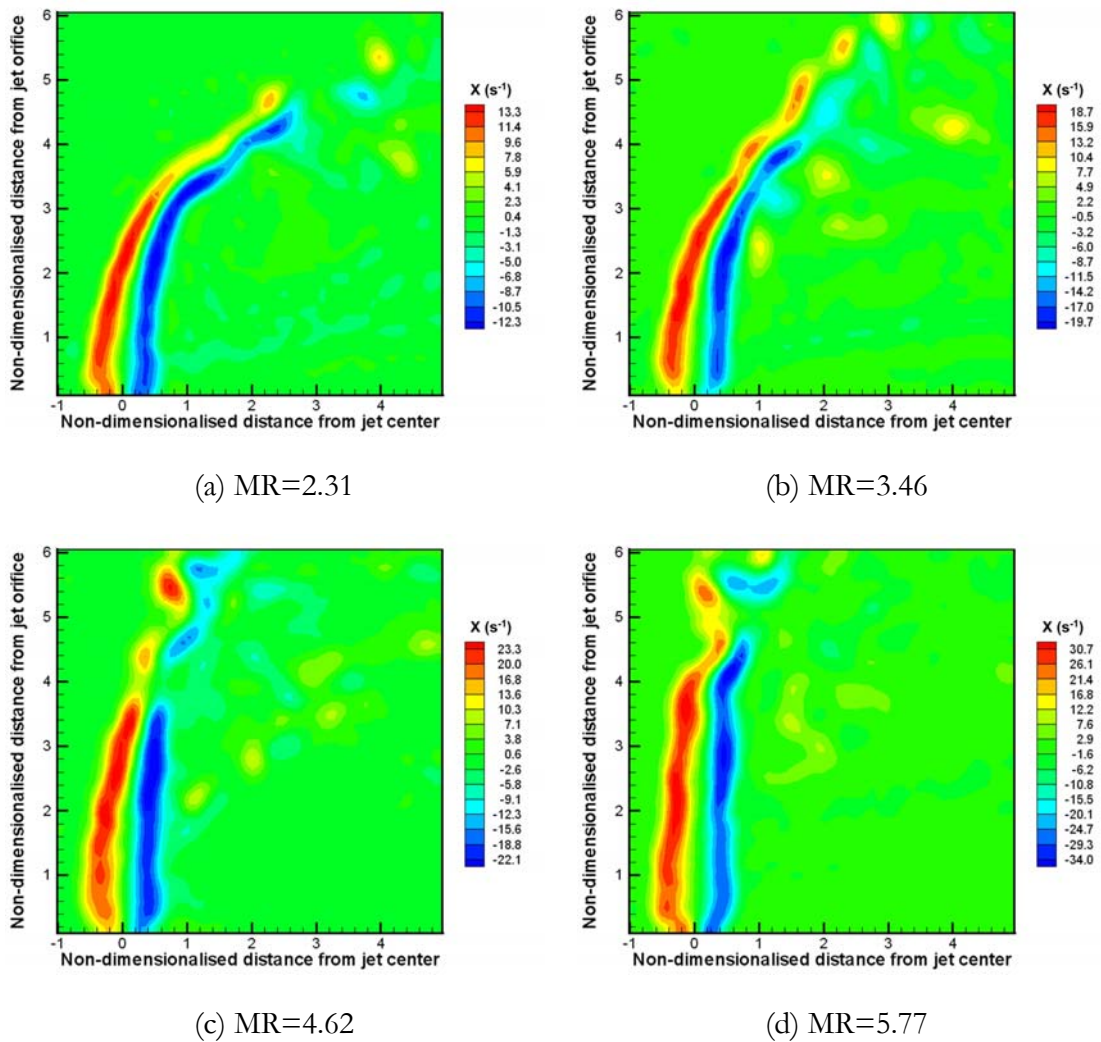
Figure 4.4.   Instantaneous vorticity plots along streamwise jet centre-line for 13.5mm parabolic JICF from MR=2.31 to 5.77.

leading-edge vortices which is considerably less regular than in the top-hat profile as was reflected in the flow visualization results.

From the vorticity plots, it can also be seen that as the momentum ratio increased, the strength of the leading-edge and lee-side vortices for both cases increased correspondingly. This is not surprising since the strength of the vortices is related to the circulation of the jet boundary layer which increases with the increase in the momentum ratio. Moreover, the maximum vorticity registered by parabolic JICF were, in most cases,

(a) MR=2.31

(b) MR=3.46

(c) MR=4.62

(d) MR=5.77
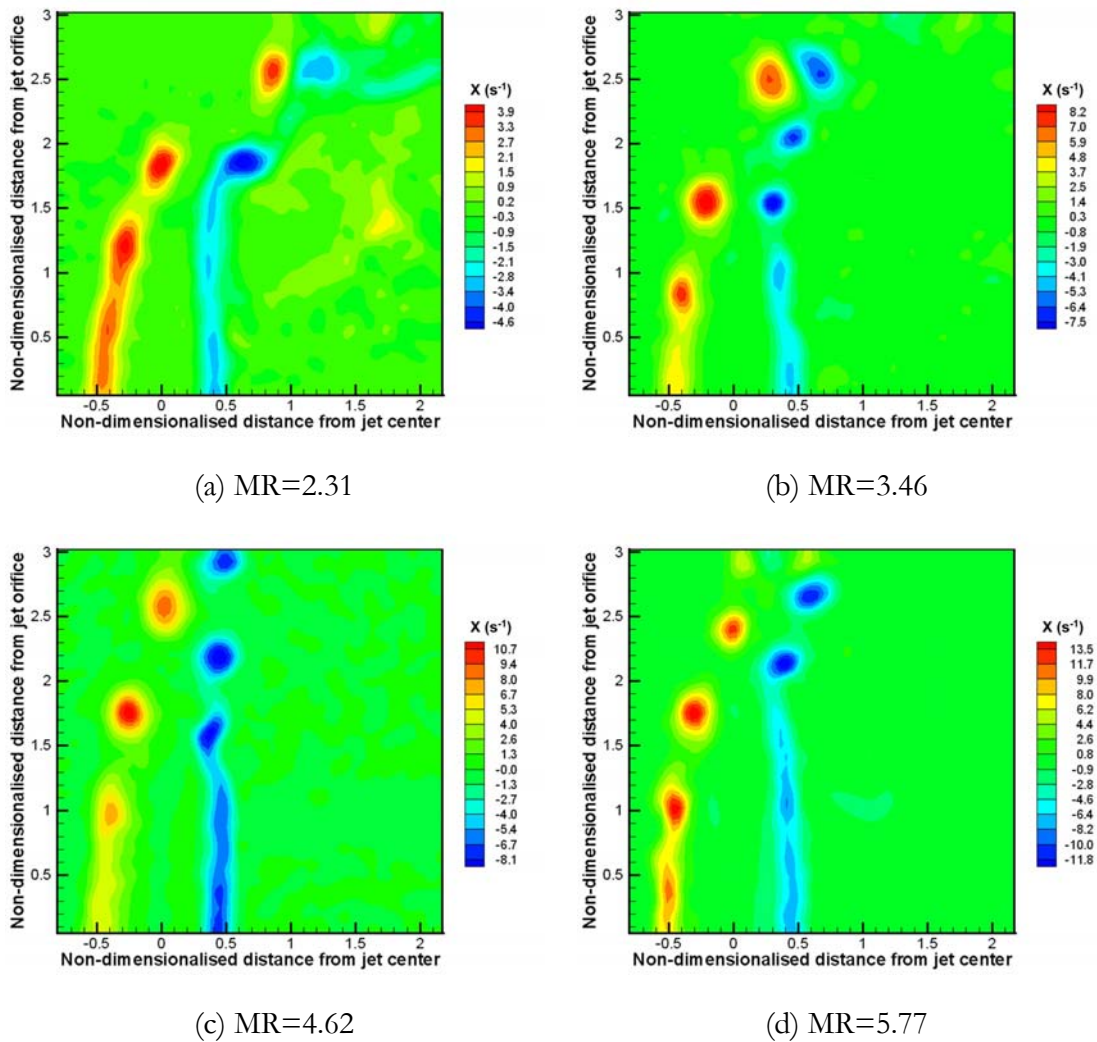
Figure 4.5.   Instantaneous vorticity plots along streamwise jet centre-line for 32.5mm top-hat JICF from MR=2.31 to 5.77.

higher than those registered by top-hat JICF for similar flow conditions. This suggests that the jet shear layer in parabolic jet may have undergone significant vortex stretching prior to the formation of the leading edge vortices, since higher vortex stretching translates into higher velocity gradients, and hence higher vorticity. In the case of the top-hat jet, the shear layer is thin to start with, and as a result, it quickly rolls up into leading vortices, before it even has a chance to undergo vortex stretching.

(a) MR=2.31

(b) MR=3.46

(c) MR=4.62

(d) MR=5.77
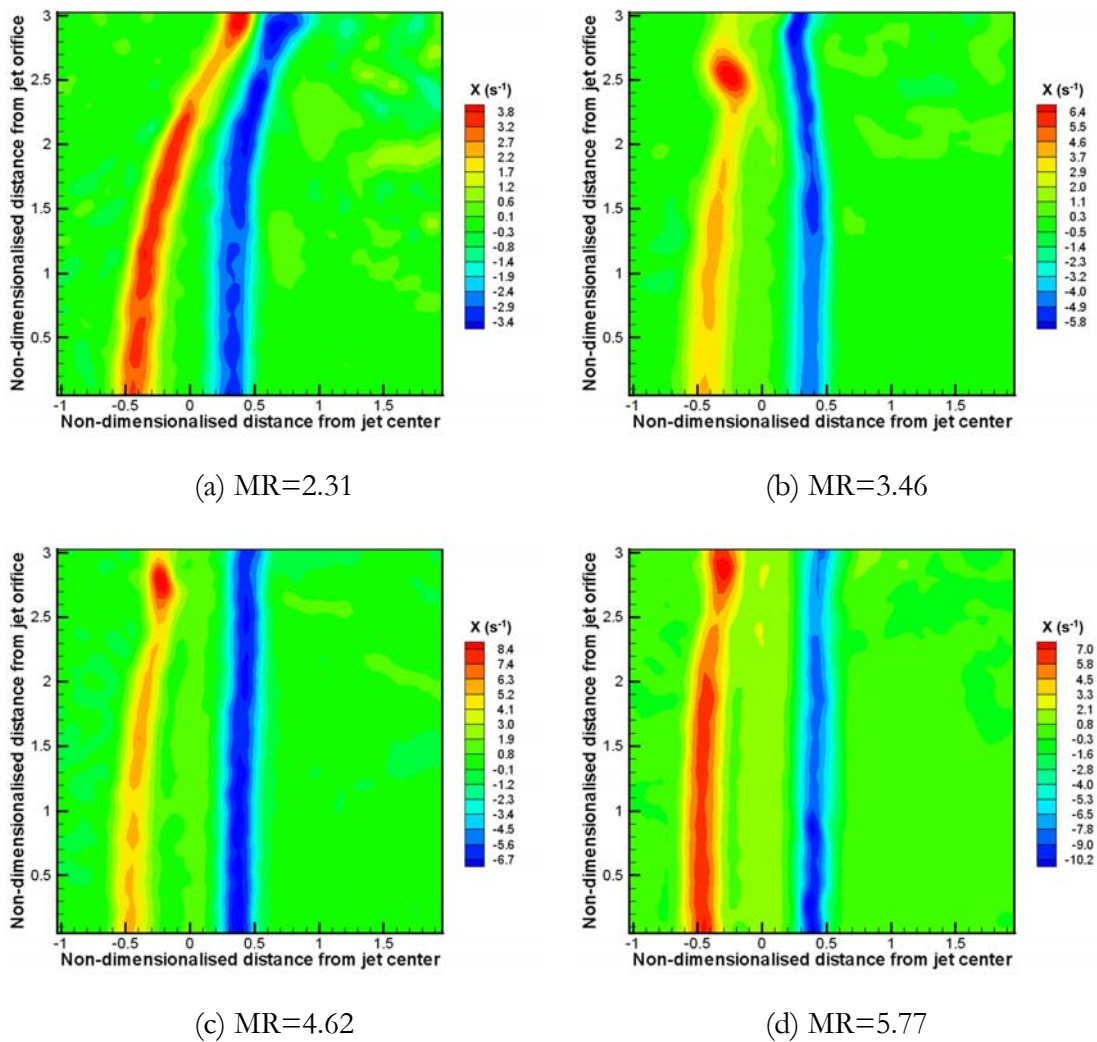
Figure 4.6.   Vorticity plots along streamwise jet centre-line for 32.5mm parabolic JICF from MR=2.31 to 5.77.

4.3   Instantaneous Velocity Fields

Figures 4.7 to 4.12 show the velocity and streamline plots corresponding to the vorticity fields in Figures 4.1 to 4.6. From the results of the top-hat JICF, the cross flow was observed to penetrate the jet fluid wherever leading-edge vortices were present, showing the effective near field entrainment of the cross flow fluid by the leading-edge vortices. On the other hand, such behaviour was not common for parabolic JICF until relatively further downstream. In fact, it could be inferred from the figures that the parabolic jet shear layers cushioned the cross flow comparatively well (i.e. relatively more

(a) MR=2.31

(b) MR=3.46

(c) MR=4.62

(d) MR=5.77
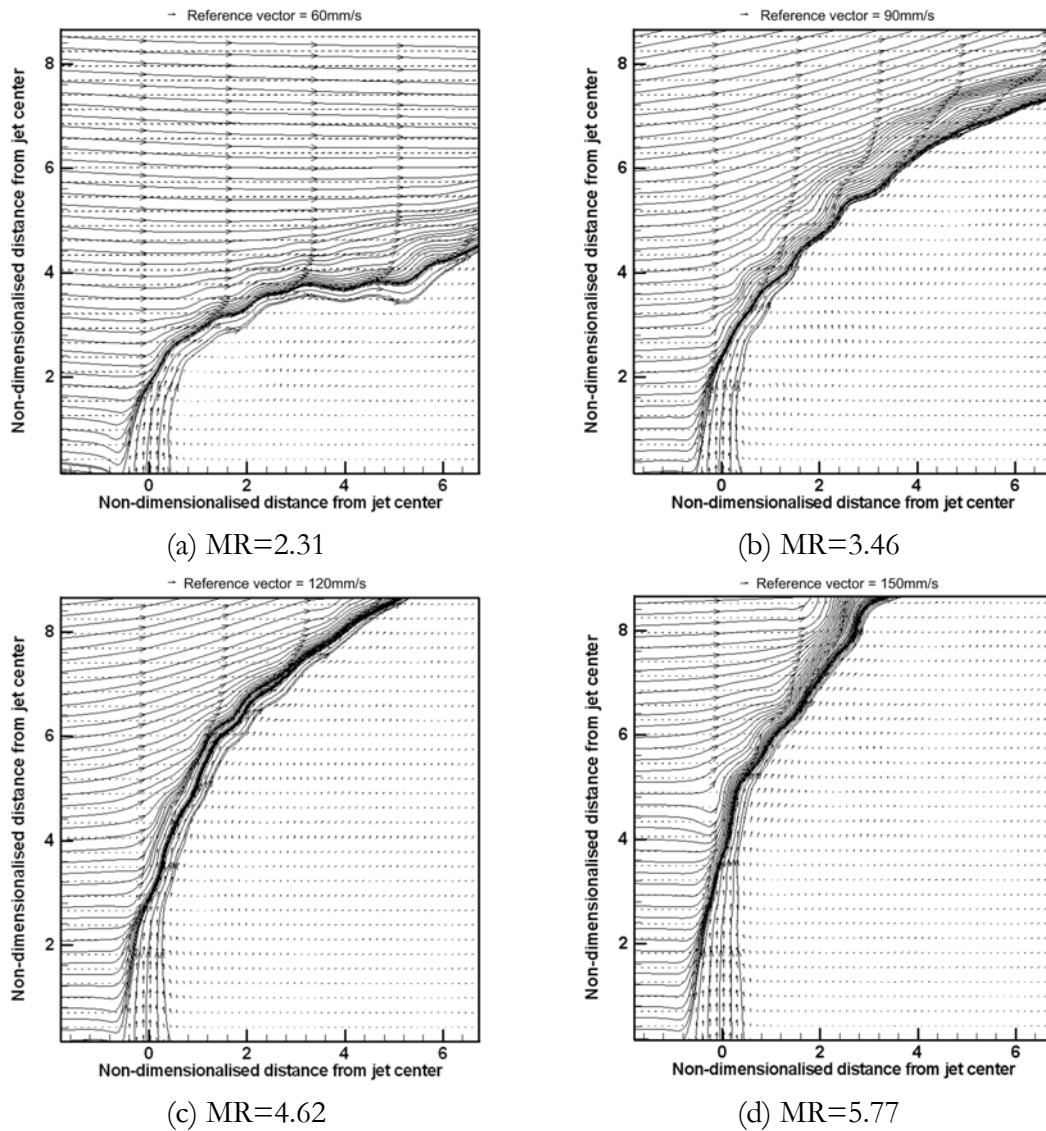
Figure 4.7.   Instantaneous velocity vector and streamline plots along streamwise jet centre-line for 9.5mm top-hat JICF from MR=2.31 to 5.77.

stable). Even then, this was usually accomplished after both the cross flow and jet streamlines were seen to align in the same approximate direction. This suggests that, in the parabolic jet shear layer, the stretching process would naturally require the gradual realignment of the cross flow fluid with that of the deflected jet.

However, these figures only gave a broadband picture of the whole scenario, so it might be interesting if one could narrow the study of the effect of jet velocity profile by

(a) MR=2.31 (b) MR=3.46

(c) MR=4.62 (d) MR=5.77
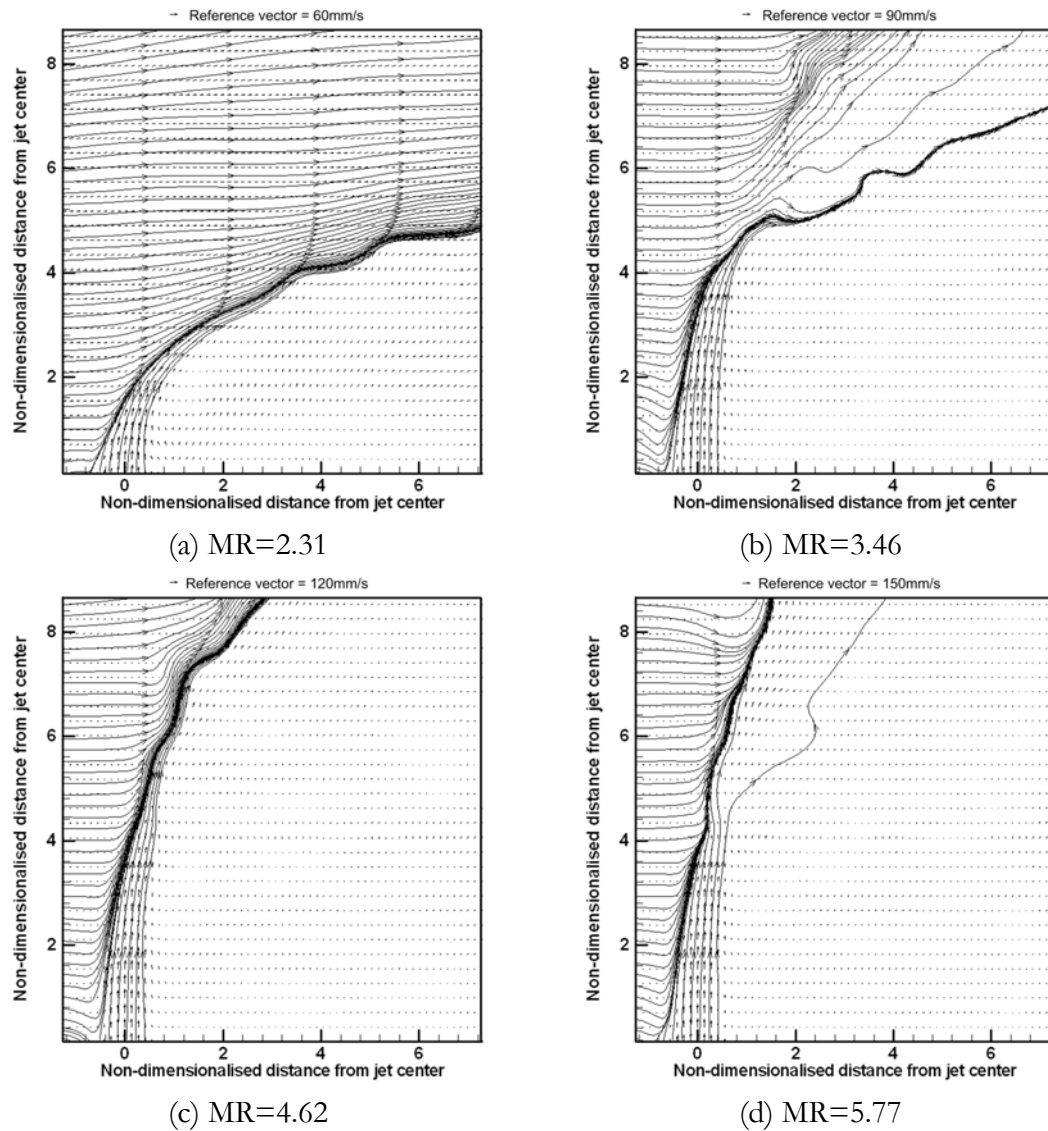
Figure 4.8. Instantaneous velocity vector and streamline plots along streamwise jet centre-line for 9.5mm parabolic JICF from MR=2.31 to 5.77.

focusing on the evolution of both the parabolic and top-hat jet velocity profiles as they progressed downstream. Figures 4.13 to 4.15 show the development the jet velocity profiles along the mean jet trajectories for both the top-hat and parabolic jets. These figures were obtained by displaying every fifth row of the velocity vector fields. Although still instantaneous in nature, the "segmented" form of representation could reveal clues to the downstream development of the jet shear layer.

(a) MR=2.31   (b) MR=3.46

(c) MR=4.62   (d) MR=5.77
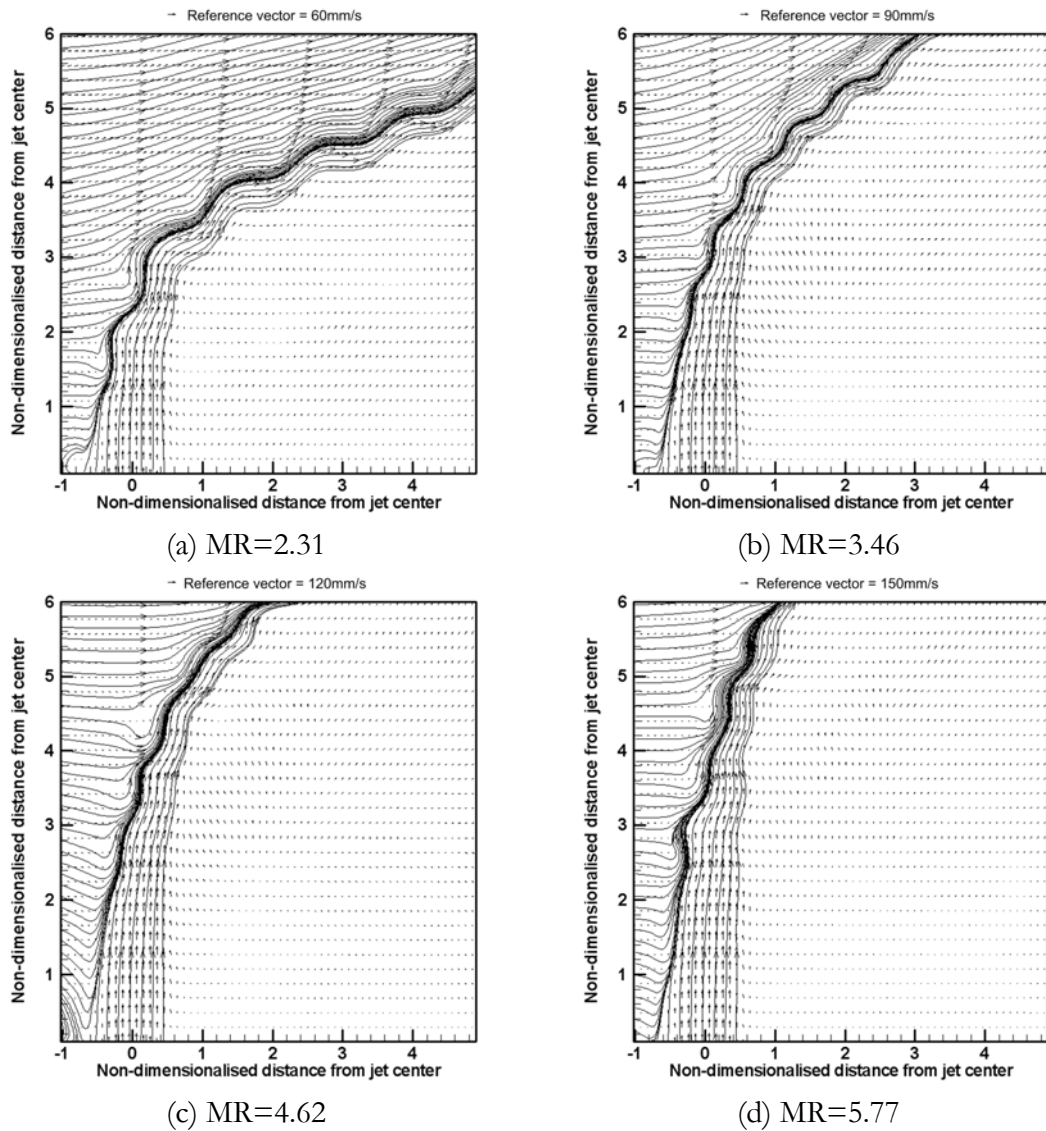
Figure 4.9.   Instantaneous velocity vector and streamline plots along streamwise jet centre-line for 13.5mm top-hat JICF from MR=2.31 to 5.77.

From these figures, it can be clearly seen that the top-hat and parabolic jets in a cross flow environment behaved differently near the exits. The thicker parabolic jet shear layer was gradually transformed by the oncoming cross flow until the velocities of the cross flow and jet fluid matched in terms of direction. During this period, the oncoming cross flow did not seem to have much of a destabilizing effect on the jet, unlike the top-hat JICF. This transition was indicated by the gradual decrease in the vorticity levels of the velocity vectors until they nearly reached the background levels. After this transition,

(a) MR=2.31

(b) MR=3.46

(c) MR=4.62

(d) MR=5.77
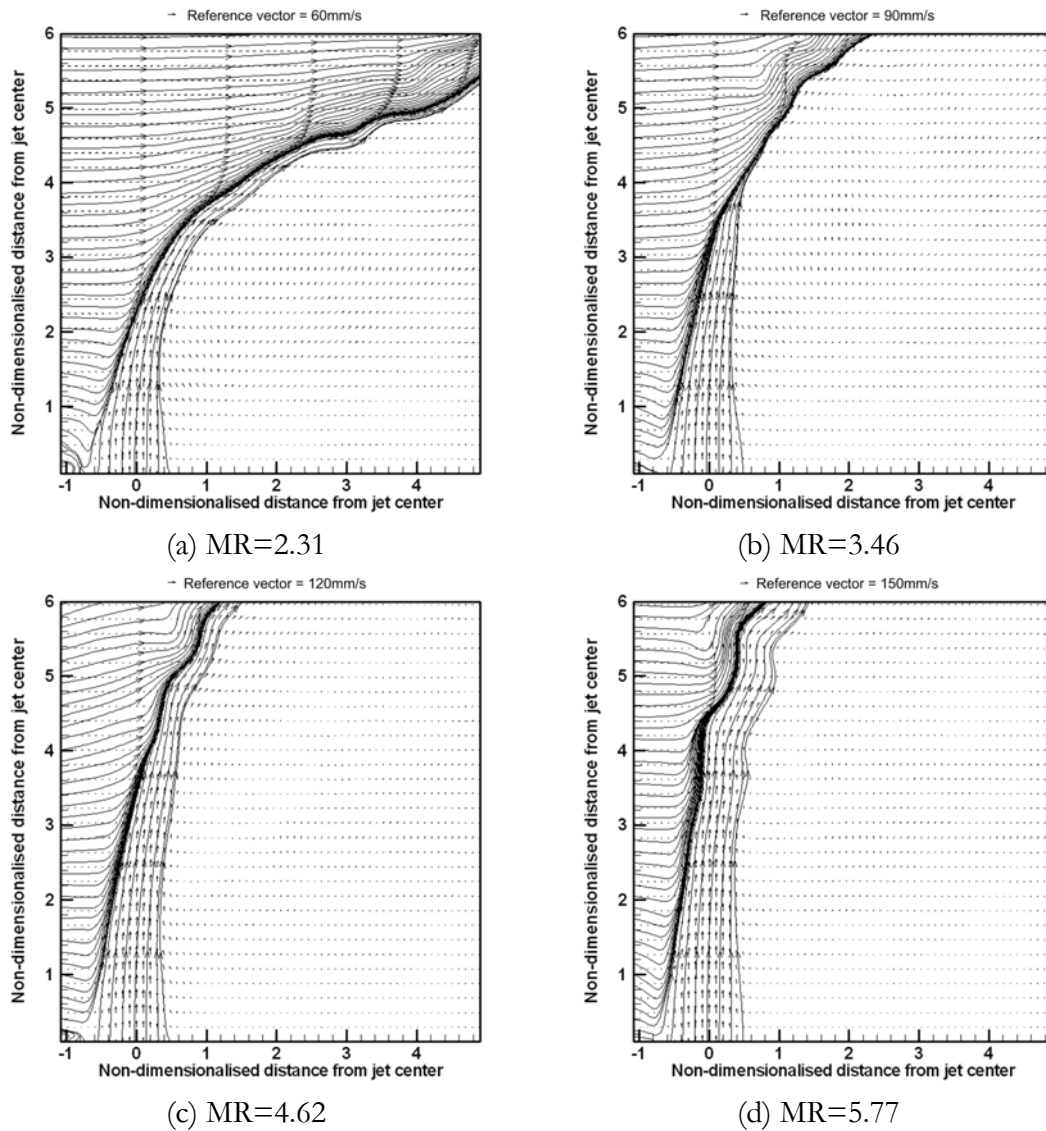
Figure 4.10.   Instantaneous velocity vector and streamline plots along streamwise jet centre-line for 13.5mm parabolic JICF from MR=2.31 to 5.77.

further interaction with the cross flow rendered the shear layer to become unstable and eventually roll-up into leading-edge vortices in an incoherent manner. In contrast, the top-hat jet was easily affected by the oncoming cross flow and rendered unstable relatively early in its development. It has been previously established that the near-field behaviour of a top-hat JICF was highly sensitive to the various saddle points existing near the upstream tips of the jet orifice as found by Kelso et al. (1996), especially the shedding of leading-edge vortices. If the shedding of these vortices for a parabolic JICF occurred

(a) MR=2.31   (b) MR=3.46

(c) MR=4.62   (d) MR=5.77
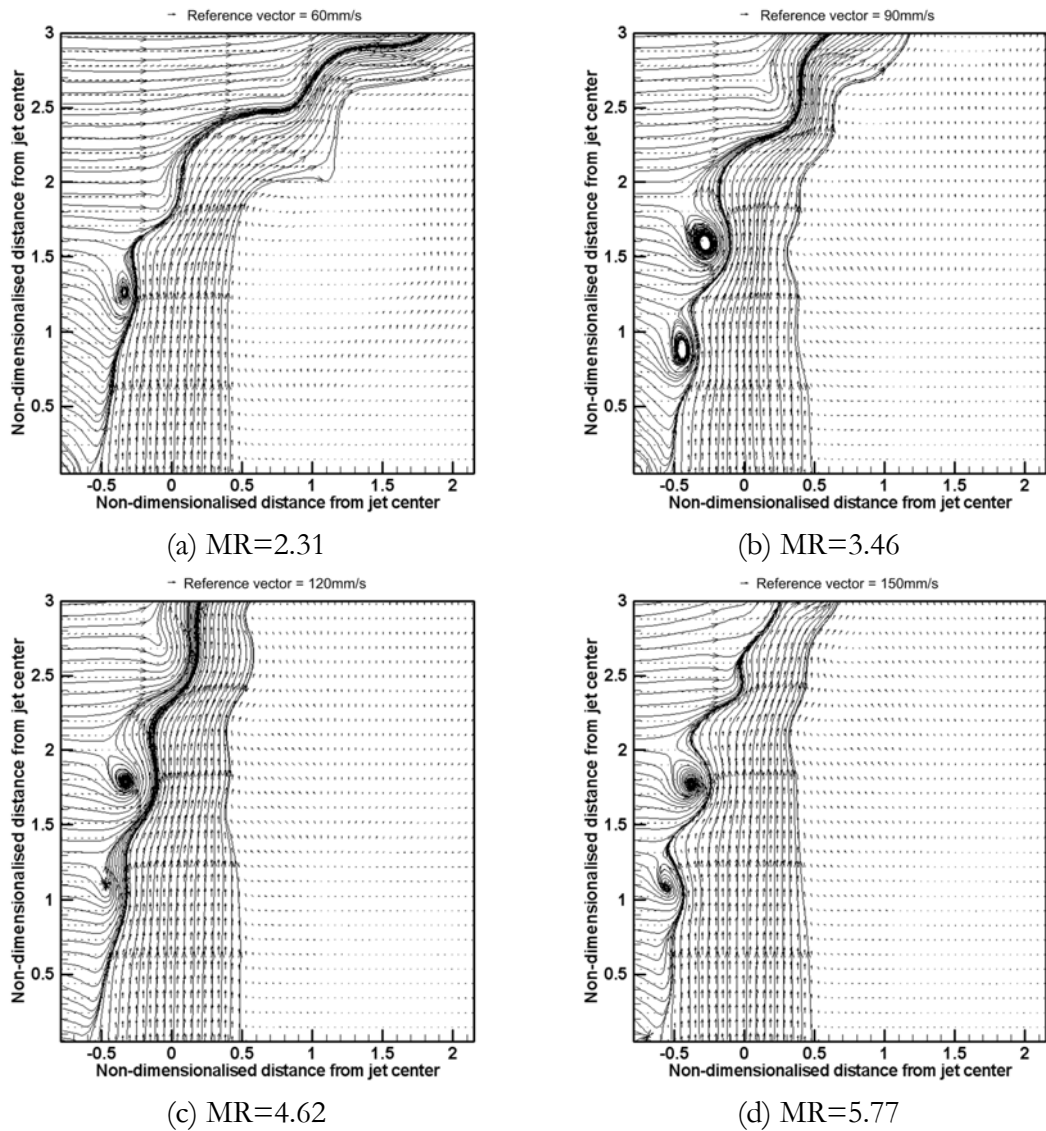
Figure 4.11.   Instantaneous velocity vector and streamline plots along streamwise jet centre-line for 32.5mm top-hat JICF from MR=2.31 to 5.77.

far away downstream, it would be reasonable then to assume that these saddle points would have little effect on the shedding process in the parabolic jet.

While conducting the flow visualization studies for both parabolic and top-hat jets, it was found that the formation of the leading edge vortices do not always coincide with the generation of the leeside vortices. The repercussion of these findings would be discussed in the next chapter.

(a) MR=2.31

(b) MR=3.46

(c) MR=4.62

(d) MR=5.77
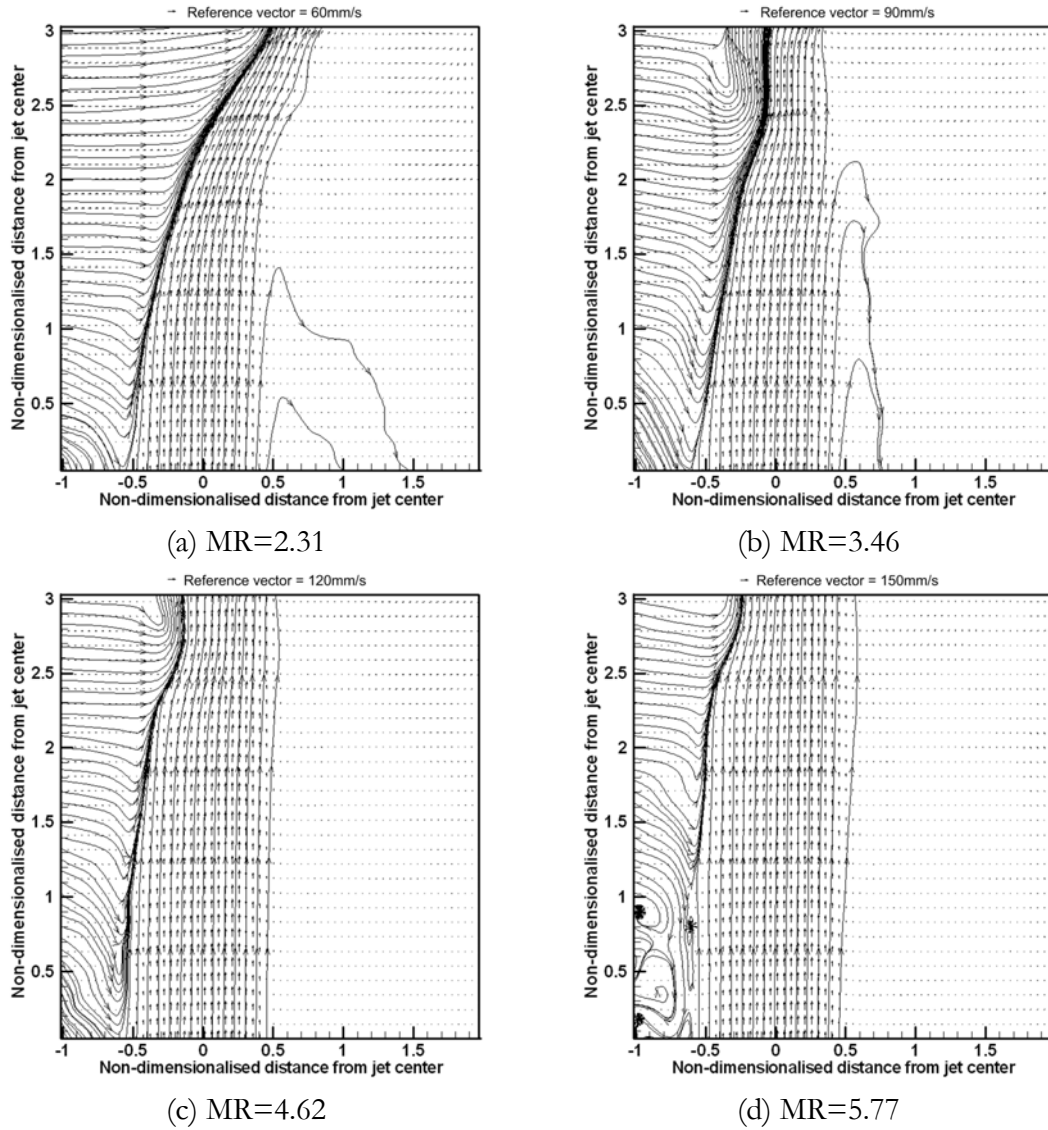
Figure 4.12.   Instantaneous velocity vector and streamline plots along streamwise jet centre-line for 32.5mm parabolic JICF from MR=2.31 to 5.77.
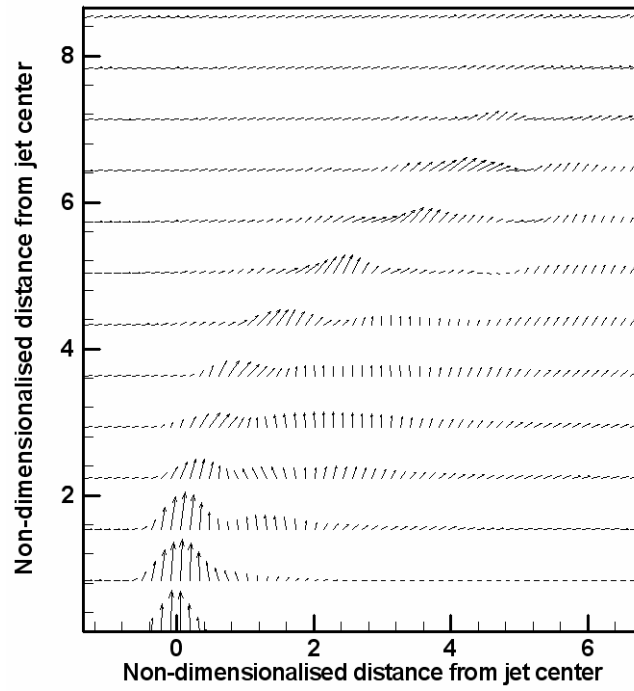
(a) 9.5mm top-hat JICF, MR=3.46
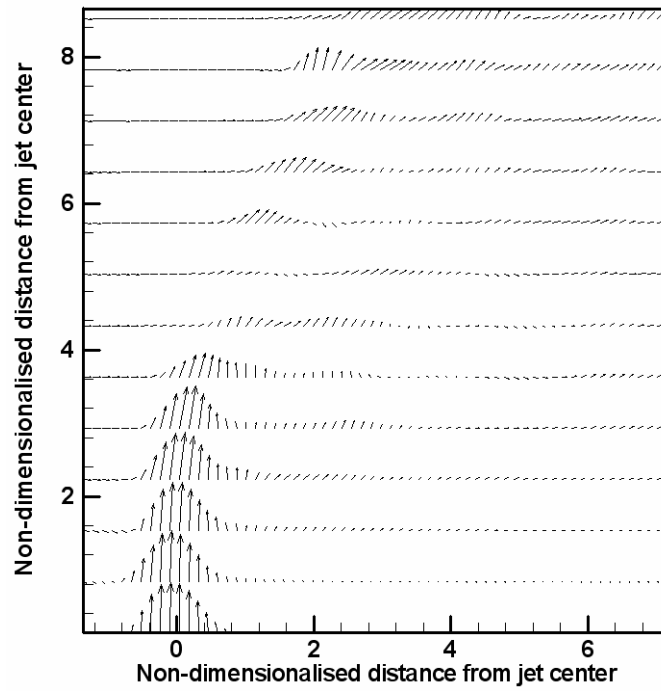
(b) 9.5mm parabolic JICF, MR=3.46

Figure 4.13. Segmented velocity field of 9.5mm JICF.
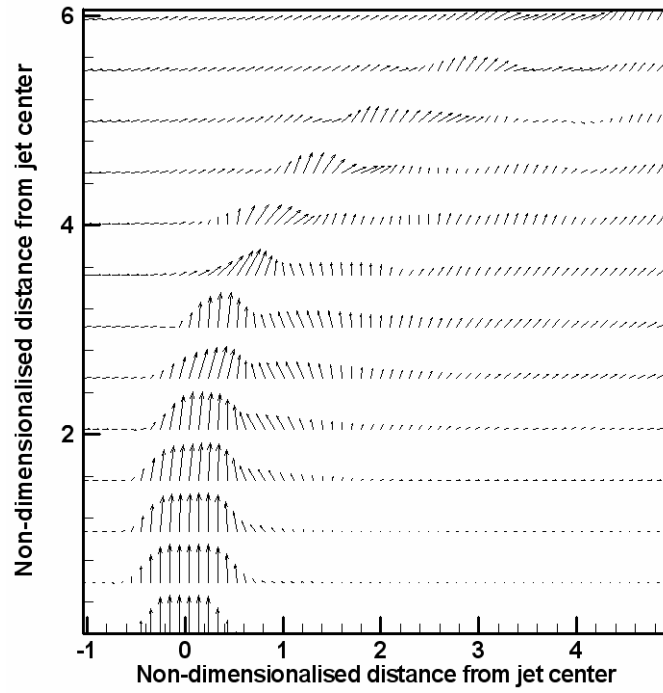
(a) 13.5mm top-hat JICF, MR=3.46
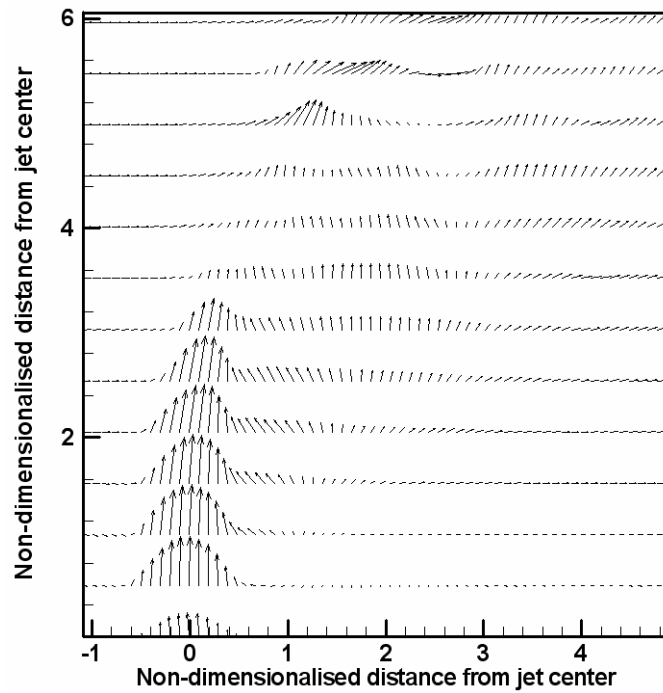
(b) 13.5mm parabolic JICF, MR=3.46

Figure 4.14. Segmented velocity field of 13.5mm JICF.
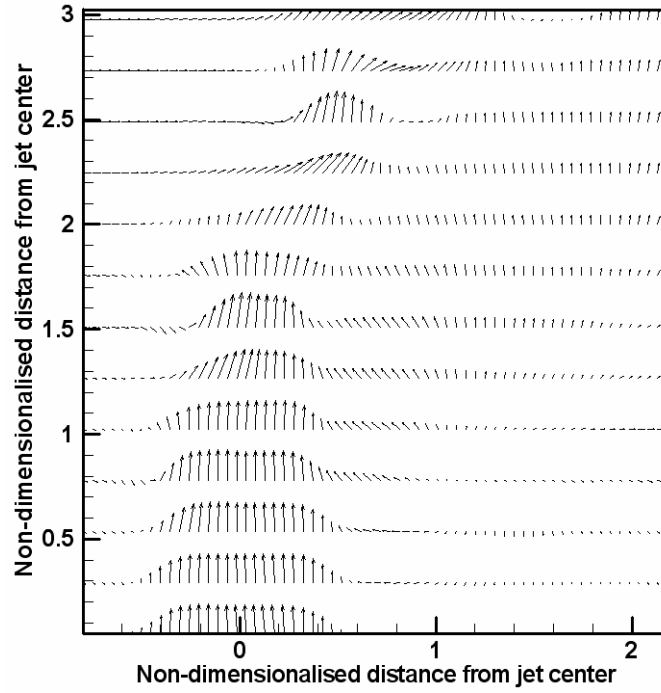
(a) 32.5mm top-hat JICF, MR=3.46
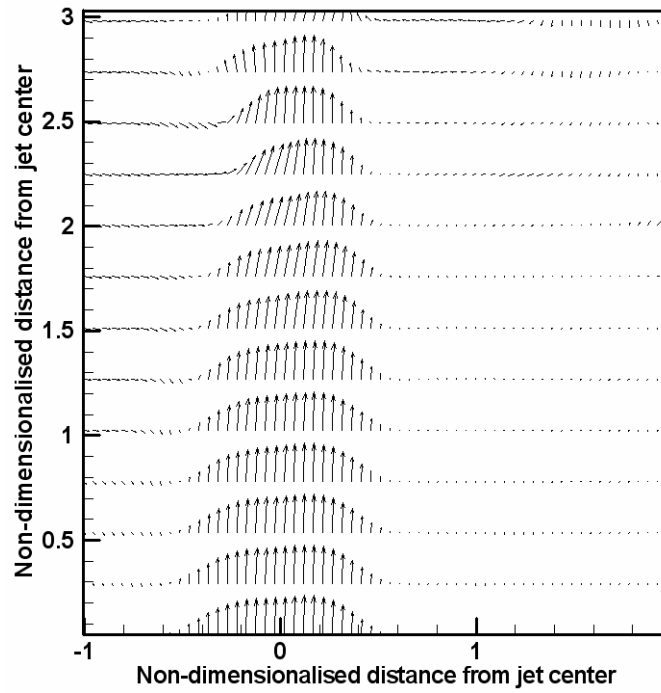
(b) 32.5mm parabolic JICF, MR=3.46

Figure 4.15. Segmented velocity field of 32.5mm JICF.

Chapter 5†

Vortex Loop Model for
Circular Jet in a Cross Flow

5.1   Introduction

During the course of the experiments on parabolic and top-hat velocity profile jets, it was frequently observed that the generation of leading-edge vortices differed significantly from that of the lee-side vortices. It seems that the generation of leading-edge vortices and lee-side vortices in parabolic jets is significantly different from that of the top-hat jets to warrant a closer look (for example, see Figure 3.3). This observation suggests contradictions to the commonly held belief that the large-scale flow structures from JICF consisted of ring vortices, which would produce corresponding pairs of leading-edge and lee-side vortices. This anomaly motivated us to have a closer examination of the vortex evolution of a JICF.

5.2   Vortex Loop Model for Circular Jet in a Cross Flow

Since the purpose of the present study was to resolve the issue of the vortex structures in JICF, extra care was taken during the generation of these vortices near the jet exit. Figure 5.1 shows a sequence of flow visualization images depicting how a typical cylindrical jet shear layer of a top-hat circular jet issuing from the nozzle would deform and roll up to form leading-edge vortices. Here, the velocity ratio was approximately 4.62 and the Reynolds number, based on the mean jet velocity and diameter, was about 1600. These particular flow parameters were chosen because of the ease in detailed observation

---

due to the excellent combination of physical scale and the flow conditions offered. The scale of the pictures could be inferred through the nozzle diameter (D) of 32.47mm. These images were obtained by releasing dye uniformly around a circumferential slit within the jet pipe as discussed earlier in Chapter 2. For all cases, the dye concentration was kept to a minimum so that the salient features of the flow were not unduly obscured by the "thickness" of the dye. In many of the previous studies, high concentration of dye or smoke had made the interpretation of the flow difficult or even impossible, and in some extreme cases might even lead to misinterpretation of the flowfield, particularly in the lee-side region of the jet. In this study, since the dye was released at the location where vorticity was generated (into the jet shear layer), it was not unreasonable to assume that the dye followed the jet vorticity, at least during the early stages of the flow development. Hence, the behaviour of the dye sheet depicted in Figure 5.1 gave a good indication of the behaviour of the vortex sheet. However, one should be cautioned that since dye generally diffused much slower than vorticity (Sc >> 1), and over a long period of time, the region occupied by the dye might no longer give a true indication of the region of vorticity (see Lim, 2000).

Inspection of Figure 5.1 clearly shows that as the cylindrical vortex sheet (or jet shear layer) emerged from the nozzle, it underwent three distinct folding processes almost immediately. The first of these processes led to the formation of the CVP on both sides of the jet column, and the other two resulted in the formation of two rows of vortices; one at the leading-edge (or leading-edge vortices, identified as A, in Figures 5.1 and 5.2), and the other at the lee-side of the jet (or lee-side vortices, identified as B). These vortices resemble a "daisy chain" of interlocking loops, which were similar to the buoyant jet structures observed by Perry and Lim (1978). One very interesting feature about these loop vortices was that they were not observed to be a product of the bending or folding
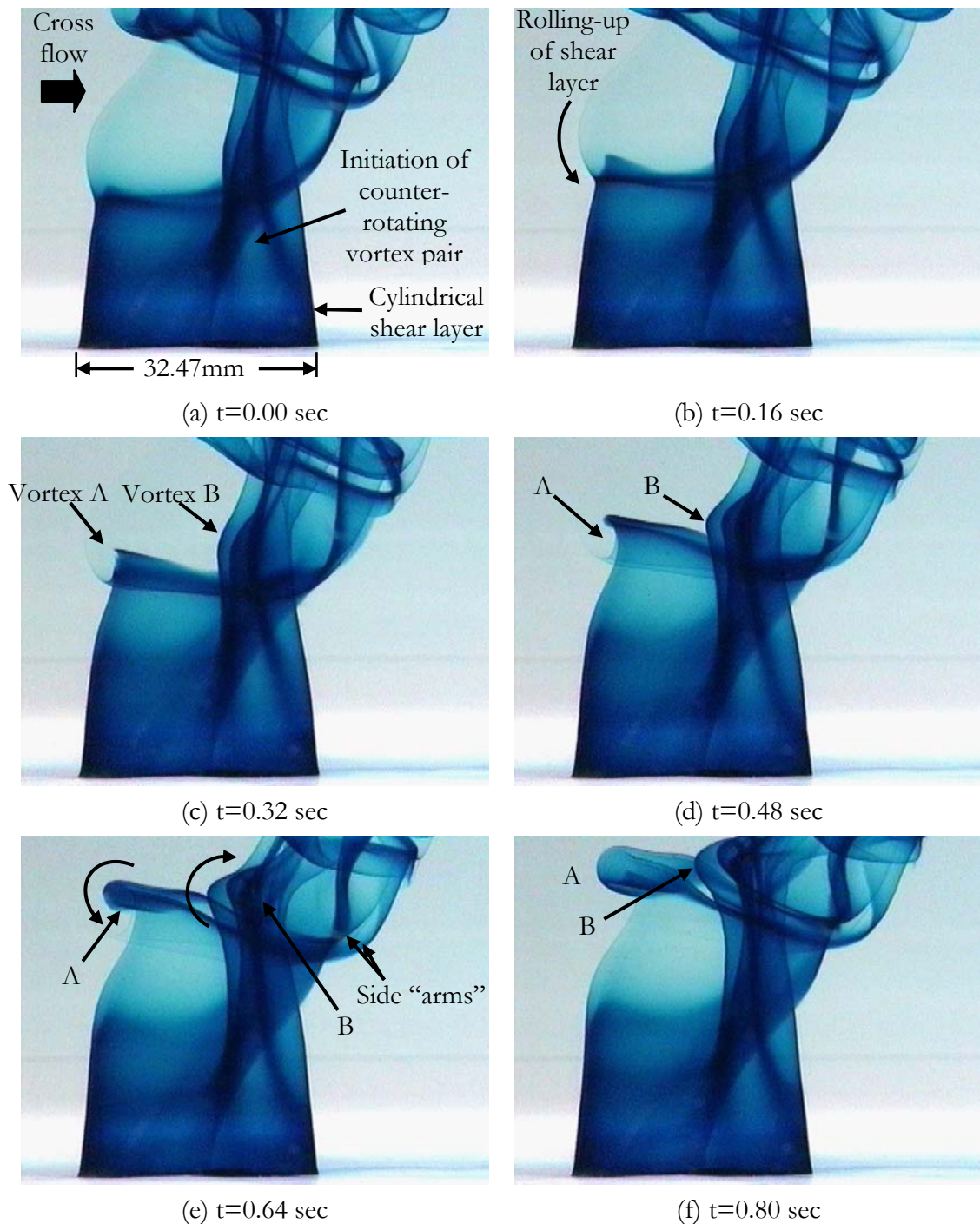
Figure 5.1   A sequence of images showing how the folding of the cylindrical shear layer (or vortex sheet) from the jet nozzle leads to the eventual formation of the counter-rotating vortex pair (CVP), with the leading-edge and lee-side vortices indicated as A and B, respectively. In image (a), the time has been arbitrarily set to 0.00s. It is important to note that although the flow structures look complicated, the original fluid leaving the nozzle remains in its original boundary.

of the vortex rings, as some researchers were previously led to believe, for example, Sykes et al. (1986) and Kelso et al. (1996). In fact, no evidence of vortex rings was found in any of our study. This observation is strengthened by Yuan et al.'s observation (1999) in their large eddy simulation of a round JICF.

To have a better idea of how these loop vortices could have evolved and developed, captured video clips of the flowfield were replayed in slow motion. And they clearly showed that as soon as the cylindrical vortex sheet (see also figure 5.1) emerged from the nozzle, it folded up almost immediately at its edges along both sides of the jet column to form a CVP. This finding was consistent with the previous experimental observation of Kelso et al. (1996), and the large-eddy simulation of Yuan et al. (1999). Furthermore, it was found that the formation of CVP played a crucial role in preventing the cylindrical vortex sheet, which contained "circular" vortex lines, from rolling up into individual vortex rings. This was in contrast to the free circular jet, where the absence of CVP enabled the vortex sheet to roll up freely into axisymmetric vortex rings. In the case of a JICF, the vortex sheet could only roll up freely at the leading-edge and the lee-side of the jet column, since the CVP suppressed similar roll-ups along the two sides. This resulted in two distinct rows of loop vortices separated by the CVP along the sides. Further examination showed that this formation process was somewhat similar to the buoyant jet structures observed by Perry and Lim (1978), although the details were different. During the entire folding process of the vortex sheet, the jet fluid that originated from the nozzle remained bounded within the cylindrical boundary, and there was no visual indication of holes or openings in the original vortex sheet. This feature was clearly illustrated in Figure 5.2, where the jet fluid, which had been premixed with fluorescein dye, was illuminated with a thin laser sheet along the streamwise jet center-plane. Here, both the leading-edge and lee-side vortices could be clearly seen while the
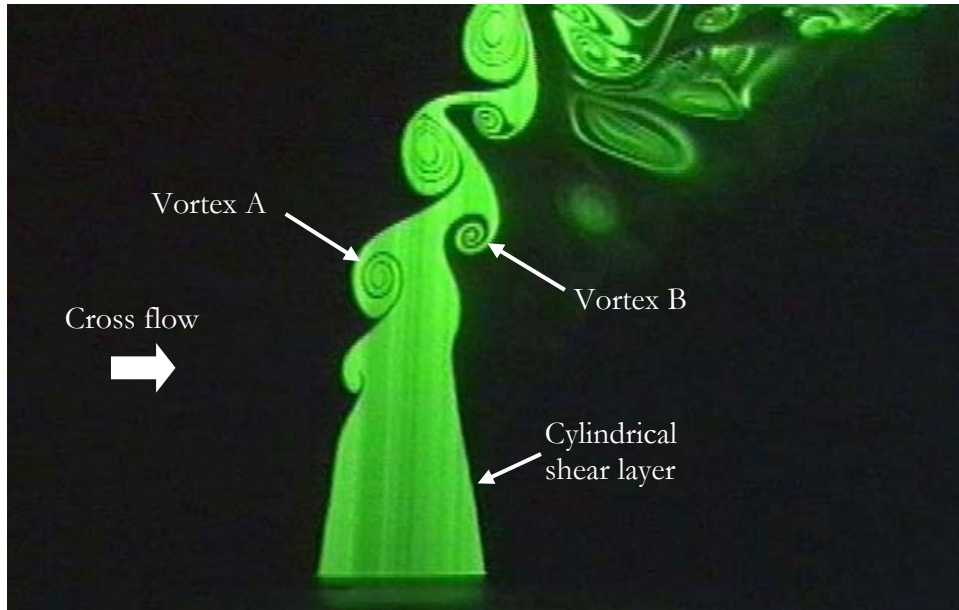
Figure 5.2.   Sectional view of the vortex structures in the centre-plane of a jet issuing normal to a cross flow. The photograph is obtained by premixing the jet fluid with the fluorescein dye, and then illuminated with a narrow sheet of laser light. Note that the vortices A and B correspond approximately to those in Figure 5.1(f). The counter rotating vortex pair (CVP) is not visible in the photograph because it is out of the illumination plane. This picture also clearly shows that the original fluid leaving the nozzle remains in the cylindrical boundary.

CVP was not visible as it was outside the laser plane. Although the sectional views such as the one shown in Figure 5.2 provided valuable information about the internal structures of the flowfield, one should be aware that it was not an easy matter to deduce three-dimensional flow structures simply from studying two-dimensional views alone. For example, the "mushroom-shape" vortices in Figure 5.2 could have easily misled one to believe that they are part of the same vortex rings. However, as the broadband pictures in Figure 5.1 clearly show, they were actually part of the two separate rows of vortex loops.

As the vortex loops convected further downstream, their "side-arms" were swept downstream by the cross flow and subsequently paired up with the CVP (see Figure 5.1(e)). During the merging, the side-arms were stretched by the CVP, and this resulted

in the realignment of the vorticity with that of the CVP. Although not shown in the photographs, it was suspected that the mutual interaction between these loop vortices far downstream was partly responsible for causing the vortices to undergo instability and became turbulent, leaving behind only the CVP with fine-scale motions superimposed on it. Figure 5.3 shows the proposed interpretation of the finally developed flow structure. Note how the CVP was initiated at the sides of the cylindrical vortex sheet shortly after the jet exited from the nozzle and how the vortex loops (side-arms) were produced from the folding of the vortex sheet. The "break" in the figure indicated that the section D-D was taken far away from nozzle exit. To avoid confusion, the fine-scale flow structures were not included in the figure. In fact, the best way to understand the finally developed structure was to make a model using wire gauze tube; a technique used successfully by Perry and Lim (1979) to illustrate how buoyant wake and jet structures were formed. By continuing wrapping both sides of the wire gauze tube, the CVP could be obtained. Similarly, by continuing folding the leading-edge and the lee-side of the same wire gauze tube, one could further obtain the two rows of vortex loops as shown in Figure 5.3. Indeed, a wire gauze model was built and used as an aid to visualize and construct the 3-D view of the proposed model. Figure 5.4(a) shows the 3-D view of the proposed jet structures, depicting how the leading-edge and lee side vortex loops might have interacted to produce Section B-B via their side-arms. And Figure 5.4(b) shows the cross-section E-E along the deflected jet centre-line, illustrating the same cross-sectional view depicted in Figure 5.2.

To demonstrate that the proposed model was consistent with the experimental observations, laser cross-sections of the actual jet structures normal to the jet axis (see Figure 5.5) were compared with the corresponding cross-sections of the proposed model (see Figure 5.6), and the agreement between them is very good. It is of interest to also
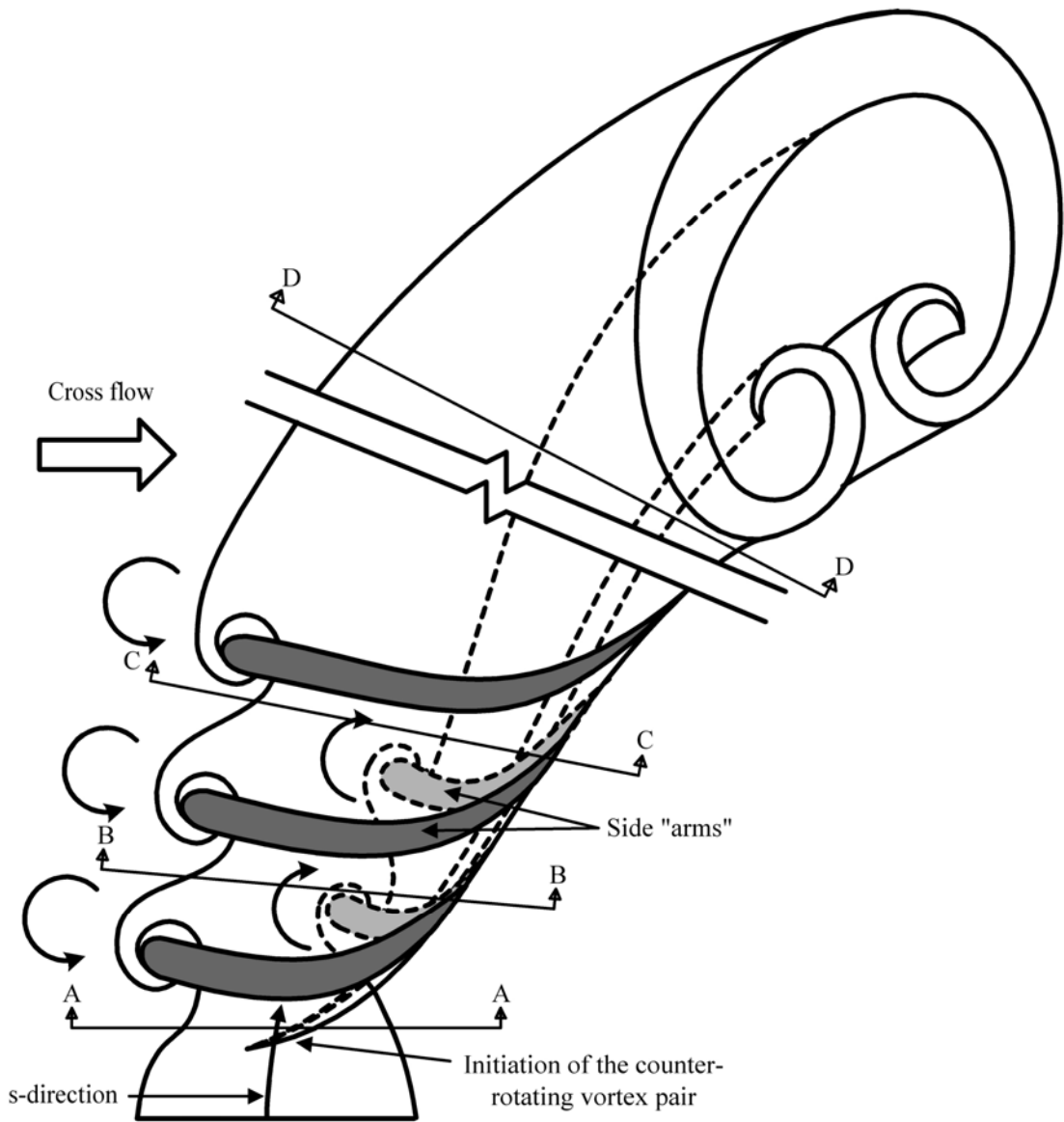
Figure 5.3.   Author's interpretation of the finally developed vortex structures of a circular JICF. Note how the "side-arms" of the vortex loops merged with one of the counter rotating vortices.
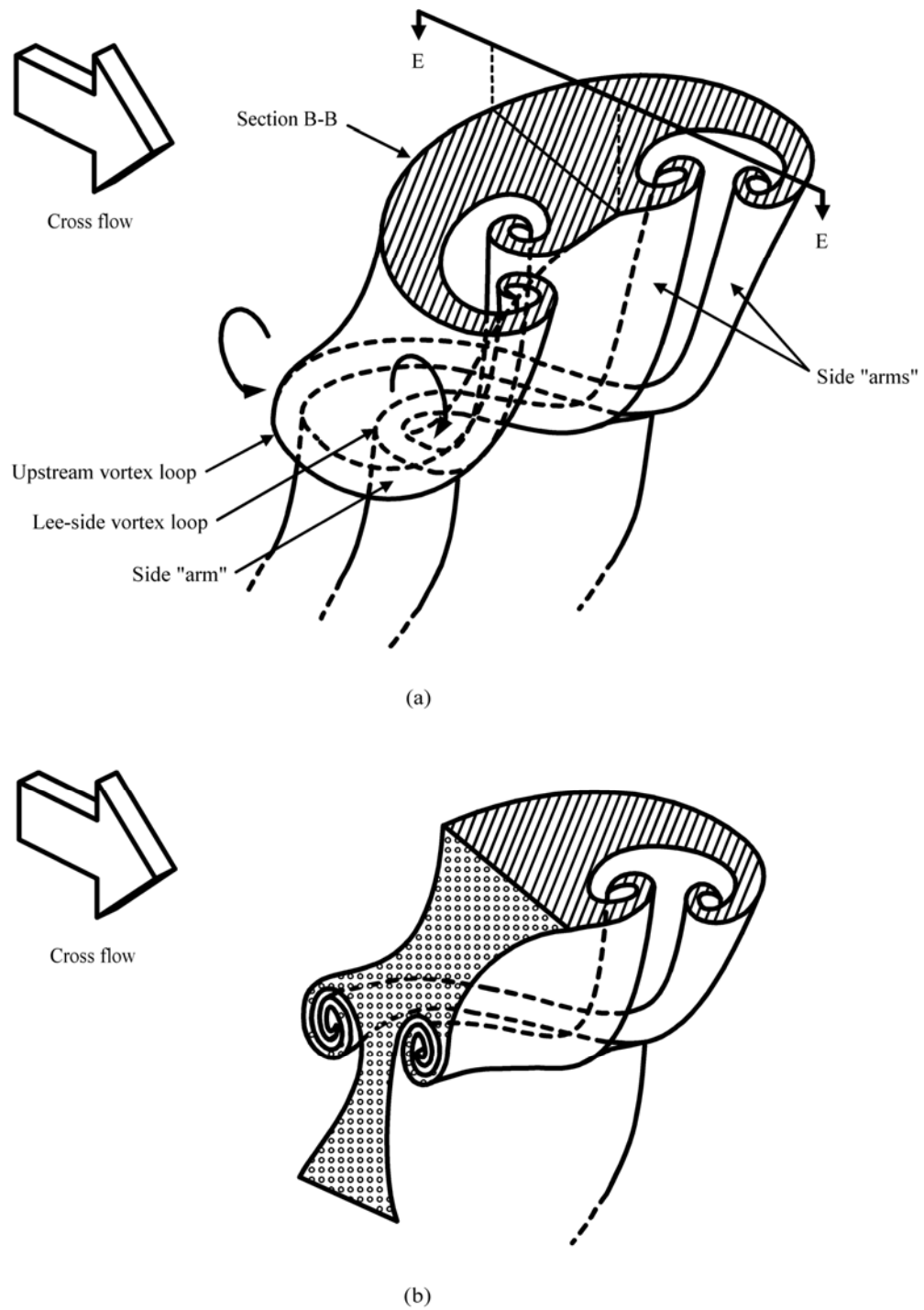
Figure 5.4.   Detail sketches of the proposed model. The sketches show how the vortex loops give rise to the resultant Section B-B in (a), and Section E-E in (b) along the deflected jet centerline in the streamwise direction. The latter sketch represents the laser cross-section of JICF depicted in figure 5.2.

(a) s=0.5D

(b) s=1.0D

(c) s=1.5D

(d) s=2.0D
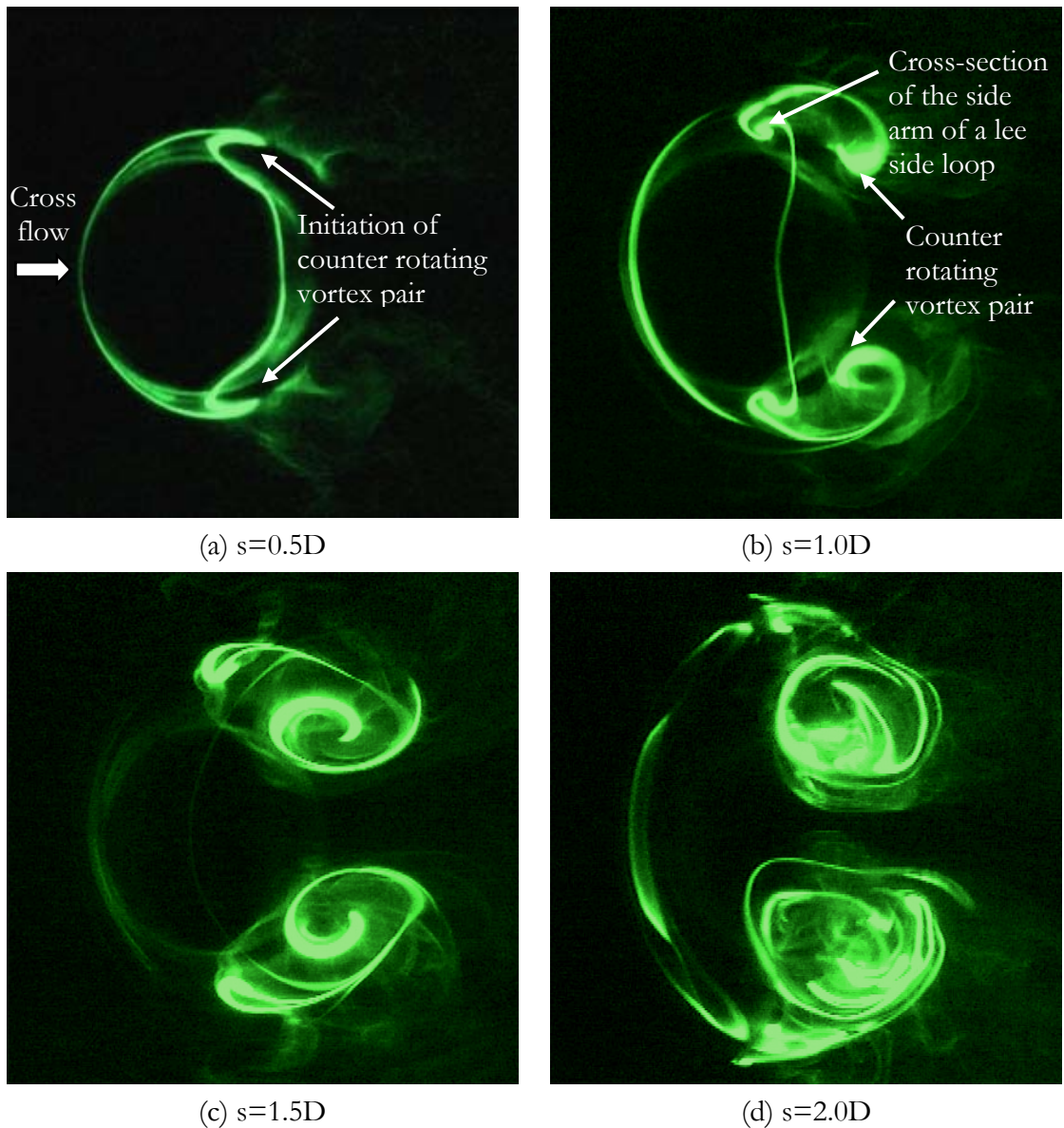
Figure 5.5.   Laser cross-sections of a jet taken with the laser plane perpendicular to the jet axis. s is measured from the floor and along the jet trajectory, and D is the nozzle diameter. Note how the "side-arms" of the lee-side vortex loop are merged with the CVP.

note that in a recent large-eddy simulation of a round JICF by Yuan et al. (1999), the near-field of the jet was found to consist of three different vortical structures, namely "spanwise rollers", "hanging vortices", and "vertical streaks". These structures were presented in terms of isosurface of vorticity as shown in Figure 20(a) of their paper. While it was clear that their "spanwise rollers" corresponds to the leading-edge and thelee-side vortices in the present study, it was not so clear as to how the "hanging

(a) Section A-A   (b) Section B-B

(c) Section C-C   (d) Section D-D
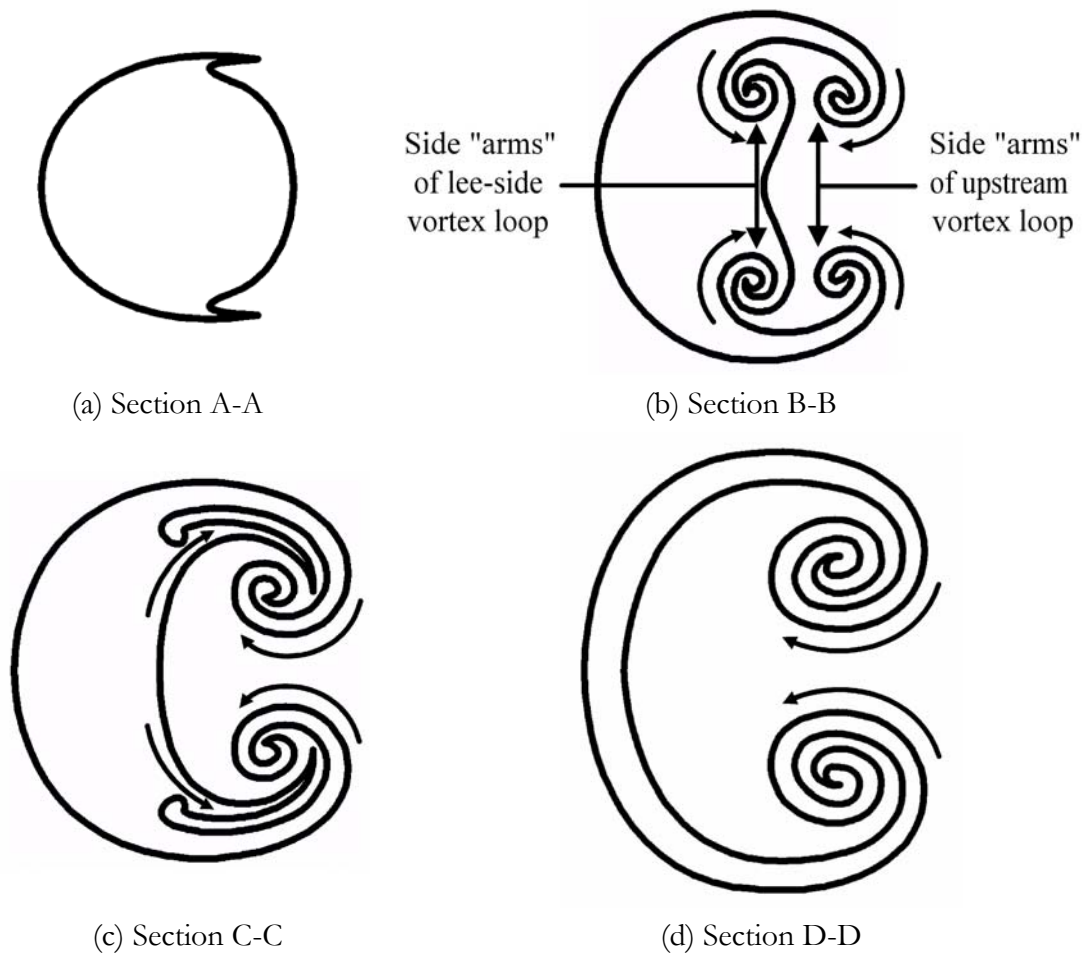
Figure 5.6.   Cross-sectional views of the proposed flow model at various downstream locations along s-direction.

vortices" and the "vertical streaks" were formed. The uncertainty arises because their isosurface of vorticity plots do not give a clear picture of how the three vortex structures are interconnected. But the comment by Yuan et al. (1999) that the "hanging vortices" underwent vortex breakdown similar to that reported by Kelso et al. (1996) suggested that the "hanging vortices" were likely to be the side-arms of the leading-edge vortex loops before it merged with the CVP. As for the "vertical streaks", it is believed that they were also the side-arms of both the leading-edge and lee-side vortex loop vortices, which have been stretched by the CVP during merging. The stretching caused the vorticity of the side arms to realign with that of the CVP. Overall, the present observation agrees well with that of Yuan et al. (1999).
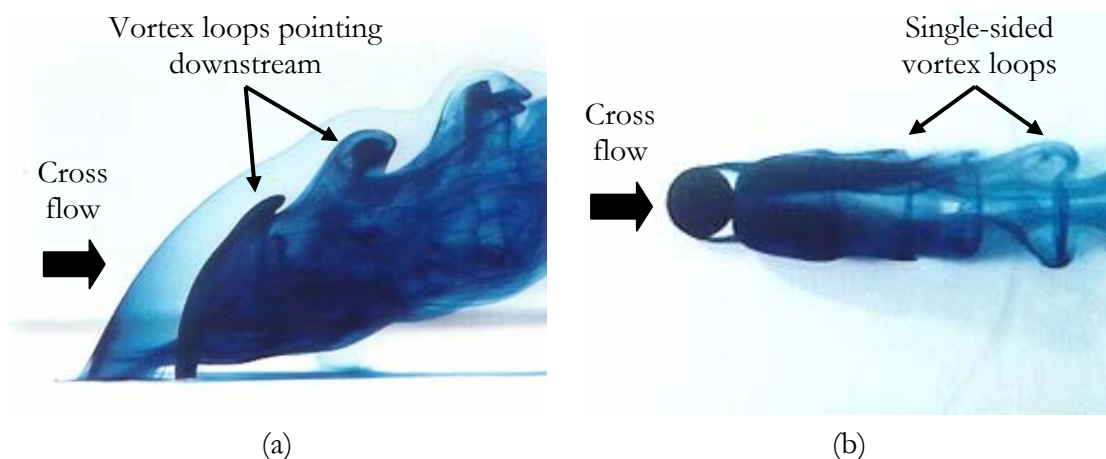
Figure 5.7.   Photographs showing the wake structures from the nozzle at the velocity ratio of about 1. (a) Side view. (b) Plan view taken at a different instance. Note that the vortex loops are pointed downstream. (New (1998)).

An important feature of the model depicted in Figures 5.3 and 5.4 is that the leading-edge vortex loops could exist without the lee-side loops. This is in contrast to the model using vortex rings, which implies that for every leading-edge vortex loop, there must be a corresponding one on the lee side. However, from present experimental results and the results of Kelso et al. (1996), single-sided vortex loops were known to exist in JICF when the velocity ratio was low, typically less than or equals to one. This is clearly illustrated in Figure 5.7. Here, one could see that the vortex loops were pointed downstream rather than upstream as was commonly observed in high velocity ratio cases. The orientation of the vortex loops suggested that at low velocity ratio, the "jet structures" have transformed into wake structures. Under this condition, the buoyant wake model of Perry and Lim (1978) is equally applicable here. Other examples in nature where single sided loops are known to occur include the smoke structures issuing from factory chimney in cross flow, and a cigarette smoke in a slight draft (see Perry and Lim (1978)). However, one should be aware that, for these two cases, the inherent buoyancy of the hot smoke does play an important role in determining the final structures of the flow. Nevertheless, these examples provide further support to our model that the large-scale structures of JICF consist essentially of loop vortices and not caused by the bending

and folding of the vortex rings. We believe that vortex rings will not form "naturally" in JICF unless they are deliberately fired into a cross flow (see Sykes et al. (1986), Chang and Vakili (1995), and Lim et al. (1998)), or when the velocity ratio is close to infinity (i.e. a free jet). Far away from these conditions, the cross flow would cause the circular vortex lines surrounding the cylindrical vortex sheet to tilt, and the vortex sheet to roll up into loop vortices.

Chapter 6[††]

Flow Visualization of Elliptic Jets in Cross Flow

6.1   Introduction

In recent years, various attempts have been made to improve the mixing efficiency of a JICF by using non-circular jet geometry such as ellipse, square and rectangle (for example, see Ajersch et al. (1995), Haven and Kurosaka (1997), Zaman and Foss (1997), Gogineni et al. (1998) and Findlay et al. (1999)). Although altering the jet exit geometry has been found to be one of many effective means of enhancing jet mixing with the surroundings, many fundamental questions about the flow field have not yet been fully answered, particularly those related to the formation of large-scale jet structures, and their role in the entrainment of the surrounding fluid. These questions are of practical importance in applications such as the design of fuel injectors in burners. In this section, the studies are focused on the elliptic jet geometry only. This geometry is chosen for study because it is the simplest of the non-circular jets, and is more stable than the square or rectangular jets. In addition, an elliptic jet has the added advantage of having the smallest possible momentum thickness variation for a symmetrical non-circular jet exit, due to the smooth variation in its perimeter curvature.

An elliptic jet in a cross flow (EJICF) has previously been investigated by Haven and Kurosaka (1997), but their study was confined to low velocity ratios (VR) only (i.e. VR=0.4 to 2.0) since they are concerned primarily with the effect of jet geometry on film cooling. The main finding of their investigation was the existence of the "double-decked kidney and anti-kidney vortices". They found that the lower-deck structures were kidney-

---

[††] A major part of this work has been published in "Elliptic jets in cross flow," J. Fluid Mech., 494, 119-140, 2003, by T.H. New, T.T. Lim and S.C. Luo.

shaped and established to be the primary CVP inherent in all jet geometries in cross flow, while the upper-deck structures were dependent on the jet geometries, and could be either unsteady kidney-shaped or unsteady anti-kidney shaped. Accordingly, they classified the flow into two distinct groups: unsteady kidney-shaped for low AR elliptic jets, and unsteady anti-kidney shaped for high AR elliptic jets. The fact that their studies were conducted at low VRs raised the inevitable question as to whether "anti-kidney" vortices are also prevalent at high VRs or are they inherent only at low VRs. It has been shown in earlier sections that for a circular JICF (CJICF), the large-scale flow topology could be very different between low and high VRs. The desire to address this question was one of the motivations of the present investigation. Another motivation was to ascertain whether the vortex skeleton model previously proposed by us for a CJICF (see Lim et al. (2001)) was also applicable to the elliptic geometry for both low and high ARs.

Two elliptic jets of AR=2 and 3 are studied together with a comparing circular jet with equal cross-sectional areas. Before any further experiments are carried out, the velocity profiles across the major- and minor-axes of the elliptic jets, and the diameter of the comparing circular jet without cross flow are obtained using hot-film anemometry of similar setup listed in Chapter 2. They are shown in Figure 6.1. It may be worthy to note that the velocity profiles across the major-axes resemble more "top-hat"-like that those across the minor-axes.

The discussions of the results are organized as follows: They begin with flow visualization analysis of the low AR elliptic jets in Section 6.2, followed by high AR elliptic jets in Section 6.3.

(a) AR=3, major-axis

(b) AR=3, minor-axis

(c) AR=2, major-axis

(d) AR=2, minor-axis

(e) Circular

Figure 6.1.   Velocity profiles for the AR=2 and 3 free elliptic jets and comparing circular jet.
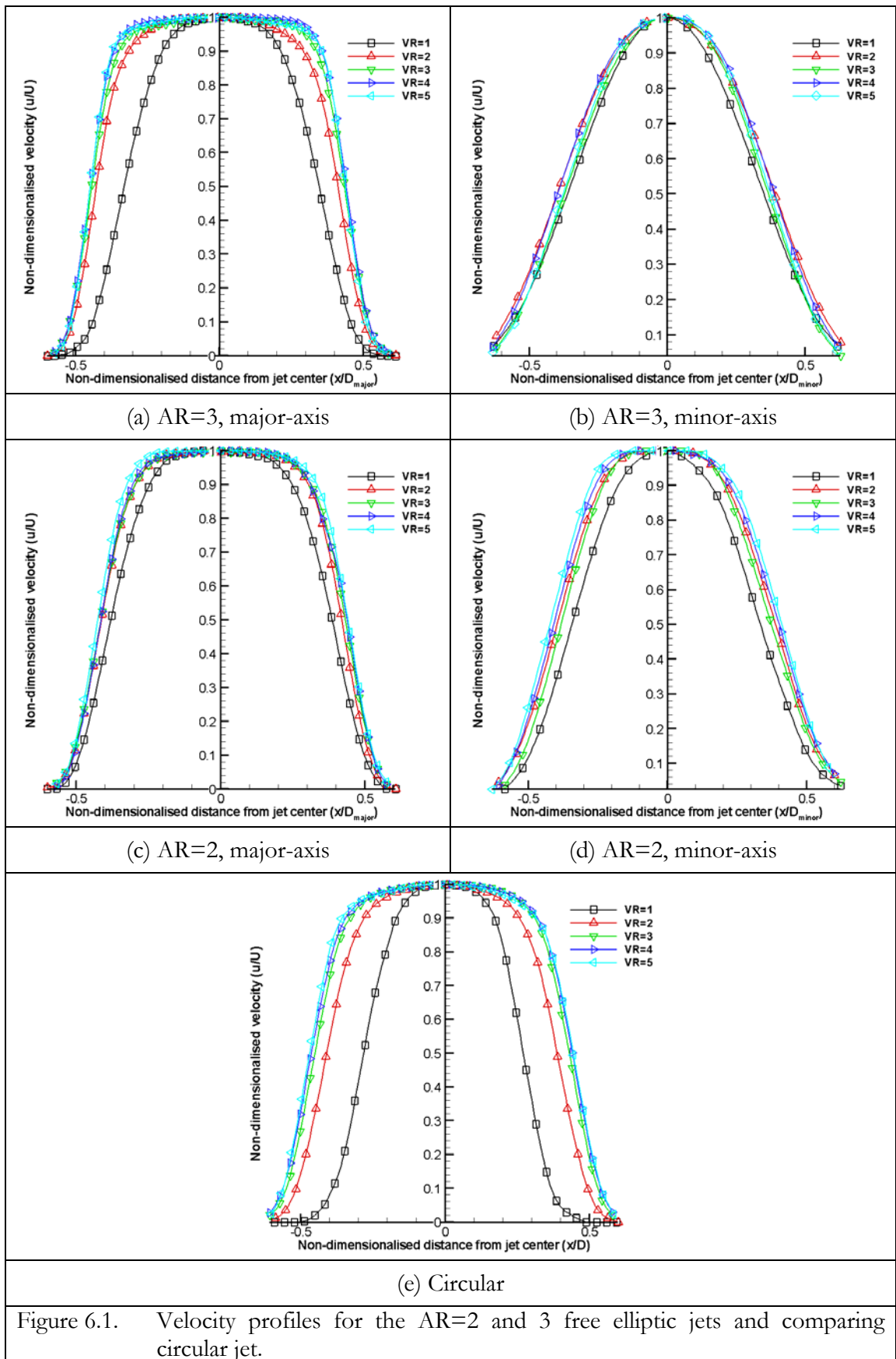
6.2   Low Aspect Ratio Elliptic Jets in Cross Flow

In Figures 6.2(a) and (b), the large-scale structures of EJICF, made visible by food dye, are presented for the AR of 0.3 and 0.5 elliptic jets, respectively. The Reynolds numbers of the flow based on the hydraulic diameters ranges from about 890 to 4440 for AR=0.3 elliptic jet and 1020 to 5090 for AR=0.5 elliptic jet, keeping in mind that both the geometries are subjected to the same VR. In all cases, dye was released through a dye port of 1.3mm diameter located inside the nozzle immediately upstream of the pipe exit, and sequence (i) to (v) shows the effects of increasing the VR. It can be seen from the figures that once the dye was introduced into the flow, it was immediately swept downstream to both sides of the elliptic jets and then rolled up to form a CVP. Although the leading-edge vortices rolled up periodically, there was no deliberate forcing applied to the flow. Much like the CJICF, the penetration of the elliptic jets into the cross flow for both ARs increased with the VR, and it can also be seen that when the VR was increased to about 3, the interaction between the adjacent leading-edge vortices was so intense that it led to vortex entanglement and subsequent vortex pairing further downstream. The intensity of the interaction could be due to a combination of the higher curvature of the vortex filament at the leading-edge of the low AR elliptic jet exits and higher vorticity generated at high VR. This behavior was in sharp contrast to CJICF where vortex entanglement was invariably absent although there was evidence of pairing of the leading-edge vortices some distance away from the jet exit.

Since point-injection of dye gave only a localized view of the overall flow field, an attempt was made to release the dye uniformly around the circumference of the nozzle further upstream from the dye port, and Figure 6.3 shows a typical flow pattern for the elliptic jet of AR=0.3 at VR=3. Here, the lee-side vortices can be clearly seen to form

(i) VR=1   (i) VR=1

(ii) VR=2   (ii) VR=2

(iii) VR=3   (iii) VR=3

(iv) VR=4   (iv) VR=4

(v) VR=5   (v) VR=5
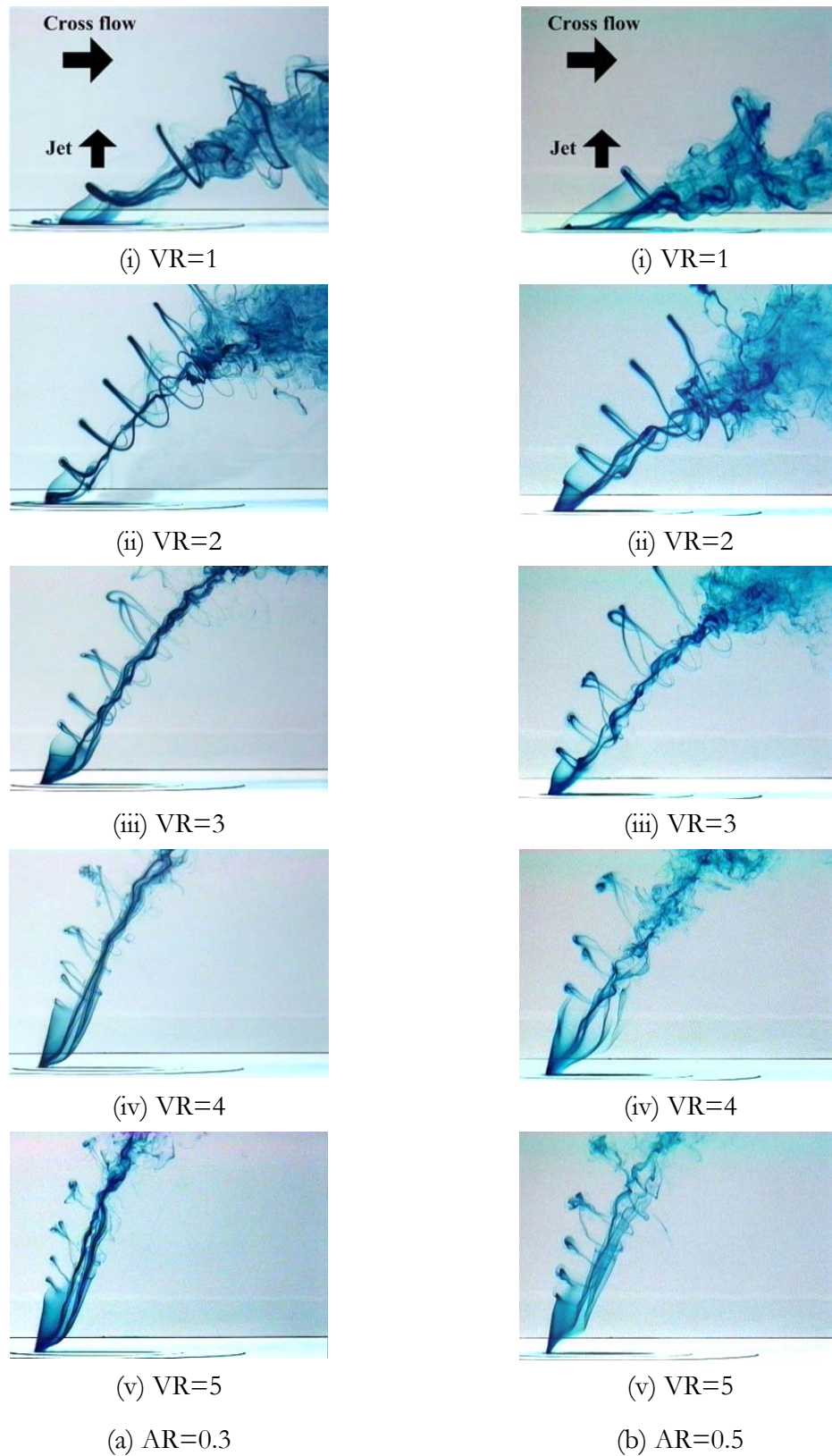
(a) AR=0.3   (b) AR=0.5

Figure 6.2.   Flow pattern of low AR elliptic jets, observed when blue dye is released through a dye port located slightly upstream of the jet exit. (a) AR=0.3 (b) AR=0.5. Note the strong interaction between neighbouring leading-edge vortices when the VR is above 3.
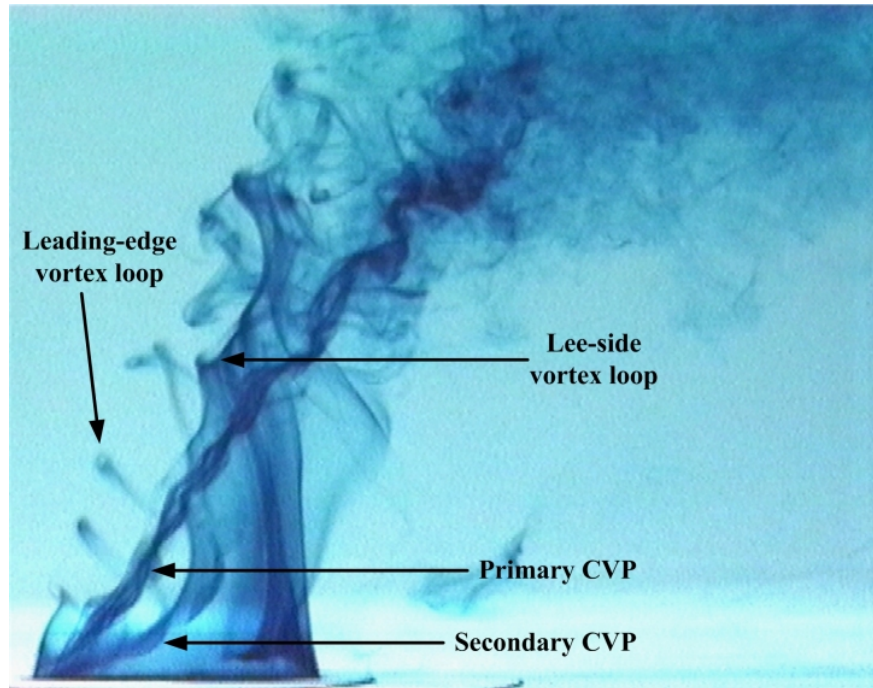
Figure 6.3.   A typical flow pattern of low AR elliptic jet captured when dye is released through a dye port located slightly upstream of the jet exit as well as through a circumferential slit further upstream of the dye port, AR=0.3 and VR=3. Notice that how the first lee-side vortex is generated much further downstream than the first leading-edge vortex.

much further downstream of the jet exit than the corresponding vortices for the circular exit geometry (see Lim et al. (2001) or Figure 5.1 for comparison). The delay in the formation of the lee-side vortices was found to occur for all the VR and AR investigated here. With the circumferential injection of dye, valuable information about the development of the whole jet column can be obtained. In fact, it was through detailed observation during the experiment that the two sets of adjacent CVPs were noticed to be generated at the sides of the jet column near the leading-edge. These CVPs had the same rotational sense (see Figure 6.3), although one was qualitatively stronger than the other.

The visually stronger pair was referred to as the primary CVP and the weaker pair as the secondary CVP. Through their mutual interaction, the secondary CVP was eventually entrained by the primary CVP, and the paired up CVP subsequently became

the dominant flow structure in the far-field much like the case in CJICF. This suggests that the effects of jet geometry were confined to the near-field structures only, and the far-field flow structures depended only on the gross geometry. However, it should be noted that there exist contrary experimental data which illustrated differences in the final CVP strength, trajectory and spreading due to initial differences in the jet geometries (see Brundage et al. (1999), Hale et al. (1999) and Peterson and Plesniak (2002)).

Figure 6.4 is a vortex skeleton model showing the proposed interpretation of the low AR elliptic jet structures, applicable to both AR=0.3 and 0.5. The leading-edge vortices are represented by the dark-blue counter-clockwise vortex loops while the lee-side vortices are shown as the light-green clockwise vortex loops. The double folding of the jet shear layer near the jet exit signifies the formation of the primary and secondary CVPs prior to the generation of the leading-edge and lee-side vortices. For simplicity, the pairing of leading- edge vortices is not shown in the figure although it could have been included in the model without too much difficulty. Moreover, the pairing does not alter the more important fundamental behaviour of the vortex structures. Due to the presence of the CVP, the "side-arms" of the leading-edge vortex loops took a sudden change in direction and got entrained into the CVP. Close examination during the experiment showed that the mechanism leading to the formation of the leading-edge and lee-side vortices in EJICF, after the primary and secondary CVPs have merged, was similar to that in CJICF proposed by Lim et al. (2001). For clarity, conjectured cross-sections of the model in a plane normal to the jet trajectory (A-A plane in Figure 6.4) at various locations along the jet axis (specified by different values of s) are displayed in Figure 6.5 and the perspective views of Figure 6.5(a) and (f) are presented in Figure 6.6(a) and (b), respectively. Notice how the lee-side vortex loop is produced from the folding of the
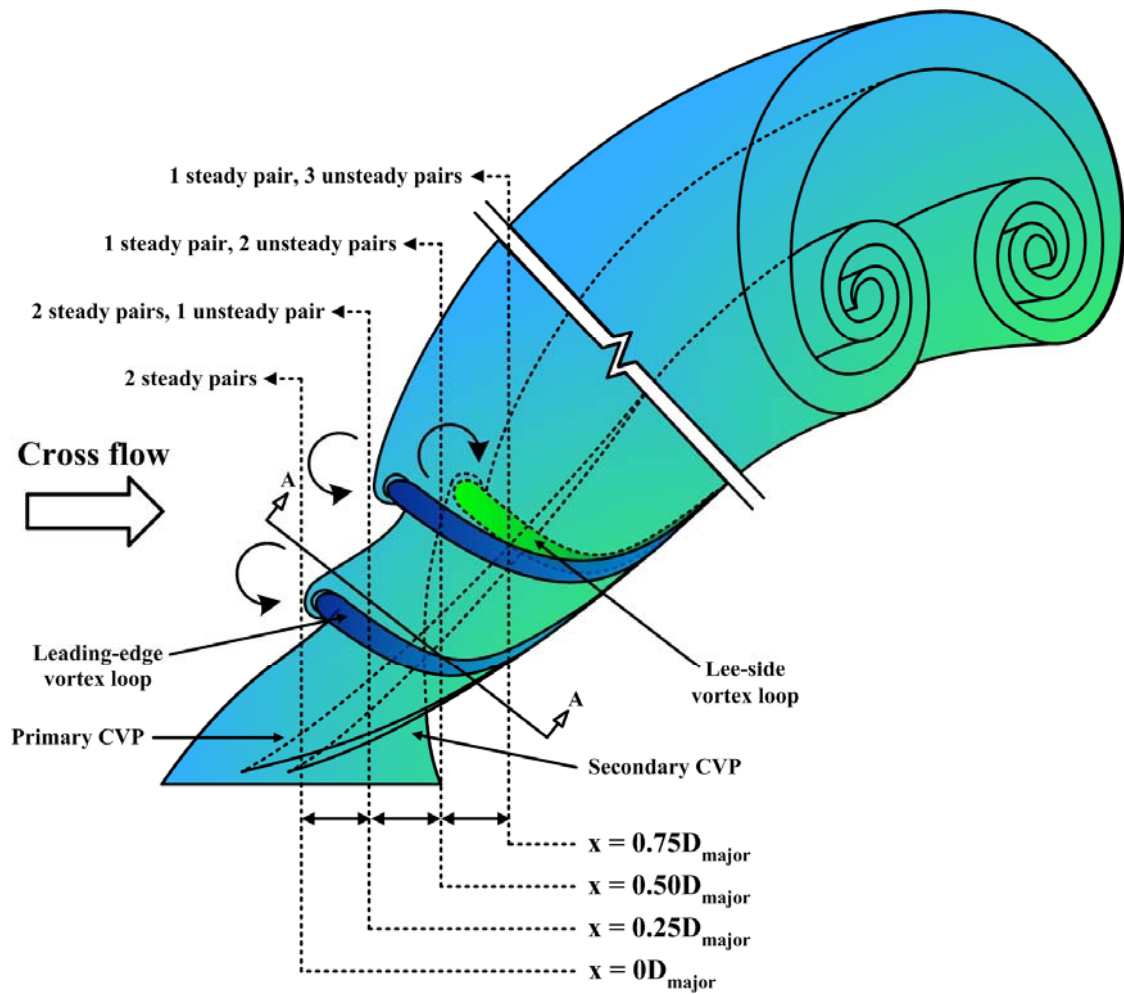
Figure 6.4.   Vortex skeleton model for low AR elliptic jets in cross flow (i.e. AR=0.3 and 0.5). Notice the presence of a secondary CVP adjacent to the primary CVP at the side of the jet column. Section A-A indicates a typical location where sectioning of the flow structures have been made in a plane normal to the jet axis. Vertical broken lines indicate the locations where cross-sectional views of the structures in a plane normal to the cross flow direction are taken.

vortex sheet from the trailing side of the jet.

To verify the validity of the model, typical laser cross-sections of the actual jet structures in a plane normal to the mean jet trajectory are displayed in Figure 6.7 for the AR of 0.3 elliptic jet. They are used to compare with the conjectured cross-sections of the proposed model displayed in Figure 6.5 taken along the same downstream distances.

(a) s=0.5D$_h$

(b) s=1.0D$_h$

(c) s=1.5D$_h$

(d) s=2.0D$_h$

(e) s=2.5D$_h$

(f) s=3.0D$_h$
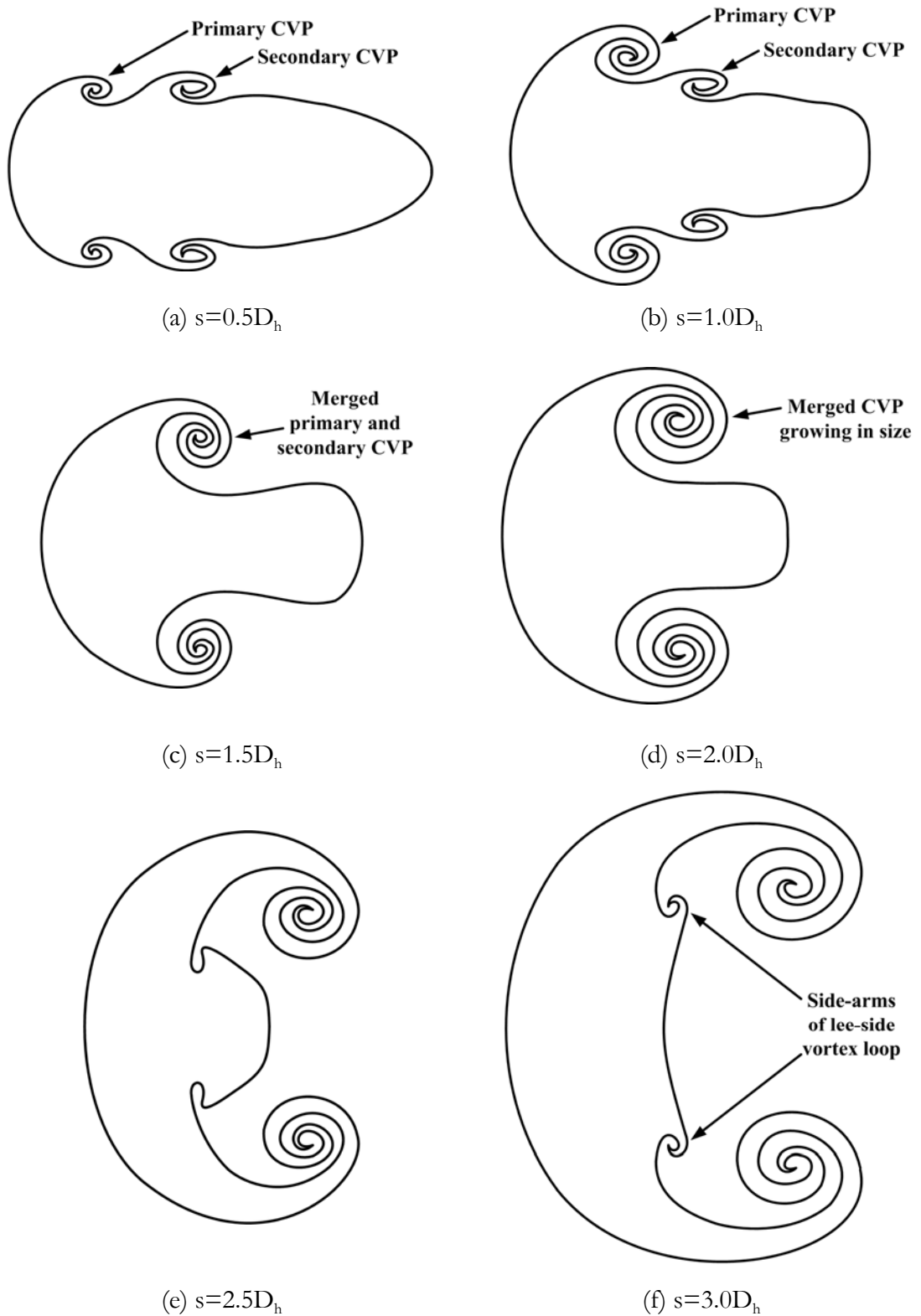
Figure 6.5.   Conjectured cross-sections of the elliptic jet (AR=0.3, VR=3) in different planes *normal to the mean jet trajectory* (see section A-A in Figure 6.4).   s indicates the distance measured along the mean jet trajectory from the exit of the nozzle.

(a)

(b)
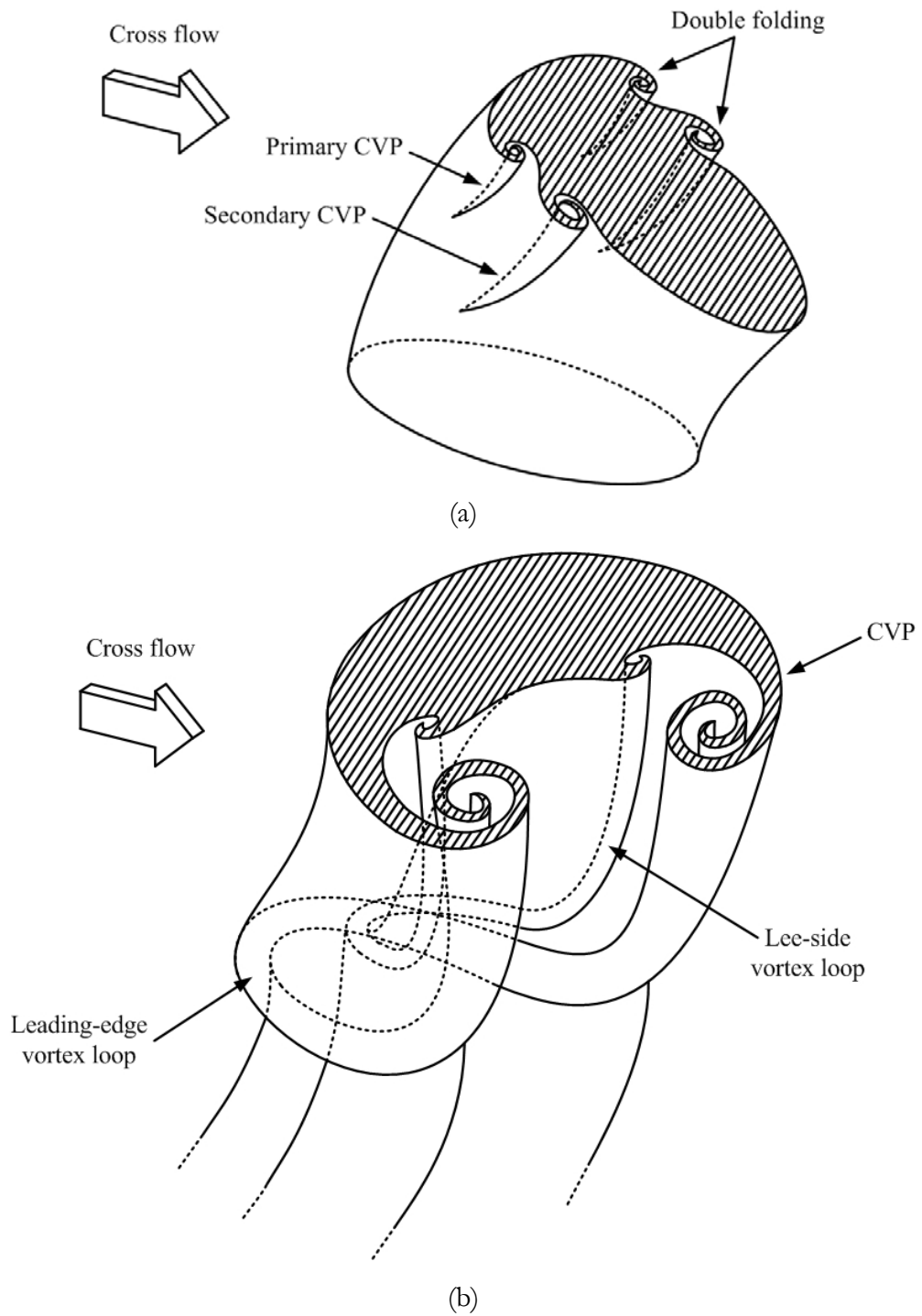
Figure 6.6.   Perspective views showing: (a) the initial folding of the jet shear layer, and (b) fully developed structure corresponding to the sectional views in Figure 6.5(a) and (f), respectively.

(a) s=0.5D_h (b) s=1.0D_h

(c) s=1.5D_h (d) s=2.0D_h

(e) s=2.5D_h (f) s=3.0D_h
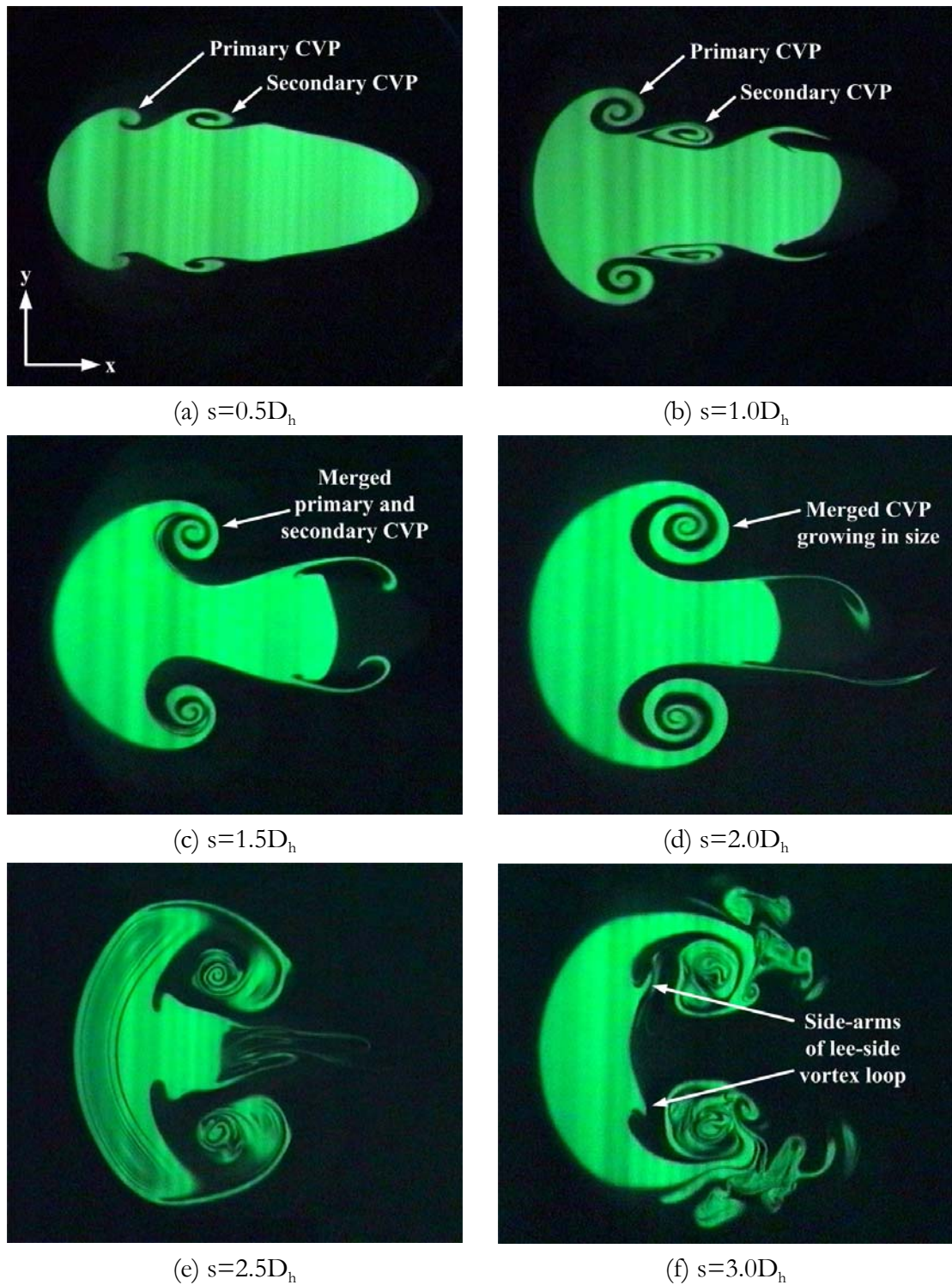
Figure 6.7.   Laser-induced fluorescence (LIF) images of AR=0.3 elliptic jet captured along various discrete locations normal to the mean jet trajectory at VR=3. (a) Two pairs of jet shear layer foldings to form the primary and secondary CVPs. Sequence (b)-(f) depicts how the secondary CVP is induced by and subsequently engulfed by the primary CVP.

As Figures 6.5 and 6.7 clearly show, apart from a slight flow deviation near the trailing-edge of the jet in the experiment, the agreement between the model and the experiment is very good. The deviation at the trailing edge gives the appearance of another pair of CVP in addition to the primary and secondary CVP (Figure 6.7(b)-(d)). But after much careful observation, we believed that this pair of CVP is merely the deformation of the jet column by the cross flow as the latter closed-in at the trailing-edge, and is unlikely to have any significant effect on the overall flow structures development, as can be inferred from its demise at later times. For simplicity, they are left out in the final flow model with negligible effects. It is also worth noting that near the jet exit, the secondary CVP was noticeably larger in size than the primary CVP (see Figure 6.7(a)), but further downstream it was entrained by the stronger primary CVP, as can be see in Figure 6.7(b) and (c). It is not clear why the secondary CVP started off larger than the primary CVP.

As further confirmation of the validity of the model, cross-sectional views of the jet structures for the AR of 0.3 elliptic jet in a vertical plane normal to the cross flow are presented in Figure 6.8 for $x=0D_{major}$ (where $x=0D_{major}$ corresponds to the centre of the elliptic jet, as shown in Figure 6.4), $0.25D_{major}$, $0.50D_{major}$ and $0.75D_{major}$ and notice the good agreement between the model and the experiment. The expected number and type of CVPs along the same downstream distances based on the flow model is indicated in Figure 6.4 and it could be seen that they match very well with the experimental results. It may be noteworthy to mention again here that the existence of the pair of primary unsteady anti-kidney vortices is the result of the laser sheet slicing across the lee-side vortex loop formed further downstream. However when compared to Figure 6.7, the primary CVP is actually larger in size than the secondary CVP, probably due to the selected visualization plane. It is important to note that the LIF images in Figure 6.8 were

(i) x=0D$_{major}$ (i) x=0D$_{major}$

(ii) x=0.25D$_{major}$ (ii) x=0.25D$_{major}$

(iii) x=0.50D$_{major}$ (iii) x=0.50D$_{major}$

(iv) x=0.75D$_{major}$ (iv) x=0.75D$_{major}$

(a) Flow model   (b) Experimental result
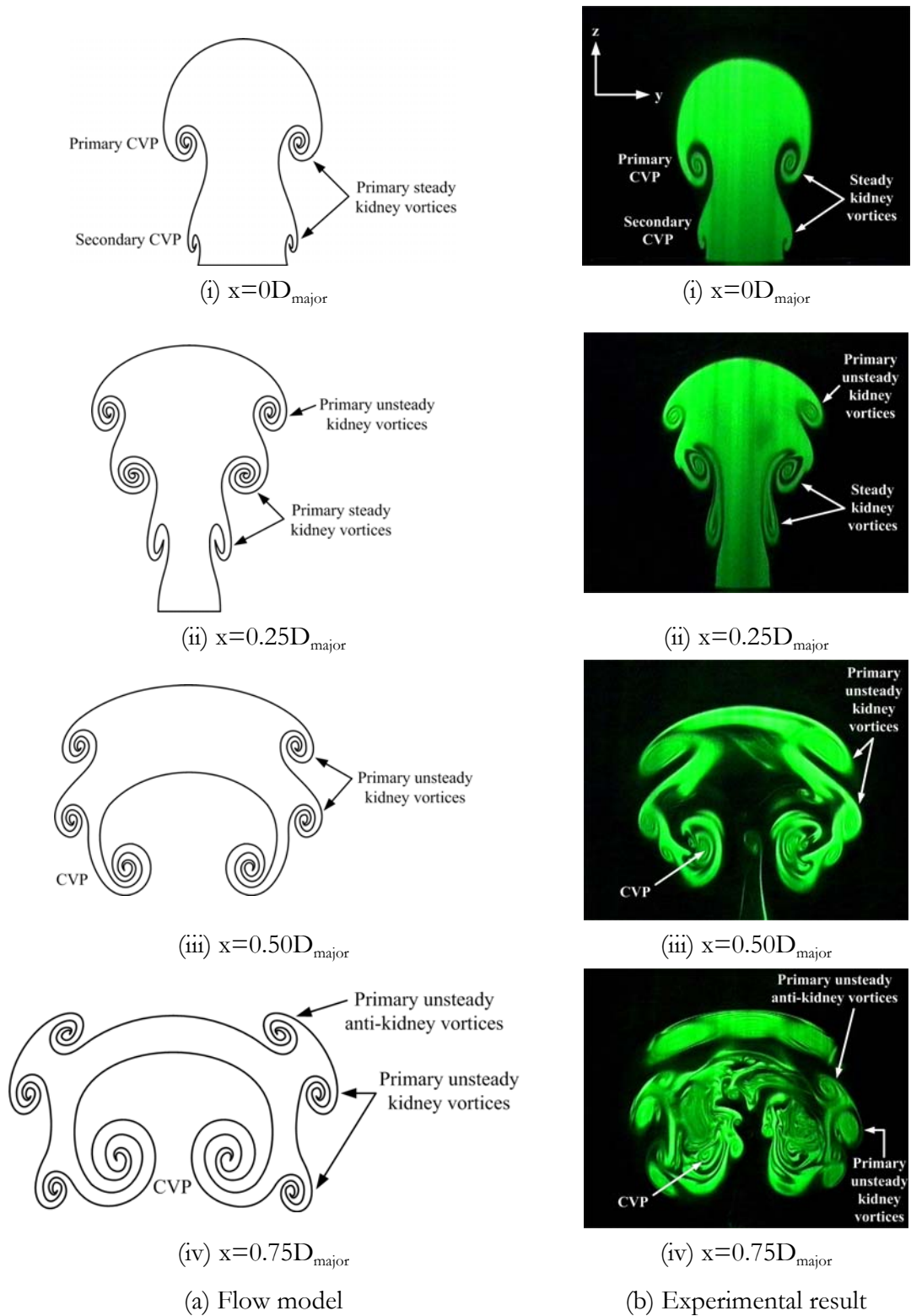
Figure 6.8.   Cross-sections of low AR elliptic jet structures in a vertical plane normal to cross flow at various downstream distances from the jet origin (x=0D$_{major}$). Comparison between the model and the experiment (AR=3, VR=2).

reproduced from the video recordings, by selecting at each laser sheet location, the appropriate video frame based on the same passage of time from the first appearance of a leading-edge vortex loop. This was easily accomplished with the aid of a time-code card in the video recorder. Although not shown here for the sake of brevity, similar good agreement between the model and the experiment is also found for the AR of 0.5 elliptic jet.

From Figure 6.8, one could see what Haven and Kurosaka (1997) termed as "unsteady upper-deck kidney vortices" or what the present authors termed as "primary unsteady kidney vortices" in the laser cross-sections at $x=0.25D_{major}$ and $0.50D_{major}$. The decision to use a different term here is based on the necessity to differentiate "primary unsteady kidney vortices" from "secondary unsteady kidney vortices" which Haven and Kurosaka (1997) did not see in their experimental study. To have a better idea of how the primary unsteady kidney vortices are generated, Figure 6.9 shows time-sequenced LIF images of a deflected low AR elliptic jet of AR=0.5 traveling past a laser sheet (which is normal to the cross flow direction) at $x=0.25D_{major}$ downstream from the jet origin. As can be seen from the figure, there are actually three sets of CVPs arranged in triple deck, with the two pairs closer to the floor exhibiting steady behavior. While it is obvious that the qualitatively larger pair (vortex pair A) of the two steady vortex pairs is the "steady lower-deck kidney vortex" labeled by Haven and Kurosaka (1997), it is unclear whether they have seen the pair closest to the floor (vortex pair B). Close examination of the results, aided by slow motion replay of the captured video images show that the two steady vortex pairs are nothing more than the primary and secondary CVP discussed earlier for low AR elliptic jets. While the evidence agreed with Haven and Kurosaka (1997) that the uppermost pair, which they referred to as "unsteady upper-deck kidney

(a) t=0.0 sec

(b) t=0.08 sec

(c) t=0.16 sec

(d) t=0.24 sec

(e) t=0.32 sec

(f) t=0.40 sec
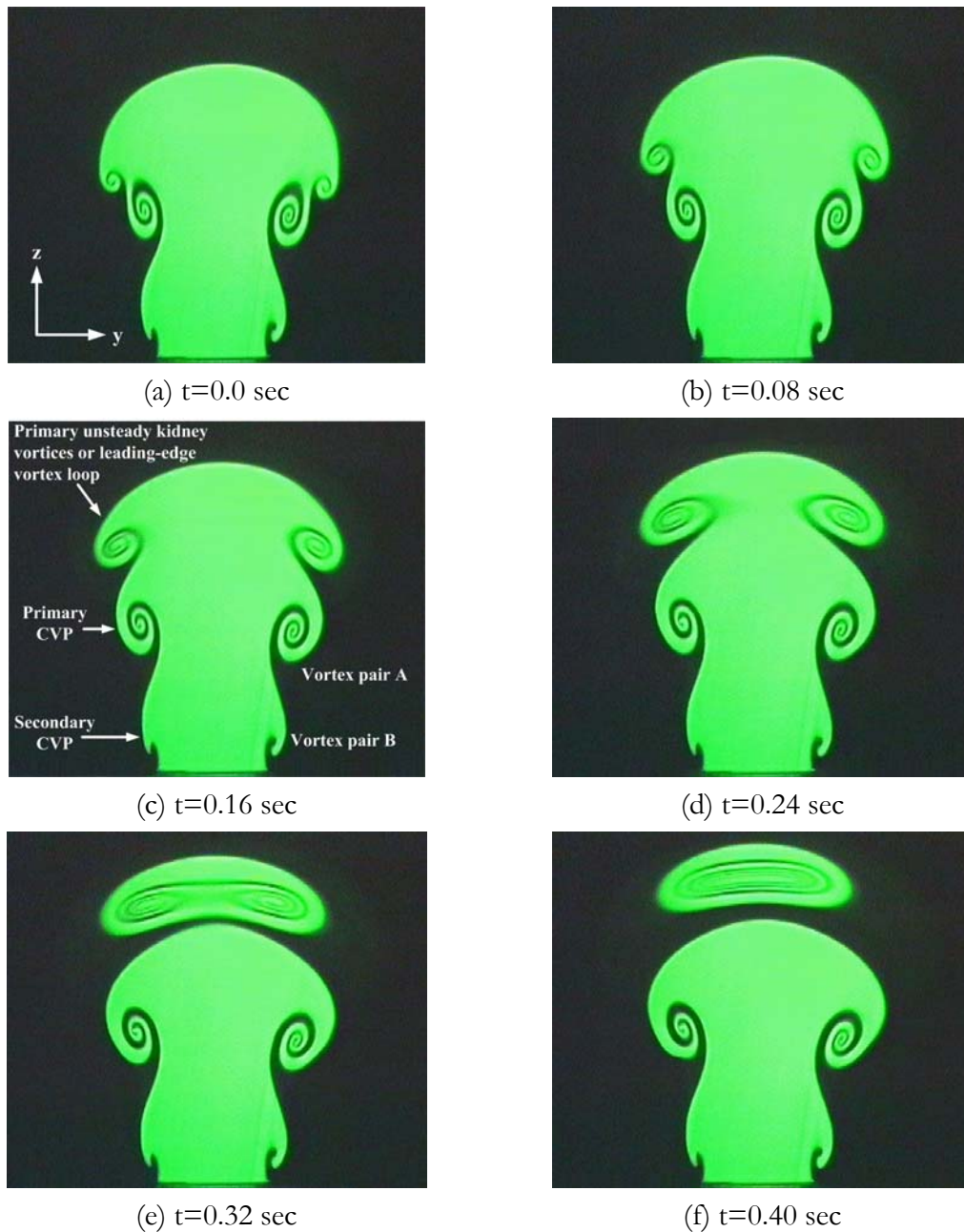
Figure 6.9.   Time-sequence LIF images showing laser cross-sections of the leading-edge vortices (or primary unsteady kidney vortices), primary CVP and secondary CVP (or steady kidney vortices) in a vertical plane normal to cross flow at x=0.25D$_{major}$.

vortices", are the manifestation of the leading-edge vortices periodically passing through the laser sheet, no convex warping of the frontal shear layer surface was observed, which they believed to be responsible for their appearances. This matter shall be touched on again when discussing high AR elliptic jets in the next section.

Although the discussions above are made with reference to the AR=0.3 elliptic jet at VR=3, the topological structures for the other low AR elliptic jet (i.e. AR=0.5), as well as the other VR studied, are similar to that of AR=0.3 elliptic jet at VR=3, apart from differences in the length scale.

6.3   High Aspect Ratio Elliptic Jets in Cross Flow

6.3.1   General Discussion

Figure 6.10(a)-(b) shows the flow patterns of high AR elliptic jets (i.e. AR=2 and 3) when dye was released from the injection port into the upstream side of the nozzle. The sequence (i) to (v) shows the effect of increasing the VR. It can be seen from the photographs that increasing the jet nozzle configuration from low to high AR reduces not only the regularity of the leading-edge vortex shedding, but also the intensity of the interaction between neighbouring vortices. These changes can be attributed to the leading-edge vortex filaments having a frontal curvature significantly lower than their counterparts in the low AR cases. Smaller radius of curvature results in lower self-induced velocity, and therefore less intense vortex interaction.

Although it cannot be clearly seen in the photographs in Figure 6.10, detailed observation during the experiment showed that, prior to the formation of the leading-edge vortices, the windward side of the vortex sheet developed one or more pairs of streamwise foldings, depending on the AR and VR. It was decided to call these foldings "streamwise foldings" rather than secondary CVPs so as to differentiate them from those of the low AR elliptic jet. This behaviour is in sharp contrast to the case for low AR jet, where only two pairs of foldings (primary and secondary CVPs) with the same sense of rotation, are always formed adjacent to each other at the sides of the jet column regardless

100

(i) VR=1

(i) VR=1

(ii) VR=2

(ii) VR=2

(iii) VR=3

(iii) VR=3

(iv) VR=4

(iv) VR=4

(v) VR=5

(v) VR=5
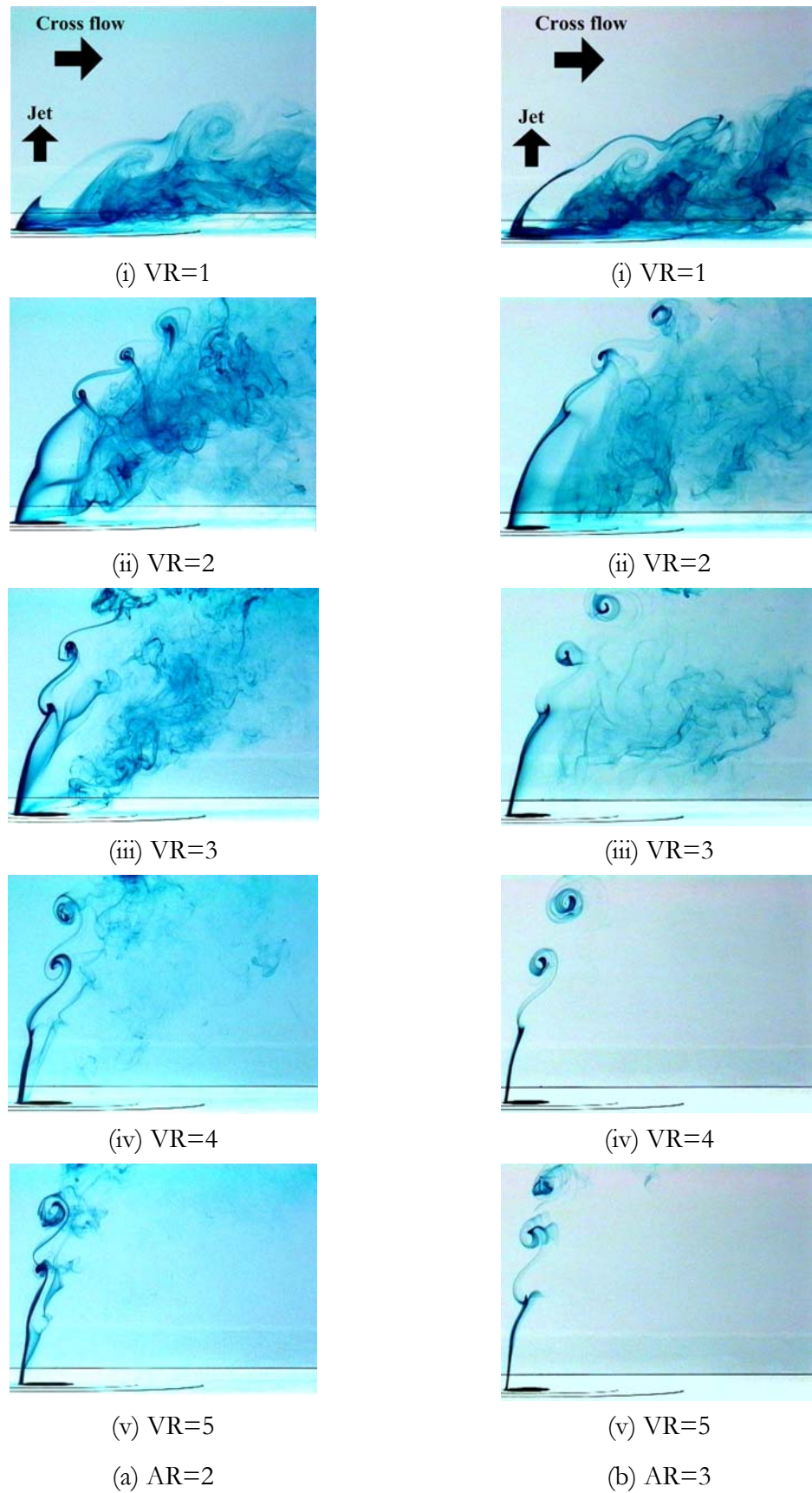
(a) AR=2

(b) AR=3

Figure 6.10.   Flow pattern of high AR elliptic jets obtained by releasing blue dye through a dye port located upstream of the jet exit. (a) AR=2 (b) AR=3.

of the AR and VR. Due to their close proximity, and aided by the same sense of rotation, they eventually merge to form one dominant CVP further downstream. In high AR elliptic jets however, the streamwise folding of the vortex sheet can take on any one of the three possible routes depicted in Figure 6.11, and are referred to as Scenario 1, Scenario 2 and Scenario 3, respectively. Which scenario will dominate depends on the AR and VR, and sometimes it is possible for two scenarios to exist (though not at the same time), for the same AR but different VR. It can be seen from Figures 6.11 (a) and (b) that both Scenario 1 and 2 possess one pair of primary CVP at the lee-side and one streamwise folding at the windward side of the jet column. The feature that distinguishes these two scenarios is the manner in which the windward side jet shear layer is folded to form either streamwise folding. In Scenario 1, the sense of rotation of the streamwise folding is opposite to that of the primary CVP, while in Scenario 2 both the streamwise folding and the primary CVP have the same sense of rotation, as can be seen in Figure 6.11. Unlike the low AR jets, these two pairs of vortex structures do not merge, partly due to their larger distance of separation. They remain as separate entities. When the jet shear layer eventually rolls up to form the leading-edge vortices, these streamwise foldings are also being rolled up by them and become part of the leading-edge vortices, as will be shown later. In Scenario 3, it can be seen from Figure 6.11(c) that its basic structure is similar to that of Scenario 2, except for the presence of two additional pairs of streamwise foldings which are formed slightly downstream than the one at the centre. The existence of Scenario 3 raises an inevitable question as to whether Scenario 1 also develops similar additional pairs of streamwise foldings adjacent to the central pair, but so far no evidence of them has been found in the present experiment. Such a scenario is depicted in Figure 6.11(d) as Scenario 4, where three WVPs of opposite rotational sense to Scenario 3 exist along the windward side of the jet shear layer. Although topologically feasible, we did not see this scenario in any of our experiments. The reason for its absence is not entirely

(a) Scenario 1   (b) Scenario 2

(c) Scenario 3   (d) Scenario 4
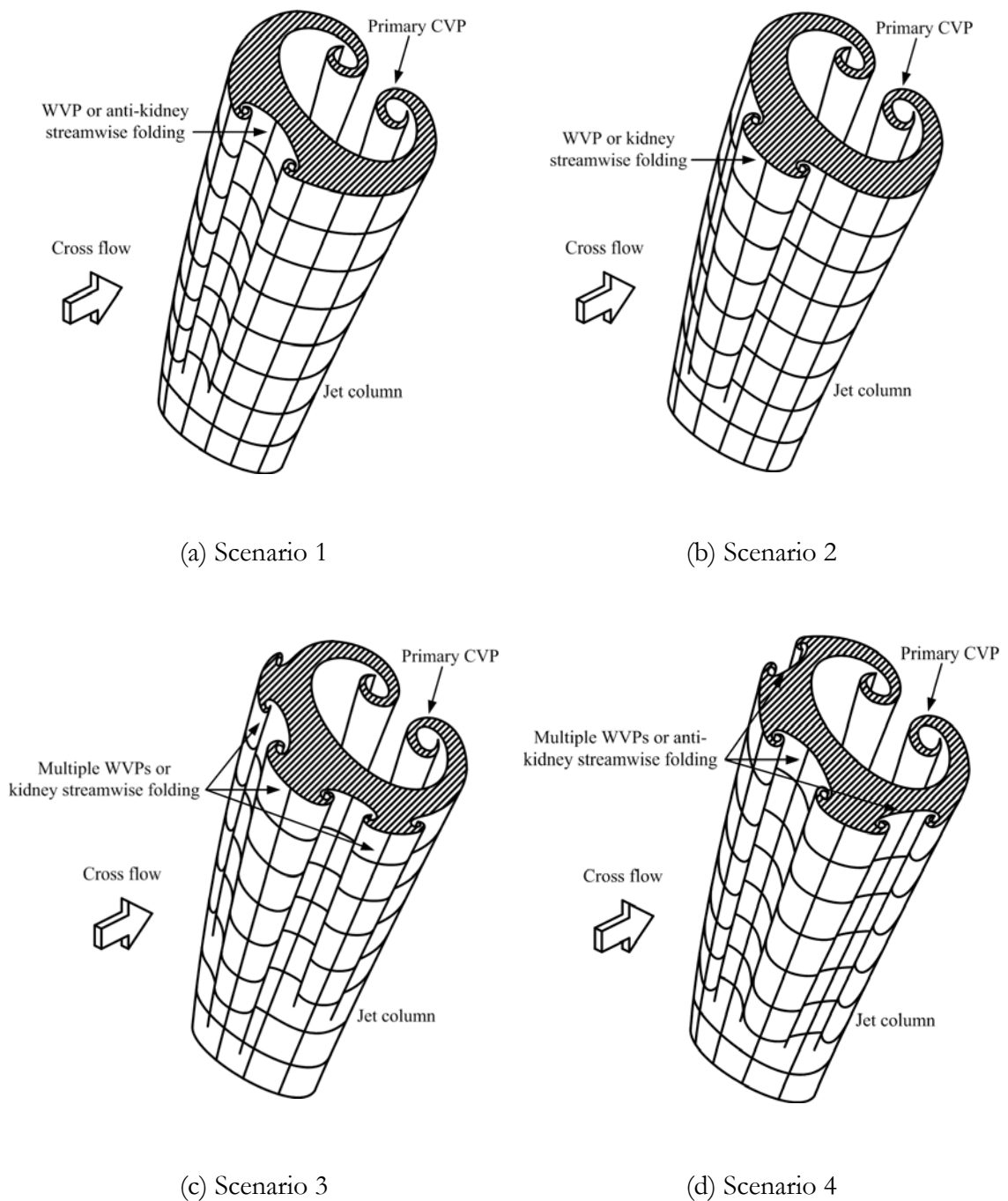
Figure 6.11. Authors' interpretation of the three possible scenarios for a high AR jet, depending on the sense of rotation of the WVP. Scenario 1 is responsible for what Haven and Kurosaka (1997) refer to as unsteady anti-kidney vortices, and Scenario 2 is responsible for unsteady kidney vortices. Scenario 3 is a variation of Scenario 2. While not observed in the present study, the hypothetical Scenario 4 (a variation of Scenario 1) is shown here.
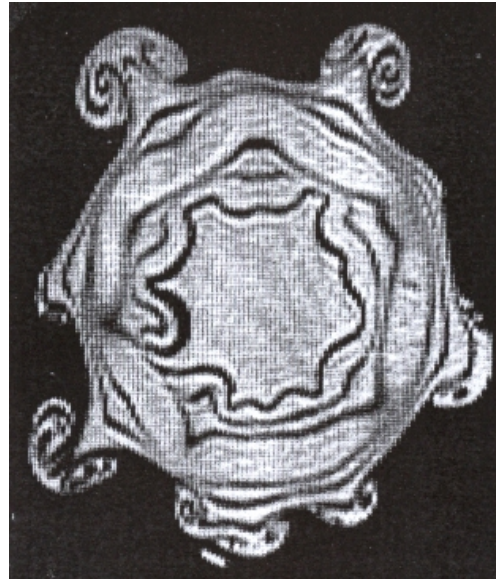
Figure 6.12.   LIF cross-section of an axisymmetric free jet illuminated with a thin laser sheet normal to the jet axis at x/d= 3.25. The formation of streamwise foldings around the circumference of the cylindrical shear layer is manifested as CVPs in the laser plane (Reproduced with permission from Liepmann and Gharib (1992)).

clear.

It is believed that the existence of the WVPs could be due to the "convex" and "concave" warping of the leading-edge vorticity similar to that suggested by Haven and Kurosaka (1997). Their transient model of the interaction between the jet and the cross flow along the windward jet/cross flow interface could account for the present observations in Scenario 1 and 2. As for Scenario 3 (and Scenario 4, for that matter), they are merely an extension of Scenario 1 and 2 as a result of further shear layer instability similar to the one observed by Liepmann and Gharib (1992) for a free circular jet (see Figure 6.12). The author agrees with Haven and Kurosaka (1997) that the "convex" and "concave" warping or folding of the vortex sheet is instrumental in the formation of unsteady kidney and unsteady anti-kidney vortices. However, the similarity ends here because it is believed that the subsequent process leading to the formation of these vortices is significantly different from their interpretation. This will be discussed further

Type	Nomenclature used by the present authors	Actual flow structures	Nomenclature used by Haven and Kurosaka (1997)
1	Primary steady kidney vortices	Manifestation of the primary CVP upon the laser plane.	Steady kidney vortices
2	Secondary steady kidney vortices	Manifestation of the secondary CVP upon the laser plane	Not reported
3	Primary unsteady kidney vortices	Manifestation of the leading-edge vortices on the cross-plane LIF visualization. These vortices will always be observed irrespective of the type of secondary unsteady vortices observed.	Unsteady kidney vortices
4	Secondary unsteady kidney vortices	Manifestation of the streamwise foldings riding on top of the jet shear layer or leading-edge vortices as they cross the laser plane. As to which type of secondary unsteady vortices will prevail depend on the rotational sense of the streamwise foldings.	
5	Secondary unsteady anti-kidney vortices		Unsteady anti-kidney vortices

Table 6.1. A comparison between the nomenclature used by Haven and Kurosaka (1997) and those used by the present authors for high AR EJICF.

later.

At this juncture, it is important to clarify some of the nomenclature used in the present thesis, so as to avoid any confusion with the terms used previously by Haven & Kurosaka (1997). A summary of nomenclature used is listed in Table 6.1 together with that of Haven & Kurosaka (1997). Notice from the table that what Haven & Kurosaka (1997) referred to as "unsteady kidney vortices" has been further sub-divided into "primary unsteady kidney vortices" and "secondary unsteady kidney vortices". This is to better reflect the additional flow features observed by us for high AR elliptic jets, but

105

were not reported by Haven and Kurosaka (1997). So, instead of classifying all unsteady kidney vortices under one common group, it was decided to differentiate them into those resulted from the manifestation of the leading-edge vortices on the laser plane (primary unsteady kidney vortices), and those resulted from the manifestation of the streamwise foldings riding on top of the jet shear layer or leading-edge vortices as they cross the laser plane (secondary unsteady kidney vortices). More on the secondary unsteady kidney vortices will be discussed later.

Despite the added complexity due to the development of the streamwise foldings, detailed study indicates that the mechanism responsible for the formation of the leading-edge and lee-side vortices for all the three scenarios is the same as in the low AR elliptic jet discussed in section 3.1 and the circular geometry described by Lim et al. (2001). Moreover, the effects of the initial conditions (i.e. jet geometry) are found to be important only in the near-field and eventually damp out in the far-field where the large-scale structures are dominated by the primary CVP which depends only on gross jet geometry. It is important to stress that far from the jet exit, the primary CVP is contaminated by fine-scale flow structures, which are absent near the jet exit. Figure 6.13 shows the author's interpretations of the fully-developed high AR elliptic jets for the three scenarios, and the break in each figure is merely to differentiate the near-field structures from that of the far-field, of which the smaller-scale structures have been removed for simplicity. For clarity, the state of the streamwise folding after it has been rolled up by one of the leading-edge vortices is enlarged and shown in Figure 6.14(b)-(d). A hypothetical cut through a leading-edge vortex loop at section A-A (Figure 6.14(a)), with the resulting cross-sections displayed in Figure 6.14(e)-(g) clearly illustrates how Scenario 1 and 2 can lead to what Haven and Kurosaka (1997) referred to as "unsteady anti-kidney vortices" and "unsteady kidney vortices", respectively. However, their interpretations of how these
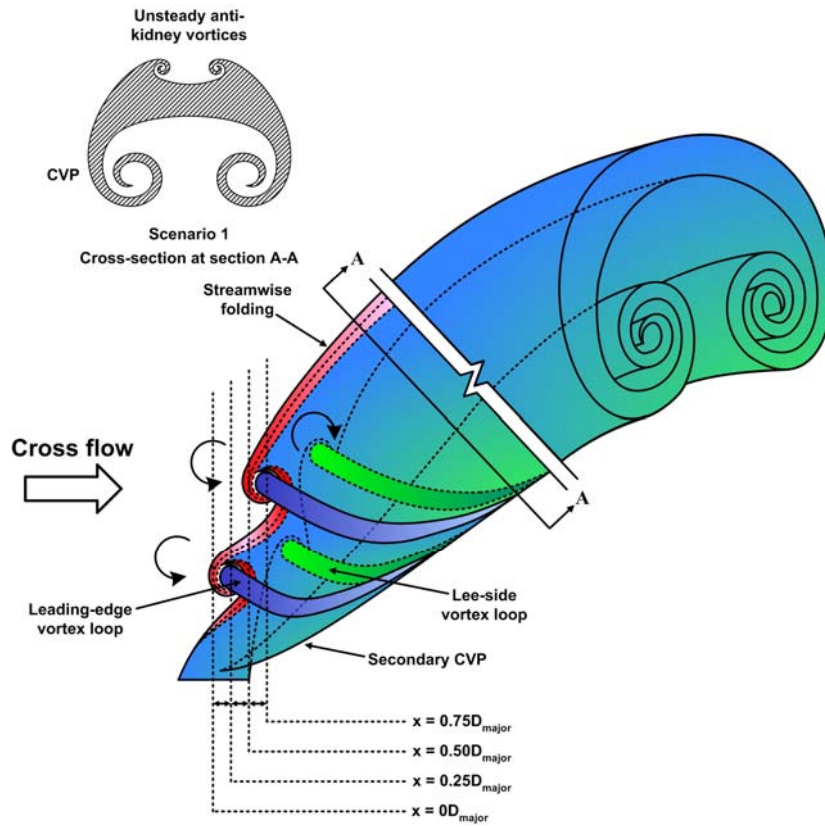
(a) Scenario 1
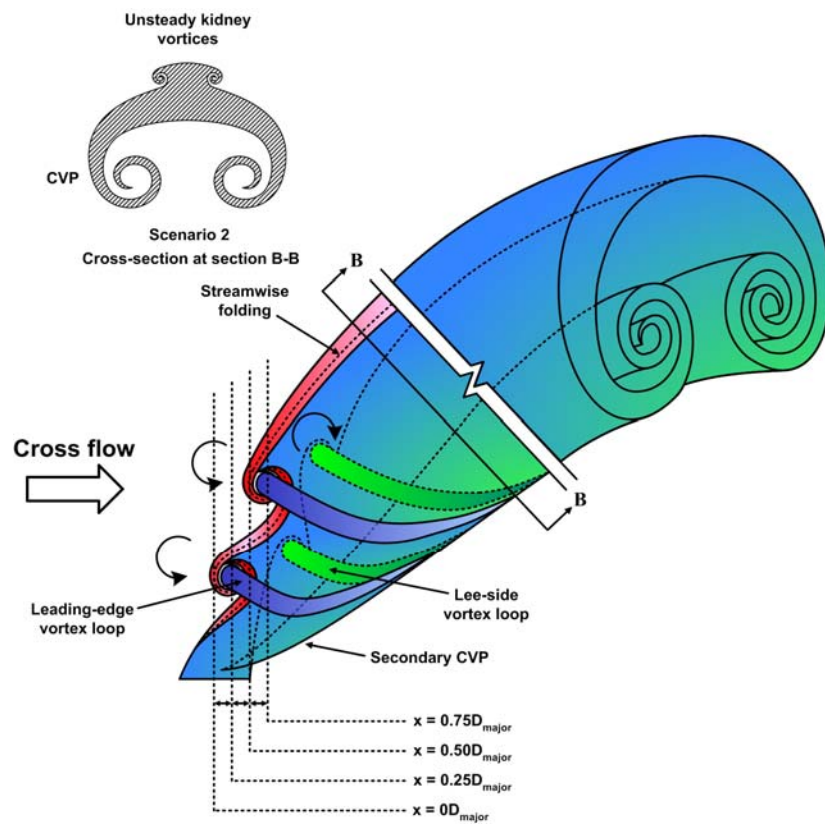
(b) Scenario 2
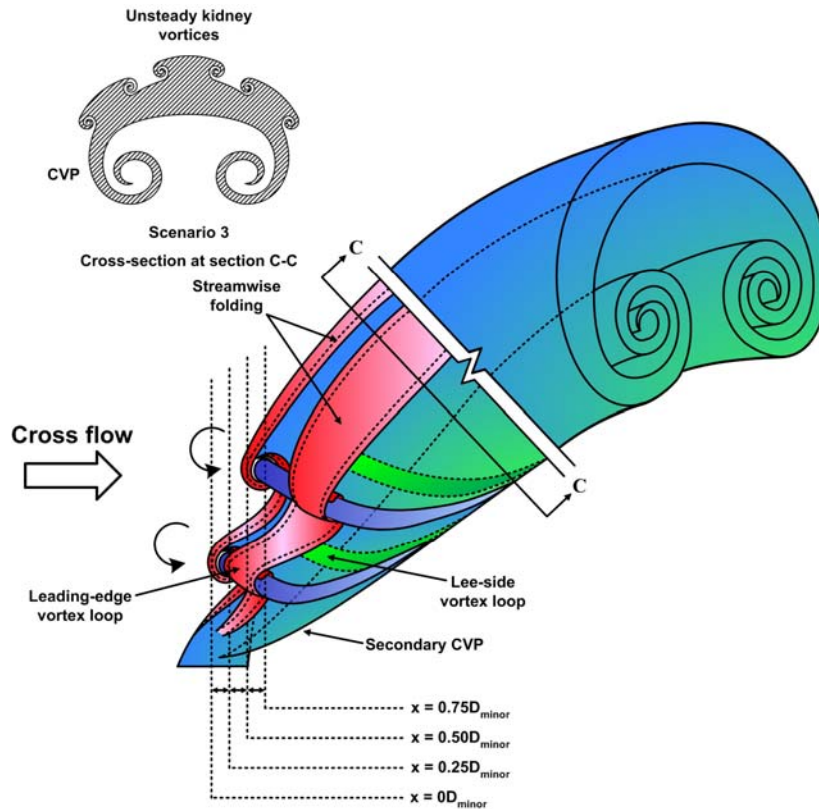
(c) Scenario 3

Figure 6.13.   Authors' interpretation of the vortex skeleton models for high AR elliptic jets. They are derived from the three scenarios shown in Figure 6.11. (a) Scenario 1, (b) Scenario 2 and (c) Scenario 3. The break in each figure is merely to differentiate the near-field structures from the far-field structures. Notice that how the streamwise foldings on the shear layer are being rolled up by much stronger leading-edge vortices.

vortices are generated differ from the present case. To be consistent with the definition presented in table 2, "secondary unsteady anti-kidney vortices" and "secondary unsteady kidney vortices" will be used hereafter when referring to the above-mentioned vortices.

This matter will be further discussed later. For now, it can be seen from Figure 6.14(e)-(g) that section A-A also reveals the undersides of the secondary unsteady anti-kidney and secondary unsteady kidney vortices. The opposite sense of rotation of the undersides is the manifestation of the streamwise folding of either Scenario 1 or Scenario 2, being tucked underneath the leading-edge vortex loop. Haven and Kurosaka (1997)

108

(a)

(b) Scenario 1

(e) Section A-A: unsteady anti-kidney vortices and their undersides.

(c) Scenario 2

(f) Section A-A: unsteady kidney vortices and their undersides.

(d) Scenario 3

(g) Section A-A: unsteady kidney/ anti-kidney vortices and their undersides.
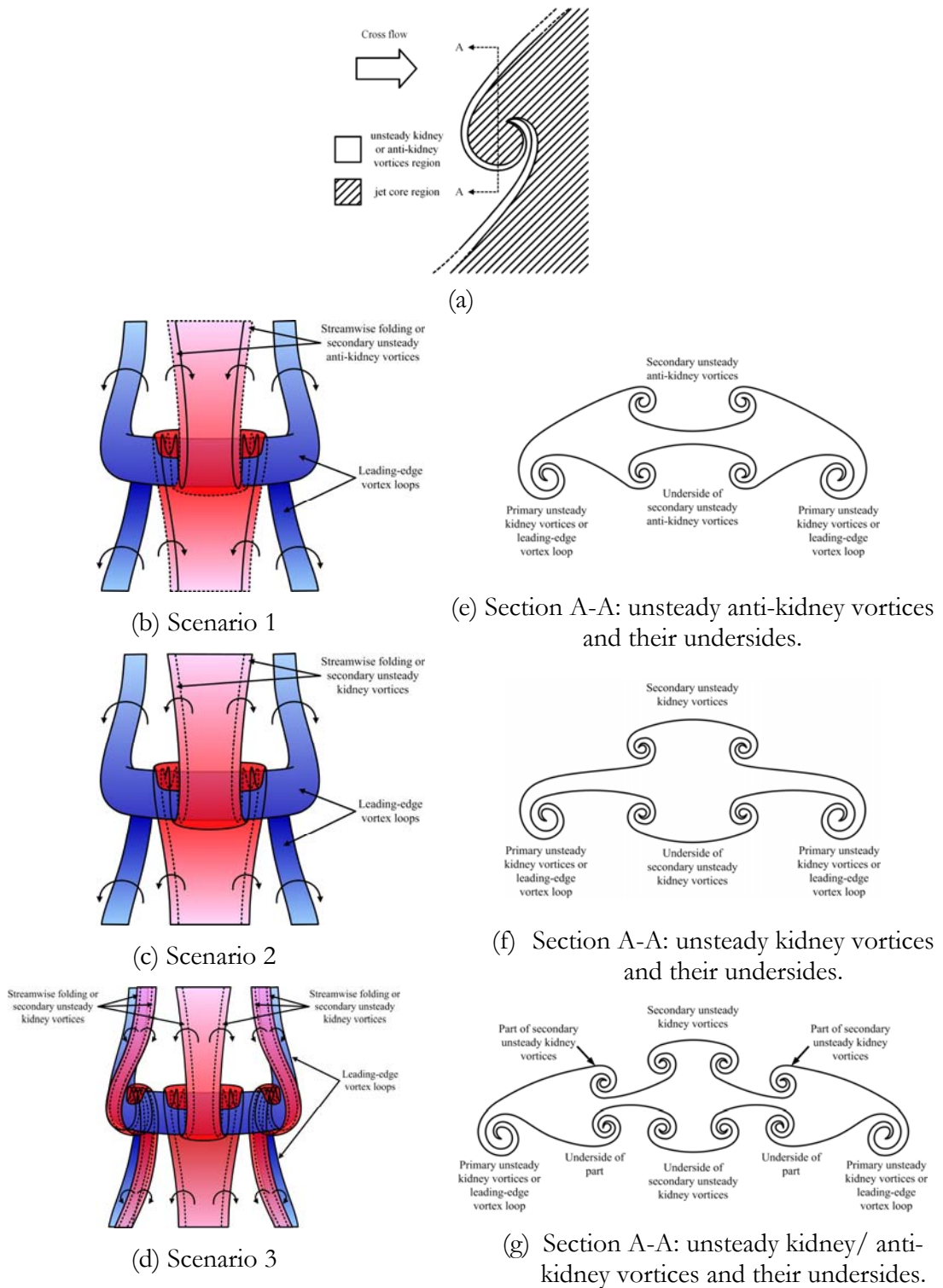
Figure 6.14.   (a) Cross-sectional view of a leading-edge vortex loop dissected by a plane parallel to the cross flow. (b)-(d) enlarged sketches showing typical leading-edge vortices as viewed in the cross flow plane for Scenario 1, Scenario 2 and Scenario 3, respectively. Notice the difference in the sense of rotation of the streamwise folding in Scenario 1 and Scenario 2. (e)-(g) show cross-sectional views of the leading-edge vortex dissected by section A-A indicated in (a). In (g), parts of the two streamwise foldings adjacent to the primary CVP (indicated by A in Figure 6.11) are assumed to have paired up with the CVP.
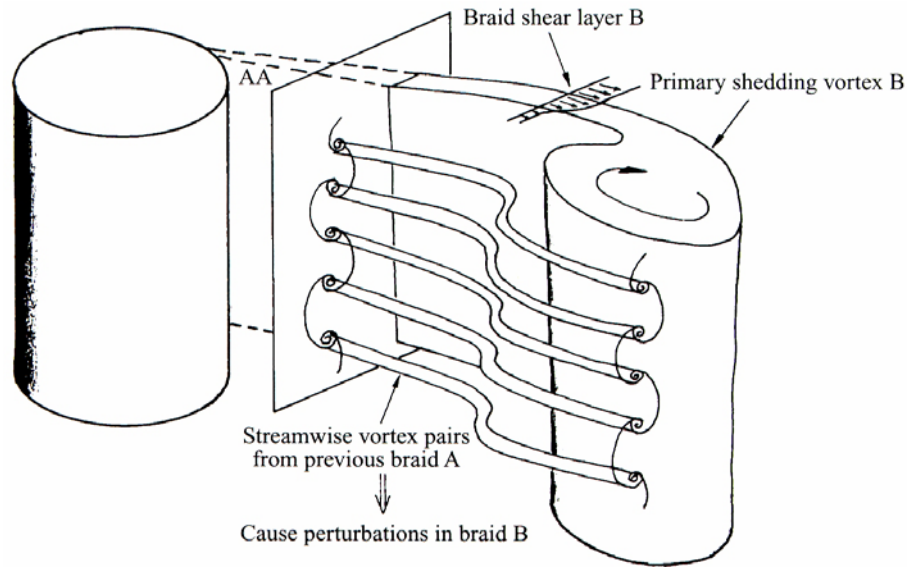
(a)
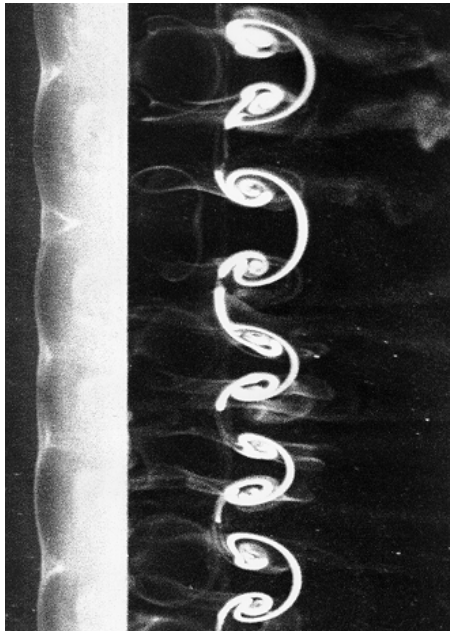
Figure 6.15. (a) Williamson's interpretation of the formation of braided shear layer from a cylinder to produce mode-B streamwise vortices. (b) Cross-sectional view of mode-B streamwise vortices. Note the similarity between the "mushroom-like" structure and the folding on the vortex sheet depicted in Figure 6.11. (Reproduced with permission from Williamson (1996)).

did not observe this feature in their investigation. In Scenario 3, the situation is slightly more complicated because in addition to the one in the centre, there are two more pairs of secondary unsteady kidney vortices, one on each side.

It is worth noting in passing that, apart from the free axisymmetric jet investigated by Liepmann and Gharib (1992) (see Figure 6.12), there is remarkable similarity between the streamwise foldings depicted in Figure 6.14(b)-(d) and the B-mode streamwise vortex

structures behind a circular cylinder in cross flow studied by Williamson (1996) as shown in Figure 6.15. The latter is caused by the shear layer leaving the circular cylinder undergoing span-wise undulation, which culminates in the formation of interconnected CVPs along the span-wise direction. One can envisage that the shear layer from the cylinder is a 2-D counterpart of the cylindrical vortex sheet from an axisymmetric jet. When cut by a laser sheet close to and parallel to the wake centre-plane, these vortex pairs appear as "mushroom-like" pattern as shown in Figure 6.15(b), a pattern similar to that depicted in Figure 6.14(b)-(d). Having said that, one should be aware that the mechanism leading to formation of secondary unsteady vortices in present study may well be different from the formation of "mushroom-like" vortices in cylinder wakes. However, the important outcome of this comparison is that it is possible for a vortex filament with a given orientation to overwhelm and intertwine with another weaker vortex filament that is orthogonal to it.

With the three vortex skeleton models for the three scenarios in place, the next thing to do is to compare them with the experimental results, beginning with AR=3 and then followed by AR=2.

6.3.2 Aspect Ratio of 3 Elliptic Jet in Cross Flow

For this particular AR, the near-field jet structures can take on the appearance of either Scenario 1 or Scenario 2, depending on the VR. When the VR was equal to or less than 2, only Scenario 2 was found to occur and the near-field flow structures were dominated by the primary CVP and secondary unsteady kidney vortices. Above the VR of 2, either Scenario 1 or Scenario 2 could occur, although not at the same time. This suggests that the jet structures can actually switch from one Scenario to another. This also means that while Scenario 1 is topologically possible when the VR is less than 2, no

Figure 6.16. Conjectured time-sequence of the cross-sections of the flow taken at a fixed plane at $x=0.25D_{minor}$ for Scenario 1. Note how the anti-kidney vortices riding on the top of the leading-edge vortex loop as shown in (a) are subsequently lifted off by the vortex loop at a latter time as shown in (c) and (d). This finding is consistent with the observation of Haven and Kurosaka (1997).

convincing evidence was observed in the present study. As to what causes the switch is not clear, although flow unsteadiness cannot be ruled out.

To show that the vortex skeleton models do give a good representation of actual flow structures, conjectured time-sequence of the cross-sectional views of the model for Scenario 1, viewed in the upstream direction (see Figure 6.16), are compared with the corresponding LIF pictures obtained during the experiment (see Figure 6.17) for the jet with the AR of 3 and VR of 4, when Scenario 1 had been observed. It should be noted that when constructing the time-sequence in Figure 6.16, the flow is assumed to move through a vertical plane aligned normal to the cross flow $0.25D_{minor}$ downstream from the jet origin (i.e. $x=0.25D_{minor}$). Moreover, distance is assumed to be time-like, meaning that

(a) t=0.0 sec

(b) t=0.04 sec

(c) t=0.12 sec

(d) t=0.16 sec

Figure 6.17.   A series of LIF images showing the cross-sections of low AR elliptic jet structures (Scenario 1) at x=0.25D$_{minor}$, AR=3 and VR=4. Compare this with the corresponding model in Figure 6.16.

the temporal variation at one location is taken to be the same as the spatial variation at a given instant in time.   For this particular flow, the latter assumption is only an approximate one.   It can be seen from Figure 6.16 and Figure 6.17 that the model agrees reasonably well with the experiment, apart from minor flow asymmetry due probably to flow unsteadiness.   Also, because the jet fluid had been premixed with fluorescent dye before entering the nozzle, details of the roll-up associated with the leading-edge vortex had been obscured and appeared as "blobs" in Figure 6.17(a) and (b).   However, what is more important is that both the model and the experiment clearly show that the secondary unsteady anti-kidney vortices started out first as streamwise folding riding on top of the leading-edge vortex (see Figure 6.16(a)-(b) and 6.17(a)-(b)).   As they traveled

past the visualization plane, the secondary unsteady anti-kidney vortices appeared to be lifted off the main jet body, revealing their underside as is clearly displayed in Figures 6.16(c) and 6.17(c). Moments later, the side arms of the leading-edge vortices disappeared from the laser plane (see Figures 6.16(d) and 6.17(d)), and was followed by the disappearance of the secondary unsteady anti-kidney vortices. The whole process was then repeated.

To further confirm the validity of the above model, cross-sectional views of the jet structures for the AR of 3 in a vertical plane normal to the cross flow are presented in Figure 6.18 for $x=0D_{major}$, $0.25D_{major}$, $0.50D_{major}$ and $0.75D_{major}$ and compared with the corresponding LIF images of the actual flow-field. Again, the agreement is reasonably good, considering the general unsteadiness of the flow. Note that the lee-side vortices depicted in Figure 6.18(a)(iii)-(iv) cannot be detected in the actual flow images in Figure 6.18(b)(iii)-(iv) as the entire jet was premixed with fluorescent dye, causing the lee-side vortices to be indistinguishable from the primary CVP.

For Scenario 2, the sequence of events is similar to Scenario 1 except that now secondary unsteady kidney vortices are formed instead. Figure 6.19 shows the conjectured time-sequence of the cross-section of the jet at $x=0.25D_{minor}$, and Figure 6.20 shows the corresponding LIF images for AR=3 elliptic jet at VR=4, where Scenario 2 is also found. Notice the underside of the secondary unsteady kidney vortices in Figure 6.20(c), which is consistent with Figure 6.19(c) for the model. Again, there is a good agreement between the model and the experiment, except for minor imperfections in the flow structures. Figure 6.21 shows a further comparison of the model for Scenario 2 with the corresponding LIF images at various downstream distances, similar to that shown in Figure 6.18 for Scenario 1. The good agreement between model and the experiment

(i) x=0D$_{minor}$ — (i) x=0D$_{minor}$

(ii) x=0.25D$_{minor}$ — (ii) x=0.25D$_{minor}$

(iii) x=0.50D$_{minor}$ — (iii) x=0.50D$_{minor}$

(iv) x=0.75D$_{minor}$ — (iv) x=0.75D$_{minor}$

(a) Flow model (Scenario 1)   (b) Experimental result

Figure 6.18.   Cross-sections of high AR elliptic jet structures in a vertical plane normal to cross flow at various downstream distances from jet origin. Comparison between the model for Scenario 1 and the experiment (AR=3, VR=4).
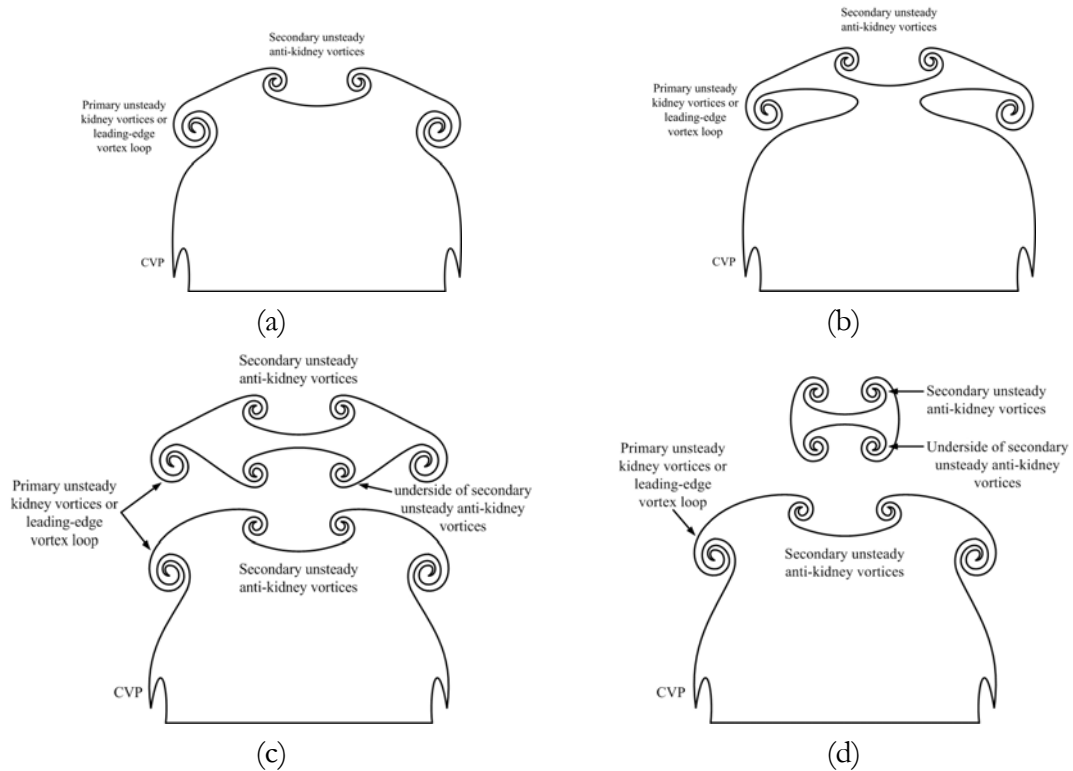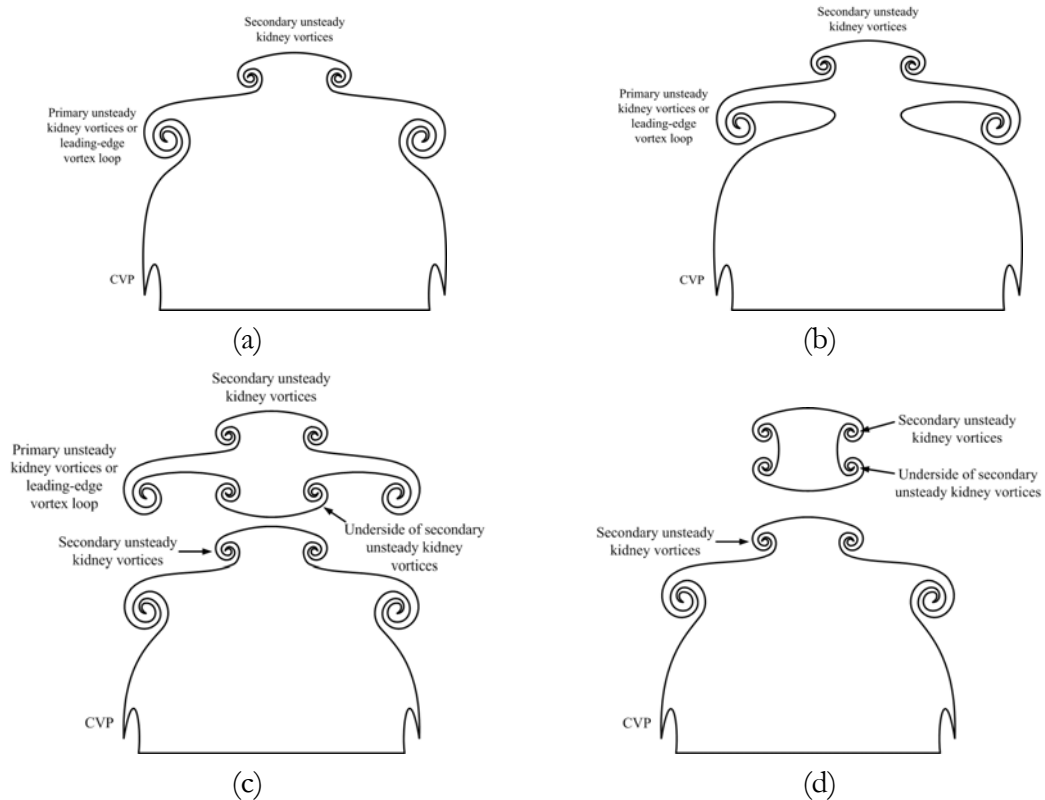
Figure 6.19.   Conjectured time-sequence of the cross-sections of the flow taken at a fixed plane at x=0.25D$_{minor}$ for Scenario 2. Notice how the kidney vortices riding on the top of the leading edge vortex loops are subsequently lifted off by the vortex loops. This scenario was not observed by Haven and Kurosaka (1997).

provides further support to the validity of the model, while noting the resemblance between spatial and temporal variation.

As pointed out earlier, Haven and Kurosaka (1997) have also observed the formation of unsteady kidney and unsteady anti-kidney vortices during their investigation of the non-circular (i.e. rectangle, square and elliptic) jet in cross flow. According to them, these vortices occur on the upper-deck of the so-called "double-decked" jet structures. They referred to the lower deck structure as steady-kidney vortices, which is the manifestation of the primary CVP observed in the present experiment. Although some of present results agree with their experimental observations of the flow structures, the difference lies in the interpretation of how their unsteady kidney and unsteady anti-

(a) t=0.0 sec   (b) t=0.04 sec

(c) t=0.12 sec   (d) t=0.2 sec
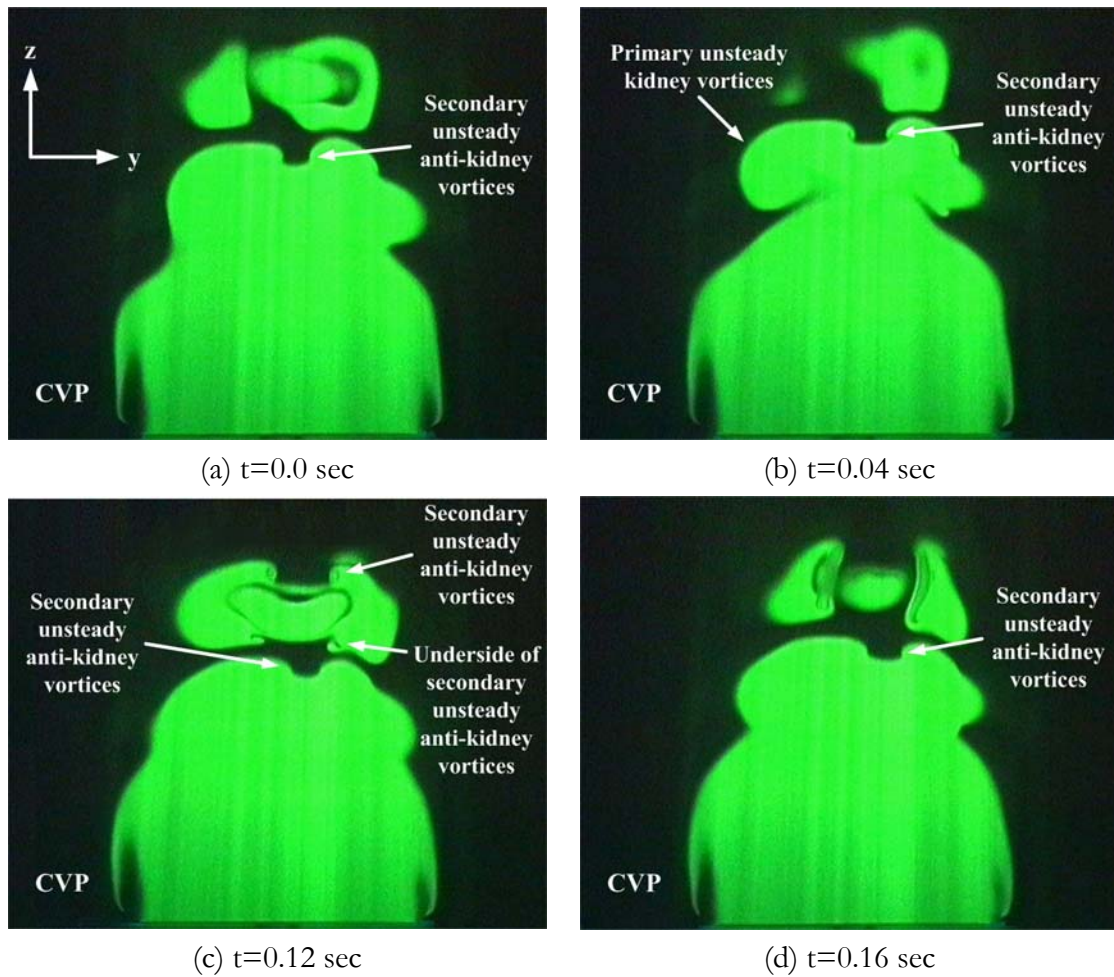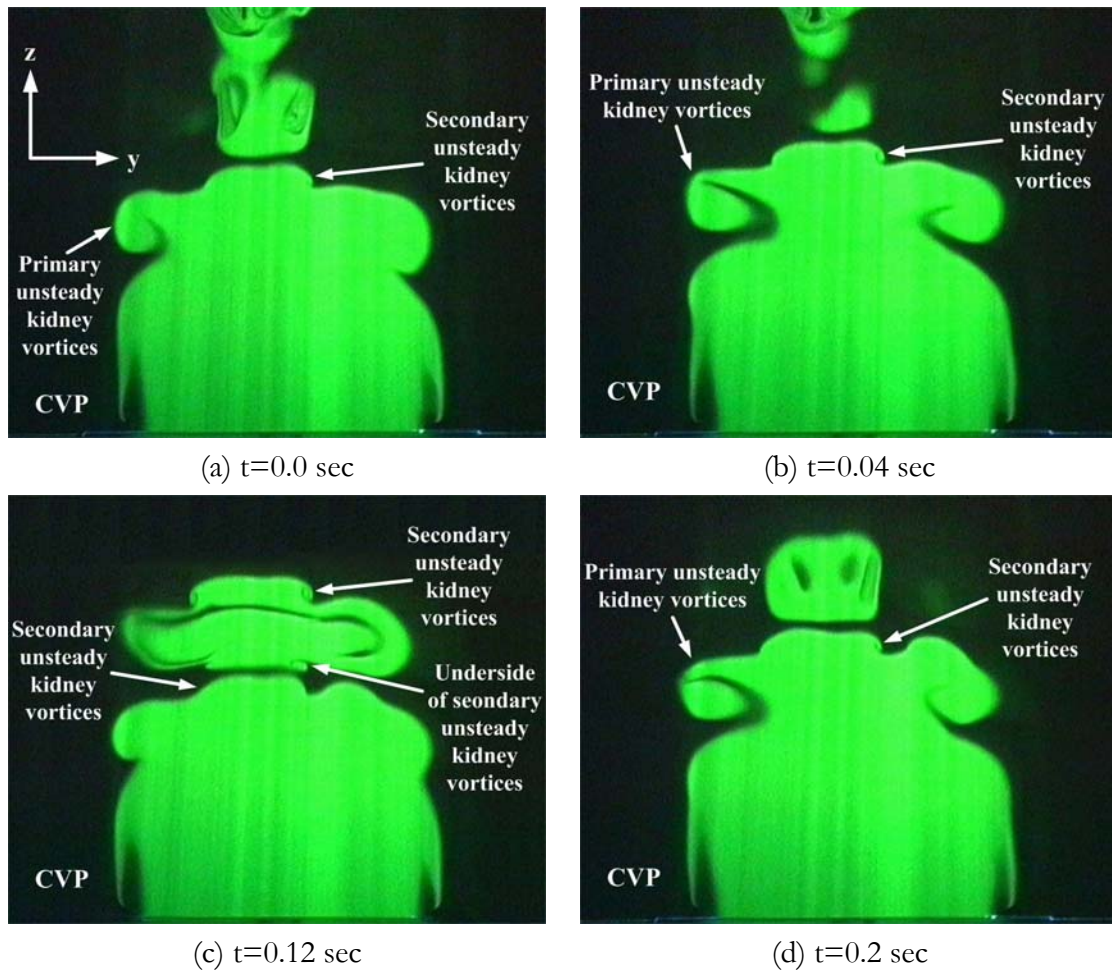
Figure 6.20.   A series of LIF images showing the cross-sections of low AR elliptic jet structures (Scenario 2) at x=0.25D$_{minor}$, AR=3 and VR=4. Compare this with the corresponding model in Figure 6.19.

kidney vortices are formed. They attributed their unsteady kidney vortices as cross-plane manifestation of leading-edge vortices caused by convex warping of the windward side vortex sheet, meaning that the frontal vortex sheet first undergoes convex warping, and then the formation of the leading-edge vortices follows the contour of the warping as can be seen in Figure 6.22(a). What that means is that the leading-edge vortex filaments are highly contorted. As for their unsteady anti-kidney vortices, the formation process is exactly the same except that the frontal vortex sheet first started off with concave warping (see Figure 6.22(b)). Although Haven and Kurosaka's (1997) interpretation of the formation of their unsteady kidney and anti-kidney vortices is topological feasible, it has not been seen in any of the experiments. In fact, it is believed that their unsteady

(i) x=0D$_{minor}$

(i) x=0D$_{minor}$

(ii) x=0.25D$_{minor}$

(ii) x=0.25D$_{minor}$

(iii) x=0.50D$_{minor}$

(iii) x=0.50D$_{minor}$

(iv) x=0.75D$_{minor}$

(iv) x=0.75D$_{minor}$
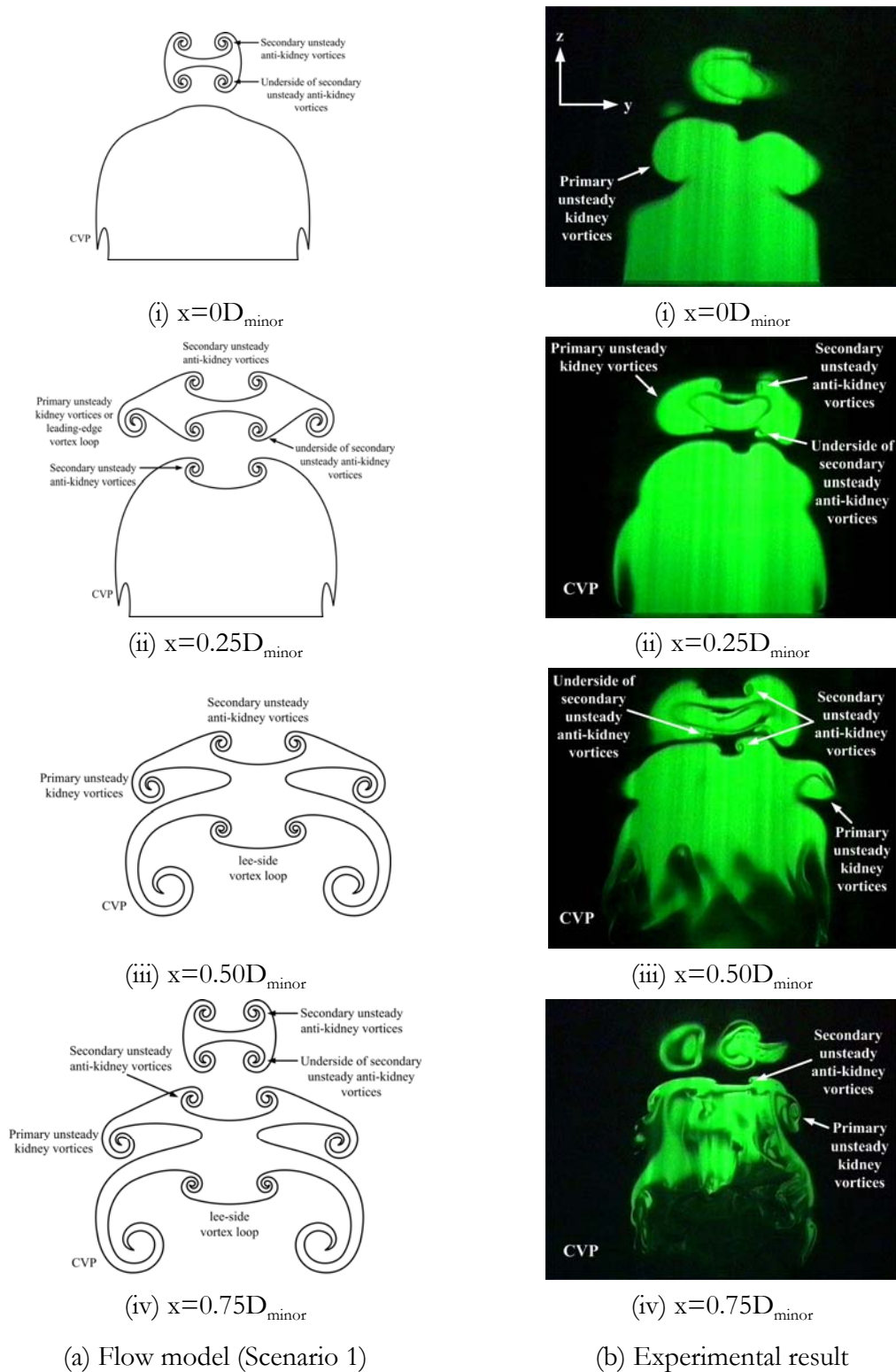
(a) Flow Model (Scenario 2)

(b) Experimental result
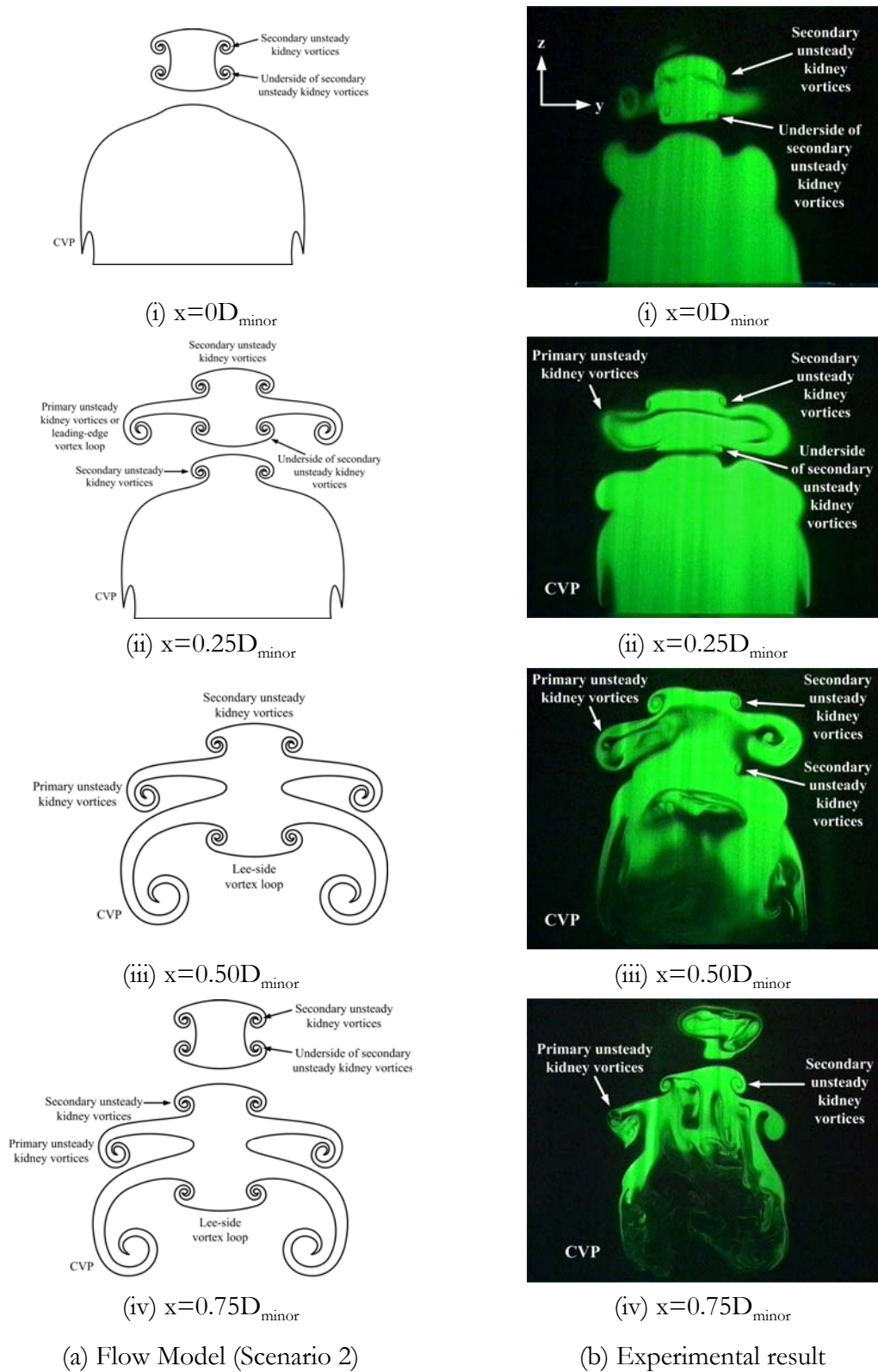
Figure 6.21.   Cross-sections of high AR elliptic jet structures in a vertical plane normal to cross flow at various downstream distances from jet axis. Comparison between the model for Scenario 2 and the experiment (AR=3, VR=4).

(a)   (b)
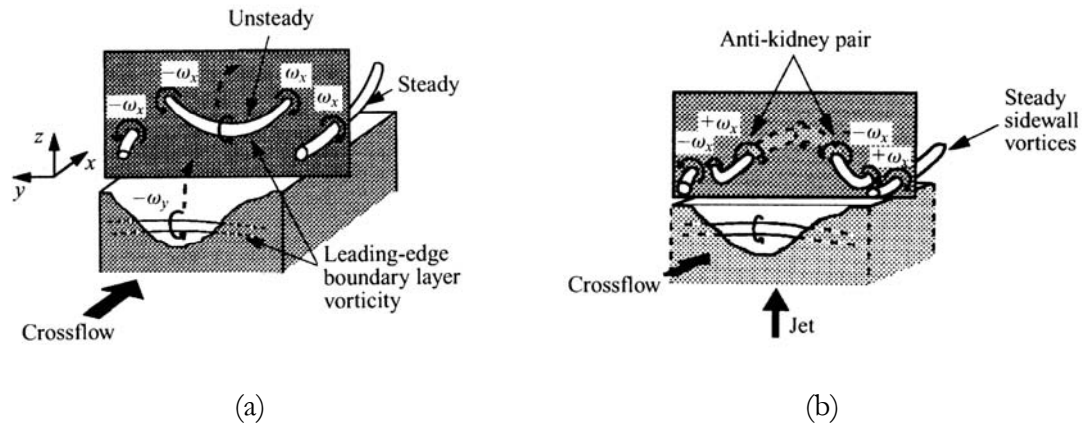
Figure 6.22.   Schematic drawing by Haven and Kurosaka (1997) depicting the formation of (a) unsteady kidney vortices and (b) unsteady anti-kidney vortices. Haven and Kurosaka (1997) interpreted unsteady kidney vortices as cross plane manifestation of leading-edge vortices caused by convex warping of the windward side vortex sheet, and the unsteady kidney vortices are caused by concave warping of the leading-edge vortices. (Reproduced with permission from Haven and Kurosaka (1997)).

kidney and unsteady anti-kidney vortices formed very differently from each other and could not have all originated from the leading-edge vortices. Their side-view photographs for low and high AR EJICF all showed shedding of the leading-edge vortices, therefore cross-plane LIF visualizations of these leading-edge vortices should always yield at least one pair of unsteady kidney vortices. This implies that the source of the unsteady anti-kidney and the second pair of unsteady kidney vortices has to come from elsewhere, which in the present case will be the streamwise foldings discussed previously. This is the reason why the unsteady kidney vortices were further differentiated into primary (resulting from leading-edge vortices) and secondary unsteady (resulting from streamwise foldings) kidney vortices in Table 6.1.

The present results though agree with Haven and Kurosaka (1997) that, regardless of whether the secondary unsteady vortices are kidney or anti-kidney, the frontal vortex sheet must first undergo convex or concave warping or folding, however, the present model differs on the manner in which the vortex sheet subsequently rolls up to form

119

leading-edge vortices. Whether the difference in the observation is due to the low VR used in their experiment (VR=0.4 to 2) remains unclear. In the present case, it is believed that the streamwise foldings are much weaker than the leading-edge vortices, as can be inferred from the manner in which the streamwise foldings are rolled up by the leading-edge vortices (see Figure 6.14(b)-(d)). Unfortunately this could not be shown quantitatively using the PIV system because the presence of a large cross-plane velocity component in the present experiment renders accurate PIV measurements difficult. Nevertheless, the results of Haven and Kurosaka (1997), which were obtained at a lower VR indicates that the strength of the secondary unsteady anti-kidney vortices is significantly lower than that of the primary unsteady kidney vortices, with the maximum value of the former being approximately 40% lower than the latter. This information supports the contention that the secondary unsteady anti-kidney vortices, and for that matter, secondary unsteady kidney vortices, are much weaker than the leading-edge vortices. This information, together with the observation of the underside of the secondary unsteady anti-kidney vortices in Figure 6.17(c), and the secondary unsteady kidney vortices in Figure 6.20(c), suggests that the proposed vortex skeleton models for Scenario 1 and 2 are highly likely.

6.3.3 Aspect Ratio of 2 Elliptic Jet in Cross Flow

When the AR of the nozzle was reduced from 3 to 2, no evidence of Scenario 1 or secondary unsteady anti-kidney vortices was to be found. This is in contrast to the findings of Haven and Kurosaka (1997), which showed the presence of unsteady anti-kidney vortices for the AR=2 elliptic jet, but at a significantly lower VR. When the VR was increased to 3, Scenario 2 was still present, particularly near the centre-axis of the nozzle. But further downstream, the jet shear layer as shown in Scenario 2 undergoes
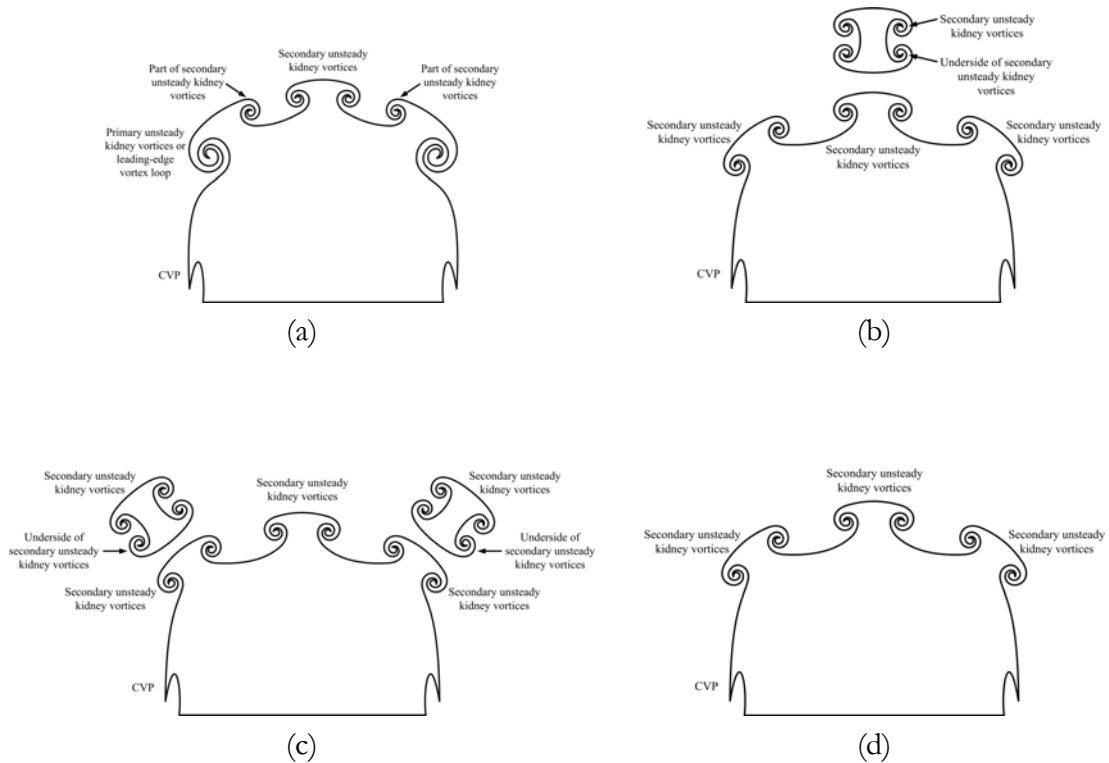
Figure 6.23.   Conjectured time-sequence of the cross-sections of the flow taken at a fixed plane at x=0.25D$_{minor}$ for Scenario 3. Note how the kidney vortices riding on the top of the leading edge vortex loops are subsequently lifted off by the vortex loops.

further instability to produce two additional pairs of streamwise foldings on the windward side of the shear layer. The jet structures formed are referred to as Scenario 3, and this was discussed in some details in the previous section. In fact, it was only through many hours of observation during the experiment that Scenario 3 was conceived. Topologically speaking, Scenario 3 is merely a variation of Scenario 2, with the initiation of the two additional pairs of streamwise folding occurring slightly downstream of the pair in the middle, and this is reflected in Figure 6.13(c). As in Scenario 2, all the three streamwise foldings shed secondary unsteady kidney vortices in the same manner as discussed previously. For reason which is not clear, Haven and Kurosaka (1997) did not see this scenario in their experiment.

(a) t=0.0 sec

(b) t=0.08 sec

(c) t=0.12 sec

(d) t=0.2 sec
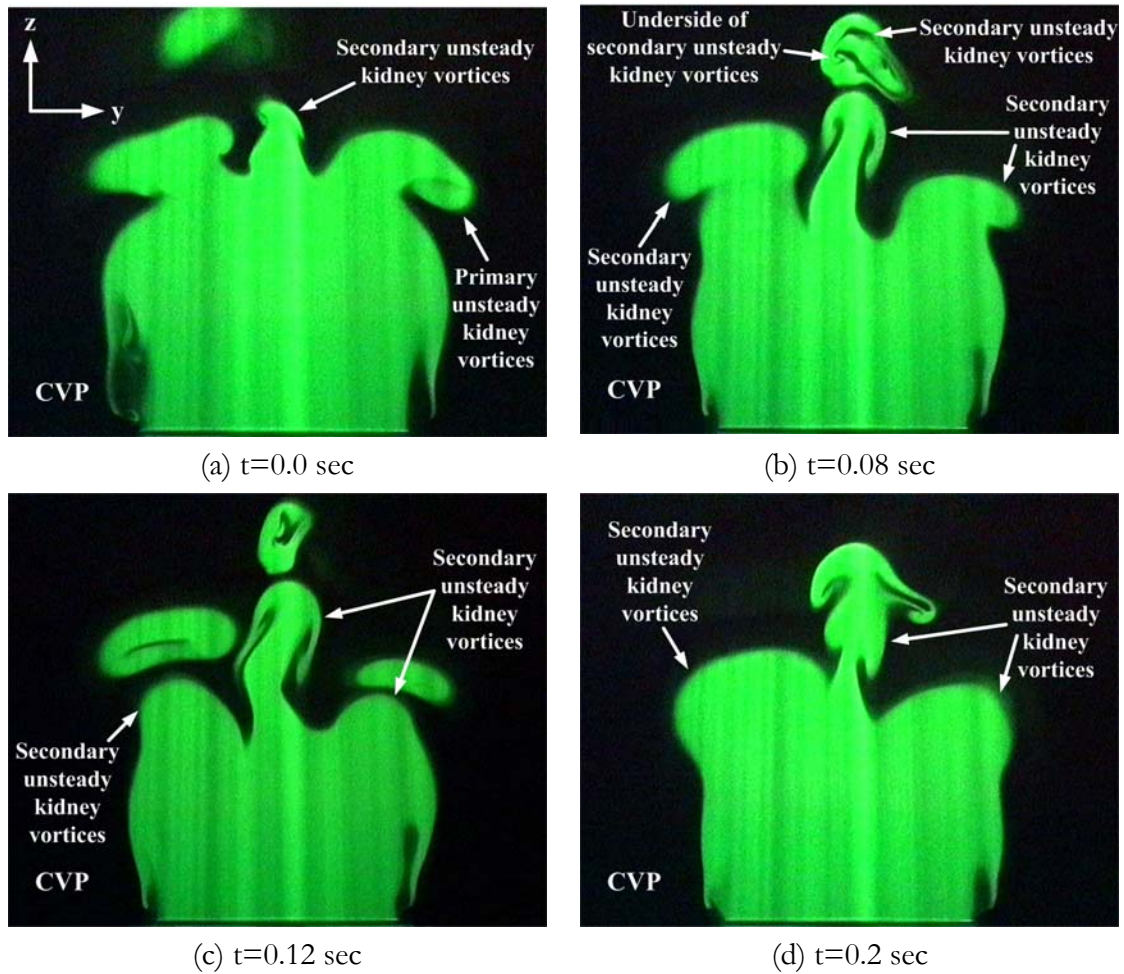
Figure 6.24.   A series of LIF images showing the cross-sections of high AR elliptic jet structures (Scenario 3) at x=0.25D_{minor}, AR=2 and VR=3. Compare this with the corresponding model in Figure 6.23.

To provide further proof of the existence of Scenario 3, cross-sectional views of the vortex skeleton model in a plane normal to the cross flow as viewed in the upstream direction, are presented in Figure 6.23 for various instances in time. Compare this with the corresponding LIF pictures of the flow field in Figure 6.24, it can be seen that there is a good agreement between the model and the corresponding experiment results depicted in Figure 6.24. Minor variations were very likely to be caused by general flow unsteadiness that might have distorted the actual flow field, and could also explain why the corresponding cross-section presented in Figure 6.14(g) could not be located in the experiment. Nevertheless, the fact that the rest of the flow pattern agrees with the model gives confidence that the skeleton model for Scenario 3 is correct. A further

122

(i) x=0D$_{minor}$

(i) x=0D$_{minor}$

(ii) x=0.25D$_{minor}$

(ii) x=0.25D$_{minor}$

(iii) x=0.50D$_{minor}$

(iii) x=0.50D$_{minor}$

(iv) x=0.75D$_{minor}$

(iv) x=0.75D$_{minor}$

(a) Flow model (Scenario 3)

(b) Experimental result
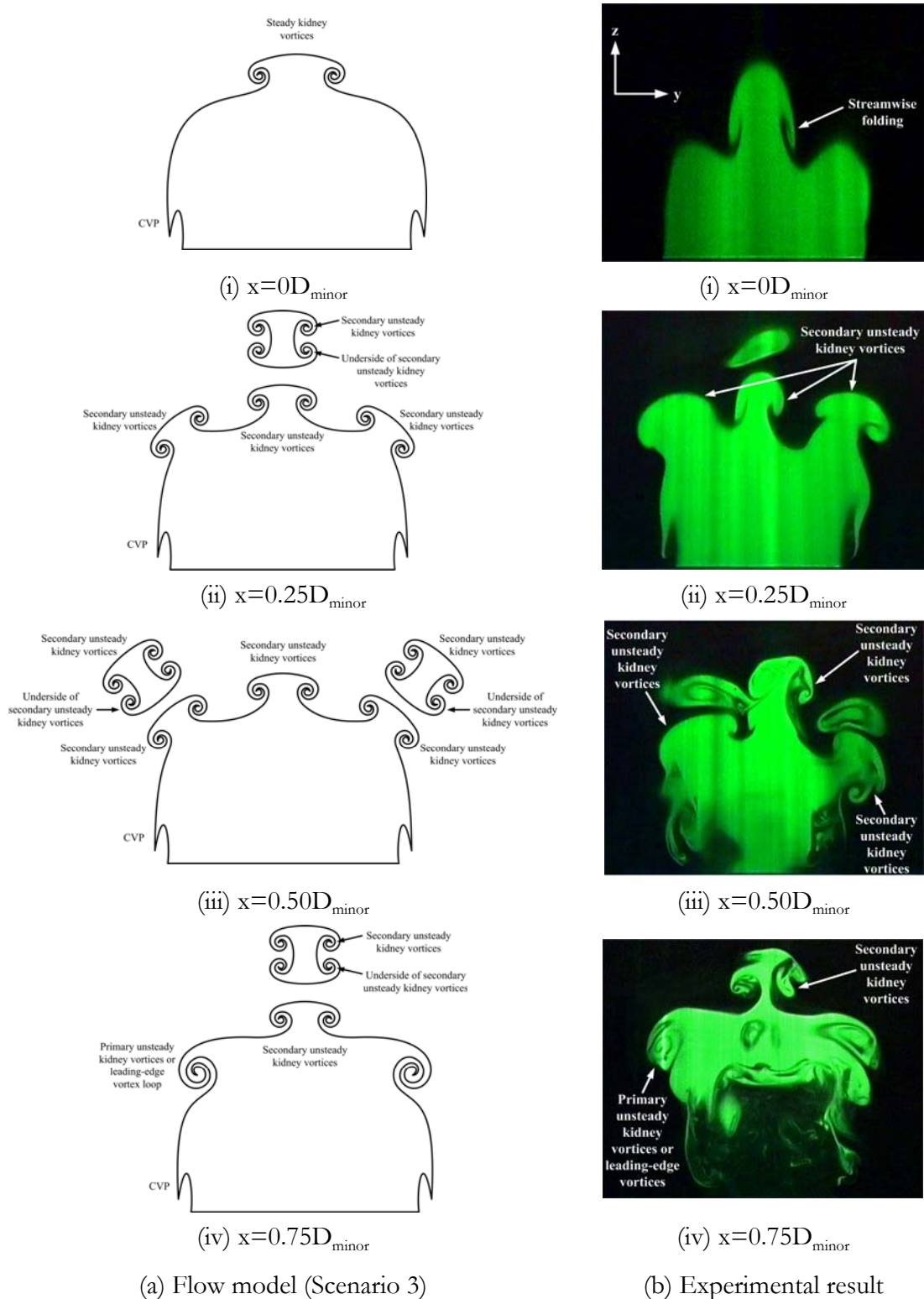
Figure 6.25.   Cross-sections of high AR elliptic jet structures in a vertical plane normal to cross flow at various downstream distances from jet axis. Comparison between the model for Scenario 3 and the experiment (AR=2, VR=3).

AR	VR				
	1	**2**	**3**	**4**	**5**
0.3	Topologically similar to circular jet in a cross flow, except for the presence of a secondary CVP near the jet exit				
0.5					
1.0	Wake-like structures	Circular jet in a cross flow (see model in Lim et. al. (2001))			
2.0	Scenario 2		Scenario 2 and 3		
3.0	Scenario 2		Scenario 1 and 2		

confirmation of the validity of the model for Scenario 3 can be seen in the comparison between the model and the experimental results presented in Figure 6.25 for various downstream distances from the jet origin.

Table 6.2 shows a summary of the possible jet structures, which exist for low and high AR EJICF for the VR from 1 to 5 in the present study.

Chapter 7[†††]

PIV Measurements of Elliptic Jets in Cross Flow

7.1   Introduction

In Chapter 6, we examined the flow structures of an EJICF in two different orientations using flow visualization techniques. Although flow visualization provides useful qualitative information about the flowfield, it does not provide any quantitative data, which may be essential for the better understanding of the characteristics of the flow structures. And this led us to conduct PIV measurements on EJICF, with the aim of obtaining their velocity and vorticity fields. In all cases, measurements were taken along the jet centerlines in the cross flow direction.

7.2   Instantaneous Vorticity Fields

Figures 7.1 to 7.4 show the vorticity plots obtained for both the low and high AR elliptic jets, and Figure 7.5 shows the corresponding vorticity plots for a circular jet. The latter is included for the purpose of comparison. The vorticity measured was the out-of-plane vorticity component and calculated using an analytic differentiation of the relationship

$$X = \frac{\partial v}{\partial x} - \frac{\partial u}{\partial y}$$

It was calculated that the CCD camera has an initial resolution of 0.11mm/pixel, both horizontally and vertically, and covered an effective imaging area of approximately 112.18mm by 112.18mm. The spatial resolution of the final derived velocity was

---

estimated to be 1.81mm. In terms of the jet diameters studied, the resolution represents 0.03D, 0.04D, 0.06D, 0.08D and 0.1D of the axes aligned parallel with the cross flow for AR=0.3, 0.5, 1, 2 and 3 jets respectively.

It is important to note that although the same colour coding is used for the three configurations, the actual magnitude of the vorticity for each colour is different for different configurations. Nevertheless, the dark red colour in all cases corresponds to the maximum positive vorticity (counter-clockwise direction) and the dark blue corresponds to the maximum negative vorticity (clockwise direction). X (s^{-1}) denotes the vorticity contour levels. The orientation of the jets with respect to the cross flow is clearly indicated in each figure, and the horizontal and vertical distances have been normalized by the length of the streamwise jet axis, namely D_{major} for the low aspect ratio jet and D_{minor} for the high aspect ratio jet.

Broadly speaking, an increase in the velocity ratio leads to an increase in the strength of the leading-edge vortices, and in the penetration height of the jet, irrespective of the aspect ratio. These characteristics are similar to that of CJICF. The similarities, however, end there, and the next section discusses the differences between the low and high aspect ratio jets, and how they differ from the CJICF.

7.2.1 Low Aspect Ratio Elliptic Jets in Cross Flow

The vorticity plots for this configuration are presented in Figures 7.1 and 7.2. Here, it can be seen that at low velocity ratios, the leading-edge region remains either as a continuous shear layer (at VR=1) or rolled-up as individual concentrated vortices (at VR=2). As for the lee-side vortices, the vortex shedding is initiated much earlier at VR=1 (see Figures 7.1(a) and 7.2(a)), and their peak vorticities either matches or surpasses that

(a) VR=1

(b) VR=2

(c) VR=3

(d) VR=4

(e) VR=5
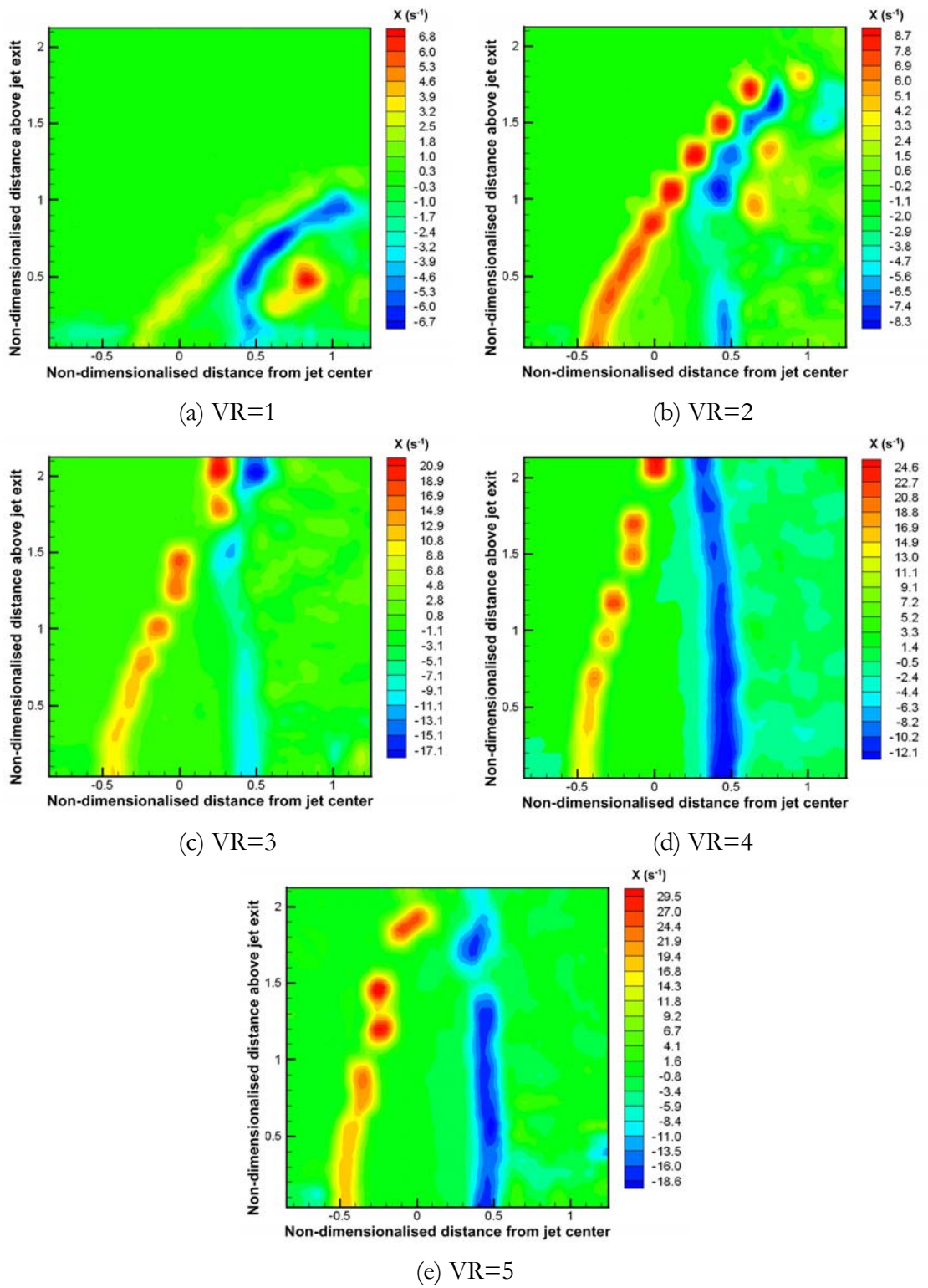
Figure 7.1.   Instantaneous vorticity plots for AR=0.3 EJICF along streamwise jet centerline from VR=1 to 5.

(a) VR=1   (b) VR=2

(c) VR=3   (d) VR=4

(e) VR=5
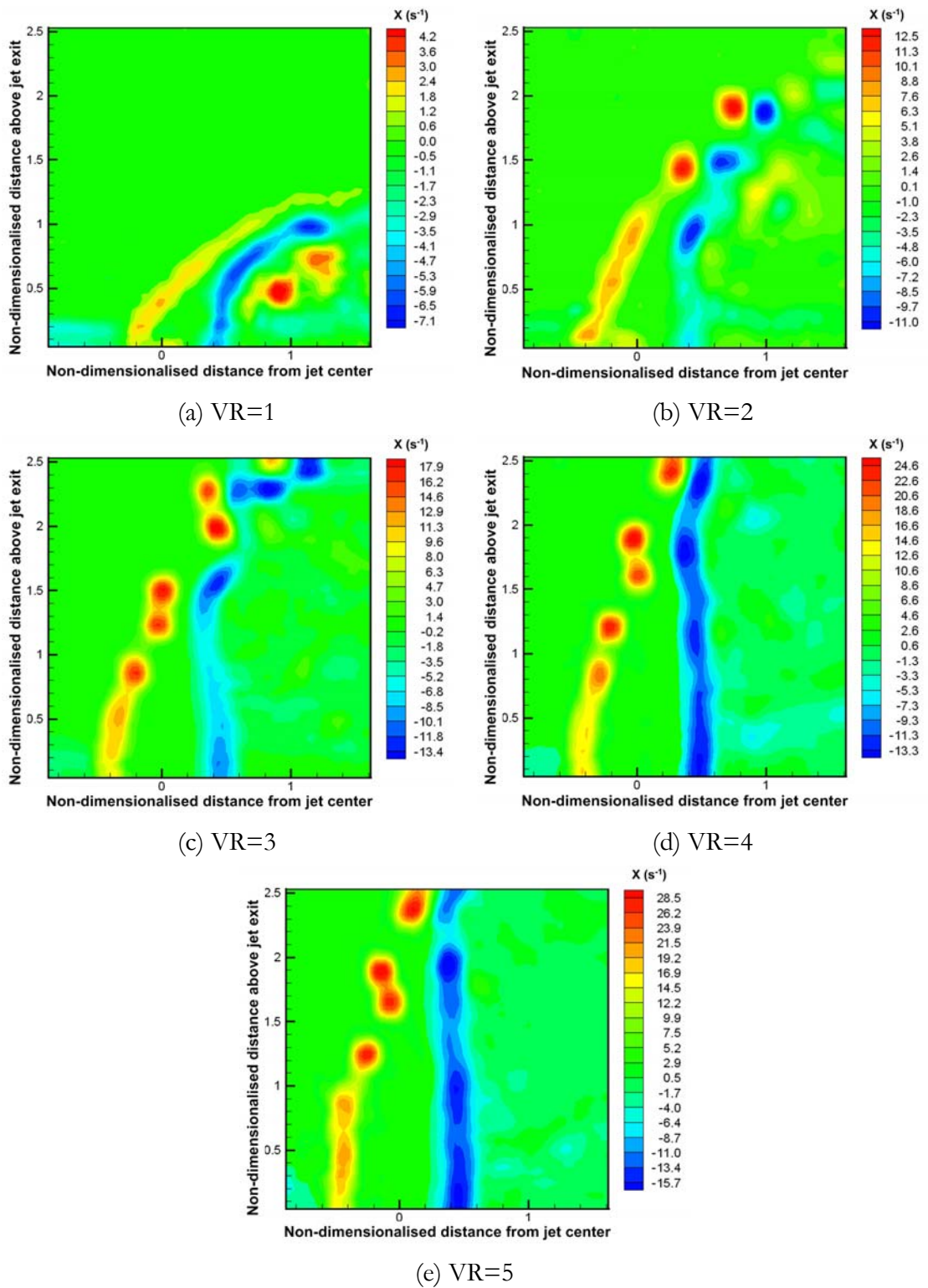
Figure 7.2.   Instantaneous vorticity plots for AR=0.5 EJICF along streamwise jet centerline from VR=1 to 5.

of the leading-edge vorticity. For example, the leading-edge and lee-side peak vorticity at VR=1 and VR=2 for the AR=0.3 jet are approximately ($+6.8s^{-1}$, $-6.7s^{-1}$) and ($+8.7s^{-1}$, $-8.3s^{-1}$), respectively, and their counterparts for the AR=0.5 jet are approximately ($+4.2s^{-1}$, $-7.1s^{-1}$) and ($+12.5s^{-1}$, $-11.0s^{-1}$), respectively. The reference CJICF follows a similar trend (see Figure 7.5) up to VR=3, with the leading-edge and lee-side peak vorticity measured approximately ($+3.4s^{-1}$, $-6.9s^{-1}$), ($+14.7s^{-1}$, $-12.9s^{-1}$) and ($+18.7s^{-1}$, $-17.5s^{-1}$) at VR=1, 2 and 3 respectively. On close examination of the results in Figures 7.1(a) and 7.2(a) for VR=1, it can be seen that there is a region of high positive vorticity immediately downstream of jet, which disappears when the velocity ratio is increased. This "patch" of vorticity can be traced to the downstream jet structures, which happened to be in the measurement window, as a result of a lower jet trajectory when the velocity ratio is low.

With the initiation of the vortex-pairing phenomenon from VR=3 to 5, the leading-edge peak vorticity increases sharply. For instance, the leading-edge and lee-side peak vorticity for AR=0.3 jet at VR=3, 4 and 5 are approximately ($+20.9s^{-1}$, $-17.1s^{-1}$), ($+24.6s^{-1}$, $-12.1s^{-1}$) and ($+29.5s^{-1}$, $-18.6s^{-1}$), respectively. However, no corresponding increase in the peak vorticity is found in the lee-side of the jet, due of the absence of the vortex-pairing there. Also, for a fixed velocity ratio, it is found that both AR=0.3 and AR=0.5 jets display comparable peak vorticities, a finding which is not unexpected since both the jets have the same exit area.

7.2.2 High Aspect Ratio Elliptic Jets in Cross Flow

For the high AR jets, the vorticity plots are shown in Figures 7.3 and 7.4. Unlike the low aspect ratio jet discussed above, the leading-edge vortices remain distinct, and the absence of vortex-pairing is reflected in the absence of a sudden jump in the peak vorticity between VR=3 to 5. Instead, both the leading-edge and lee-side vorticity

(a) VR=1

(b) VR=2

(c) VR=3

(d) VR=4

(e) VR=5
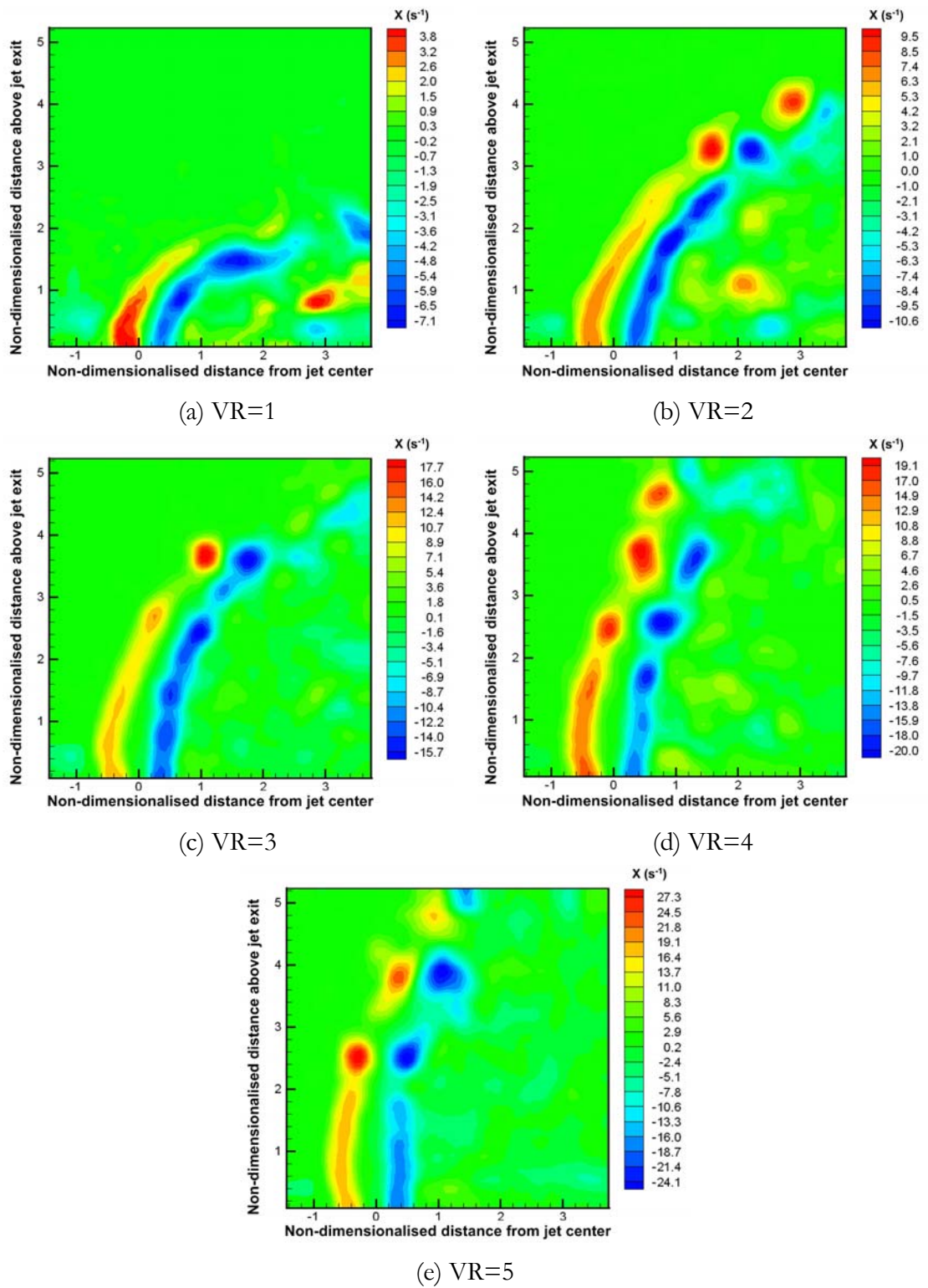
Figure 7.3.   Instantaneous vorticity plots for AR=2 EJICF along streamwise jet centerline from VR=1 to 5.

(a) VR=1

(b) VR=2

(c) VR=3

(d) VR=4

(e) VR=5
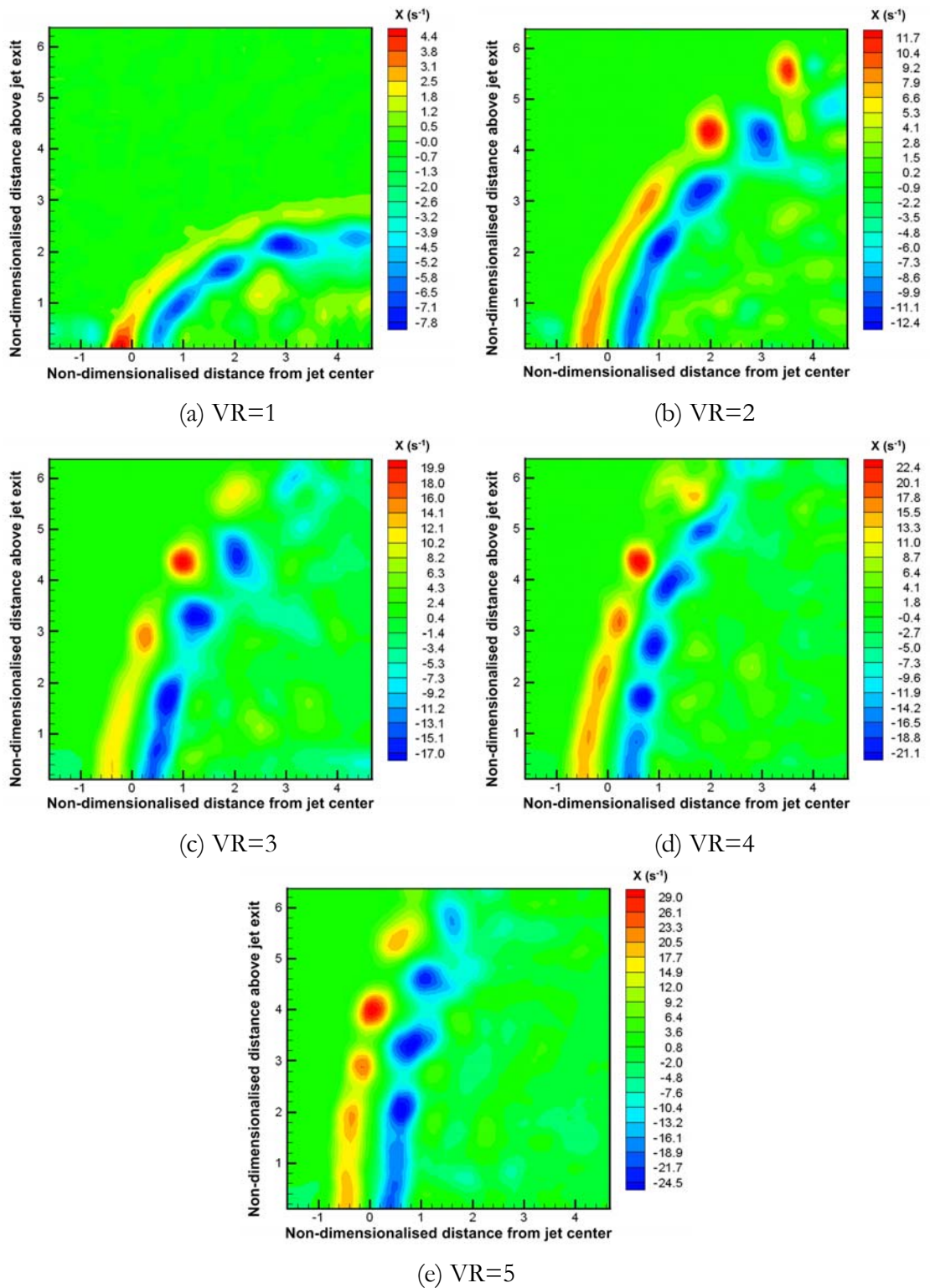
Figure 7.4.   Instantaneous vorticity plots for AR=3 EJICF along streamwise jet centerline from VR=1 to 5.

(a) VR=1   (b) VR=2

(c) VR=3   (d) VR=4

(e) VR=5
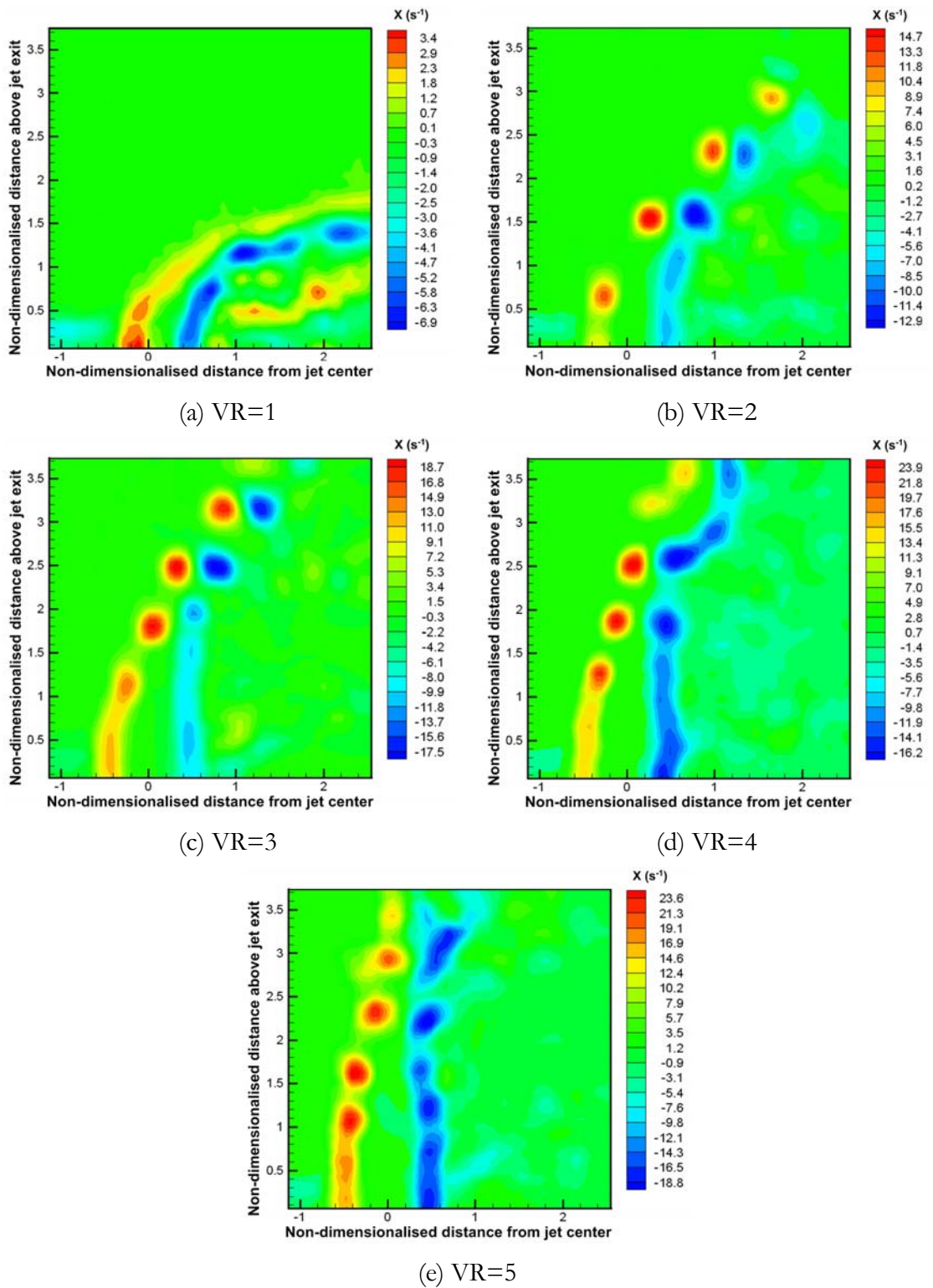
Figure 7.5.   Instantaneous vorticity plots for comparing CJICF along streamwise jet centerline from VR=1 to 5.

increase monotonically with the velocity ratio, a behavior which is similar to CJICF. Similar to the low aspect ratio jets, there is also a region of high positive vorticity downstream of the jet when VR=1.

Interestingly, for a fixed velocity ratio, the peak vorticity of the high aspect ratio jets appears to depend on the aspect ratio. This is in contrast to the low aspect ratio jets, where the peak vorticity is found to be independent of the aspect ratio. As Figures 7.3 and 7.4 clearly show, the AR=2 jet consistently registers lower leading-edge peak vorticity than the AR=3 jet, except when VR=4, where flow unsteadiness may have caused some aberration in the results. For example, when velocity ratio increases from 1 to 5, the peak vorticity for the AR=2 jet are $+3.8s^{-1}$, $+9.5s^{-1}$, $+17.7s^{-1}$, $+19.1s^{-1}$ and $27.3s^{-1}$, as compared to $+4.4s^{-1}$, $+11.7s^{-1}$, $+19.9s^{-1}$, $+22.4s^{-1}$ and $+29.0s^{-1}$ respectively for the AR=3 jet. The dissimilarity in the peak vorticity for high aspect ratio jets at a given velocity ratio, could be due to the difference in the momentum thickness/velocity profile of the high aspect ratio jets facing the incoming cross flow. Furthermore, it has been shown that for high aspect ratio jets, it is possible for the windward side shear layer to undergo streamwise folding(s), which is not found in the low aspect ratio jet. This may also alter the peak vorticity levels of the leading-edge vortices.

Another obvious feature of the low AR jets is the pairing of the leading-edge vortices which was discussed in Chapter 6. However, unlike the flow visualization images, these vorticity plots are able to show the complete interaction process leading to the coalescence of the leading-edge vortices. A time-sequence of PIV vorticity plots in Figure 7.6 illustrates this very clearly. Here, it can be seen that there is a substantial increase in the vorticity after the vortices have paired up. However, further downstream, the vorticity decreases presumably due to viscous diffusion. Consistent with the flow

(a) t=0.0 sec   (b) t=0.1 sec

(c) t=0.2 sec   (d) t=0.3 sec

(e) t=0.4 sec   (f) t=0.5 sec

Figure 7.6.   A time-sequenced series of instantaneous PIV vorticity plots depicting the pairing process of the leading-edge vortices. (AR=0.5, VR=4)

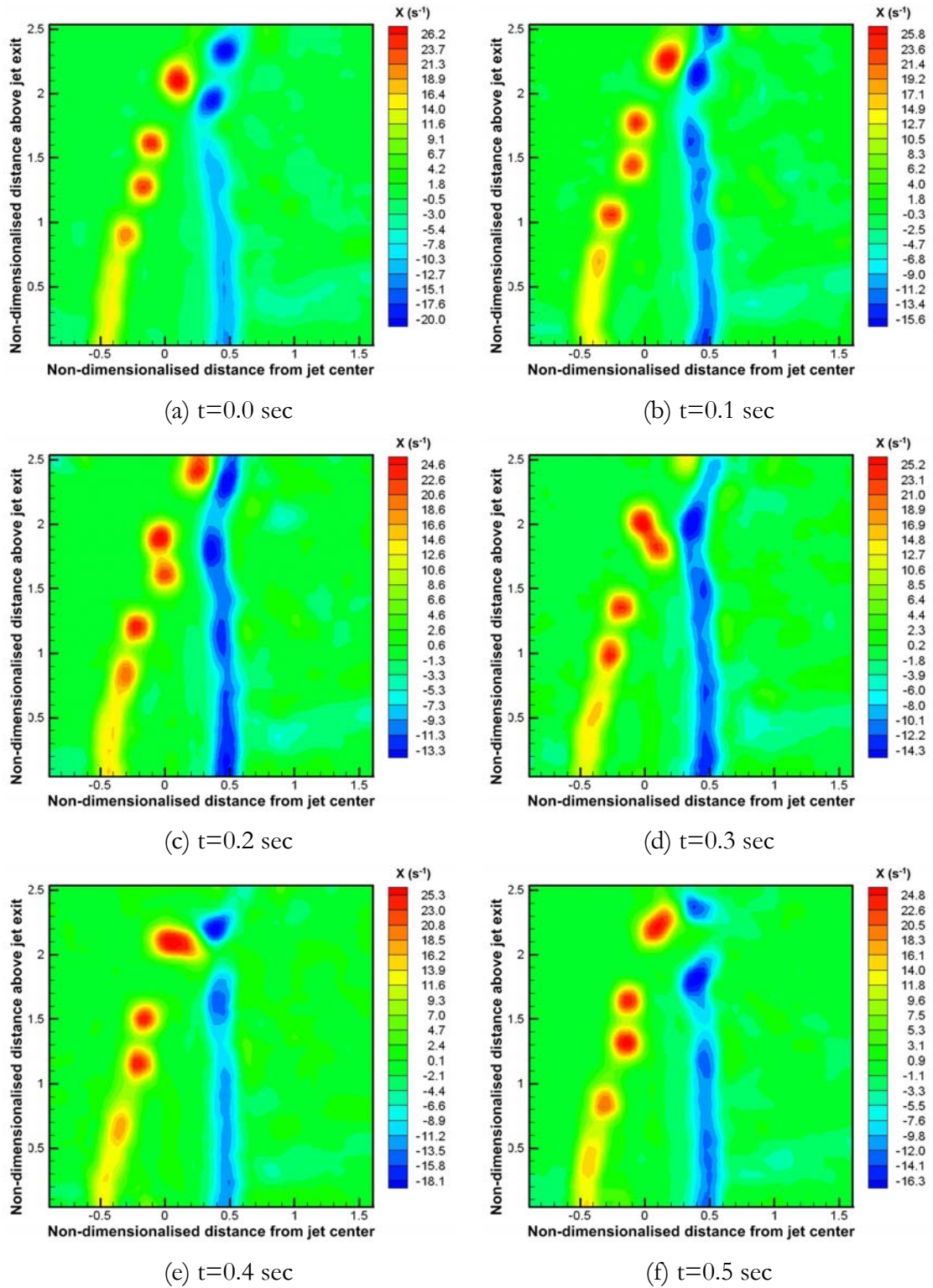visualization results discussed earlier, no such pairing was demonstrated by the lee-side vortices for both the low and high AR jets.

7.3   Instantaneous Velocity Fields

The instantaneous velocity and streamline plots corresponding to the vorticity plots shown in Figures 7.1 to 7.5 are displayed in Figures 7.7 to 7.11. With the streamline plots, one could clearly see the interaction between the cross flow and the jets, especially in terms of local entrainment process. However, when comparing velocity plots with the vorticity plots, one should be aware that the topological structures of the velocity plots are dependent on the velocity of the observer while vorticity plots are not. To correctly observe the flow pattern, one should move with the convection velocity of the vortices. In the case of JICF, because the convection velocity of the leading edge vortices changes with downstream distance, it is therefore not possible to obtain a "correct" instantaneous "global" picture of the velocity field. In view of this, it was decided that the velocity fields are plotted relative to a laboratory frame of reference, and these results should be viewed together with the corresponding vorticity plots. It is also worth noting that the absence of the critical points, foci in the streamline plots does not mean that there is an absence of vortices in the flow as the vorticity plots have shown. As noted above, these vortices can be seen only when one moves with their convection velocities. Back to the streamline plots, it is of interest to note that wherever there were leading-edge vortices forming along the leading-edge regions of the jets, there existed regions of local entrainment of the cross flow fluid into the jet core. This suggests that one of the main mechanisms for cross flow fluid entrainment in the near-field relies heavily on the generation of the leading-edge vortices. Also, it is clear that with each pairing of the leading-edge vortices, local entrainment of the cross flow fluid into the jet core became significantly higher than when there was no pairing. This is not too surprising since the combined induced velocity of the paired up vortex is significantly higher.

In some instances, the streamline plots seemed to show a higher occurrence of

(a) VR=1   (b) VR=2

(c) VR=3   (d) VR=4

(e) VR=5

Figure 7.7.   Instantaneous velocity vector and streamline plots for AR=0.3 EJICF along streamwise jet centerline from VR=1 to 5.

(a) VR=1

(b) VR=2

(c) VR=3

(d) VR=4

(e) VR=5

Figure 7.8.   Instantaneous velocity vector and streamline plots for AR=0.5 EJICF along streamwise jet centerline from VR=1 to 5.

(a) VR=1

(b) VR=2

(c) VR=3

(d) VR=4

(e) VR=5

Figure 7.9. Instantaneous velocity vector and streamline plots for AR=2 EJICF along streamwise jet centerline from VR=1 to 5.

(a) VR=1

(b) VR=2

(c) VR=3

(d) VR=4

(e) VR=5

Figure 7.10.   Instantaneous velocity vector and streamline plots for AR=3 EJICF along streamwise jet centerline from VR=1 to 5.

(a) VR=1

(b) VR=2

(c) VR=3

(d) VR=4

(e) VR=5
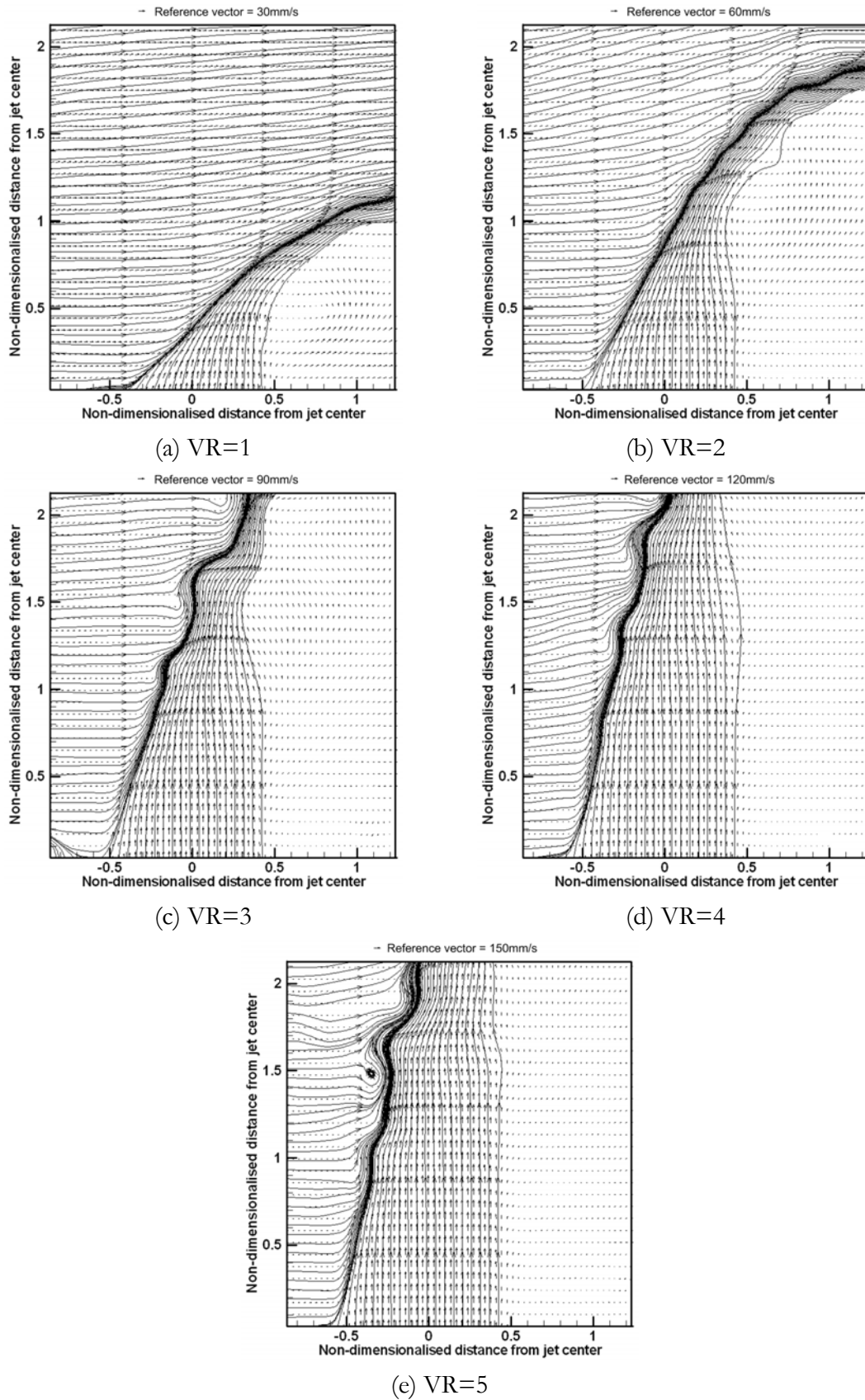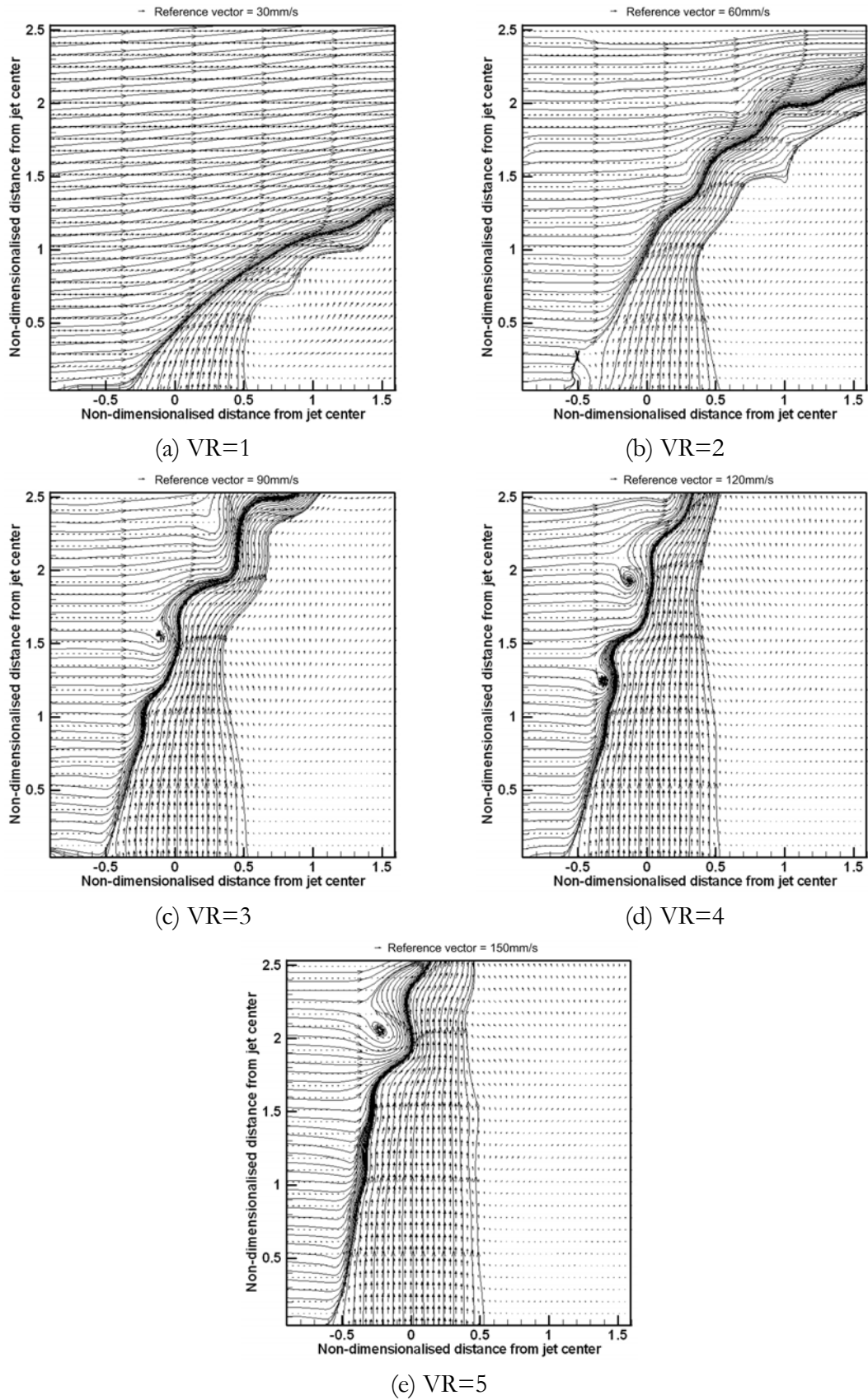
Figure 7.11.   Instantaneous velocity vector and streamline plots for comparing CJICF along streamwise jet centerline from VR=1 to 5.
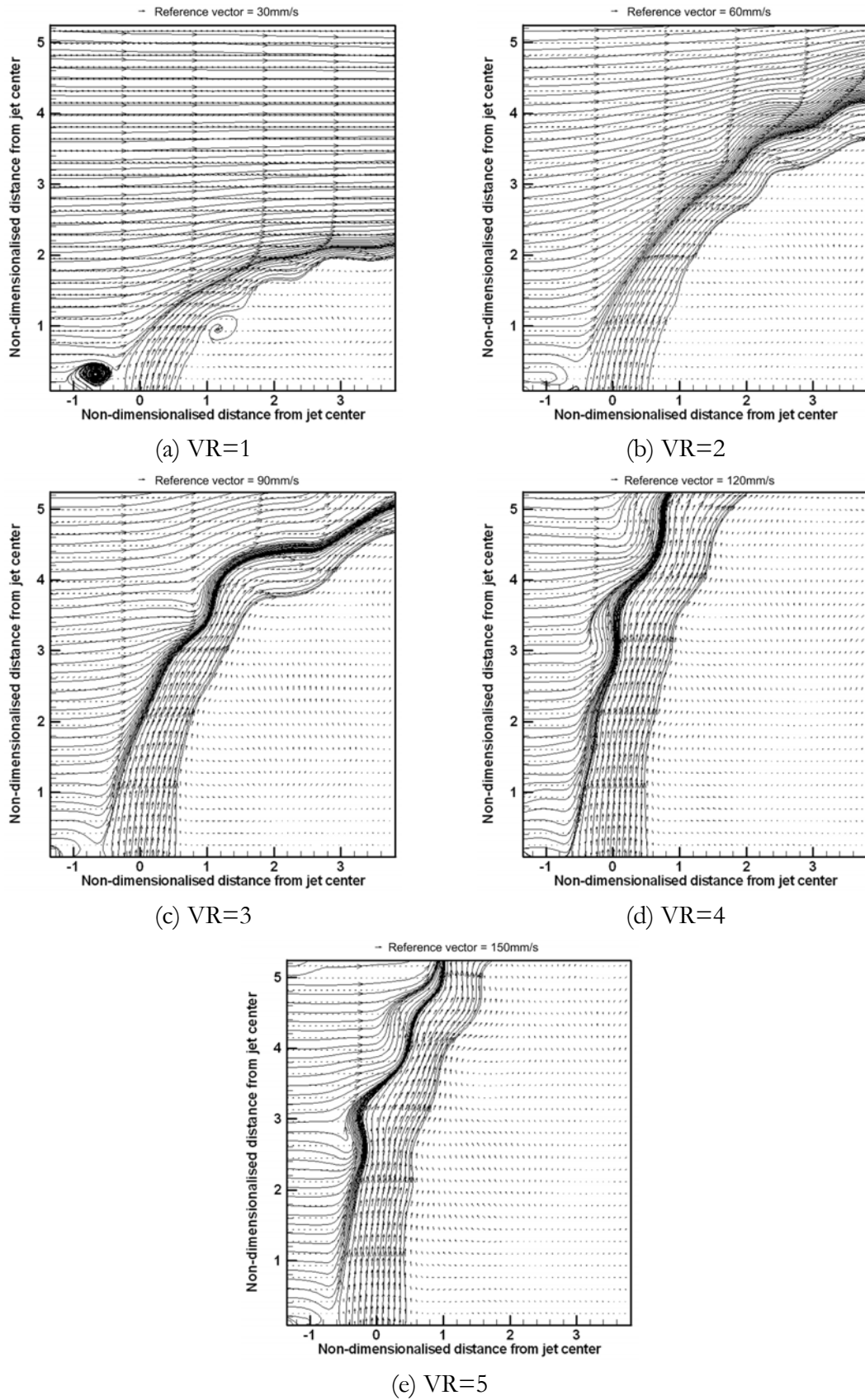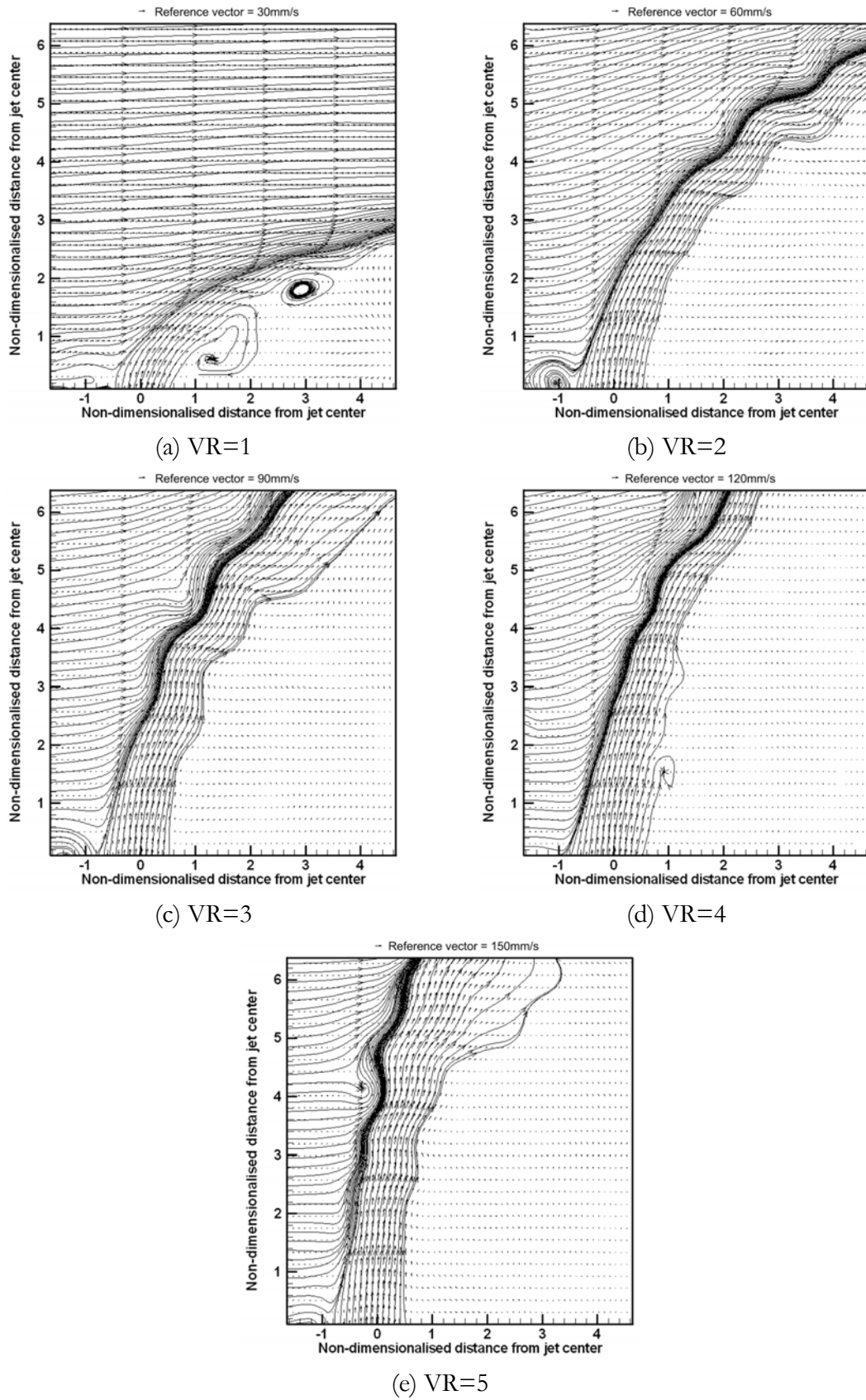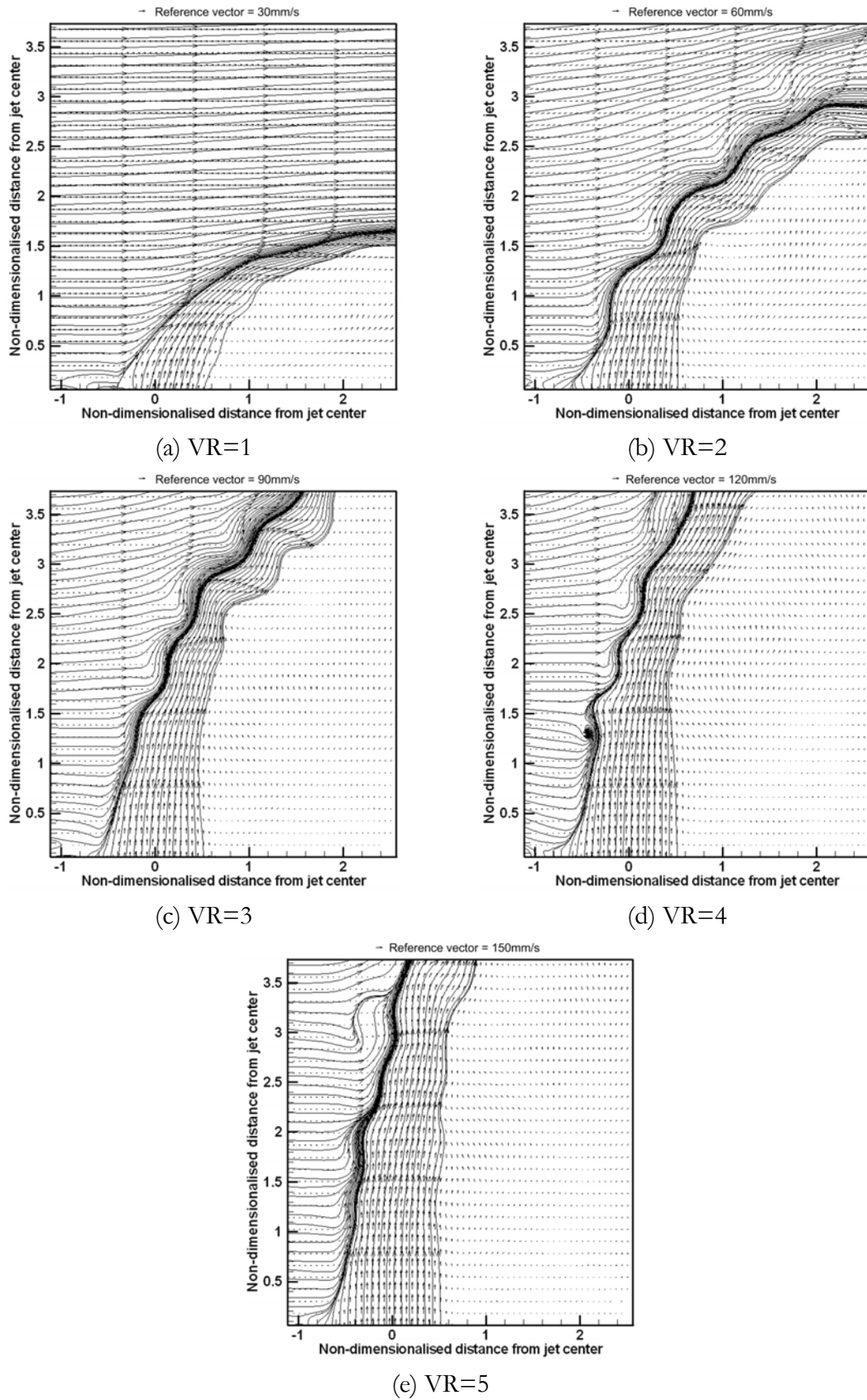
the horseshoe vortices upstream of the high AR and circular jets (see Figures 7.9 to 7.11) than for corresponding low AR jets, even though their locations and strengths might differ. However, it has to be noted here that the plots are instantaneous in nature and moreover, the spatial resolution of the PIV results does influence to a certain extent the observation of these horseshoe vortices, especially when the latter are physically smaller. But this observation is intuitively expected since the high AR and circular jets form a larger "blockage" to the cross flow than corresponding low AR jets. Hence, it is not surprising that little or no sign of these horseshoe vortices was observed for the low AR jets. There are two possible explanations for the above observations: Firstly, due to the high curvature at the leading edge of the low AR jets, any horseshoe vortex forming upstream of them are likely to be highly stretched by the cross flow accelerating around the jet. The end result is a considerable reduction in the core size of the horseshoe vortex, making it less detectable. Secondly, the highly stretched vortex filament is also likely to lead to higher viscous diffusion and may have further contributed to its demise.

Other than depicting the interaction between the cross flow and leading edge of the jets, the streamline plots also revealed some interesting features about the lee-side region. They consistently hinted a near-wall vortex behind the jet which can be safely assumed to be a result of the closing-in of the cross flow at the lee-side region. It is very likely that this vortex is the manifestation of the near-wall secondary CVP upon the 2D PIV imaging plane. Perhaps due to the more streamlined nature of the jet geometry with respect to the cross flow, the closing-in of the cross flow for low AR jets takes place almost immediately behind the jets and in a more orderly manner. This can be seen from the streamline plots where the lee-side regions did not seem to be considerably disturbed. In contrast, the closing-in of the cross flow seems to take place further behind away from the jet body for high AR jets and from the streamline plots, appears to cause considerable

flow disturbances along the way. This observation suggests that the formation of the CVP for low AR jets is likely to be more organized and perhaps more stable compared with the high AR jets. This will be taken up again in the discussion with ensemble-averaged results.

7.4 Time-Averaged Velocity and Vorticity Fields

The availability of PIV data provides a unique opportunity to study both instantaneous and time-averaged velocity field data. While typical sampling rate of PIV technique is considered low compared to hot-wire measurements, at least PIV allows a much larger sampling area to be analyzed at any one time, and this motivated the author to carry out the present analysis. Moreover, if sufficient measurements were taken, the flow field information will be accurate enough for comparison.

It should pointed out that acquisition of mean velocity field data for a JICF is not new, as is evident in numerous papers published in the literature. However, much of the attentions were concentrated on mean deflected jet trajectories, downstream centerline velocity profiles and the growth of the main CVP. Andreopoulos and Rodi (1982) were one of the earliest researchers to successfully utilise a three-sensor hot-wire probe to obtain three-dimensional mean-velocity components, turbulent kinetic energy and turbulent shear stresses for a circular JICF. Their results showed very clearly the various flow structures associated with a JICF. Most noticeably was the detection of a near-wall jet phenomenon beneath the main CVP. The wall jet phenomenon was later identified as a weaker near-wall secondary CVP having a sense of rotation opposite to the main CVP. The above investigation shows the usefulness of mean velocity field information. Therefore, the author decided to carry out a similar analysis to obtain the average velocity field. No attempt was made to obtain turbulent kinetic energy and turbulent shear stresses because the number of PIV images available is not sufficient to provide adequate

accuracy to these quantities to be useful. To achieve the same degree of accuracy as provided by hot-wire anemometry, tens of thousand of PIV images are required. Also, in view of the large amount of data needed to obtain average velocity field, the present analysis was restricted to the AR=2 elliptic jet for both orientations (ie. AR=0.5 and 2). The primary purpose is to compare the effects of the orientation of the elliptic jet on the flow field.

A total of 1000 image pairs were used to obtain 1000 sets of velocity fields which were then time-averaged using a self-written program to obtain average u and v velocity components, as well as the average magnitudes for all points spaced at 2.7mm or $0.095D_h$ apart. The average velocity magnitude fields are analogous to using a normal single hot-wire probe with no differentiation in the direction of flow, while the separation of u and v velocity components resemble the usage of cross-wire probe. The latter case would prove to be useful if detection of certain flow structures were to be carried out.

7.4.1 Velocity and Vorticity Distribution of The Near-Field Flow Structures

In line with the earlier observation, the time-averaged results in Figures 7.12 and 7.13 clearly show that the penetration height of an elliptic jet exhausting into the cross flow increases with the velocity ratio. Furthermore, the blockage effect brought about by the exhausting jet appears to have caused the streamlines at the windward side of the jet/cross flow interface to be highly strained. Above all, the most interesting feature of the flow patterns in the figures is the existence of a critical point downstream of the jet (see Perry and Fairlie (1974) and Perry and Chong (2000)). Although such a point has been predicted numerically by Sykes et al. (1986) for a CJICF, its existence was not confirmed until the flying-hot-wire results of Kelso et al. (1996) for the same jet

(a) VR=1   (b) VR=2

(c) VR=3   (d) VR=4

(e) VR=5

Figure 7.12.   Time-averaged velocity vector and streamline plots for AR=0.5 EJICF along streamwise jet centerline from VR=1 to 5. UN=unstable node, UF=unstable focus.
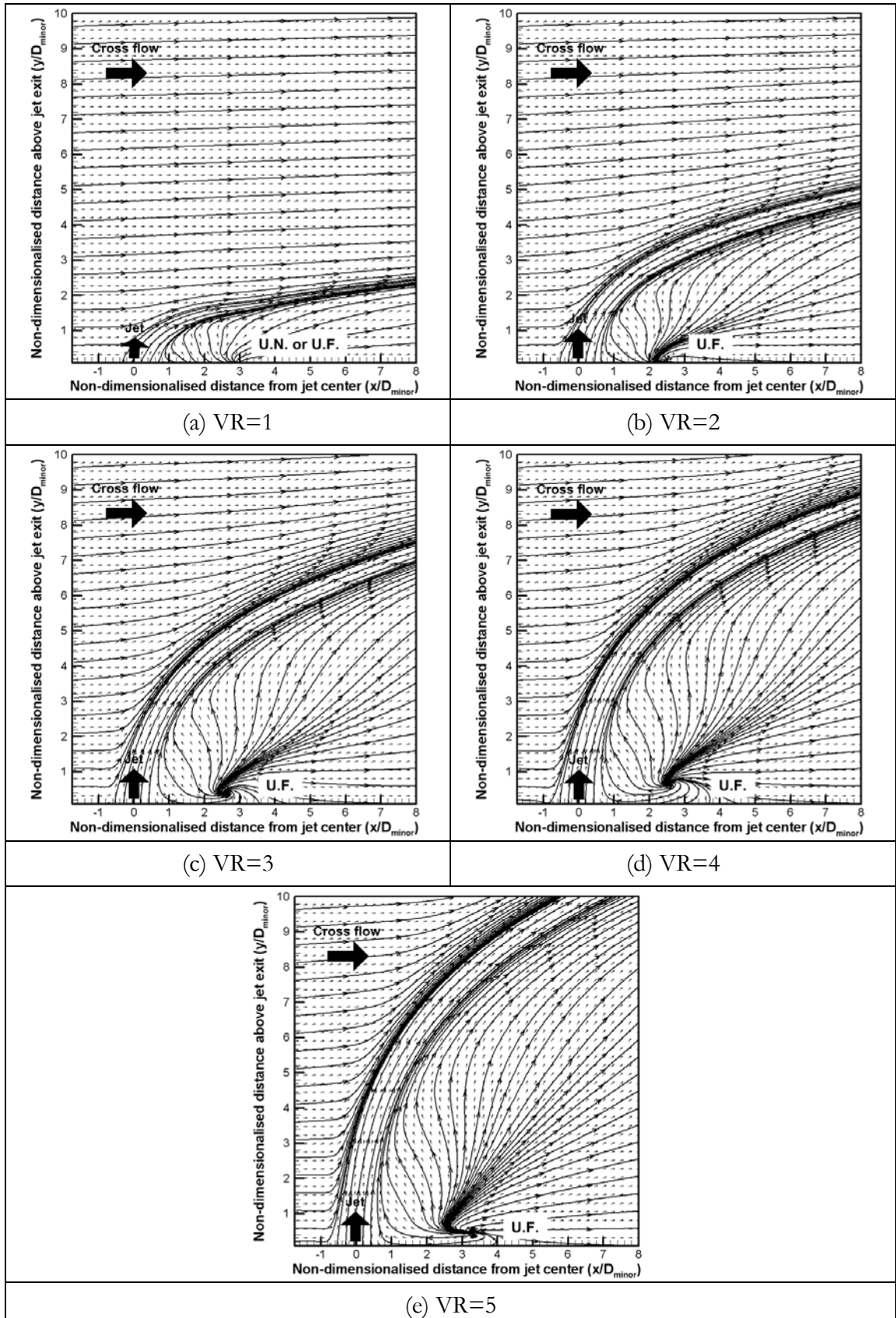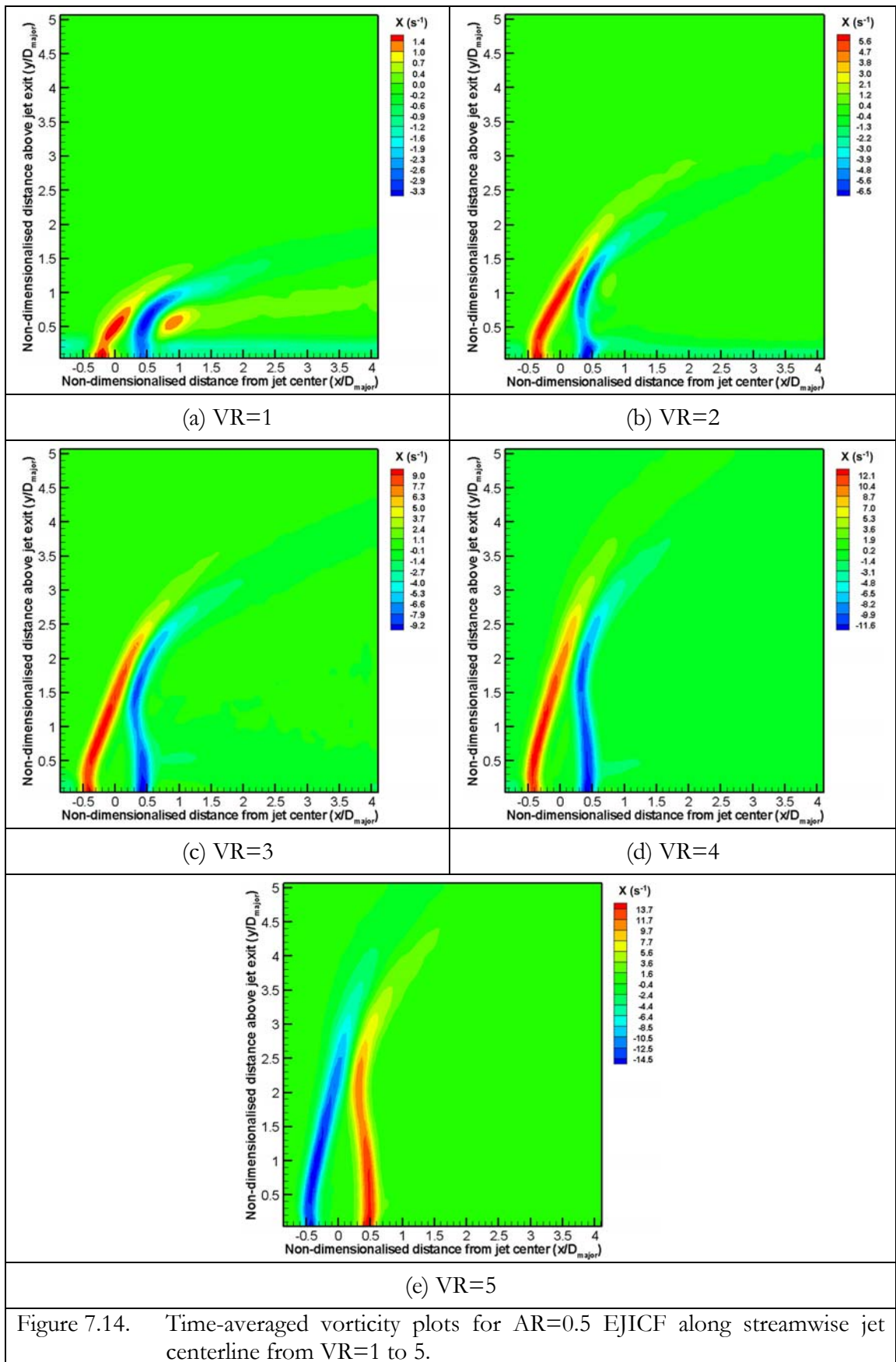
(a) VR=1

(b) VR=2

(c) VR=3

(d) VR=4

(e) VR=5
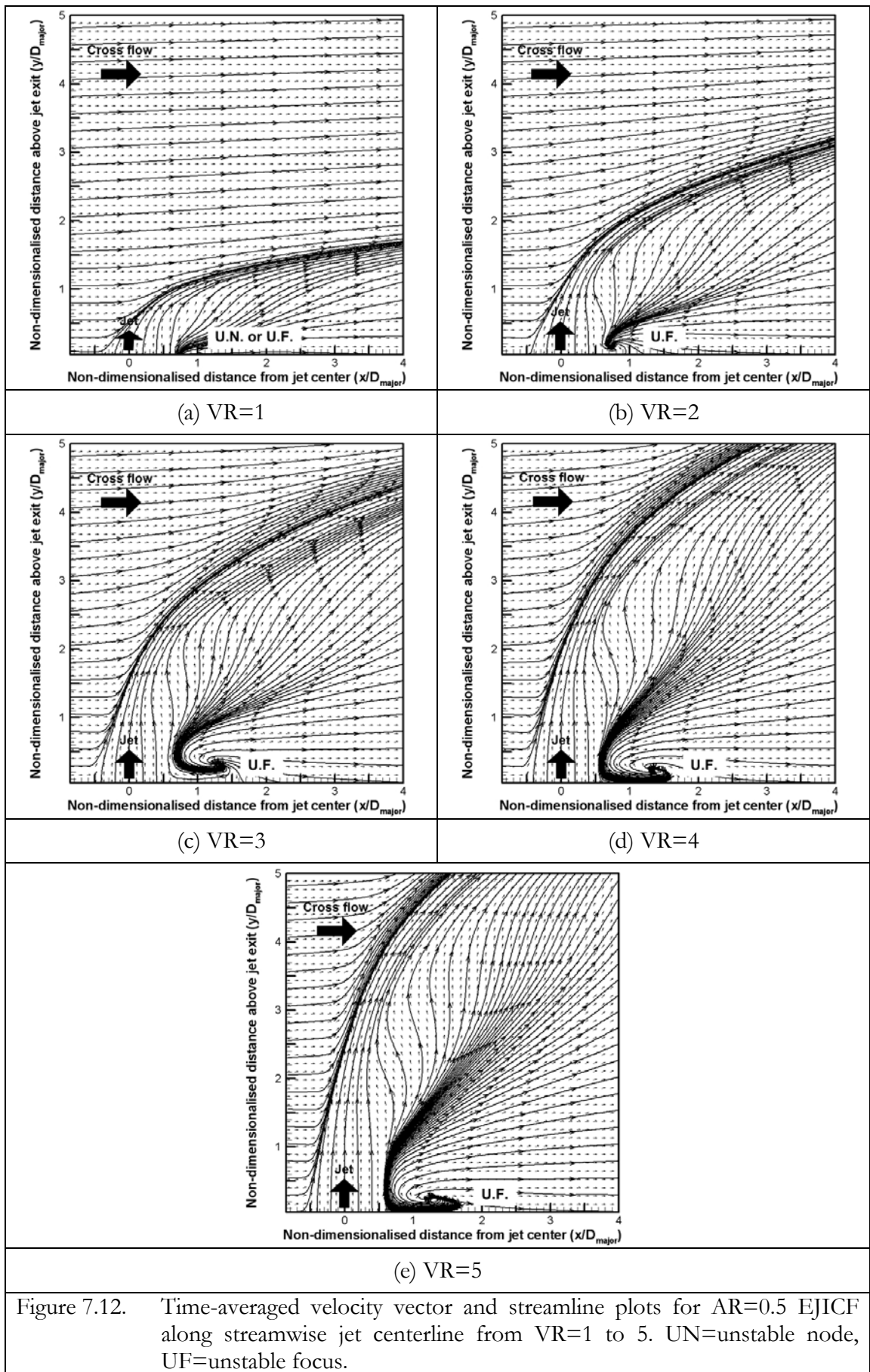
Figure 7.13.   Time-averaged velocity vector and streamline plots for AR=2 EJICF along streamwise jet centerline from VR=1 to 5. UN=unstable node, UF=unstable focus.
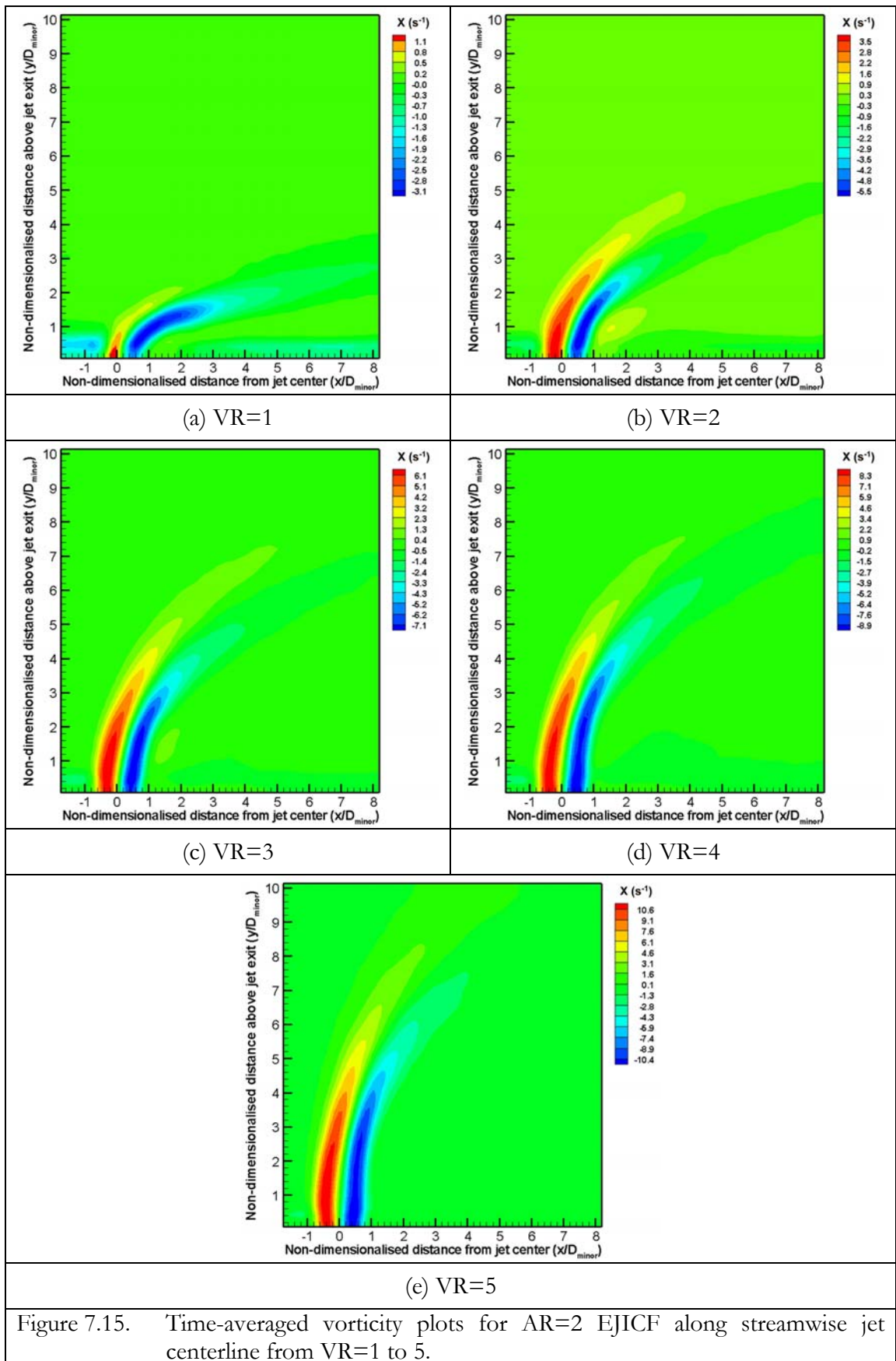
geometry, and in a chimney JICF study by Hasselbrink and Mungal (2001). While it is clear from the figures that the critical point observed for VR≥2 is an "unstable focus", the identity of the corresponding point at VR=1 is not so clear because it's close proximity to the wall prevented accurate PIV measurements. Nevertheless, it bears close resemblance to an unstable node in the flying hot-wire data of Kelso et al. (1996) for CJICF, although it has to be mentioned that the resolution of the Kelso et al. data is not particularly high. Interestingly, Hasselbrink and Mungal (2001) have also reported seeing a critical point behind a chimney JICF at VR=10. Although, they identified it as an unstable "node", close examination of their results shows that it looks more like an "unstable focus".

As for the "unstable focus" observed here, its location is found to be a function of both the velocity ratio and the aspect ratio. For a given jet geometry, an increase in the velocity ratio leads to a downstream shift in the position of the "unstable focus", and an increase in the circulation (as can be inferred from the manner with which the streamlines spiral out). More specifically, the focus for the AR=0.5 jet are located approximately at $x=0.7D_{major}$, $1.3D_{major}$, $1.4D_{major}$ and $1.5D_{major}$ from the jet exit center when the velocity ratio is increased from 2 to 5, respectively. For the case of AR=2 jet, they are located at approximately $x=2.2D_{minor}$, $2.5D_{minor}$, $2.6D_{minor}$ and $3.3D_{minor}$ for the same velocity ratio range.

According to the analysis by Coelho and Hunt (1989), and subsequently supported by Hasselbrink and Mungal (2001), the jet deflection is an indication of the entrainment rate of the cross flow by the jet in the near-field. Based on this argument, it is reasonable to say that with a relatively larger streamwise deflection, high aspect ratio jets have a higher near-field entrainment rate than low aspect ratio jets.

Figures 7.14 and 7.15 depict the time-averaged vorticity fields for the AR=0.5 and AR=2 jets, respectively. Although the dynamics of the vortex structures are difficult to deduce from the mean quantities, the results do provide useful comparison of the effect of jet orientation on the overall vorticity distribution. For example, Figure 7.16 shows a consistently higher peak average vorticity in lee-side region than in the leading-edge region at low velocity ratios. However, with increasing velocity ratio, the role is reversed. This finding is supported by the earlier observations of Kelso et al. (1996) and Lim et al. (2001) that a deflected jet at low velocity ratios behaves more wake-like, which is characterized by highly-recurring "loop-like" vortices at the lee-side with little or no shedding of leading-edge vortices. More importantly, the low aspect ratio jet produces a significantly higher peak averaged vorticity along both the leading-edge and lee-side regions than the high aspect ratio jet. It is likely that a higher curvature of the vortex filament facing the cross flow in low aspect ratio jet and their mutual interaction may have contributed to a greater vortex stretching, and therefore higher vorticity.

(a) VR=1

(b) VR=2

(c) VR=3

(d) VR=4

(e) VR=5

Figure 7.14.   Time-averaged vorticity plots for AR=0.5 EJICF along streamwise jet centerline from VR=1 to 5.

(a) VR=1

(b) VR=2

(c) VR=3

(d) VR=4

(e) VR=5

Figure 7.15.   Time-averaged vorticity plots for AR=2 EJICF along streamwise jet centerline from VR=1 to 5.
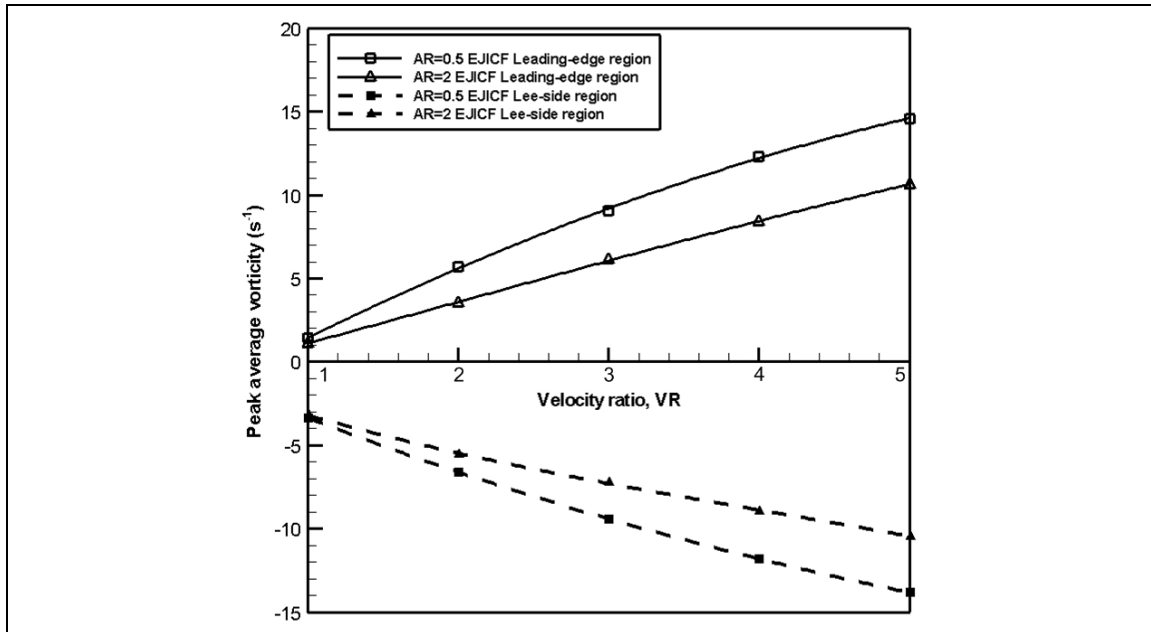
Figure 7.16.   A comparison between the peak time-averaged vorticity along the leading-edge and lee-side regions for the low and high AR EJICF (AR=0.5 and 2 respectively).

7.4.2 Mean Velocity Profiles Along Symmetrical plane

Figures 7.17 to 7.21 present the mean center-line velocity profiles for u, v and $\langle V \rangle$ velocity components for the case of AR=0.5 EJICF with VR=1 to 5, and for downstream distances of up to $6D_h$. Attempts have also been made to compare the present results with those obtained by Andreopoulos and Rodi (1984) using hot-wire anemometry. However, it was discovered that while similar trends could be found in both the present results and theirs, the deviation between them are significant enough for any meaningful comparison and conclusion. The most probable reason is that the jet geometries used by them and the present study are quite different to begin with. Moreover, Andreopoulos and Rodi's (1984) results ranged from $x/D=4$ to 16 with an interval of $x/D=4$. Compared to the range of the present study where $x/D_h=0$ to 6 with an interval of $x/D_h=1$, there are only two downstream distances where comparisons can be carried out. Due to the above issues, it was decided that a direct comparison might

not be beneficial to the present discussion and instead, deductions based on the present results will be made with appropriate considerations from available literature.

With reference to the figures showing the u-velocity component only, there exists two persistent velocity peaks in both near and far-wall, with one progressively lifting away from the test-section floor and the other staying close to the test-section (hereafter known as "far-wall" and "near-wall" velocity peaks respectively). Presumably, the former is the jet element within the dominant primary CVP with the latter being associated with the near-wall secondary CVP. There is clear indication of flow reversal in the near-field (two instances, in fact) as shown in the velocity profiles for $x=1.0D_h$ to $2.0D_h$, very possibly due to the near-field development of the two CVPs. The stronger flow-reversal region is resultant of the primary CVP and the weaker one corresponding to the secondary CVP. As the downstream distance increases, the far-wall velocity peak representing the primary CVP slowly reduces its U-velocity component, though not as fast as the near-wall velocity peak representing the secondary CVP. True to its historical origins, the secondary CVP started out resembling very much a near-wall jet as reported by Andreopoulos and Rodi (1984) but increased viscous effects due to its interaction with the cross flow boundary layer meant that it transits to turbulence thereafter.

On the other hand, with reference to the figures illustrating the v-velocity component, two velocity peaks are sighted once again with one further away from the test-section floor than the other. While a first glance might induce one to believe that the near-wall velocity peak would be the secondary CVP, a check with the separation distances between the relevant velocity peaks and the test-section floor observed at corresponding downstream centerline locations revealed that these two velocity peaks were due to different flow components. Firstly, the near-wall velocity peaks in the u-
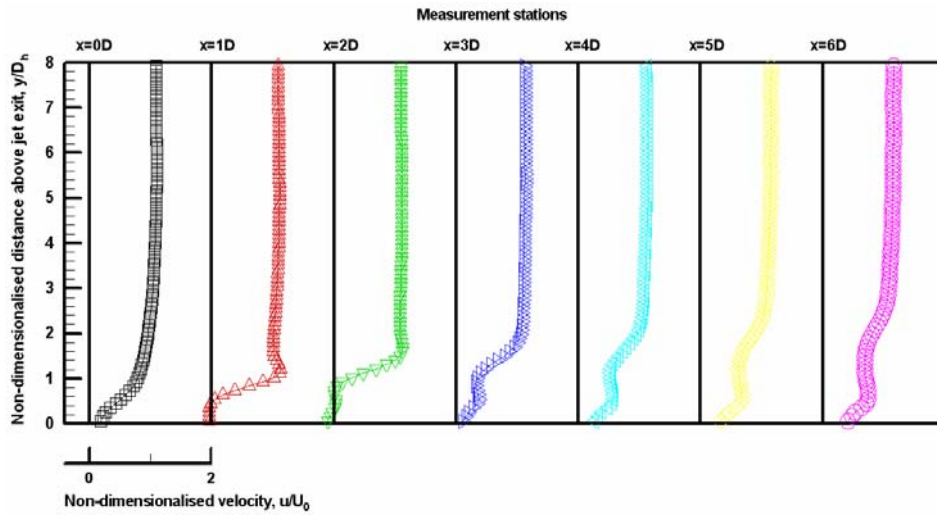
(a) u-velocity component
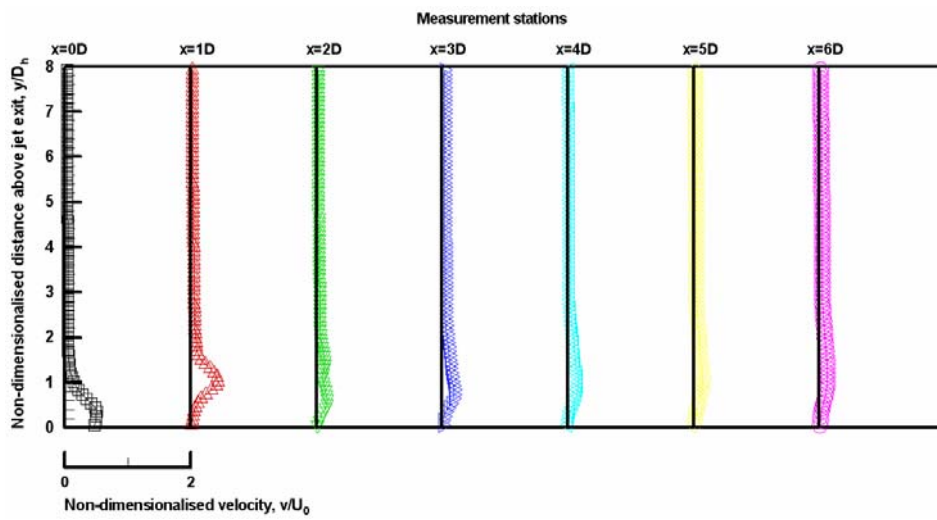
(b) v-velocity component
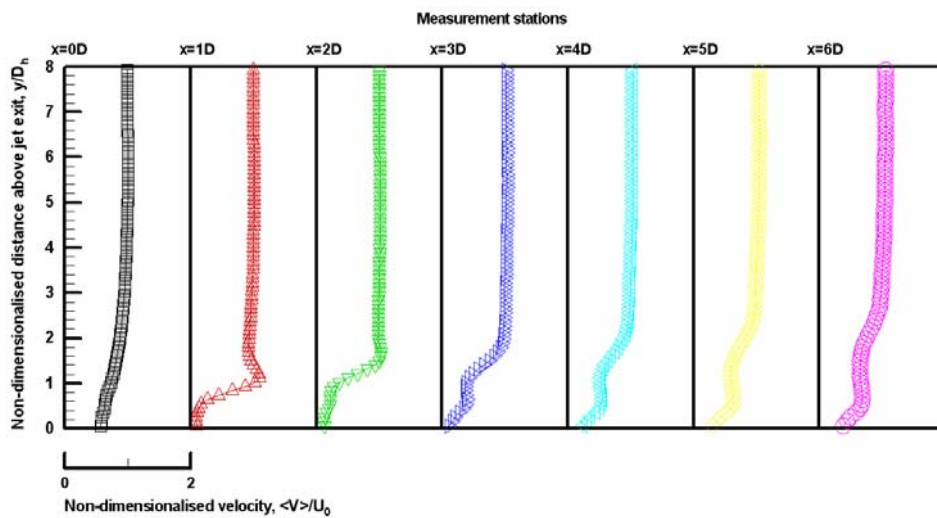
(c) Magnitude

Figure 7.17. u, v and $\langle V \rangle$ velocity components for AR=0.5, VR=1 EJICF.

(a) u-velocity component

(b) v-velocity component

(c) Magnitude

Figure 7.18. u, v and $\langle V \rangle$ velocity components for AR=0.5, VR=2 EJICF.

(a) u-velocity component

(b) v-velocity component

(c) Magnitude

Figure 7.19. u, v and $\langle V \rangle$ velocity components for AR=0.5, VR=3 EJICF.

(a) u-velocity component

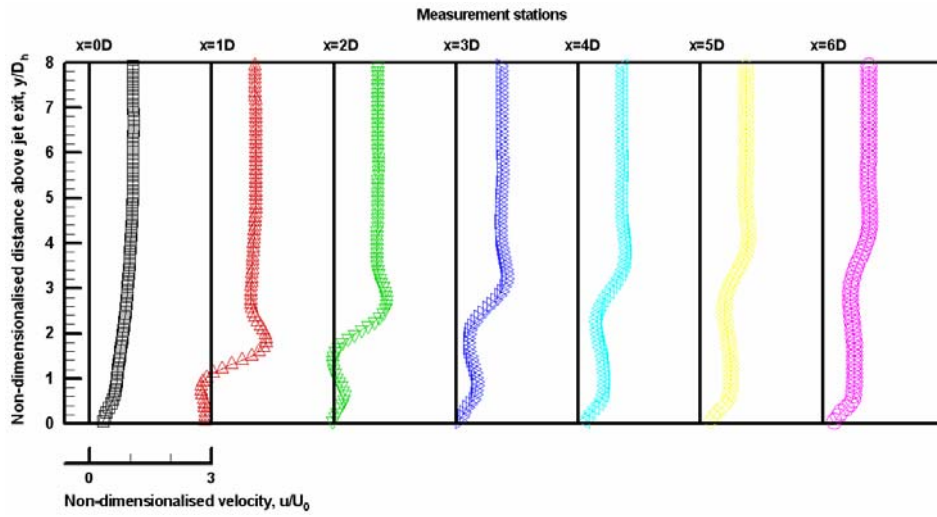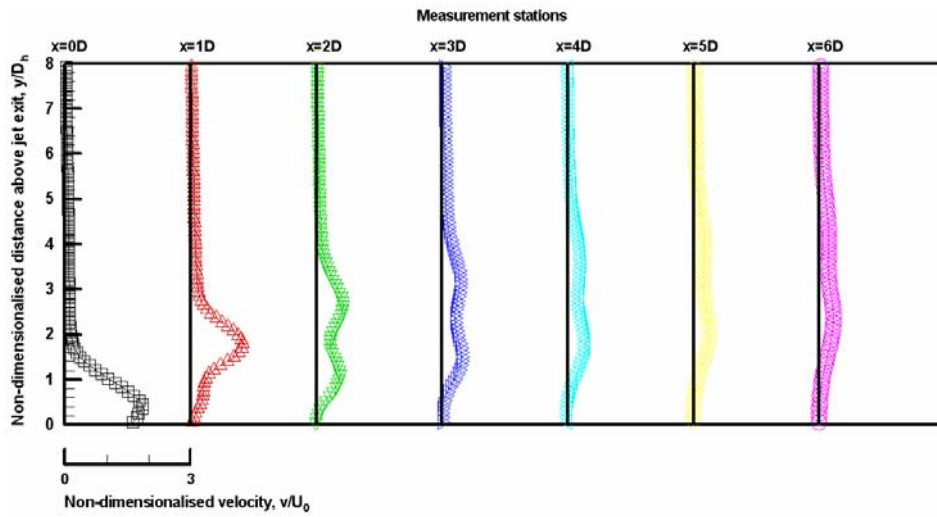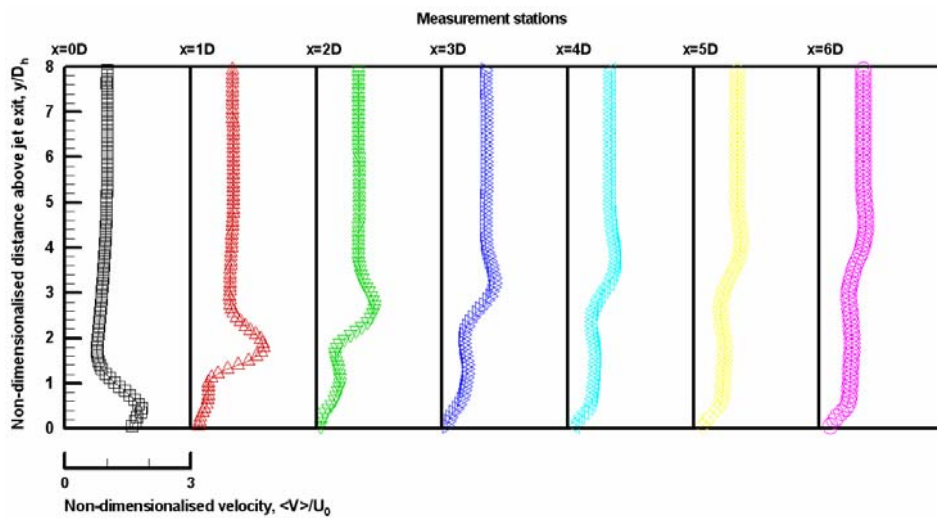(b) v-velocity component

(c) Magnitude

Figure 7.20. u, v and $\langle V \rangle$ velocity components for AR=0.5, VR=4 EJICF.

(a) u-velocity component

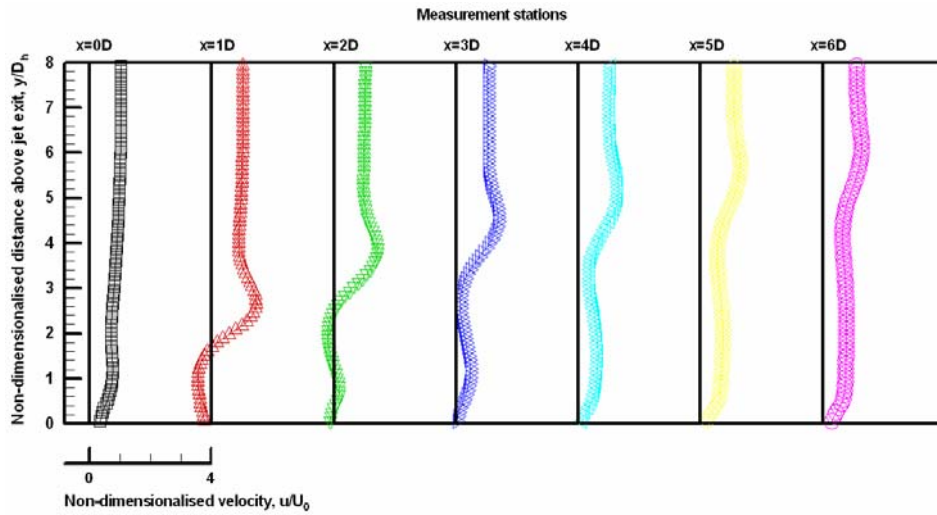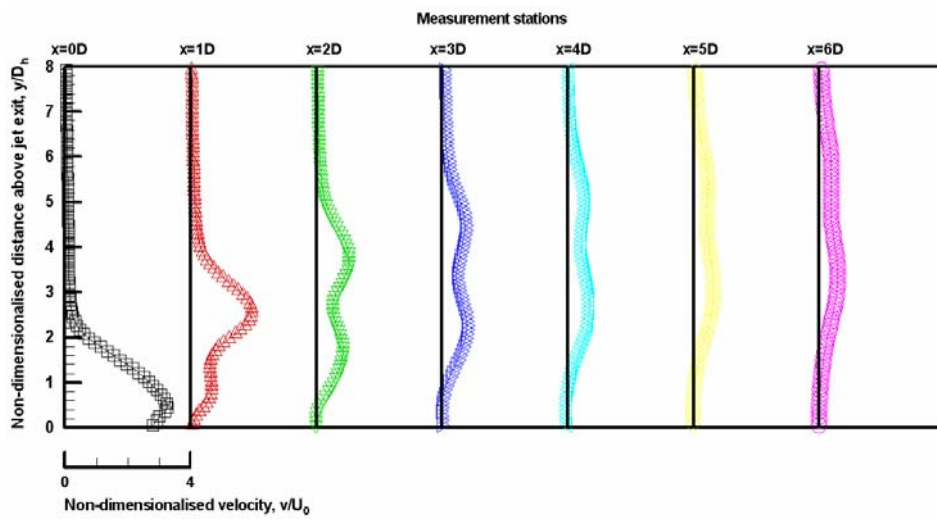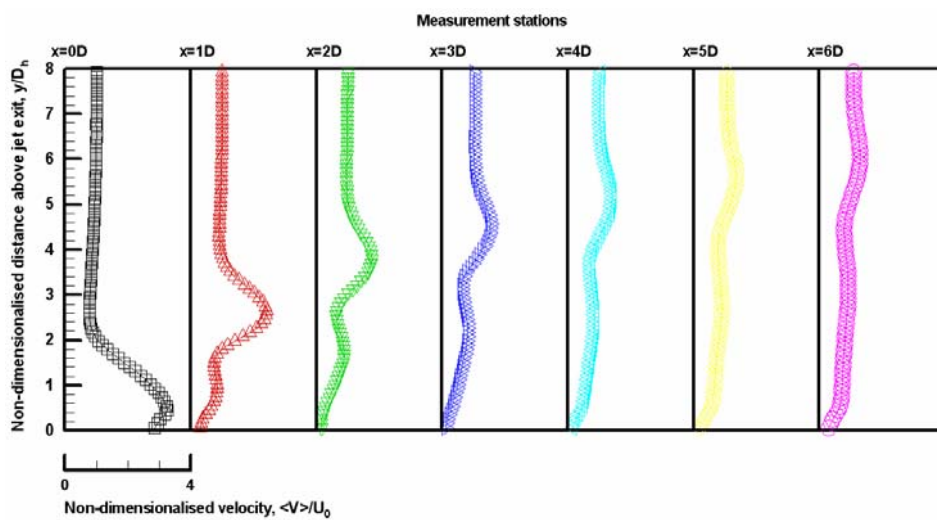(b) v-velocity component

(c) Magnitude

Figure 7.21. u, v and $\langle V \rangle$ velocity components for AR=0.5, VR=5 EJICF.

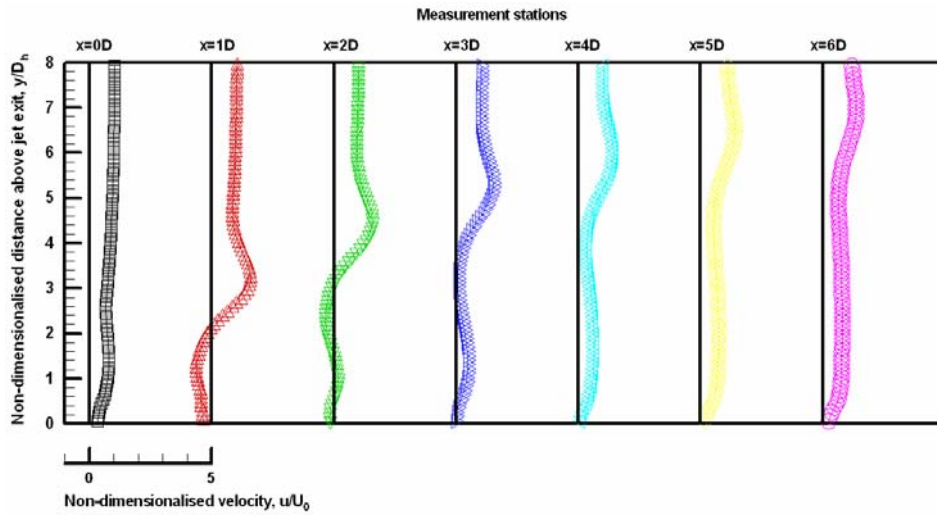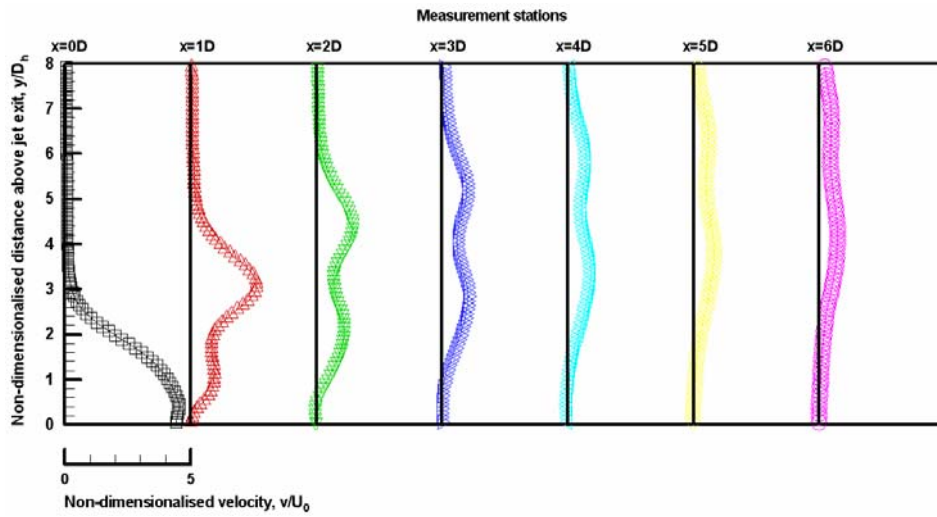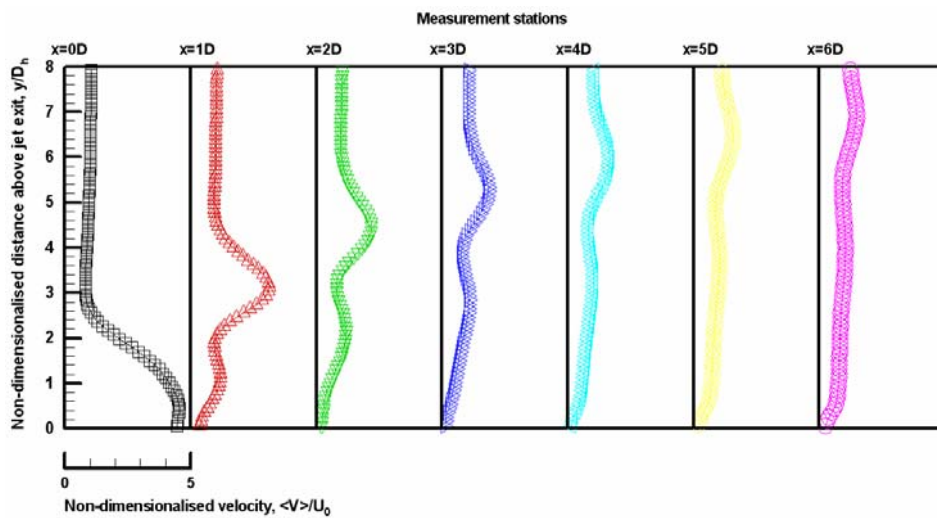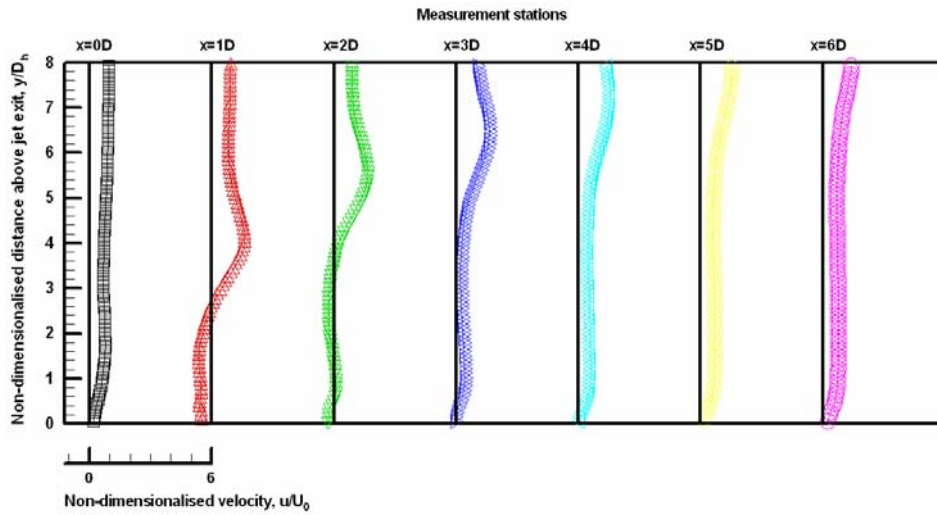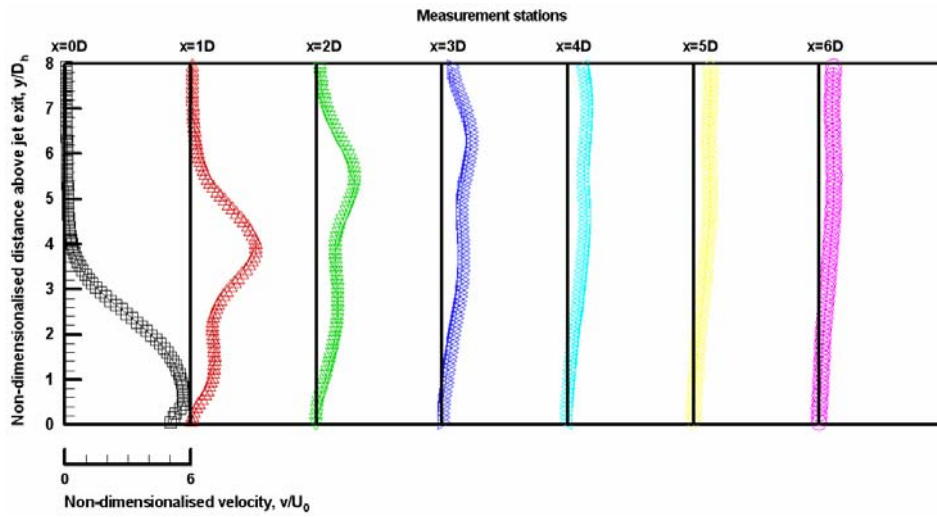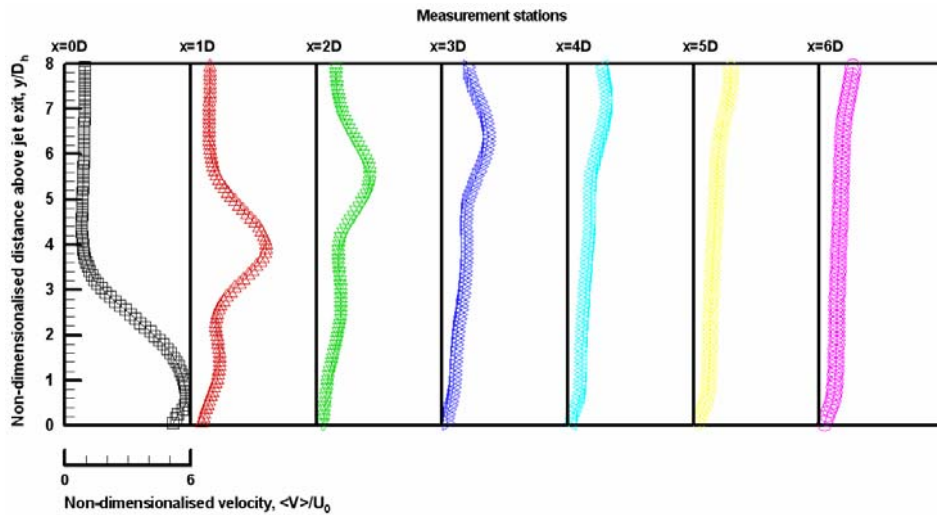velocity component figures were consistently at a shorter distance away from the test-section floor than the corresponding near-wall velocity peaks in the v-velocity component figures for the same velocity ratios. In fact, the far-wall velocity peaks progressively elevated away from the test-section floor, in contrast to the relatively constant separation distance between the near-wall velocity peaks and test-section floor. Secondly, the near-wall velocity peaks in the u-velocity component figures were observed to "flatten out" and gradually lose their peak-like characteristics with resultant velocity profiles inching towards that of a uniform cross flow. Whereas for the near-wall velocity peaks in the v-velocity component figures, instead of losing their peak-like characteristics they became more accentuated and eventually overtook the far-wall velocity peaks further downstream. However, this overtaking of velocity peak as the dominant peak did not entail any increase in the velocity magnitudes. The far-wall velocity peaks simply suffered a more severe decrease in their near-wall counterparts.

A few conclusive comments could be made of the above behaviour of the velocity peaks observed for the low AR EJICF. Firstly, similar to previous measurements of a circular JICF, a near-wall secondary CVP exists as well for the low AR EJICF. It exhibits almost similar jet-like characteristics in the near-field before being dissipated by viscous interaction with the cross flow boundary layer. Secondly, the lead transition between the two velocity peaks observed in the v-velocity component figures strongly suggested a direct correlation with the theoretical framework and previous experimental work. The latter indicated that as the jet was gradually deflected by the cross flow, there would be a corresponding realignment of the flow dynamics associated with the jet into those associated with the CVP. The eventual overtaking of the above-mentioned near-wall velocity peaks over the far-wall velocity peaks indicated this decrease in the jet dynamics with an increase in the CVP dynamics. The jet dynamics, which were originally

in the vertical direction, were realigned eventually to become the lead velocity peak in the u-velocity component. But the growth in the v-velocity component due to the lateral counter-rotating of the CVP gave the CVP the lead in the v-velocity component.

Figures 7.22 to 7.26 show the mean centerline velocity profiles in both u and v-velocity components for the AR=2 EJICF with VR=1 to 5 up to a downstream distance of $6D_h$. Similar to the low AR EJICF, velocity peaks were observed in both u and v-velocity components which behave in similar fashions. One small discrepancy though, would be that development of the near-wall velocity peaks in both u and v-velocity components were weaker than in the low AR EJICF case. This could be due to the "blunt" nature of the jet orientation which created a much wider wake region at the lee-side region of the jet. This wake region would very likely contribute to a larger recirculating region and caused a faster transition to turbulence. In addition, jet vorticity at both tips of the major-axis did not have a large enough distance to be gradually realigned in a smooth manner by the cross flow, unlike in the case for low AR EJICF. Therefore, it was not surprising that CVP development would be relatively weaker in the beginning. However, subsequent development remained almost invariant from that of the low AR EJICF.

(a) u-velocity component
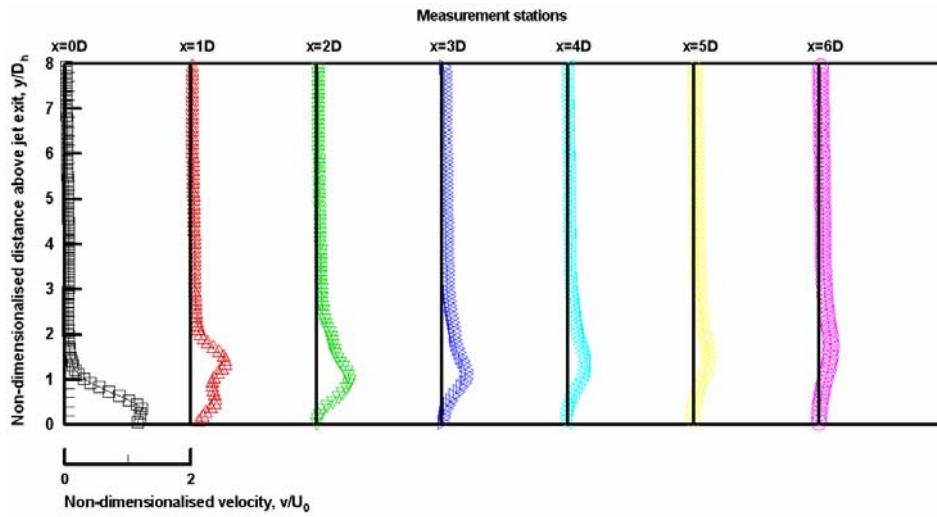
(b) v-velocity component
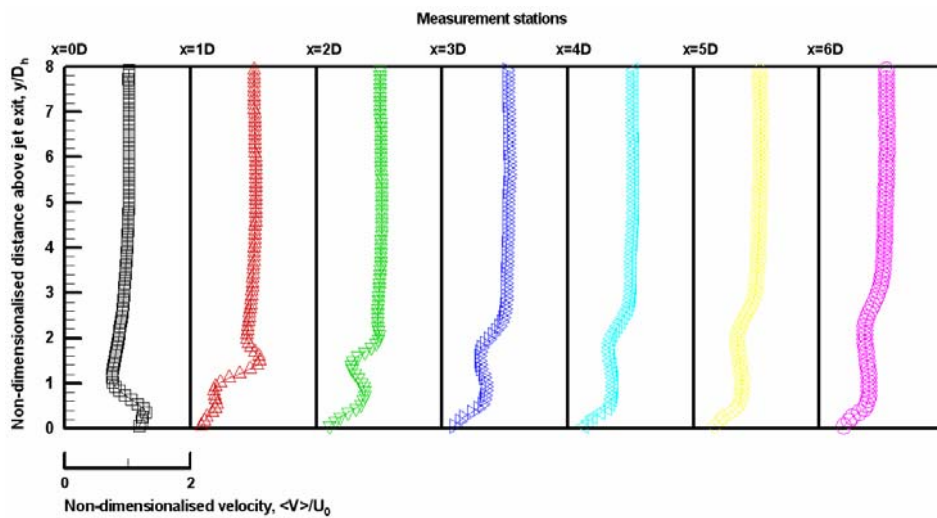
(c) Magnitude

Figure 7.22. u, v and $\langle V \rangle$ velocity components for AR=2, VR=1 EJICF.

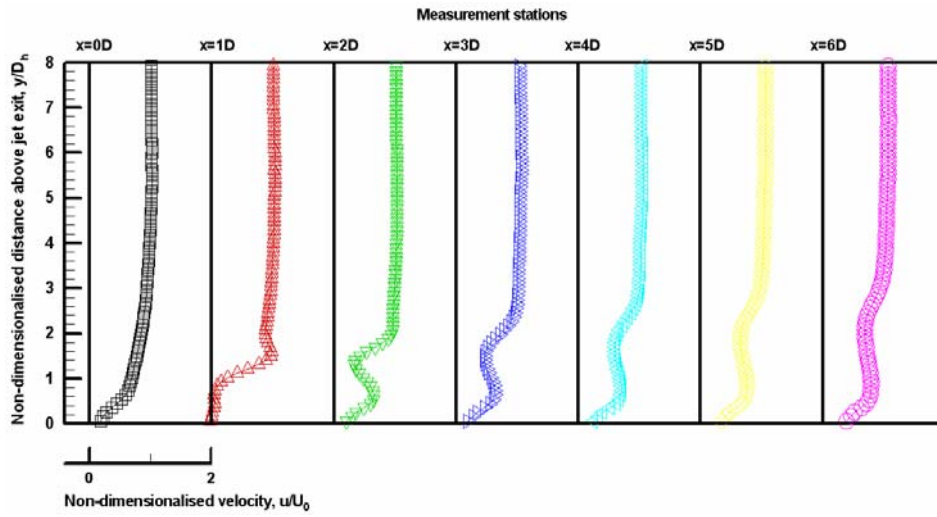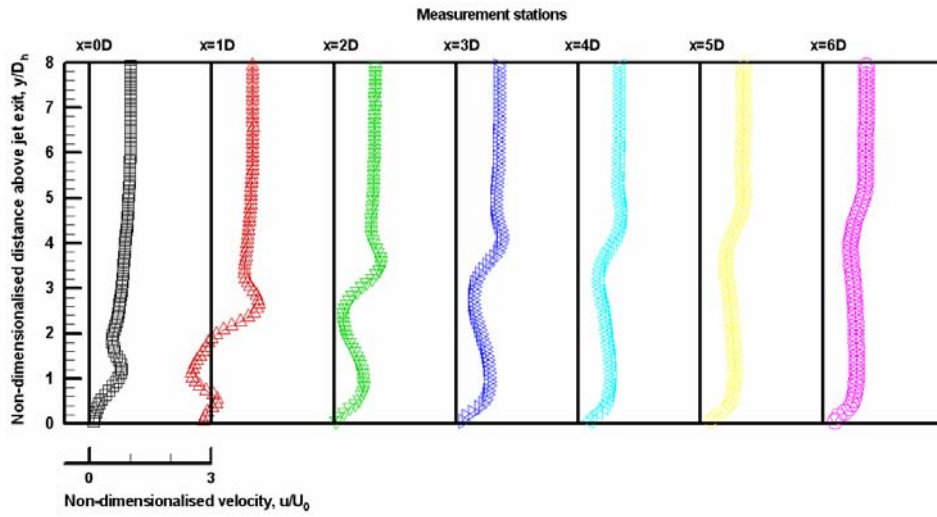(a) u-velocity component
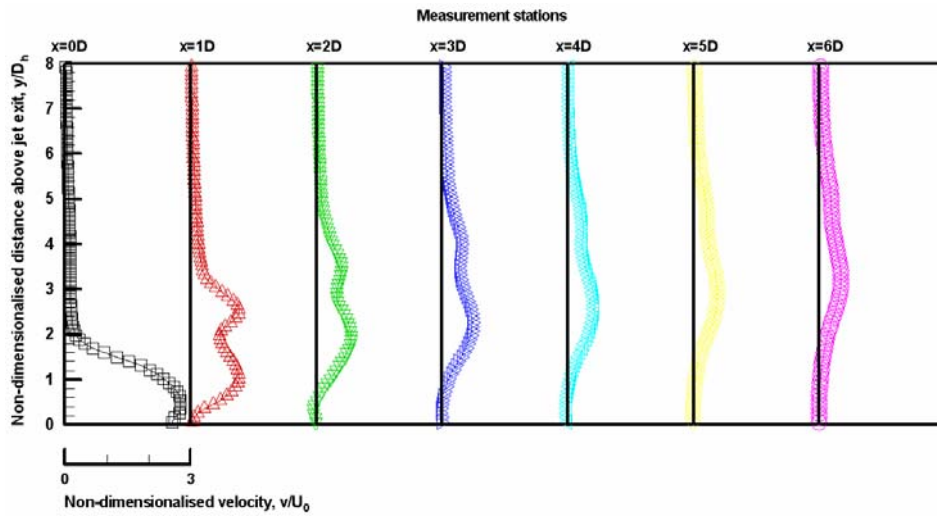
(b) v-velocity component
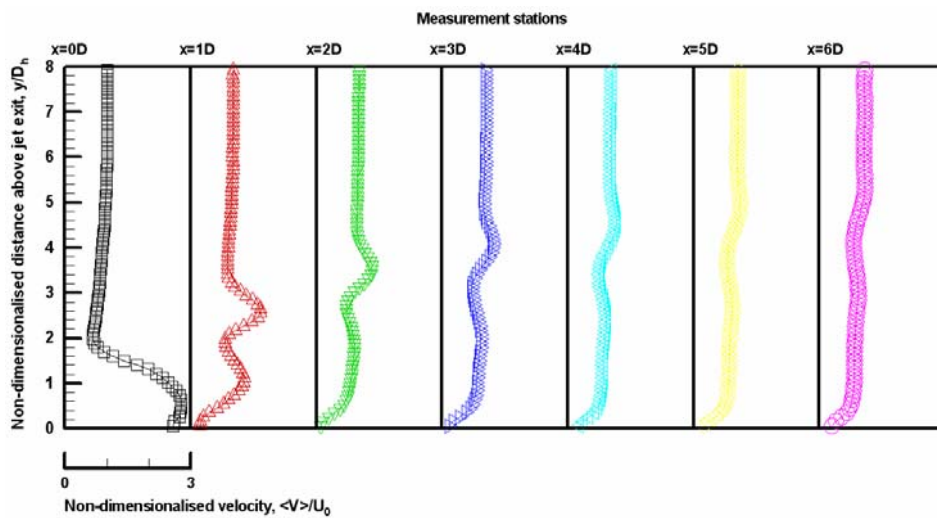
(c) Magnitude

Figure 7.23. u, v and $\langle V \rangle$ velocity components for AR=2, VR=2 EJICF.
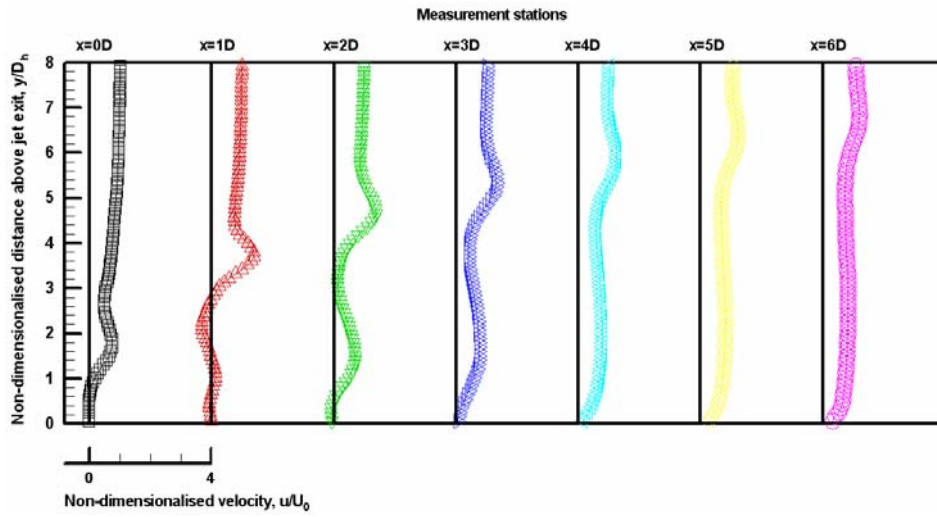
(a) u-velocity component
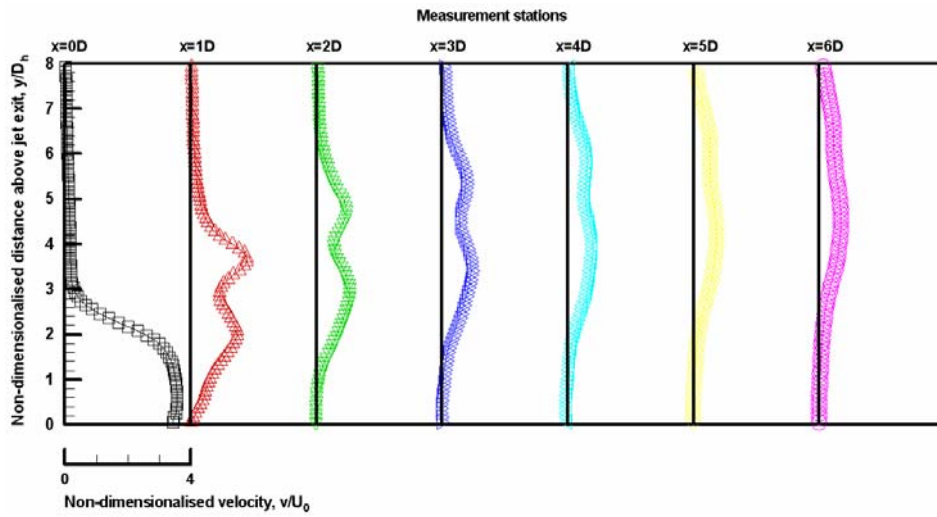
(b) v-velocity component
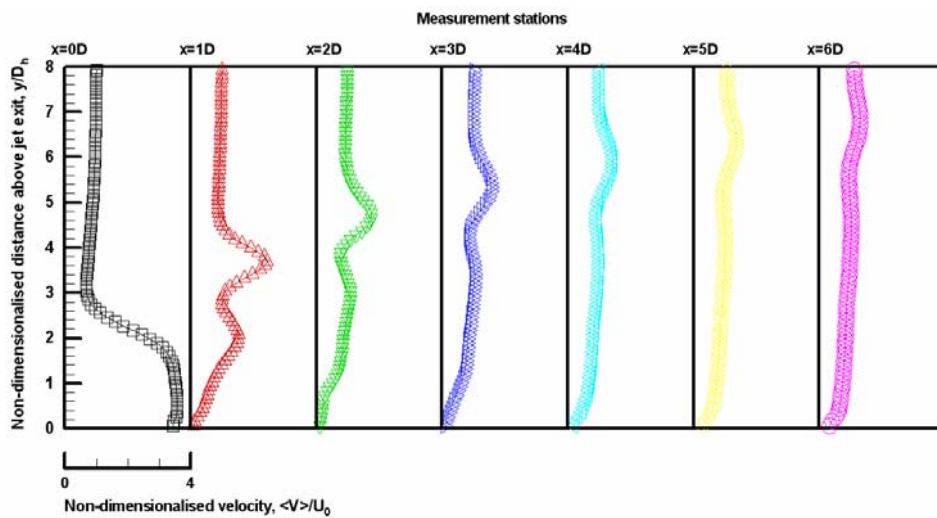
(c) Magnitude

Figure 7.24. u, v and $\langle V \rangle$ velocity components for AR=2, VR=3 EJICF.
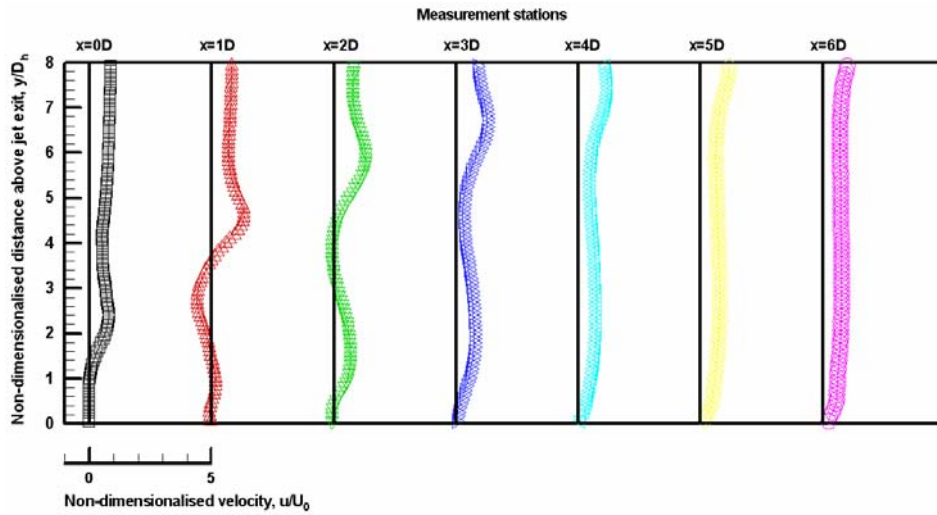
(a) u-velocity component
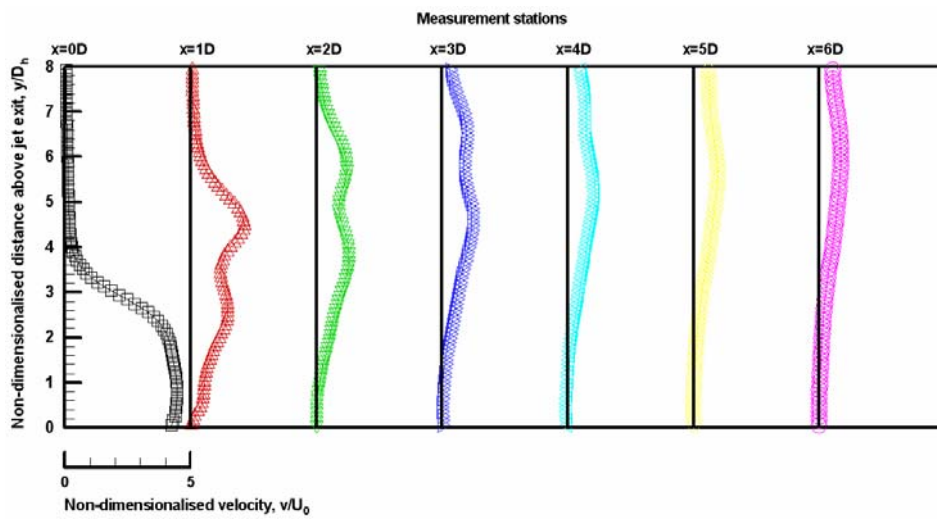
(b) v-velocity component
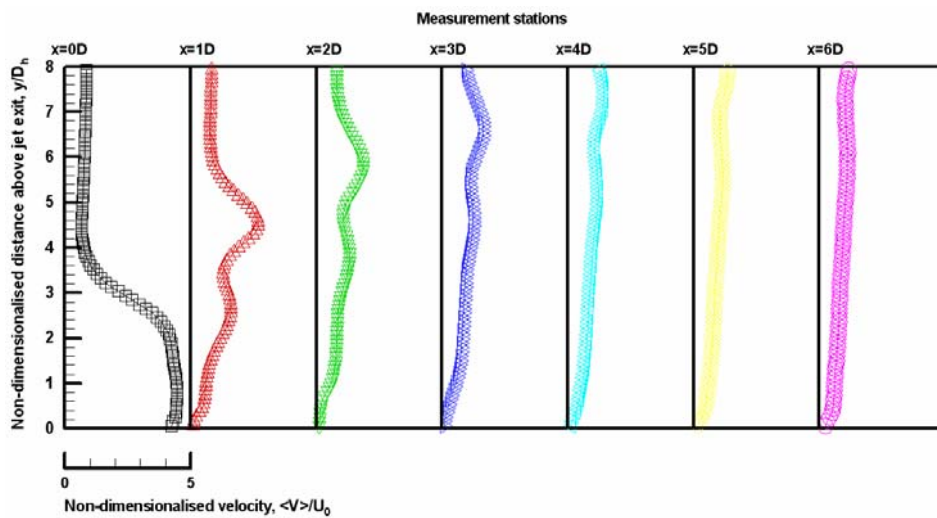
(c) Magnitude

Figure 7.25. u, v and $\langle V \rangle$ velocity components for AR=2, VR=4 EJICF.
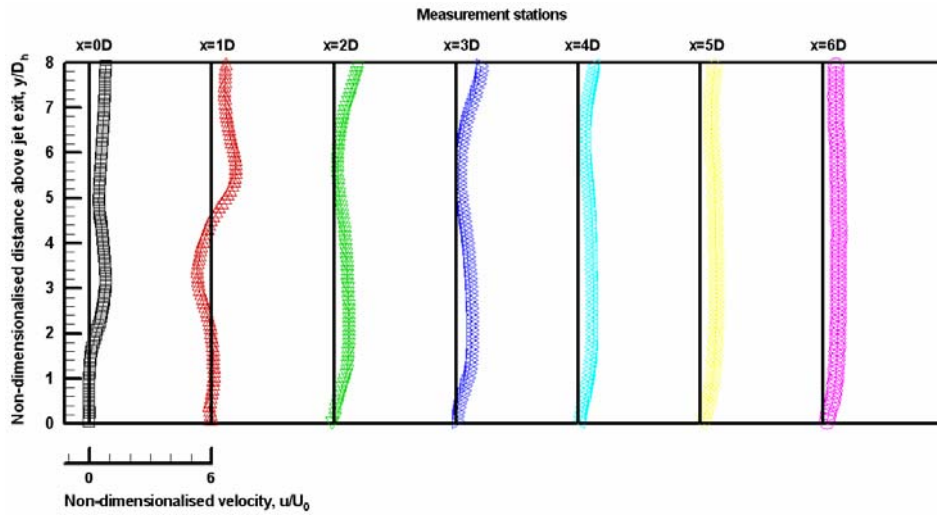
(a) u-velocity component
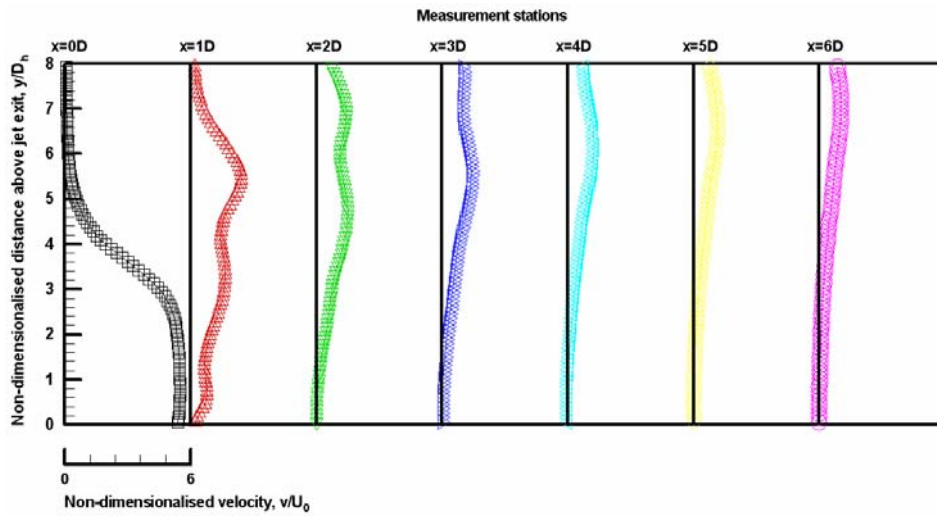
(b) v-velocity component
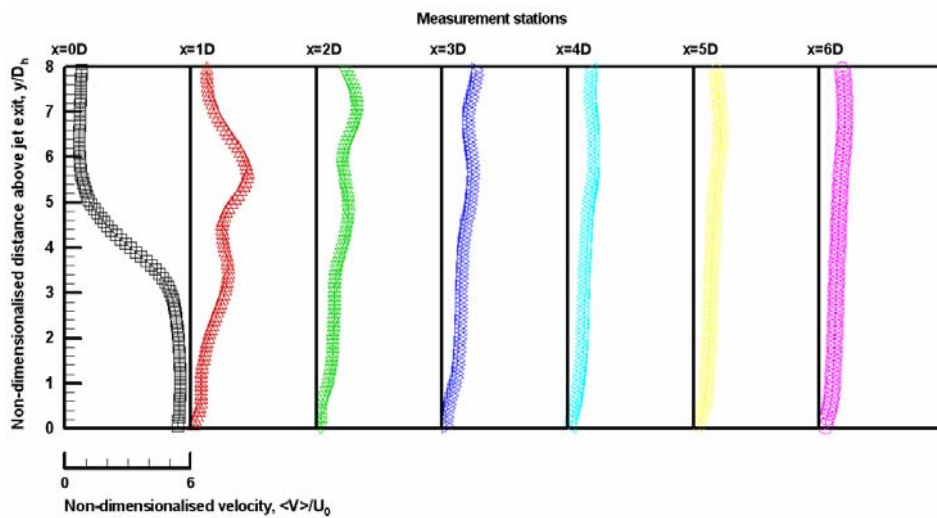
(c) Magnitude

Figure 7.26. u, v and $\langle V \rangle$ velocity components for AR=2, VR=5 EJICF.

Chapter 8

Conclusions

Since the experiments conducted were in distinct areas, the conclusions drawn will be summarized in point form.

8.1 Effects of Jet Shear Layer Thickness on Circular Jets in Cross Flow

a. In the study of parabolic and top-hat circular jets in a laminar cross flow (Re=625 to 1645, depending on exact jet geometry and MR=2.31 to 5.77), formation of the leading-edge vortices for top-hat jets and their subsequent pairing downstream are observed to occur much closer to the jet exits than the corresponding vortices in parabolic jets for all the VRs investigated.   In the latter's case, the vortices are usually formed 2 to 3 jet diameters downstream of the jet exits, and their generation and subsequent pairing are less coherent than their top-hat counterparts.

b. The above observations can be attributed to the difference in the thickness of the jet shear layer. In the case of the top-hat jets, the shear layer is thin and therefore highly unstable. This results in the early formation of the leading edge vortices. In contrast, the thicker shear layers in the parabolic are more stable and less susceptible to instabilities introduced during the interaction between the jet and the cross flow until much further downstream.

c. Together with the quantitative measurements using PIV, it is postulated that the "thinning" of the jet shear layer due to its interaction with the cross flow is responsible for the eventual generation of the leading-edge vortices for parabolic JICF.

8.2   Vortex Loop Model for a Circular Jet in Cross Flow

a. A vortex skeleton model has been proposed to overcome some of the shortcomings associated with previously proposed models based on vortex rings. For example, the tilting-and-folding vortex ring model proposed by Kelso et al. (1996) does not adequately describe the early development of the flow structures.

b. Unlike the model using vortex rings, the revised model using vortex loops does not require the concurrent formation of the leading edge and leeside vortices. It also removes the difficulties associated with unrealistic twisting and deformation of vortex ring filaments to leading edge vortices and leeside vortices.

c. The absence of vortex rings in JICF can be attributed to the formation of CVP which inhibits their formation. This is in sharp contrast to the free-jet where nonappearance CVP ensures easily formation of vortex rings, and this had misled many earlier workers to believe that similar vortex ring structures are also present in JICF.

d. The proposed model is valid as long as the CVP is present near the jet exit, except at very high velocity ratios where the flow behaves more like a free jet. Under this circumstance, it is possible for the vortex rings to develop.

8.3 Elliptic Jets in Cross Flow

a. The results of elliptic jets in a laminar cross flow (AR=0.3, 0.5, 2 and 3 for VR=1 to 5, Re_h=890 to 4440 for AR=0.3 and 3 elliptic jet, and 1020 to 5090 for AR=0.5 and 2 elliptic jet) show that, regardless of the AR of the ellipse, the flows possess the same fundamental structures, such as the leading-edge vortices, lee-side vortices and CVP etc, as in circular jets.

b. The effects of exit geometry are confined to the near-field only, and are eventually damped out in the far-field. Therefore, the vortex skeleton model proposed for the CJICF is also applicable to elliptic jets.

c. In the near-field, the smaller radius of curvature in a low AR jet facing the cross flow translates into higher self-induced velocity, and therefore more regular shedding of the leading-edge vortices, and more intense interaction. When VR reaches 3 or higher, the interaction often leads to regular vortex entangling and subsequent pairing, resulting in much stronger leading edge vortices as the PIV results have shown. No such regular leading-edge vortex interaction was found for the case of high AR EJICF, even though they did pair up occasionally.

d. In all the cases of the low AR elliptic jets considered here, prior to the formation of leading-edge and lee-side vortices, the jet shear layer in the vicinity of the jet exit always rolls up into one primary CVP and one secondary CVP at the sides of the jet, with the latter possessing the same sense of rotation as the primary CVP. As both CVPs travel downstream, they interact and are subsequently paired together to form one larger CVP. When dissected by a laser sheet normal to the

cross flow, both the primary and secondary CVP appear as steady kidney vortices, while the leading-edge vortices appear as primary unsteady kidney vortices.

e. For high AR elliptic jets, it is possible for the jet shear layer to develop more than one pair of streamwise foldings on the leading-edge, in addition to the primary CVP at the sides of the elliptic jet. These streamwise foldings remain as separate entities, even when the jet shear layer has already rolled up to form leading-edge vortices. Depending on the AR and VR, the jet structures can evolve along any one of three possible routes, which are referred to as Scenario 1, Scenario 2 and Scenario 3 in this thesis.

f. Both Scenario 1 and 2 possess one streamwise folding, with the former having their sense of rotation opposite to and the latter the same as the primary CVP. It is the difference in the sense of rotation of the streamwise foldings that leads to formation of secondary unsteady anti-kidney and secondary unsteady kidney vortices in Scenario 1 and Scenario 2, respectively. In Scenario 3, three pairs of streamwise foldings, in addition to the primary CVP at the sides of the elliptic jet, are observed.

g. While secondary unsteady kidney vortices in Scenario 2 are found across the entire range of the VR considered for AR=3 elliptic jet (i.e. VR=1 to 5), secondary unsteady anti-kidney vortices are found occasionally to occur only when the velocity ratio is greater than 3. This is in contrast to the observation of Haven and Kurosaka (1997) which shows only the existence of primary unsteady kidney vortices from VR=1.6 to 2. One possible explanation might be that the velocity ratios used by them were not as high as the present case to allow these flow structures to manifest. However, beyond VR=3, the results show that either

secondary unsteady anti-kidney vortices or secondary unsteady kidney vortices are possible, and that the flow may switch from one scenario to the next, probably caused by flow unsteadiness.

h. Whilst the present results agree with the interpretation of Haven and Kurosaka (1997) on the initial formation of the primary unsteady kidney and secondary unsteady anti-kidney vortices, the difference lies in the manner with which these vortices are subsequently formed. Haven and Kurosaka (1997) attributed the formation of their unsteady kidney or anti-kidney vortices to the convex or concave warping of the leading-edge shear layer, and in the process of rolling-up to form leading-edge vortex filaments, these filaments follow the same contour as the original warping, thus giving them a rather convoluted appearance. While the present study also attributes the initial formation of the secondary unsteady kidney and secondary unsteady anti-kidney vortices to the convex and concave warping of the shear layer, it is believed that these warpings subsequently roll up to form what was labeled as streamwise foldings prior to the formation of leading-edge and lee-side vortices. When the jet shear layer eventually rolls up to form leading-edge vortices, these streamwise foldings are also rolled up by much stronger leading-edge vortices.

i. In the case of high AR=2 elliptic jet, the results show that as long as the VR>3, the near-field jet structures are dominated by secondary unsteady kidney vortices depicted in Scenario 3, and below VR=3, Scenario 2 prevails with the former occurring near the axis of symmetry of the nozzle.

8.4 Recommendations for Future Work

Based on the results obtained from the present work, the following recommendations are made regarding possible future work:

a. While the instantaneous velocity and vorticity field information provided in Chapter 4 is useful in helping us understand more about the differences between parabolic and top-hat JICF, time-averaged velocity and vorticity field results may offer yet another look from another angle at their differences. Take for example, the time-averaged velocity and vorticity field results of EJICF in Chapter 7 have shown that the trajectories of low AR EJICF are higher than high AR EJICF and thus implying that the latter's near-field entrainment may be higher. Similar results on parabolic and top-hat JICF will allow us to assess whether the delay in the generation of leading-edge vortices for parabolic JICF will lead to higher trajectories. Additionally, time-averaged results enable a clearer depiction of the "unstable focus" or "unstable node" at the jet lee-side regions. It has been known that shedding of leading-edge vortices will influence the cross flow boundary layer upstream of the jet to a certain extent (Kelso, 1991, Kelso and Smits, 1995). Hence, the delay in leading-edge vortices generation for parabolic may also affect both the strength as well as the location of the "unstable focus or node".

b. The existence of different possible scenarios for high AR EJICF points out the possibility of making use of these naturally occurring streamwise folding(s) for enhanced near-field entrainment. Hence, there is a need to obtain detailed instantaneous and time-averaged velocity and vorticity fields of the streamwise folding(s) with respect to the other large-scale flow structures in the flow field. This will allow direct comparison between the strengths of the various flow

structures so as to assess the entrainment abilities of the streamwise foldings. While Haven and Kurosaka (1997) have carried out similar proposed cross-stream PIV work, the low VR range studied and significantly large particles used meant that the need still exist for a better and accurate understanding, especially at higher VRs. The recommended cross-stream PIV measurements should made along similar locations where earlier flow visualizations have been made such that both results can be correlated. As the flow field is intermittent in nature, phase-averaging of the flow field is advisable as well if time-averaging results

c. The presence of streamwise folding(s) for EJICF naturally brings on the question of whether similar streamwise folding(s) appears for other jet geometries. This question is compounded by the fact that Haven and Kurosaka (1997) did not observe them in their study of various jet geometries in cross flow, including elliptic, square and rectangle jets. Perhaps the low VR range studied did not permit their sightings. Therefore, a look at these jet geometries in a cross flow environment at similar VR range used here is needed to understand whether the behaviour is unique to the high AR elliptic geometry or other geometries (in particular, high AR rectangle geometry) as well. While the reasons for the occurrence of streamwise folding(s) and the exact conditions under which the scenarios exist are still not too clear, further studies on other jet geometries will shed more light upon the phenomenon. Moreover, jet geometries with corners (i.e. square and rectangle jets) may produce corner-induced streamwise vortices (much like the streamwise folding(s) for EJICF) at higher VR range as well as in the near-field region where the jet effects are much stronger than at low VR. If they do so, it will be interesting to observe and study the differences between

those streamwise vortices and the streamwise folding(s) observed in the present study.

References

Ajersch, P., Zhou, J.-M., Ketler, S., Salcudean, M. and Gartshore, I. S. Multiple jets in a crossflow: Detailed measurements and numerical simulations, *ASME Paper 95-GT-9*, 1995.

Andreopoulos, J. Measurements in a jet-pipe flow issuing perpendicularly into a cross stream, *Trans. ASME: J. Fluids Engrg,* **104**, 493-499, 1982.

Andreopoulos, J. and Rodi, W. Experimental investigation of jets in a cross flow, *J. Fluid Mech.,* **138,** 93-127, 1984.

Arms, R. and Hama, F.R. Localized-induction concept on a curved vortex and motion of an elliptic vortex ring, *Phy. Fluids,* **8**, 1965.

Batchelor, G.K. An introduction to fluid dynamics, *Cambridge University Press*, 1967.

Becker, H.A. and Massaro, T.A. Vortex evolution in a round jet, *J. Fluid Mech.*, **31**, 435-448, 1968.

Bergeles, G., Gosman, A.D. and Launder, B.E. The near-field character of a jet discharged through a wall 90 degrees to a main stream, *Trans. ASME: J. Heat Trans.,* **98**, 373-376, 1976.

Blanchard, J.N., Brunet, Y. and Merlen, A. Influence of a counter rotating vortex pair on the stability of a jet in a cross flow: an experimental study by flow visualizations, *Exp. Fluids*, **26**, 63-74, 1999.

Brizzi, L.-E., Foucault, E. and Bousgarbiès, J.-L. Vortices organization in the near field of a jet issuing normally into a crossflow, *J. Flow Vis. & Image Processing,* **5**, 17-28, 1998.

Broadwell, J.E. and Briedenthal, R.E. Structure and mixing of a transverse jet in incompressible flow, *J. Fluid Mech.*, **148**, 405-412, 1984.

Brundage, A.L., Plesniak, M.W. and Ramadhyani, S. Influence of coolant feed direction and hole strength on film cooling jet velocity profiles, *ASME Paper 99-GT-35*, 1999.

Bryant, L.W. and Cowdry, C.F. Effects of velocity and temperature of discharge on the shape of smoke plumes from a funnel or chimney, *Proc. Inst. Mech. Engr, London*, **169**, 371-384, 1955.

Chang Y.K. and Vakili, A.D. Dynamics of vortex rings in cross-flow, *Phy. Fluids,* **7**, 1583-1597, 1995.

Chassaing, P., George, J. Claria, A. and Sananes, F. Physical characteristics of subsonic jets in a cross stream, *J. Fluid Mech.*, **62**, 41-64, 1974.

Claus, R.W. and Vanka, S.P. Multigrid calculations of a jet in cross-flow, *J Prop. Power*, **8**, 425-431, 1992.

Coelho, S.L.V. and Hunt, J.C.R. The dynamics of the near field of strong jets in crossflows, *J. Fluid Mech.*, **200**, 95-120, 1989.

Cortelezzi, L. and Karagozian, A.R. On the formation of the counter-rotating vortex pair in transverse jets, *J. Fluid Mech.*, **446**, 347-373, 2001.

Crabb, D., Durao, D.F.G. and Whitelaw, J.H. A round jet normal to a crossflow, *Trans. ASME J. Fluids Engrg,* **103**, 142-153, 1981.

Délery, J.M. Robert Legendre and Henri Werlé: Towards the elucidation of three-dimensional separation, *Annu. Rev. Fluid Mech.,* **33**, 129-154, 2001.

Dhanak, M.R. and de Bernardinis, B. The evolution of an elliptic vortex ring, *J. Fluid Mech.,* **109**, 189, 1981.

Durando, N.A. Vortices induced in a jet by a subsonic crossflow, *AIAA J.,* **9**, 325-327, 1971.

Eiff, O.S. and Keffer, J.F. On the structures in the near-wake region of an elevated turbulent jet in a crossflow, *J. Fluid Mech.,* **333**, 161-195, 1997.

Fearn, R. and Weston R.P. Vorticity associated with a jet in a cross flow, *AIAA J.,* **12**, 1666-1671, 1974.

Findlay, M.J., Salcudean, M. and Gartshore, I. Jets in a crossflow: Effects of geometry and blowing ratio", *Trans. ASME: J. Fluids Engrg,* 121, 373-378, 1999.

Fric, T.F. and Roshko, A. Vortical structure in the wake of a transverse jet, *J. Fluid Mech.,* **217**, 1-47, 1994.

Gogineni, S., Goss, L. and Roquemore, M. Manipulation of a jet in a cross flow, *Exp. Therm. Fluid Sci.,* **16**, 3, 209-219, 1998.

Gollahalli, S.R. and Pardiwalla, D. Comparison of the flame characteristics of turbulent circular and elliptic jets in a crossflow, *Trans. ASME: J. Energy Res. Tech.,* **124**, 3, 197-203, 2002.

Gordier, R.L. Studies on fluid jets discharging normally into moving liquid, *Univ. Minnesota Tech. Pap. **28**,* Ser. B, 1959.

Gutmark, E. and Ho, C.M. Preferred modes and the spreading rates of jets, *Phy. Fluids,* **26**, 2932-2938, 1983.

Hale, C.A., Plesniak, M.W. and Ramadhyani, S. Structural features and surface heat transfer associated with a row of short-hole jets in crossflow. *Int. J. Heat and Fluid Flow,* **21**, 542-553, 2000.

Hasselbrink, E.F. and Mungal, M.G. Transverse jets and jet flames. Part 1. Scaling laws for strong transverse jets, *J. Fluid Mech.*, **443**, 1-25, 2001.

Hasselbrink, E.F. and Mungal, M.G. Transverse jets and jet flames. Part 2. Velocity and OH field imaging, *J. Fluid Mech.*, **443**, 27-68, 2001.

Haven, B.A. and Kurosaka, M. Kidney and anti-kidney vortices in cross flow jets, *J. Fluid Mech.,* **352**, 27-64, 1997.

Ho, C.M. and Gutmark, E. Vortex induction and mass entrainment in a small-aspect-ratio elliptic jet, *J. Fluid Mech.,* **179**, 383-405, 1987.

Husain, H.S. and Hussain, F. Elliptic jets. Part 2. Dynamics of coherent structures: pairing, *J. Fluid Mech.,* **233**, 439-482, 1991.

Ivanov, Yu.V. Equations for trajectories of jets with acute blast, *Sovetskoe Kotloturbostroenie*, **8**, 1952.

Jordinson, R. Flow in a jet directed normal to the wind, *Aero. Research. Council, London, R and M*, 3074, 1956.

Kamotani Y. and Greber, I. Experiments on a turbulent jet in a cross flow, *AIAA J.,* **10**, 1425-1429, 1972.

Karagozian, A.R. An analytical model for the vorticity associated with a transverse jet, *AIAA J.,* **24**, 429-436, 1986.

Keffer, J.F. and Baines, W.D. The round turbulent jet in a crosswind, *J. Fluid Mech.,* **15**, 481-496, 1963.

Kelso, R.M., A study of shear flows near rigid boundaries, *Ph.D. Dissertation*, University of Melbourne, 1991.

Kelso, R.M., Lim, T.T. and Perry, A.E. An experimental study of round jet in cross flow, *J. Fluid Mech.,* **306**, 111-144, 1996.

Kelso, R.M. and Smits, A.J. Horseshoe vortex systems resulting from the interaction between a laminar boundary layer and a transverse jet, *Phy. Fluids,* **7**, 153-158, 1995.

Kim, K.C., Kim, S.K. and Yoon, S.Y. PIV measurements of the flow and turbulent characteristics of a round jet in crossflow, *J. Visualization*, **3**, 2, 157-164, 2000.

Krothapalli, A., Lourenco L. and Buchlin, J.M. Separated flow upstream of a jet in a crossflow, *AIAA J.,* **28**, 414-420, 1990.

Lee, J.H.W., Li, L. and Cheung, V. Semianalytical self-similar solution of bent-over jet in cross-flow, *J. Eng Mech-ASCE,* **125**, 733-746, 1999.

Liepmann, D. and Gharib, M. The role of streamwise vorticity in the near-field entrainment of round jets, *J. Fluid Mech.*, **245**, 643-668, 1992.

Lim, T.T. Dye and smoke visualization, In *Flow Visualization: Techniques and Examples*, (ed. Smits, A.J. and Lim, T.T.), Imperial College Press, 43-69, 2000.

Lim, T.T., New, T.H. and Luo, S.C. On the development of large-scale structures of a jet normal to a cross flow, *Phys. Fluids,* **13**, 770-775, 2001.

Lim, T.T., Kelso, R.M. and Perry, A.E. A visual study of vortex rings fired transversely into a cross-flow, *13ᵗʰ Australasian Fluid Mechanics Conference*, Monash University, Australia. **2**, 961-964, 1998.

Margason, R.J. Fifty years of jet in cross flow research, *AGARD-CP-**534***, 1-1 - 1-41, 1993.

McMahon, H.M., Hester, D.D. and Palfrey, J.G. Vortex shedding from a turbulent jet in a cross-wind, *J. Fluid Mech.,* **48**, 73-80, 1971.

Mehta, R.D. and Bradshaw, P. Design rules for small low speed wind tunnels, *Aero. J.,* **83**, 443, 1979.

Michalke, A. Survey on jet instability theory, *Prog. Aerospace Sci.*, **21**, 159-199, 1984.

Moussa, Z.M., Trischka, J.W. and Eskinazi, S. The near field in the mixing of a round jet with a cross-stream, *J. Fluid Mech.,* **80**, 49-80, 1977.

Needham, D.J., Riley, N. and Smith, J.H.B. A jet in cross-flow, *J. Fluid Mech.,* **188**, 159-184, 1988.

Needham, D.J., Riley, N., Lytton, C.C., and Smith, J.H.B. A jet in cross-flow. Part 2, *J. Fluid Mech.,* **211**, 515-528, 1990.

New, T.H., Lim, T.T. and Luo, S.C. On the effects of velocity profiles on the topological structures of a jet in cross flow, *Turbulent Shear Flow and Phenomena-1 Proc.*, 647-652, 1999.

New, T.H. A topological study of a jet in cross flow, *B.Eng. Dissertation*, National University of Singapore, 1998.

New, T.H., Lim, T.T. and Luo, S.C. A visual study on elliptical jets in cross flow, *9ᵗʰ Int Symp Flow Vis*, Paper **224**, 2000.

New, T.H., Lim, T.T. and Luo, S.C. Elliptic jets in cross-flow, *J. Fluid Mech.*, **494**, 119-140, 2003.

New, T.H., Lim, T.T. and Luo, S.C. A flow field study of an elliptic jet in cross flow using DPIV techniques, Accepted for publication by *Exp. Fluids,* 2003.

Nunn, R.H. Vorticity growth and decay in the jet in crossflow, *AIAA J.,* **23**, 473-475, 1985.

Patankar, S.V., Basu D.K. and Alpay, S.A. Prediction of the three-dimensional velocity field of a deflected turbulent jet, *Trans. ASME: J. Fluid Engrg.,* **758-762**, 1977.

Patrick, M.A. Experimental investigation of the mixing and penetration of a round turbulent jet injected perpendicularly into a transverse stream, *Trans. Inst. Chem. Engrg.,* **45**, T16-31, 1967.

Perry, A.E. and Lim, T.T. Coherent structures in coflowing jets and wakes, *J. Fluid Mech.,* **88**, 451-463, 1978.

Peterson, S.D. and Plesniak, M.W. Short-hole jet-in-crossflow velocity field and its relationship to film-cooling performance, *Exp. Fluids*, **33**, 889-898, 2002.

Pratte, B.D. and Baines, M. Profiles of the round turbulent jet in a crossflow *J. Hydronaut. Div. ASCE,* **92**, 53-64, 1967.

Rajarantnam, N. and Gangadharaiah, T. Vortex structure of circular jets in crossflow, *J. Wind Eng. and Industrial Aero.,* **12**, 155-164, 1983.

Rivero, A., Ferre, J.A. and Giralt, F. Organized motions in a jet in crossflow, *J. Fluid Mech.*, **444**, 117-149, 2001.

Rudman, M. Simulation of the near field of a jet in a cross flow, *Exp. Thermal Fluid Sci.,* **12,** 134-141, 1996.

Ruggeri, R.S., Callaghan, E.E. and Bowden, D.T. Penetration of air jets issuing from circular, square and elliptical orifices directly perpendicularly to an air stream, *NACA TN, 2019*, 1950.

Scorer, R.S. Natural aerodynamics, *Pergamon Press,* 1958.

Shandorov, G.S. Flow from a channel into stationary and moving media, *Zh. Tekhn. Fiz.,* **37**, 1, 1957.

Smith, S.H. and Mungal, M.G. Mixing, Structure and scaling of the jet in cross flow, *J. Fluid Mech.,* **357**, 83-122, 1998.

Sykes, R.I., Lewellen, W.S. and Parker, S.F. On the vorticity dynamics of a turbulent jet in a crossflow, *J. Fluid Mech.,* **168**, 393-413, 1986.

Weston R.P. and Thames, F.C. Properties of aspect-ratio 4.0 rectangular jets into a subsonic crossflow, *J. Aircraft*, **16**, 10, 701-707, 1979.

Williamson, C.H.K. Three-dimensional wake transition, *J. Fluid Mech.,* **328**, 345-407, 1996.

Wu, J.W., Vakili, A.D. and Yu, F.M. Investigation of the interacting flow of nonsymmetric jets in crossflow, *AIAA J.,* **26**, 940-947, 1988.

Yuan, L.L., Street, R.L. and Ferziger, J.H. Large-eddy simulations of a round jet in crossflow, *J. Fluid Mech.,* **379**, 71-104, 1999.

Zaman, K.B.M.Q. and Foss, J.K. The effect of vortex generators on a jet in a cross-flow, *Phys. Fluids*, **9**, 106-114, 1997.